Seismic Risk Analysis for Nuclear Energy Facilities

by

Zhaoliang Wang

A thesis
presented to the University of Waterloo
in fulfilment of the
thesis requirement for the degree of
Doctor of Philosophy
in
Civil Engineering

Waterloo, Ontario, Canada, 2015

Author's Declaration

I hereby declare that I am the sole author of this thesis. This is a true copy of the thesis, including any required final revisions, as accepted by my examiners.

I understand that my thesis may be made electronically available to the public.

Abstract

Earthquakes are destructive natural disasters that can inflict various levels of damage on engineering structures and lead to other adverse consequences. Accurate seismic risk quantification of critical engineering structures such as nuclear power plants is of great importance, not only for answering public safety concern but also for facilitating risk-informed decision making.

Seismic Probabilistic Risk Analysis (SPRA) has been widely used for seismic analysis and design of critical engineering structures. It combines the probabilistic model of the behavior of structural response given a ground-motion parameter (GMP) value (e.g., seismic fragility model) and the Probabilistic Seismic Hazard Analysis (PSHA) for the GMP in a mathematically rigorous manner. However, there are a number of issues on the engineering application of SPRA that need to be addressed before it can be readily implemented into current engineering practice.

In current SPRA practice, both the fragility model and PSHA are based on a single GMP, which is adequate for the single-mode-dominant structures. For multiple-mode-dominant structures whose response could be better predicted using multiple GMP, a vector-valued SPRA is conceptually more appropriate. However, vector-valued SPRA requires extensive computational efforts and extensive consultation of vector-valued PSHA from seismologists, which prevent it from being ready for engineering purposes.

The objective of this study is to bridge the gaps between seismological analyses and engineering applications, i.e., to address the immediate issues in current vector-valued SPRA so that it can be readily applied into engineering practice. A new seismic hazard deaggregation procedure is developed for seismic risk analysis, which determines a set of controlling earthquakes that induce dominant hazard to the site of interest. A simplified approach to vector-valued SPRA is developed based on the controlling earthquakes. Integration over all possible earthquake occurrences in standard vector-valued SPRA is then avoided, which substantially improves the computational efficiency without losing accuracy. This overcomes the deficiencies and preserves the advantages of standard vector-valued SPRA. To

facilitate performing the simplified approach, factors affecting the accuracy of the simplified approach are discussed and illustrated through the numerical examples.

In addition, seismic capacity evaluation of nuclear facilities is an important task in a SPRA. However, following the current evaluation procedures, inconsistency in seismic capacity estimates are often obtained for the same facility in similar plants at different locations. The inconsistency also shows dependency on the GMP selected for defining seismic capacity. This inconsistency is conceptually undesirable for engineering purposes.

To characterize the possible factors affecting the consistency in seismic capacity estimates, a comprehensive parametric study is performed in an analytical manner. Theoretical derivations and graphical illustrations are resorted to facilitate the analysis. Both general and case-by-case analyses are performed to show how each of these factors affects the consistency in seismic capacity estimates. This parametric study represents a wide coverage of seismic capacity evaluating problems for nuclear facilities, and hence can be used for interpreting results of similar kinds in current engineering practice.

Acknowledgments

The author wishes to express his most sincere gratitude to his supervisors, Professor Mahesh D. Pandey and Professor Wei-Chau Xie, for their on-going and inspiring guidance, encouragement, and support during the course of this study.

Special thanks are due to research group members, Dr. Sun-Hao Ni, Bo Li, Wei Jiang, Zhen Cai, Sen Long, for many enlightening discussions and suggestions.

Extended thanks go to author's friends and colleagues, Dr. Dong-Liang Lu, Woody Wan, Jingnan Liu, Shuo Yu, Scarlet Liu, Xiaoli Yuan, Shijun Yang, Kevin Goorts, Justin Breg, Jacob Guenther, Andrew Hilliard, Dave Elliott, for sharing unforgettable days in Waterloo.

The financial support by the Natural Sciences and Engineering Research Council of Canada (NSERC) and the University Network of Excellence in Nuclear Engineering (UNENE) in the form of Research Assistantship is gratefully acknowledged.

Last but not least, the author wishes to express special appreciation to his grandma and his parents for their silent support and encouragement.

TO

My Grandma

Contents

List of Figures xi

Nomenclature xvii

1 **Introduction** 1

1.1 Overview 1

1.2 Research Objectives 5

1.3 Organization of This Study 5

2 **Seismic Risk Analysis of Engineering Structures** 8

2.1 Introduction 8

2.2 Probabilistic Seismic Hazard Analysis 9

2.2.1 Seismic Source Model 10

2.2.2 Ground-Motion Prediction Equations 13

2.2.3 Scalar Probabilistic Seismic Hazard Analysis 19

2.3 Scalar Seismic Risk Analysis 23

2.3.1 Fragility Model Considering a Single Ground Motion Parameter 23

2.3.2 Integrating Seismic Hazard to Seismic Risk 24

2.4 Summary 25

3 **Vector-valued Seismic Risk Analysis** 26

3.1 Background 26

3.2 Vector-valued Seismic Risk Analysis — A Standard Formulation 27

3.2.1 Vector-valued Probabilistic Seismic Hazard Analysis 27

3.2.2 Fragility Model Considering Multiple Ground motion Parameters 30
3.2.3 Integration for Seismic Risk 30
3.3 Vector-valued Seismic Risk Analysis — A Simplified Approach 34
3.3.1 Dominant Hazard Range for Risk Analysis 34
3.3.2 Seismic Hazard Deaggregation 37
3.3.3 Proposed Procedure for Simplified Seismic Risk Analysis 43
3.4 Numerical Examples 54
3.4.1 20-storey Steel Moment Resisting Frame 54
3.4.2 Seismic Risk Analysis at a Hypothetical Site 57
3.4.3 Seismic Risk Analysis at a Realistic Site 63
3.5 Conclusions 81

4 Seismic Fragility Analysis for Nuclear Facilities 92
4.1 Seismic Fragility Analysis Methodology 93
4.1.1 Definition of Seismic Fragility 95
4.1.2 Seismic Fragility Model 95
4.1.3 Failure Modes 99
4.1.4 Estimation of Fragility Parameters 100
4.1.5 Procedure of Fragility Analysis 102
4.2 Fragility Analysis of the Block Masonry Wall 107
4.2.1 Background 107
4.2.2 Basic Variables 110
4.2.3 Static Capacity Analysis 110
4.2.4 Demand Analysis 116
4.2.5 Median Seismic Capacity 119
4.2.6 Logarithmic Standard Deviations 120
4.2.7 CDFM-Calculated Capacity 123
4.2.8 Comparison of Results 127

4.3 Fragility Analysis of the Horizontal Heat Exchanger 129
4.3.1 Background 129
4.3.2 Basic Variables 133
4.3.3 Demand Analysis 136
4.3.4 Capacity Analysis 142
4.3.5 Strength Factor and the Median Seismic Capacity 143
4.3.6 Logarithmic Standard Deviations 144
4.3.7 CDFM-calculated Capacity 144
4.3.8 Comparison of Results 147
4.4 Summary 148

5 Parametric Evaluation of Seismic Capacity for Nuclear Facilities 149
5.1 Background 149
5.2 Scope of the Parametric Study 151
5.2.1 Input Ground Response Spectra 152
5.2.2 Primary Structures 154
5.2.3 Floor Response Spectra 155
5.2.4 Secondary Structures 158
5.2.5 Ground Motion Parameters 162
5.3 Parametric Study of the Uniform Shear Beam 162
5.3.1 Idealized SDOF Model 163
5.3.2 Idealized MDOF Model 175
5.3.3 Conclusions and Recommendations from Parametric Study 179
5.4 Numerical Examples 181
5.4.1 Block Wall Median Seismic Capacity 181
5.4.2 Heat Exchanger Median Seismic Capacity 182
5.5 Conclusions 184

6 **Conclusions** **187**

6.1 New Deaggregation Procedure for Seismic Risk Analysis 187

6.2 Simplified Vector-valued Seismic Risk Analysis 188

6.3 Parametric Evaluation of Seismic Capacity for Nuclear Facilities 189

A **Appendix** **191**

A.1 Spectral correlation model by Baker&Jayaram (2008) 191

A.2 Empirical Scaling Relations 192

A.3 Activity Rate 193

A.4 Basics of Lognormal Distribution 194

A.5 Basic Variables for the Block Masonry Wall 196

A.6 Model Uncertainty for Block Wall Moment Strength 201

A.7 Capacities Analyses for the Heat Exchanger 203

Bibliography **209**

List of Figures

1.1 Methodology for seismic probabilistic risk analysis 3

2.1 Probability distributions of source-site distance 11

2.2 Weighted model for magnitude recurrence by Youngs and Coppersmith (1985) 12

2.3 Renewal model for earthquake occurrence given T_e: (a)updated (lognormal) distribution of time-to-occurrence, (b) conditional probability of occurrence for different variabilities 14

2.4 Median spectral accelerations at $T = 1$ and 0.1 sec predicted by A&S-97 GMPE 18

2.5 Logarithmic standard deviations for average or arbitrary horizontal components from A&S-97 GMPE 18

2.6 Hypothetical configuration of seismic source zones 22

2.7 Seismic hazard curves for spectral accelerations at 0.1 and 1.0 sec 22

3.1 Correlation coefficients of spectral accelerations by Baker and Jayaram (2008) 29

3.2 Contours of joint hazard for spectral accelerations at 0.1 and 1.0 sec 31

3.3 Probability density of joint hazard for spectral accelerations at 0.1 and 1.0 sec 31

3.4 Energy distribution in different spectral acceleration dimensions 33

3.5 Example hazard curve and fragility curve for risk quantification 35

3.6 Seismic hazard deaggregation for SA at 0.1 and 1 sec at 3 probability levels 40

3.7 Vector-valued seismic hazard deaggregation for SA at 0.1 and 1.0 sec 42

3.8 Framework of the simplified approach to VSRA 45

3.9 Hazard curve approximations for SA at 1 sec using deaggregated earthquakes at 3 probabilities: 50%/50yr, 10%/50yr, and 2%/50yr 50

3.10 Hazard curve approximations for SA at 0.1 sec using deaggregated earthquakes at 3 probabilities: 50%/50yr, 10%/50yr, and 2%/50yr 50

3.11 Controlling earthquakes for $S_a(T=1\,\text{sec})$ (50%/50 yr) 52

3.12 Controlling earthquakes for $S_a(T=0.1\,\text{sec})$ (2%/50 yr) 52

3.13 Secondary hazard approximation for $S_a(T=1\,\text{sec})$ using the controlling earthquakes for $S_a(T=0.1\,\text{sec})$ 53

3.14 Secondary hazard approximation for $S_a(T=0.1\,\text{sec})$ using the controlling earthquakes for $S_a(T=1\,\text{sec})$ 53

3.15 Floor plans and elevations of 20-storey SMRF model 55

3.16 Fragility curves for four limit states 58

3.17 Fragility surfaces for four limit states 58

3.18 Seismic hazard curves for spectral accelerations at 4.0 sec and 1.33 sec 60

3.19 Seismic hazard surface for spectral accelerations at 4.0 sec and 1.33 sec 60

3.20 Seismic risk curves for the hypothetical site 61

3.21 Hazard curve approximations for risk analysis at the hypothetical site 62

3.22 Risk curve approximations for 20-storey SMRF at the hypothetical site 62

3.23 Seismic faults surrounding the DCPP site in California 64

3.24 Probability density function of earthquake magnitude for 12 fault segments 65

3.25 Hazard curve for PGA at the DCPP site 69

3.26 Hazard curve for SA at 0.2 sec at the DCPP site 69

3.27 Hazard curve for SA at 1.0 sec at the DCPP site 70

3.28 Hazard curve for SA at 4.0 sec at the DCPP site 70

3.29 Seismic hazard curves for SA at 4.0 and 1.33 sec at the DCPP site 72

3.30 Seismic risk curves for the 20-storey SMRF at the DCPP site 72

3.31 Contributions to hazard for $S_a(T_1 = 4\,\text{sec})$ at two probability levels 73

3.32 Hazard curve approximations for $S_a(T_1)$ achieved by deaggregation towards s_1 at 3 probabilities 74

3.33 Secondary hazard curve approximations for $S_a(T_2)$ achieved by deaggregation towards s_1 at 3 probabilities 74

3.34 Hazard curve approximations achieved by deaggregation towards $\lambda_s = 10\%/50\text{yr}$ 75

3.35 Best hazard curve approximations for both $S_a(T_1)$ and $S_a(T_2)$ 76

3.36 Best risk curve approximations for the 20-storey SMRF at DCPP site 76

3.37 Hazard curve approximations using scheme 1c, $r_{\max} = 200$ km 82

3.38 Risk curve approximations using scheme 1c, $r_{\max} = 200$ km 82

3.39 Hazard curve approximations using scheme 1d, $r_{\max} = 70$ km 83

3.40 Risk curve approximations using scheme 1d, $r_{\max} = 70$ km 83

3.41 Hazard curve approximations using scheme 2b, trisection of M 84

3.42 Risk curves approximations using scheme 2b, trisection of M 84

3.43 Hazard curve approximations using scheme 2c, trisection of R 85

3.44 Risk curves approximations using scheme 2c, trisection of R 85

3.45 Hazard curve approximations using scheme 2d, trisections of both M and R 86

3.46 Risk curves approximations using scheme 2d, trisections of both M and R 86

3.47 Hazard curve approximations using scheme 3b, $N_C = 6 \times 6$ and $s_1 = 0.035\,g$ 87

3.48 Risk curves approximations using scheme 3b, $N_C = 6 \times 6$ and $s_1 = 0.035\,g$ 87

3.49 Hazard curve approximations using scheme 3c, $N_C = 6 \times 6$ and $s_1 = 0.040\,g$ 88

3.50 Risk curves approximations using scheme 3c, $N_C = 6 \times 6$ and $s_1 = 0.040\,g$ 88

3.51 Hazard curve approximations using scheme 3d, $N_C = 2 \times 2$ 89

3.52 Risk curves approximations using scheme 3d, $N_C = 2 \times 2$ 89

3.53 Hazard curve approximations using scheme 3e, $N_C = 1 \times 1$ 90

3.54 Risk curves approximations using scheme 3e, $N_C = 1 \times 1$ 90

4.1 Procedure of performing seismic fragility analysis 94

4.2 Example fragility curves 96

4.3 HCLPF capacity on fragility curves 99

4.4 Block masonry wall 108

4.5 Hysteretic loop of centrally-reinforced block masonry wall 108

4.6 Reference ground response spectra 109

4.7 Floor response spectra 111

4.8 Modal information of primary structure 111

4.9 Block wall free body diagrams 115

4.10 Fragility curves for the block wall 123

4.11 Floor response spectrum for CDFM capacity evaluation 125

4.12 Seismic hazard curve for PGA at the DCPP site 129

4.13 Example heat exchanger 131

4.14 Stiffness of a stiffener plate 137

4.15 Rotational vibration in the transverse direction 138

4.16 Forces due to longitudinal excitation 141

4.17 Forces due to transverse rocking 141

4.18 Bilinear interaction of bolt tension and shear 143

5.1 Seismic evaluation of secondary structures 150

5.2 Three chosen median spectral shapes 153

5.3 Ground's motion $S_A(f_0, \zeta_0)$ in the entire frequency range (lines) and structure's motion $S_A(f_k, \zeta_k)$ at modal frequencies of primary structure (circles), for all 4 primary structures 157

5.4 Modal amplification factors ($\zeta_0 = \zeta_k = 5\%$) 158

5.5 Floor response spectra for structure S-1 159

5.6 Floor response spectra for structure S-2 159

5.7 Floor response spectra for structure S-3 160

5.8 Floor response spectra for structure S-4 160

5.9 Uniform shear beam models, material properties, analytic formulas of modal information and response components 161

5.10 Median seismic capacity of the SDOF beam model in structure S-1 164

5.11 Median seismic capacity of the SDOF beam model in structure S-2 165

5.12 Median seismic capacity of the SDOF beam model in structure S-3 166

5.13 Median seismic capacity of the SDOF beam model in structure S-4 167

5.14 Amplification factors of FRS for structure S-1 169

5.15 Amplification factors of FRS for structure S-2 169

5.16 Amplification factors of FRS for structure S-3 170

5.17 Amplification factors of FRS for structure S-4 170

5.18 $S_A^2(f_k, \zeta_k)/S_A^2(f_0, \zeta_0)$ ratios of mode $k = 1, 2, 3, 4$ for primary structure S-2 171

5.19 FRS, AF, Seismic capacity plots for primary structures S-1 and S-3 173

5.20 Tri-Capacity of the original 10-DOF beam model on structure S-2 177

5.21 Tri-Capacity of 10-DOF beam model on structure S-2, with designated Γ_n =[0.6 0.6 0.38 0.28 0.18 0.12 0.08 0.05 0.03 0.02] 178

5.22 Median seismic capacity of block masonry wall in structure S-2, in comparison with results from parametric study 183

5.23 Median seismic capacity of heat exchanger in structure S-2 185

A.1 Probability density function of lognormal distribution 195

A.2 Lognormal distribution of X 196

A.3 Typical force-displacement relation 202

A.4 Anchorage failure modes 203

A.5 Yield line pattern of the base plate 206

A.6 Fillet weld failure 208

Nomenclature

A_m	Best estimate of median ground motion capacity
A_{Ref}	Acceleration from a reference level earthquake
CDF	Cumulative Distribution Function
CDFM	Conservative Deterministic Failure Margin
CENA	Central and Eastern North America
COV	Coefficient of Variation
DCPP	Diablo Canyon Power Plant
DOF	Degree-of-Freedom
EDP	Engineering Demand Parameter
EP	Exceedance Probability
EPRI	Electric Power Research Institute
GMPE	Ground-Motion Prediction Equation
GSC	Geological Survey of Canada
HCLPF	High Confidence of Low Probability of Failure
MDOF	Multiple Degrees-of-Freedom
(m_C, r_C, ν_C)	Controlling earthquake in terms of magnitude, source-site distance, and occurrence rate
NEP	Non-Exceedance Probability
NGA	Next Generation Attenuation
NPP	Nuclear Power Plant
PDF	Probability Density Function
PEER	Pacific Earthquake Engineering Research

PGA	Peak Ground Acceleration
PMF	Probability Mass Function
PSHA	Probabilistic Seismic Hazard Analysis
RP	Return Period
SA	Spectral Acceleration
SDC	Seismic Design Category
SDOF	Single Degree-of-Freedom
SHD	Seismic Hazard Deaggregation
SPRA	Seismic Probabilistic Risk Analysis
SRSS	Square-Root-of-Sum-of-Squares
SSC	Structure, System, or Component
UHS	Uniform Hazard Spectrum
USGS	U.S. Geological Survey
USNRC	U.S. Nuclear Regulatory Commission
VSRA	Vector-valued Seismic Risk Analysis
WNA	Western North America

C H A P T E R 1

Introduction

Seismic probabilistic risk analysis (SPRA) is an integral part of the risk assessment of critical engineering structures such as nuclear power plants. The objectives of SPRA are to estimate the frequencies of occurrence of earthquake-induced accidents that may lead to different levels of damage and to identify the key risk contributors so that necessary risk reductions may be achieved (Kennedy and Ravindra, 1984). Quantitative assessment of seismic risk to structures, however, is challenging because of its multi-disciplinary nature and uncertainties present in many aspects of the assessment.

In Section 1.1, the general procedure of seismic risk analysis is presented and several issues regarding its engineering applications are discussed. Based on the problems stated in Section 1.1, the research objectives are presented in Section 1.2. The organization of this thesis is described in Section 1.3.

1.1 Overview

In the last 20 years, a number of destructive earthquakes occurred (e.g., 1995 Kobe, 1999 Chi-Chi, 2005 Kashmir, 2010 Chile, and 2011 Tohoku). An increasing public safety concern on nuclear energy facilities was prompted and systematic reviews of plant seismic safety have been taking place worldwide. New regulatory guidelines are developed to strengthen the protection against future seismic events (USNRC, 2007, 2012b; EPRI, 2012). Seismic evaluation need to be conducted not only for answering the public safety concern but also

for satisfaction of the request from the U.S. Nuclear Regulatory Commission (NRC) for information regarding severe accident vulnerabilities (EPRI, 2013).

Seismic probabilistic risk analysis (SPRA) has been widely used in seismic analysis and design of nuclear power plants. It combines the probability model of the behavior of structural response given a specific ground motion parameter (GMP) value (e.g., seismic fragility model) and the probabilistic seismic hazard analysis (PSHA) for the GMP in a mathematically rigorous manner. The uncertainties in the behavior of structural response, the historical seismicity, the sizes of earthquakes, the locations of earthquakes, and the variations of ground-motion characteristics with earthquake sizes and locations can be identified, quantified, and combined to describe the seismic risk of the structure at the site of interest.

The general methodology of the SPRA for nuclear energy facilities involves the following elements (McGuire, 2004; EPRI, 1994, 2013):

1. Seismic Hazard Analysis

The probability of exceedance for a selected GMP in a specified time period is evaluated using the PSHA. This analysis mainly involves the seismic sources characterization, the evaluation of regional earthquake history, and an estimate of the expected earthquake-induced ground motion intensity at the site. The result is typically represented by a *mean seismic hazard curve*, where the probability of exceedance $H(a)$ is plotted against the selected ground motion parameter a, as shown in Figure 1.1(a).

2. Seismic Fragility Analysis

The conditional probability of failure of a structure, system, or component (SSC) for a given GMP value is estimated. Seismic fragilities used in a SPRA are realistic and plant-specific, based on actual current SSC conditions in the plant. The SSC fragility is typically described by a *mean fragility curve* of the probability of failure $p_F(a)$ plotted against the selected GMP a, as shown in 1.1(b). Physically, it represents the probability of seismic capacity A of the SSC less than the seismic demand a. Evaluation of seismic capacity A, including the median seismic capacity A_m and its associated variabilities, is the core part of fragility analysis.

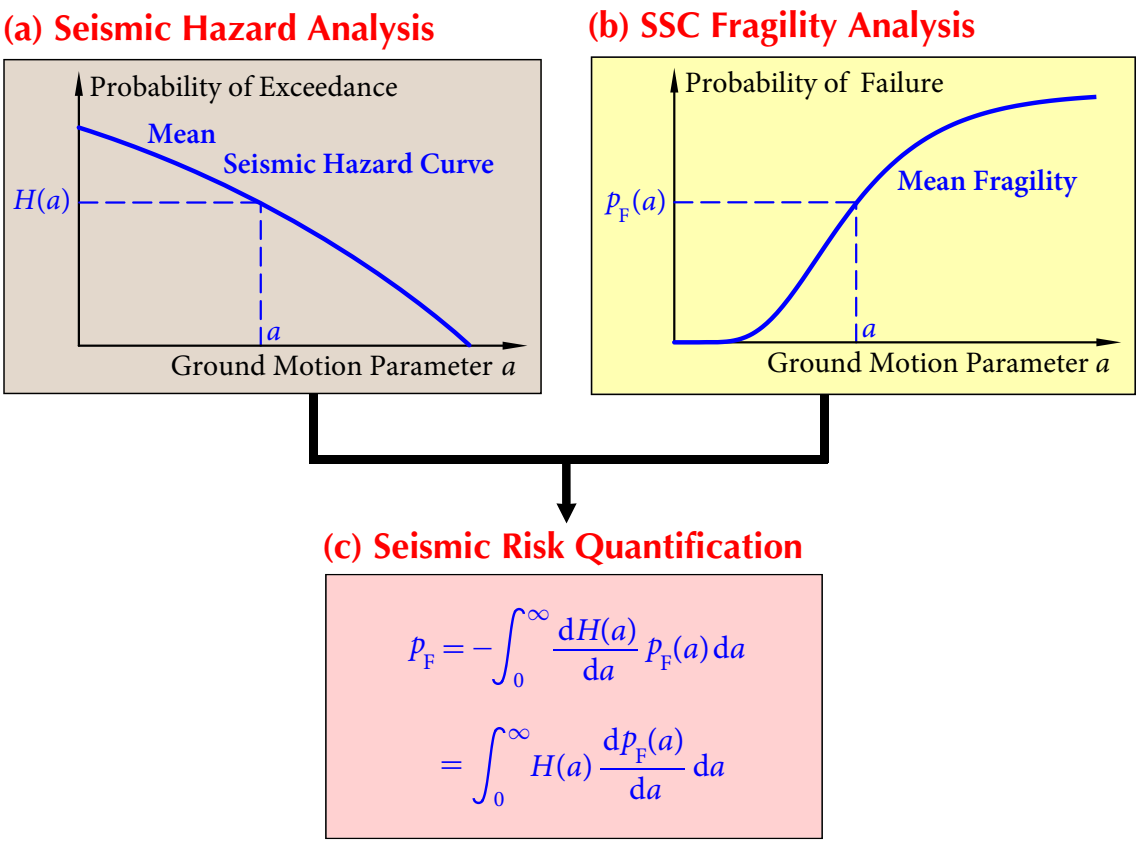

Figure 1.1 Methodology for seismic probabilistic risk analysis

3. Risk Quantification

The seismic risk (i.e., the probability of failure or any adverse consequence due to earthquake threats) for a SSC, is calculated according to the risk equation as shown in Figure 1.1(c), by using the mean seismic hazard curve and mean fragility curve. The result is given by a point risk value, indicating the probability of occurrence in a time period.

In case when the plant level seismic risk is of interest, a system analysis is required before the final risk quantification. The fragilities of all the SSCs that participate in the accident sequences, such as severe core damage, need to be included. A plant logic model, showing various combinations of the SSC failures that could initiate and propagate a seismic damage sequence, need to be constructed using the logic tree analysis. Hence, a plant level mean fragility curve obtained for the damage sequence will be used instead of a specific SSC, in the plant level risk quantification.

In general, the seismic hazard analysis is performed by seismologists while the fragility analysis is conducted by structural engineers. There are several gaps between seismological analyses and engineering applications in the framework of SPRA methodology, which are discussed in the following.

1. The risk equation shown in Figure 1.1(c) is based on the conventional PSHA (Cornell, 1968; McGuire, 1993), which determines the seismic hazard in terms of a single GMP. In case when a single GMP is sufficient for predicting the seismic response and fragility of a SSC, such as a single degree-of-freedom (DOF) structure, the risk quantification is conceptually accurate.

   In practice, an engineering structure is usually modelled as a linear/nonlinear multiple degrees-of-freedom system. In earthquake events, it will respond to different frequency contents of seismic excitations simultaneously. Structural response parameters, such as the maximum inter-story drift ratio and maximum base shear, can be strongly dependent on several important vibration modes. In this case, structural behavior subjected to seismic excitations can be more effectively predicted if more than one GMP, closely related to structural responses, are adopted.

   To provide a knowledge of joint seismic hazard in terms of multiple GMP, the recent vector-valued PSHA (Bazzurro and Cornell, 2002) needs to be performed. Extensive consultations with seismologists are inevitably needed, which include such topics as seismic source model, ground-motion prediction equations, probability distributions of spectral accelerations, and correlation of spectral accelerations.

   In current engineering practice, however, no more than one GMP has been used in seismic risk quantification due to the extensive computational efforts required for the multiple dimensional cases. Hence, seismic risk analysis cannot be performed with computational ease for structures having multiple significant modes or structural failures closely related to multiple GMP. Thus, a computationally efficient seismic risk analysis method based on multiple GMP is desired.

2. In step (b) of the SSC fragility analysis, the primary task is to determine the three fragility parameters: the median seismic capacity A_m defined by a selected GMP, and

two logarithmic standard deviations of β_R, representing the randomness in A, and β_U, representing the uncertainty in estimating A_m.

The median seismic capacity A_m is estimated through the factor of safety against a selected reference earthquake A_{ref} (response spectrum). Factors of safety associated with each of the basic demand and capacity variables affecting seismic capacity should be evaluated. The product of all factors of safety is then the overall factor of safety against the reference earthquake A_{ref}.

In engineering practice, due to the variations in seismological environment, the reference earthquake at one site often shows a very different spectral shape than that at another site. Seismic capacity estimates A_m of a SSC at different sites, obtained following the current evaluation procedures (EPRI, 1991a, 1994, 2009), can be very inconsistent. In addition, using different GMPs may also lead to inconsistent A_m estimates. This inconsistency is obviously undesirable for seismic evaluation. Efforts are needed to characterize the possible factors affecting the consistency in A_m estimates and to select an appropriate GMP to obtain more consistent A_m estimates.

1.2 Research Objectives

The research objective is to bridge the gaps between seismological analyses and engineering applications, i.e., to perform seismic analyses that can be more readily applied for engineering purpose or can facilitate current engineering practice. The computational efficiency of the multi-dimensional seismic risk analysis needs to be improved in order to put it into practical use. The factors affecting the inconsistency in seismic capacity estimates using the current evaluation procedures need to be investigated, so that the results of capacity estimates can be better explained and improvements can be actively sought.

1.3 Organization of This Study

In this study, a number of issues within the framework of the SPRA are investigated. In terms of dimension, following Professor Cornell's terminology convention of classifying PSHA into the scalar (one-dimensional) case and the vector-valued (multi-dimensional) case,

the SPRA is also classified into the scalar (one-dimensional) case and the vector-valued (multi-dimensional) case.

In Chapter 2, the basic concept of the conventional scalar SPRA is introduced. The core inputs of seismic source model, ground-motion prediction equations (GMPE), seismic hazard model, and seismic fragility model are briefly introduced. A single GMP is consistently used in the evaluation process. The scalar SPRA is the basics for the more advanced analysis presented in Chapter 3.

In Chapter 3, standard vector-valued SPRA is first established by combining the vector-valued PSHA and fragility model considering multiple GMP. Contributing factors to the computational complexity of standard vector-valued SPRA are identified. Based on the concept of mean value theorem of integration, a new seismic hazard deaggregation (SHD) procedure is proposed for purpose of risk analysis, which determines a set of controlling earthquakes in terms of magnitude, source-site distance, and occurrence rate. A simplified approach to vector-valued SPRA is developed based on the set of controlling earthquakes. Two numerical examples are presented to validate the effectiveness of the simplified approach. Factors affecting the accuracy and efficiency of the simplified approach are also investigated.

In Chapter 4, seismic fragility analyses of two commonly used components in nuclear power plants, the block masonry wall and a heat exchanger, are presented. General methodology of fragility analysis is described first. Then seismic fragilities of the two components in terms of their median seismic capacities and the associated variabilities are evaluated using a formal probabilistic fragility analysis (FA) method (EPRI, 1994). In addition, seismic fragilities in terms of the High-Confidence-of-Low-Probability-of-Failure (HCLPF) capacity are also evaluated using a simple deterministic method, called Conservative Deterministic Failure Margin (CDFM) method (EPRI, 1991a). Comparisons and discussions are made based on the results from these two popular methods. The procedure of seismic fragility/capacity analysis presented in Chapter 4 is the basics for the parametric study performed in Chapter 5.

In Chapter 5, a comprehensive parametric evaluation of seismic capacities for nuclear facilities is presented. Factors affecting the consistency of seismic capacity estimates are

evaluated in an analytical manner. The scope of the parametric study, including the input ground response spectra, primary structures, floor response spectra, secondary structures, and ground motion parameters are described. Seismic capacity evaluation starts first with the secondary structures being a simple linear single degree-of-freedom oscillator, and then being a linear multiple degrees-of-freedom structure to include the effect of higher-mode response in the analysis. General conclusions are drawn from this parametric study. Two realistic examples are presented to validate the results and conclusions from the parametric study.

C H A P T E R 2

Seismic Risk Analysis of Engineering Structures

In this chapter, the basics concept of seismic risk analysis (SRA) of engineering structures is introduced. It gives the background of vector-valued SRA presented in Chapter 3.

2.1 Introduction

Seismic risk of engineering structures has been defined as the potential damage or loss that may occur in hazardous earthquake events and the associated probabilities of occurrence (or exceedance) over a specified period of time (McGuire, 2004), where damage or loss can be measured in monetary terms, casualties, or loss of function. Seismic risk can be described by relationships of the form

$$\text{Seismic Risk} = (\text{Seismic Hazard}) \times (\text{Fragility}), \tag{2.1.1}$$

i.e., the determination of seismic risk entails seismic hazard analysis at the site, seismic fragility analysis of the structure, and combination of these analyses to obtain the probability of exceedance for any specific damage or loss.

While the ground-motion level in hazard model is continuous, the definition of structure's state in the fragility model is typically discrete. Consequently, seismic risk is typically estimated for damage state associated with a certain response threshold. For nuclear energy facilities, seismic risk estimate is typically related to the probability of failure. For ordinary

civil structures, it may be associated with a number of performance levels (Moehle and Deierlein, 2004; FEMA, 2006). In this chapter, the terminology "fragility model" is adopted for both the conventional fragility analysis for nuclear energy facilities and seismic damage (demand and capacity) analysis for ordinary civil structures.

The accuracy and efficiency in seismic risk quantification inherently depends on the approaches employed in both seismic hazard and structural response analyses. Seismic hazard at a site is typically evaluated using the Probabilistic Seismic Hazard Analysis (PSHA). Depending on the number of ground motion parameters (GMP) considered, PSHA can be either "scalar", corresponding to a single GMP, or "vector-valued", corresponding to a vector of GMP. Similarly, either scalar or vector-valued GMP can be adopted in the fragility model for predicting the damage of a structure inflicted by an earthquake. Convolution of hazard analysis and fragility analysis leads to scalar or vector-valued SRA.

In Section 2.2, the basics of scalar PSHA is described. In Section 2.3, SRA of engineering structures is performed by incorporating the fragility model considering a single GMP.

2.2 Probabilistic Seismic Hazard Analysis

Probabilistic Seismic Hazard Analysis (PSHA) (Cornell, 1968; McGuire, 2004) is a probabilistic method for quantifying the ground-motion hazard at a site of interest. By taking all possible earthquake occurrences into account and reflecting their relative contributions in the analysis, the expected seismic hazard for a specific level of ground-motion is evaluated. Three major modules of the conventional PSHA are (Atkinson and Goda, 2013):

(1) Seismic source model, a description of source geometry surrounding a particular site and the seismicity parameters of the sources;
(2) Ground-motion prediction equations, a prediction of ground-shaking intensities at the site due to surrounding seismic sources;
(3) Integration of hazard contributions using the total probability theorem and treatment of uncertainties.

The primary advantage of PSHA is that it integrates over all possible earthquake occurrences to provide a combined probability of exceedance (McGuire, 1995). Uncertainties in

historical seismicity, sizes of earthquake, locations of earthquake, and the resulting ground-motion shaking intensities, are explicitly considered. Because of these features, PSHA can be easily incorporated into seismic risk analysis and risk-informed decision making process. Besides, a design ground motion, at some acceptable level of exceedance probability, can be determined, facilitating a more intelligent and economic design.

2.2.1 Seismic Source Model

Seismic source model provides three dimensional geometry of potential seismic sources surrounding a site of interest and seismicity parameters of the sources, based on which probability distributions of source-site distance $f_R(r)$, earthquake magnitude $f_M(m)$, and the mean rate of earthquake occurrence ν can be derived. Seismic source model defines all possible earthquake occurrences (scenarios) at a site of interest.

Designation of Seismic Sources

Based on the earthquake catalog, which compiles historical and recent regional seismic activities, and geological and paleoseismic knowledge, seismic sources are designated for the region of study. Depending on the adequacy of geological data, seismic sources can be designated as active faults or areal source zones. For each source zone, three dimensional geometry along with seismicity parameters that might affect the resulting ground shaking intensities should be specified. Parameter uncertainties should also be provided.

Probability Distribution of Source-site Distance

Assuming that earthquake occurrences in a source zone are uniformly distributed and that all energy released is from the hypocenter of an earthquake, the probability distribution of source-site distance can be determined from geometrical relations between the source and the site.

For line faults, the probability distribution of source-site distance can be obtained analytically, given by the following probability density function (Kramer, 1996)

$$f_R(r) = \frac{r}{l\sqrt{r^2 - r_{\min}^2}}, \quad r_{\min} \leqslant r \leqslant r_{\max}. \tag{2.2.1}$$

where r is threshold value of R, l is the fault length, and $r_{\min}$ and $r_{\max}$ are the shortest and farthest distances from the site to the fault, respectively.

For areal source zones, usually modeled as smoothed-gridded sources, $f_R(r)$ can be estimated numerically by constructing a histogram of the percentage of distance in each bin plotted against the distance R from the gridded source-site distances (Kramer, 1996). Illustrative probability density functions $f_R(r)$ for typical sources are shown in Figure 2.1.

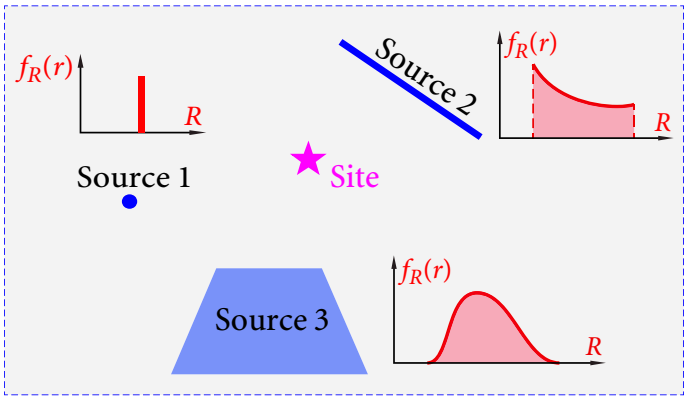

Figure 2.1 Probability distributions of source-site distance

Earthquake Recurrence Relation

The seismicity of each source can be expressed through a magnitude recurrence relation, which describes the mean annual rate of occurrence of earthquakes with magnitudes greater than m_i. The recurrence relation is computed by integrating the probability distribution of magnitude $f_M(m)$ scaled by the activity rate ν_{m_0}

$$\nu_{m_i} = \nu_{m_0} \int_{m_i}^{m_{\max}} f_M(m)\mathrm{d}m, \tag{2.2.2}$$

where m_0 is the smallest magnitude earthquake that can occur on a source, activity rate ν_{m_0} is the annual occurrence rate of earthquakes with magnitudes greater than m_0, and $m_{\max}$ is the maximum earthquake magnitude that a source can possibly produce. For engineering purpose, only earthquakes with magnitudes great than $m_{\min} = 5.0$ are of concern, and equation (2.2.2) can be used to obtain $\nu_{m_{\min}}$. It is noted that a consistent measure of magnitude scale, moment magnitude **M** (Hanks and Kanamori, 1979), related to the total moment of energy released during an earthquake, is often adopted.

1. Gutenberg-Richter (G-R) Model. The most widely used earthquake recurrence relation is given by the truncated Gutenberg-Richter (G-R) model (Gutenberg and Richter, 1944; Cosentino and Ficarra, 1977), with smaller earthquakes occurring more frequently than large ones. The probability density function of magnitude $f_M(m)$ is given by

$$f_M(m) = \frac{\beta \cdot \exp^{-\beta(m-m_{\min})}}{1 - \exp^{-\beta(m_{\max}-m_{\min})}}, \tag{2.2.3}$$

and the associated mean annual rate of occurrence $\nu_{m_{\min}}$ is given by

$$\nu_{m_{\min}} = \exp(\alpha - \beta m_{\min}), \tag{2.2.4}$$

where $\beta = b\ln(10)$ and $\alpha = a\ln(10)$. Richter a- and b- values are estimated from historical seismicity of the region, or inferred by analogy from other seismically similar regions.

2. Characteristic Earthquake Model. In some site-specific applications, geological evidence shows that individual faults tend to periodically generate large same-size or "characteristic" earthquakes within about 1/2 magnitude unit. In this case, the more complex characteristic earthquake recurrence law, governed by the geological data, can be used (Schwartz and Coppersmith, 1984; WGCEP, 2003).

A weighted combination of characteristic and G-R magnitude distributions are often used to characterize a source, e.g., most California faults. Figure 2.2 illustrates the concept of using weighted models for magnitude recurrence on a fault.

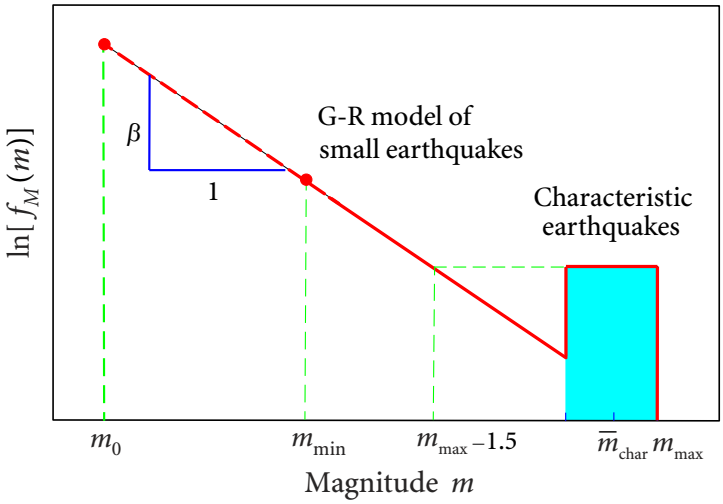

Figure 2.2 Weighted model for magnitude recurrence by Youngs and Coppersmith (1985)

Earthquake Occurrence with Time

To convert the recurrence rate of an earthquake into a probability of occurrence, the time-to-occurrence model for earthquakes is needed. The occurrence of earthquake of a given magnitude in a time interval t is often modeled as a Poisson process (Kramer, 1996; Anagnos and Kiremidjian, 1988). Assuming that an event may occur randomly at any time and the occurrence of an event in a time interval is independent of that in any other non-overlapping intervals, the probability of n events occurring in a time interval t is given by

$$p_{N_{\mathrm{E}}} = P\{N_{\mathrm{E}} = n\} = \frac{(\lambda t)^n}{n!}\mathrm{e}^{-\lambda t}, \quad n = 0, 1, 2, \cdots \tag{2.2.5}$$

where λ is a proportionality constant characterizing the mean rate of occurrence of an earthquake in a unit time interval.

Poisson estimate, based on constant occurrence rate, is appropriate in most practical cases. However, it might be problematic when seismic hazard is controlled by a single source for which the elapsed time T_{e} since the last significant event exceeds the mean time-to-occurrence (Cornell and Winterstein, 1988). The renewal model is more appropriate to capture the physical process of earthquake occurrence in predicting future event rate.

Renewal models allow the probability of earthquake occurrence to increase with T_{e} since the previous event (Matthews *et al.*, 2002) and are used in estimating occurrence probabilities of large earthquakes for California in the next 30 years interval (WGCEP, 2003). Figure 2.3 (a) shows the updated distribution for time-to-occurrence given no earthquake had occurred yet up to T_{e} since the previous event, where the Lognormal distribution with a median = 138 years and a logarithmic standard deviation $\sigma = 0.53$ is used. Its effect on the probability of occurrence $P_{30}^{T_{\mathrm{e}}}$ in the next 30 years interval depends on the variability in time-to-occurrence. Figure 2.3 (b) shows that small variability (e.g., $\sigma = 0.2$) results in a sharp increase in probability as T_{e} increases beyond some time point.

2.2.2 Ground-Motion Prediction Equations

While all possible earthquake occurrences surrounding the site are defined by the seismic source model, the ground shaking intensities induced by any earthquake scenario are predicted using the Ground-Motion Prediction Equations (GMPE).

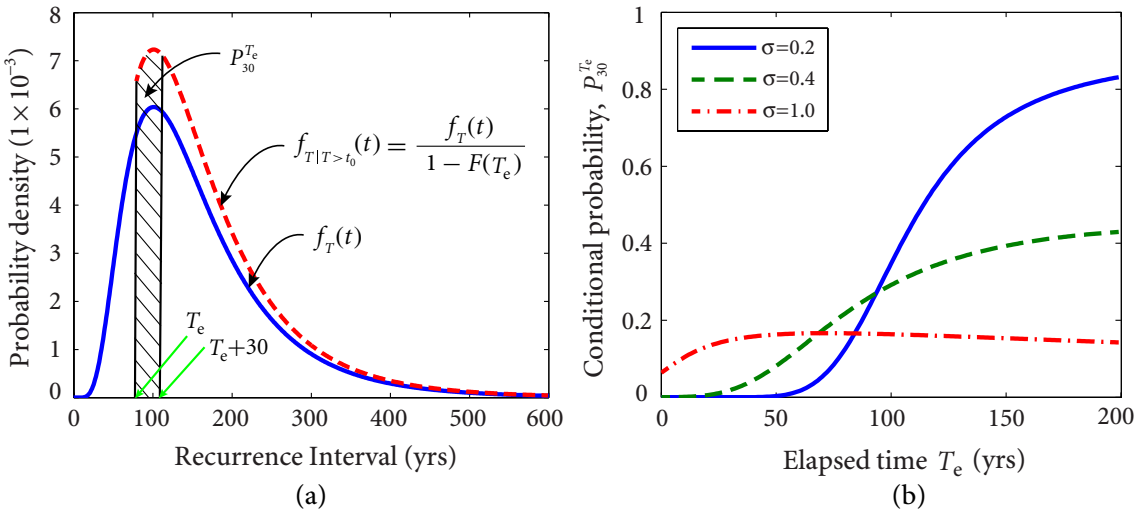

Figure 2.3 Renewal model for earthquake occurrence given T_e: (a)updated (lognormal) distribution of time-to-occurrence, (b) conditional probability of occurrence for different variabilities

General Form of Ground-Motion Prediction Equations

GMPE relate the ground shaking at the site to source characteristics (e.g., magnitude, distance to source, fault type, and rupture characteristics) and ground-motion modifications along the propagation path of seismic waves (USGS, 2008). The general form of GMPE for spectral acceleration $S_a(T_j)$ at vibration period T_j can be represented by

$$\ln S_a(T_j) = f(m, r, T_j, \boldsymbol{\theta}) + \sigma(m, T_j)\ \varepsilon(T_j), \tag{2.2.6}$$

where $f(m, r, T_j, \boldsymbol{\theta})$ is the expected value of the prediction equation, which is a function of the essential parameters of magnitude m and source-site distance r and other relevant predictor variables $\boldsymbol{\theta}$, such as fault type, hanging wall effect, seismic wave propagation path, and local site condition.

$\sigma(m, T_j)$ is the total standard deviation of the prediction equation model, which could be a combination of intra-event and inter-event aleatory uncertainties and a function of m, T_j, and other predictor variables.

$\varepsilon(T_j)$, independent of m and r, is the number of standard deviations σ by which $\ln S_a(T_j)$ deviates from the expected value $f(m, r, T_j, \boldsymbol{\theta})$ (Abrahamson and Silva, 1997; Atkinson and Boore, 2006). Given an earthquake scenario (known predictor variables m, r, and $\boldsymbol{\theta}$), $\varepsilon(T_j)$

has been verified to follow the standard normal distribution; consequently, $\ln S_a(T_j)$ follows the normal distribution given m, r, and $\boldsymbol{\theta}$ (Baker and Jayaram, 2008).

Modern GMPE invariably use moment magnitude **M** as magnitude scale. It is more critical to distinguish the distance parameter to be used. Specifically, for faults with ruptures designated as the source of energy release, the closest rupture-to-site distance should be used; for areal sources with smoothed-gridded seismicity designation, the hypocentral distance should be used (McGuire, 1993).

Due to diverse regional tectonic characteristics, GMPE are currently developed under three categories (Villaverde, 2009; USGS, 2008): (1) Shallow crustal earthquakes in active tectonic regions (e.g., western North America); (2) Shallow crustal earthquakes in stable continental regions (e.g., central and eastern North America); and (3) Subduction zones (e.g., northwest North America and Japan). In modern PSHA, multiple GMPE developed for the region of study are often used to account for the epistemic uncertainty from different GMPE developers (McGuire, 2004).

Example Ground-Motion Prediction Equations

Abrahamson and Silva (1997) developed a set of GMPE for shallow crustal earthquakes in western North America. The GMPE are applicable to both the geometric average of two horizontal components and the vertical component. Based on regression analyses of a database of 655 recordings from 58 earthquakes, the functional form $f(m, r, T_j, \boldsymbol{\theta})$ of the GMPE is given by

$$\ln S_a = f_1(\mathbf{M}, r_{\text{rup}}) + \text{F} \cdot f_3(\mathbf{M}) + \text{HW} \cdot f_4(\mathbf{M}, r_{\text{rup}}) + \text{S} \cdot f_5(\overline{\text{PGA}}_{\text{rock}}), \tag{2.2.7}$$

where S_a is spectral acceleration at a specific vibration period in g, **M** is the moment magnitude, r_{rup} is the closest distance to the rupture plane in km, F is a coefficient for style of faulting (1 for reverse, 0.5 for reverse/oblique, and 0 otherwise), HW is a coefficient for hanging-wall effect (1 for sites over the hanging wall and 0 otherwise), and S is a coefficient for generic local site conditions (0 for rock or shallow soil and 1 for deep soil).

Basic Form

Function $f_1(\mathbf{M}, r_{\text{rup}})$ in equation (2.2.7) is the basic functional form of the GMPE for

strike-slip events recorded at rock sites, given by

$$f_1(\mathbf{M}, r_{\text{rup}}) = a_1 + a(\mathbf{M}-6.4) + a_{12}(8.5-\mathbf{M})^n + \left[a_3 + a_{13}(\mathbf{M}-6.4)\right] \ln \sqrt{r_{\text{rup}}^2 + c_4^2}, \quad (2.2.8)$$

where $a = a_2$ for $\mathbf{M} \leqslant 6.4$ and $a = a_4$ for $\mathbf{M} > 6.4$.

Style-of-Faulting Factor

Difference of ground motion between reverse and strike-slip events is accounted for through function $f_3(\mathbf{M})$ in equation (2.2.7). By allowing for the magnitude and period dependence, this factor is given by

$$f_3(\mathbf{M}) = \begin{cases} a_5, & \text{for } \mathbf{M} \leqslant 5.8, \\ a_5 + \dfrac{a_6 - a_5}{6.4 - 5.8}, & \text{for } 5.8 < \mathbf{M} < 6.4, \\ a_6, & \text{for } \mathbf{M} \geqslant 6.4. \end{cases} \quad (2.2.9)$$

Hanging-Wall Effect

Function $f_4(\mathbf{M}, r_{\text{rup}})$ in equation (2.2.7) accounts for the hanging-wall effect, i.e., the differences in the motion in the hanging-wall and foot-wall of dipping faults. $f_4(\mathbf{M}, r_{\text{rup}})$ is modelled as magnitude and distance dependent

$$f_4(\mathbf{M}, r_{\text{rup}}) = f_{\text{HW}}(\mathbf{M}) \cdot f_{\text{HW}}(r_{\text{rup}}), \quad (2.2.10)$$

where

$$f_{\text{HW}}(\mathbf{M}) = \begin{cases} 0, & \text{for } \mathbf{M} \leqslant 5.5, \\ \mathbf{M} - 5.5, & \text{for } 5.5 < \mathbf{M} < 6.5, \\ 1, & \text{for } \mathbf{M} \geqslant 6.5, \end{cases}$$

$$f_{\text{HW}}(r_{\text{rup}}) = \begin{cases} 0, & \text{for } r_{\text{rup}} \leqslant 4 \text{ km}, \\ \frac{1}{4}\, a_9\, (r_{\text{rup}} - 4), & \text{for } 4 \text{ km} < r_{\text{rup}} \leqslant 8 \text{ km}, \\ a_9, & \text{for } 8 \text{ km} < r_{\text{rup}} \leqslant 18 \text{ km}, \\ a_9 \left[1 - \frac{1}{7}(r_{\text{rup}} - 18)\right], & \text{for } 18 \text{ km} < r_{\text{rup}} \leqslant 24 \text{ km}, \\ 0, & \text{for } r_{\text{rup}} > 24 \text{ km}. \end{cases}$$

Site Response

The nonlinear soil response term $f_5(\overline{\text{PGA}}_{\text{rock}})$ in equation (2.2.7) is modeled by

$$f_5(\overline{\text{PGA}}_{\text{rock}}) = a_{10} + a_{11} \ln\left(\overline{\text{PGA}}_{\text{rock}} + c_5\right), \tag{2.2.11}$$

where $\overline{\text{PGA}}_{\text{rock}}$ is the expected value of peak ground acceleration (PGA) on rock, as predicted by the expected prediction equation (2.2.7) with $\text{S} = 0$.

Standard Error

The total standard deviation $\sigma(m, T_j)$ in equation (2.2.6) of the GMPE, combining intra-event and inter-event aleatory uncertainties, is modeled as magnitude dependent and fit to the form

$$\sigma_{\text{total}}(\mathbf{M}, T_j) = \begin{cases} b_5, & \text{for } \mathbf{M} \leqslant 5.0, \\ b_5 - b_6(\mathbf{M} - 5), & \text{for } 5.0 < \mathbf{M} < 7.0, \\ b_5 - 2\,b_6, & \text{for } \mathbf{M} \geqslant 7.0. \end{cases} \tag{2.2.12}$$

In equation (2.2.12), $\sigma_{\text{total}}(\mathbf{M}, T_j)$ for the horizontal ground motions is determined for the geometric average of two horizontal components. The total standard deviation for arbitrary horizontal component can be obtained, by inflating $\sigma_{\text{total}}(\mathbf{M}, T_j)$ using a functional fit (Baker and Cornell, 2006b), as

$$\sigma_{\text{total,arb}}(\mathbf{M}, T_j) = \sigma_{\text{total}}(\mathbf{M}, T_j) \sqrt{\frac{2}{1.78 - 0.039 \ln T_j}}. \tag{2.2.13}$$

In equations (2.2.7)-(2.2.12), $a_1, \cdots, a_6, a_9, \cdots, a_{13}, c_4, c_5, n, b_5$, and b_6 are period dependent parameters of regression analysis.

Example median ground-motion predictions governed by equation (2.2.7) are shown in Figure 2.4 as a function of $\mathbf{M}$ and r_{rup}, for generic rock site with strike-slip fault. It is seen that high frequency content, $S_a(0.1\,\text{sec})$, attenuates faster than low frequency content, $S_a(1.0\,\text{sec})$, and that earthquakes with different $\mathbf{M}$ and r_{rup} induce ground motions rich in different frequency contents. Near-field earthquakes (small r_{rup}) induce ground motions rich in high frequency content, e.g., $S_a(0.1\,\text{sec}) > S_a(1.0\,\text{sec})$, while far-field earthquakes (large r_{rup}) induce ground motions sort of rich in low frequency content. The associated standard errors for both the average and arbitrary horizontal components, according to equations (2.2.12) and(2.2.13), respectively, are shown in Figure 2.5.

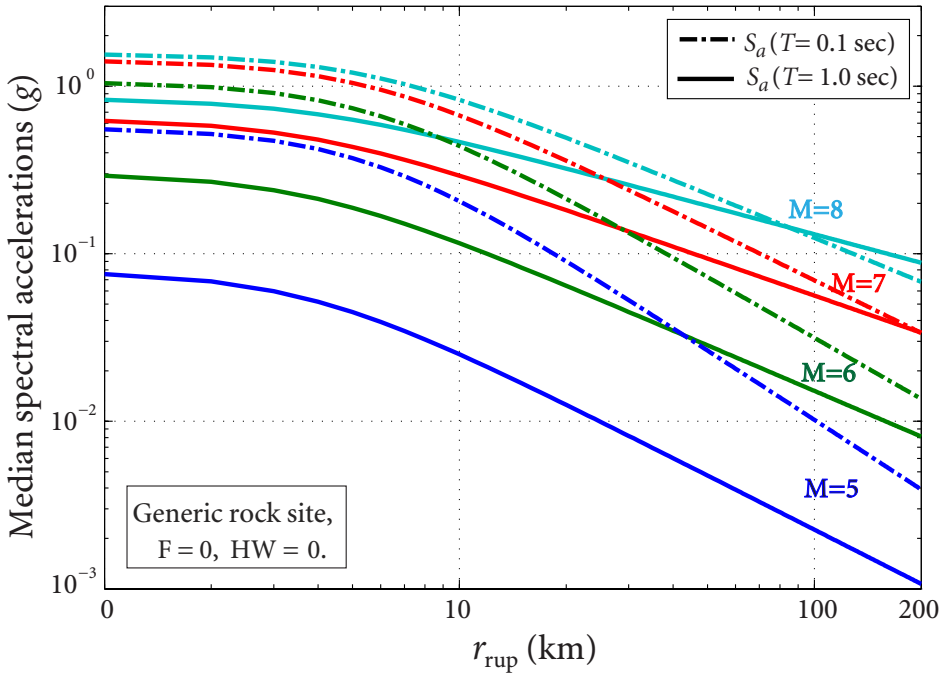

Figure 2.4 Median spectral accelerations at $T = 1$ and 0.1 sec predicted by A&S-97 GMPE

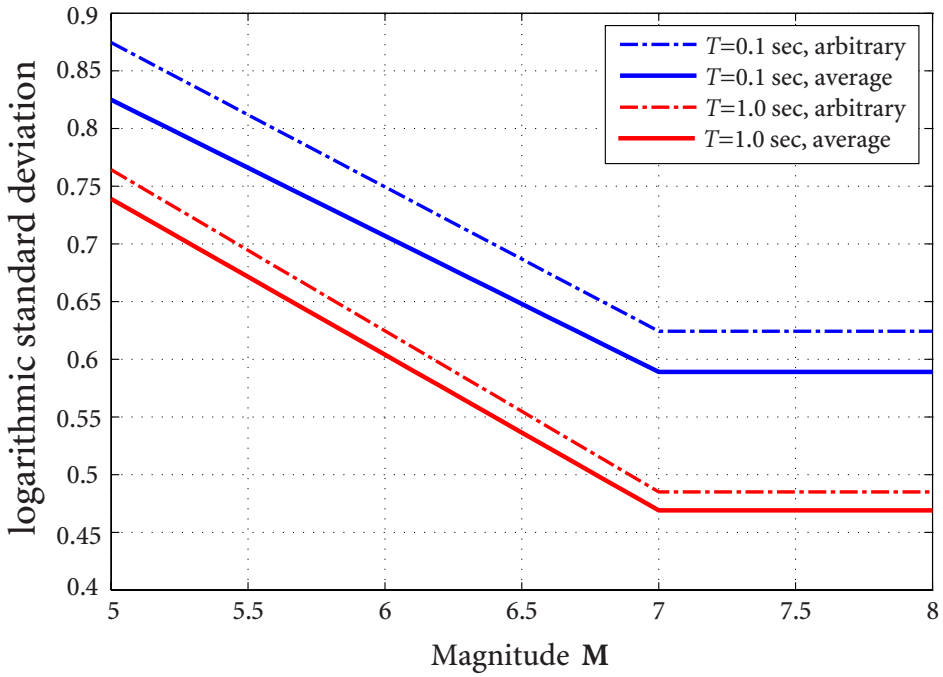

Figure 2.5 Logarithmic standard deviations for average or arbitrary horizontal components from A&S-97 GMPE

Probability Distribution of Spectral Accelerations

Equation (2.2.6) implies that, given an earthquake scenario, spectral acceleration $S_a(T_j)$ at individual period T_j follows the lognormal distribution

$$\mathcal{P}\left\{S_a(T_j) > s_j \,|\, m, r\right\} = 1 - \Phi\left(\frac{\ln s_j - \mu_{\ln S_a(T_j)\,|\,m,r}}{\sigma_{\ln S_a(T_j)\,|\,m}}\right), \tag{2.2.14}$$

where $\Phi(\cdot)$ is the standard normal distribution function, s_j is the threshold value, and $\mu_{\ln S_a(T_j)\,|\,m,r} = f(m, r, T_j, \boldsymbol{\theta})$ is the predicted mean value of $\ln S_a(T_j)$ governed by equation (2.2.7), $\sigma_{\ln S_a(T_j)\,|\,m} = \sigma(m, T_j)$ is the associated standard deviation provided by equations (2.2.12) and (2.2.13).

The probability distribution of spectral accelerations governed by equations (2.2.14) is a core input to PSHA.

2.2.3 Scalar Probabilistic Seismic Hazard Analysis

Seismic source model, described in Subsection 2.2.1, defines all possible earthquake occurrences at the site of interest. Ground-motion prediction equations, described in Subsection 2.2.2, provide an estimate of ground shaking intensity in terms of spectral acceleration at the site given an earthquake scenario. Seismic hazard is then evaluated by integrating the contributions from all possible earthquake occurrences.

Take spectral acceleration $S_a(T_j)$ at vibration period T_j as the GMP, and assume that earthquake magnitude M and source-site distance R are statistically independent in a source. The mean annual rate of $S_a(T_j)$ exceeding a threshold s_j at the site can be calculated using the total probability theorem

$$\lambda_{s_j} = \sum_{i=1}^{N_S} \lambda_{s_j}^{(i)} = \sum_{i=1}^{N_S} \nu_i \left\{ \int_r \int_m \mathcal{P}\left\{S_a(T_j) > s_j \,|\, m, r\right\} f_M(m) f_R(r) \mathrm{d}m \,\mathrm{d}r \right\}_i. \tag{2.2.15}$$

where N_S is the total number of seismic sources, $\lambda_{s_j}^{(i)}$ is the hazard contribution by source i, ν_i is the mean rate of occurrence of earthquakes above magnitude $m_{\min}$ for source i, and $\mathcal{P}\left\{S_a(T_j) > s_j \,|\, m, r\right\}$ is the probability distribution of $S_a(T_j)$ given a scenario earthquake, governed by equation (2.2.14).

Multiple hypothesis on core inputs to PSHA (seismicity parameters and the GMPE models) are explicitly considered using the logic tree approach (McGuire, 2004), so that not only the median, mean, but also any fractile of seismic hazard can be provided.

Because of the complexity of equation (2.2.15) in realistic cases, numerical integration has to be applied for performing PSHA. By dividing the range of feasible m and r values for each source into small bins with width Δm and Δr, respectively, the integrals in equation (2.2.15) are evaluated by discrete summation. This operation implies that a seismic source is capable of generating only a finite number of m and r bins or (m, r)-pairs (usually assumed to be the central value of each bin).

If the event in a Poisson process is made to signify an earthquake occurrence at the site that generates $S_a(T_j) > s_j$, and if N_{E} is the number of occurrence of such event in a time period t, then according to equation (2.2.5) the probability of $S_a(T_j) > s_j$ at the site is

$$\mathcal{P}\left\{S_a(T_j) > s_j\right\} = \mathcal{P}\left\{N_{\mathrm{E}} \geqslant 1\right\} = 1 - \mathcal{P}\left\{N_{\mathrm{E}} = 0\right\} = 1 - \mathrm{e}^{-\lambda_{s_j} t}. \tag{2.2.16}$$

In earthquake engineering practice, the time period t is usually taken as one year or 50 years. Since events of small probabilities (i.e., $\leqslant 10^{-2}$) is of interest, λ_{s_j} is numerically identical to the annual probability of exceedance $\mathcal{P}\left\{S_a(T_j) > s_j\right\}$ in equation (2.2.16) (Ni, 2012). Hence, the terminology of "annual probability of exceedance" is adopted directly for λ_{s_j} in this study, instead of the mean annual rate of exceedance.

The annual probability of exceedance ($t = 1$), probability of exceedance in $t = 50$ years, and the mean return period RP can be mutually translated, as provided in Table 2.1 for 6 common reference probability levels. For example, given the exceedance probability of 2% in 50 years, the associated λ_{s_j} and RP can be obtained using equation (2.2.16)

$$\begin{aligned} 2\% = \mathcal{P}\left\{S_a(T_j) > s_j\right\} &= 1 - \mathrm{e}^{-\lambda_{s_j} 50}, \\ \Longrightarrow \lambda_{s_j} = \frac{1}{50}\ln(1 - 2\%) = 0.000404 \ \text{ and } \ \mathrm{RP} &= \frac{1}{\lambda_{s_j}} = 2475.2 \text{ years}. \end{aligned}$$

The results of PSHA are typically represented by *seismic hazard curves* of annual probability of exceedance λ_{s_j} plotted against GMP $S_a(T_j)$, as shown in Figure 2.7. Such presentation provides more information on seismic hazard, for which engineers can gain more discretion in selecting appropriate hazard levels for structural design according to various perfor-

Table 2.1 Translations among 6 common reference probability levels

No.	Probability of exceedance in $t = 50$ years	Annual probability of exceedance λ_{s_j}	Mean return period RP
1	50%/50 years	0.0139	72.1 years
2	20%/50 years	0.0045	222 years
3	10%/50 years	0.0021	475 years
4	5%/50 years	0.0010	975 years
5	2%/50 years	0.0004	2,475 years
6	1%/50 years	0.0002	4,975 years

mance goals. For engineering seismic design, thresholds $s_1, \cdots, s_j$ from a suite of PSHA performed for $S_a(T_1), \cdots, S_a(T_k)$, for a specific probability of exceedence, can be used to construct a uniform hazard spectrum (UHS) (ASCE, 2005; NBCC, 2010).

Example Scalar PSHA

Scalar PSHA is demonstrated by a numerical example, based on a hypothetical configuration of seismic sources (two line sources and one area source) shown in Figure 2.6. The probability distribution of source-site distance governed by equation (2.2.1) is used for each source. The probability distribution of earthquake magnitude governed by equation (2.2.3) is used, in which $m_{\min} = 5.0$, $m_{\max} = 6.0$, and $\beta = 2.07$ for source 1, $m_{\min} = 5.0$, $m_{\max} = 8.0$, and $\beta = 2.07$ for sources 2 and 3. The mean annual rates ν for sources 1, 2, and 3 are taken as 0.02, 0.03, and 0.05, respectively. All focal depths are taken as 5 km.

The set of GMPE by Abrahamson and Silva (1997), summarized in Section 2.2.2, are adopted for obtaining the mean and standard deviation in the conditional probability distribution of spectral acceleration in equation (2.2.14). In the GMPE, parameters are set for rock site, reverse fault, non-hanging wall, and sigma for arbitrary component.

By performing scalar PSHA according to equation (2.2.15) for various ground motion levels, hazard curves can be developed as shown in Figure 2.7 for spectral accelerations at 0.1 and 1 sec. From hazard curves, the threshold s_j for a specific probability of exceedance λ_{s_j} can be determined. For example, the thresholds of spectral accelerations at 0.1 and 1 sec for $\lambda_{s_j} = 4 \times 10^{-4}$ are determined to be $0.586\,g$ and $0.191\,g$, respectively.

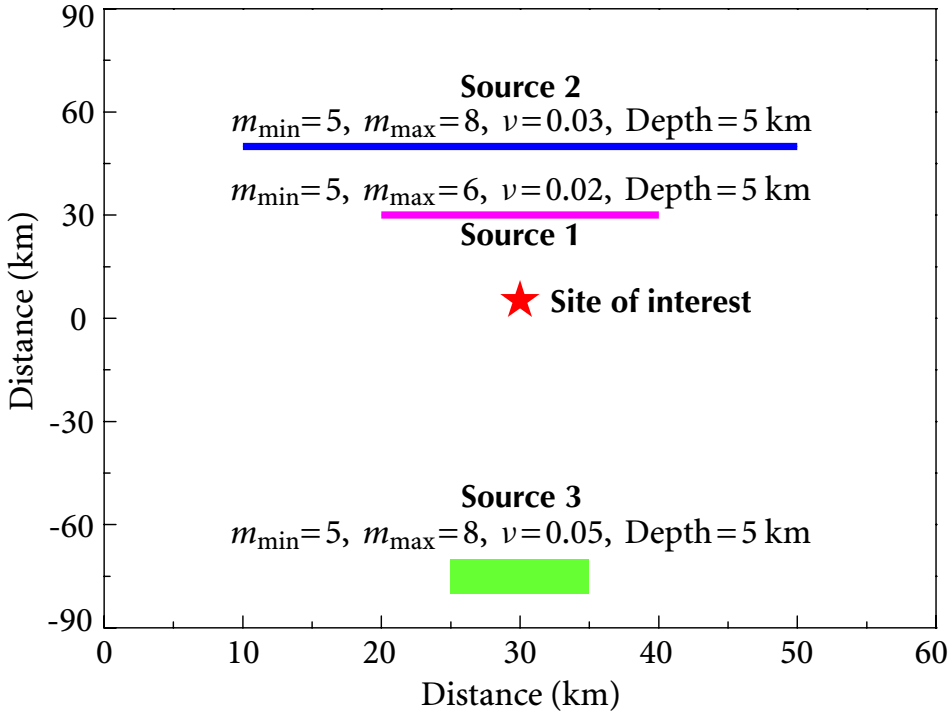

Figure 2.6 Hypothetical configuration of seismic source zones

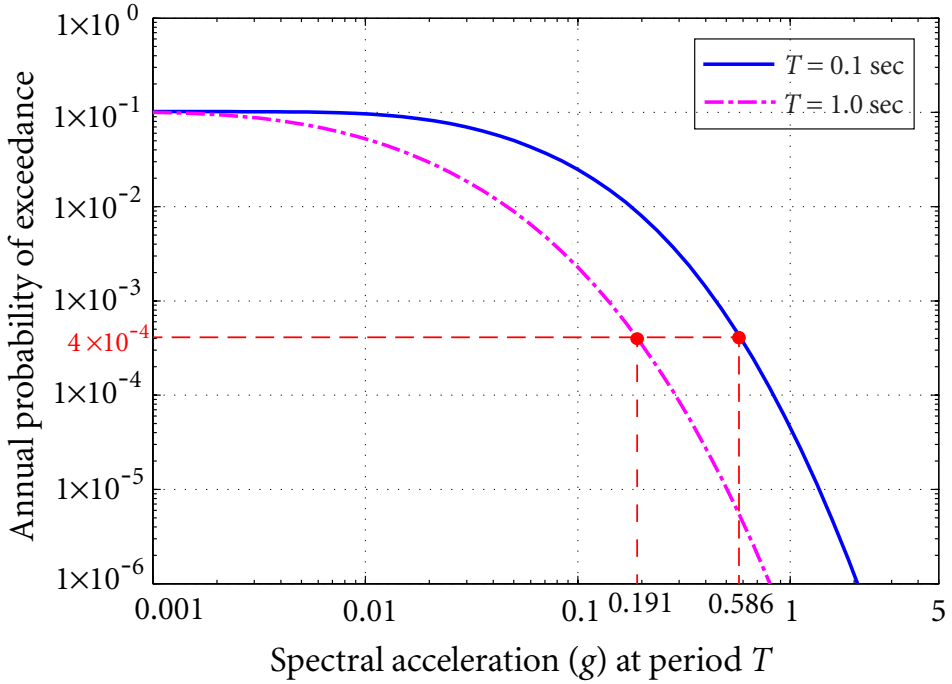

Figure 2.7 Seismic hazard curves for spectral accelerations at 0.1 and 1.0 sec

2.3 Scalar Seismic Risk Analysis

The PSHA, described in Section 2.2, can be transformed into Seismic Risk Analysis (SRA) for a structure or component by incorporating the fragility model.

2.3.1 Fragility Model Considering a Single Ground Motion Parameter

In general, seismic fragility is defined as the probability that the damage of a structure exceeds a specific damage state d for a given level of seismic hazard (McGuire, 2004)

$$\text{Fragility} = P\left\{\text{Damage} > d \,\middle|\, \text{Seismic Hazard}\right\}. \tag{2.3.1}$$

Seismic hazard is provided by either scalar or vector-valued PSHA, depending on the characteristics of structural response and the desired degree of accuracy in analysis. On the other hand, determination of damage state often necessitates a reliable structural analysis (e.g., nonlinear dynamic analysis) for demand estimate and a damage state analysis.

To calibrate the damage state, typical demand parameters D, such as maximum inter-story drift ratio or maximum floor acceleration, are often employed. For structural elements, maximum inter-story drift ratio is a commonly used demand parameter, because almost all damages to structures are related to deformation. For component and equipment, maximum floor acceleration and maximum inter-story drift ratio are both of particular interest, since most equipment mounted on the structures might be acceleration-sensitive or displacement-sensitive. By comparing the demand parameter to certain established threshold values according to structural capacity, the damage state level can be calibrated (e.g., maximum inter-story drift ratio of 0.03 for moderate damage).

Seismic demand cannot be predicted for sure; there is a great deal of uncertainty involved. Statistical characteristics of the demand parameter for given seismic hazard is required in constructing the seismic fragility model. Either empirical method based on observed damage from earthquake experience data (Shinozuka *et al.*, 2000), or analytical method based on simulations of structural models under increasing earthquake intensity (Jeong and Elnashai, 2007) could be used. Analytical method is usually applied when real data is unavailable; however, it requires extensive computer simulations to obtain the statistics.

In engineering practice, individual demand parameter D is often assumed to be lognormally distributed, so that the logarithm of demand parameter $\ln D$ is normally distributed (Shome, 1999). The functional dependency of D on a single GMP of spectral acceleration $S_a(T_j)$ is given by

$$D = a \cdot S_a^b(T_1) \cdot \varepsilon; \quad \ln D = \ln a + b \cdot \ln S_a(T_1) + \ln \varepsilon, \tag{2.3.2}$$

where a, b are the regression parameters, and ε is the random error with a median of unity and standard deviation of δ_ε.

Mean $\mu_{\ln D \,|\, S_a(T_j)=s_j}$ and standard deviation $\sigma_{\ln D \,|\, S_a(T_j)=s_j}$ of $\ln D$ are obtained from regression analysis. Generally, the mean is a function of ground motion level, and the standard deviation can be either taken as a constant or a function of ground motion level, depending on the simulation method and regression model used. It is important to ensure that the statistics be valid for a wide range of ground motion level, since further risk quantification integrate over the entire range of ground motion level.

With the statistics of $\ln D$, the fragility model can be constructed as

$$\mathcal{P}\left\{D > z \,\middle|\, S_a(T_j) = s_j\right\} = 1 - \Phi\left(\frac{\ln z - \mu_{\ln D \,|\, S_a(T_j)=s_j}}{\sigma_{\ln D \,|\, S_a(T_j)=s_j}}\right), \tag{2.3.3}$$

where z is a threshold value for a specific damage state. Given any specified threshold z, seismic fragility is a function of GMP $= S_a(T_j)$.

2.3.2 Integrating Seismic Hazard to Seismic Risk

Combining seismic hazard analysis and the fragility model with a single GMP, the seismic risk of annual probability of D exceeding a threshold value z is given by

$$\begin{aligned}\lambda_D(z) &= \int_\lambda \mathcal{P}\left\{D > z \,\middle|\, S_a(T_j) = s_j\right\} \mathrm{d}\lambda_{s_j} \\ &= \int_0^\infty \mathcal{P}\left\{D > z \,\middle|\, S_a(T_j) = s_j\right\} \cdot \sum_{i=1}^{N_S} \nu_i \left\{ \int_r \int_m f_{S_a(T_j)}(s_j \,|\, m, r)\, f_{M,R}(m, r) \mathrm{d}m \,\mathrm{d}r \right\}_i \mathrm{d}s_j,\end{aligned} \tag{2.3.4}$$

where $d\lambda_{s_j}$ is approximately the annual probability of $S_a(T_j)$ equal to s_j, which exists only when discrete numerical integration is used, and the integrand $P\left\{D > z \middle| S_a(T_j) = s_j\right\}$ is the fragility model given in equation (2.3.3).

Note that for risk analysis, $S_a(T_j)$ is usually taken as $S_a(T_1)$ at the fundamental period T_1 of a structure, since $S_a(T_1)$ is believed to be the most desirable GMP for prediction of structural response. In addition, equation (2.3.4) gives only a point risk value. It is beneficial to present the result of risk analysis through a risk curve, showing a continuous relationship between the risk level and various threshold values. Such information benefits the decision-making process and facilitates the risk-informed performance-based seismic design (Wen, 2001; Bertero and Bertero, 2002).

2.4 Summary

In this Chapter, the basics of scalar seismic risk analysis, which combined scalar probabilistic seismic hazard analysis and the fragility model with a single ground-motion parameter, is presented. It gives the background for the study of vector-valued seismic risk analysis and a simplified approach presented in Chapter 3.

CHAPTER 3

Vector-valued Seismic Risk Analysis

The scalar seismic risk analysis (SRA) described in Chapter 2 is extended to vector-valued SRA (VSRA) in this chapter. Due to the extensive computational efforts required in standard VSRA, a simplified approach is developed to achieve efficiency without losing accuracy.

3.1 Background

In many practical applications, a knowledge of seismic hazard in terms of multiple ground-motion parameters (GMP) could more accurately predict the damage inflicted on a structure or component by an earthquake, for example seismic response of multi-mode-dominant structures (e.g., a tall flexible building and a cable-supported bridge) and equipment having multiple failure modes governed by different GMP. For this purpose, a vector-valued PSHA was first performed by Bazzurro and Cornell (2002). As a generalization of scalar SRA, VSRA can provide a more accurate risk quantification for structures, the responses of which can be more accurately determined by multiple GMP.

However, there are a number of challenges in performing a VSRA. First, a proper fragility relation should be established, reflecting site-specific hazard, i.e., all realistic spectral shapes induced by site-specific earthquakes. Second, VSRA is computationally expensive, since it integrates over not only all possible earthquake occurrences but also multiple GMP to give a probability of exceedance. Due to the extensive computational efforts required, VSRA has not been widely applied Tothong and Luco (2007). Hence, seismic risk cannot be accurately

quantified with computational ease for applications entailing multiple GMP. For practical applications of VSRA, a computationally efficient approach is necessary.

In this chapter, the second challenge is addressed by developing a computationally efficient approach to VSRA. This approach takes advantage of a set of controlling earthquakes determined from a proposed seismic hazard deaggregation (SHD) procedure. VSRA is then performed approximately based on the controlling earthquakes rather than all possible earthquake occurrences.

In Section 3.2, standard VSRA is established and its computational complexity is discussed. In Section 3.3, a simplified approach to VSRA is developed and its computational efficiency is discussed. Two numerical examples are presented in Section 3.4 to validate the simplified approach. Factors affecting the accuracy and efficiency of the simplified approach are discussed through the examples.

3.2 Vector-valued Seismic Risk Analysis – A Standard Formulation

To perform a vector-valued SRA, both seismic hazard and fragility analyses should be represented in the vector-valued case, i.e., multiple GMP are adopted.

3.2.1 Vector-valued Probabilistic Seismic Hazard Analysis

Vector-valued PSHA determines a joint hazard in terms of spectral accelerations at multiple periods. In the k-dimensional case, replacing the marginal probability distribution of spectral acceleration given a scenario earthquake in equation (2.2.14) by the joint conditional probability distribution, gives the joint hazard of annual probability of exceeding spectral accelerations $S_a(T_1), \cdots, S_a(T_k)$ at vibration periods $T_1, \cdots, T_k$ simultaneously at a site

$$\lambda_{s_1 \cdots s_k} = \sum_{i=1}^{N_S} \nu_i \Big\{ \int_r \int_m P\left\{ S_a(T_1) > s_1, \cdots, S_a(T_k) > s_k \,\middle|\, m, r \right\} f_M(m) f_R(r) \mathrm{d}m \, \mathrm{d}r \Big\}_i . \quad (3.2.1)$$

As a direct extension of scalar PSHA, the only additional information required in performing a vector-valued PSHA is the joint conditional probability distribution of spectral accelerations at multiple periods.

Joint Distribution of Spectral Accelerations

Given the univariate normality of residuals $\varepsilon(T_j)$ (including inter- and intra-events) defined in equation (2.2.6), the residuals $\varepsilon(T_1), \cdots, \varepsilon(T_k)$ at multiple periods have been tested to follow the multivariate standard normal distribution based on the worldwide database of strong ground motions (Jayaram and Baker, 2008); consequently, spectral accelerations $S_a(T_1), \cdots, S_a(T_k)$ at multiple periods given a scenario earthquake follow the multivariate lognormal (joint lognormal) distribution

$$\begin{aligned} &P\left\{S_a(T_1) > s_1, \cdots, S_a(T_k) > s_k \,\middle|\, m, r\right\} \\ &\qquad = \int_{s_k}^{\infty} \cdots \int_{s_1}^{\infty} f_{S_a(T_1),\cdots,S_a(T_k)}(s_1, \cdots, s_k \,|\, m, r)\, \mathrm{d}s_1 \cdots \mathrm{d}s_k, \end{aligned} \tag{3.2.2}$$

where $s_1, \cdots, s_k$ are the thresholds of spectral accelerations, $f_{S_a(T_1),\cdots,S_a(T_k)}(s_1, \cdots, s_k \,|\, m, r)$ is the probability density function (PDF) of multivariate lognormal distribution of k spectral accelerations given m and r.

To define the multivariate lognormal distribution, the marginal mean and standard deviation of $\ln S_a(T_1), \cdots, \ln S_a(T_k)$ given m and r can be obtained from the GMPE for each vibration period, the correlation coefficients between $\ln S_a(T_i)$ and $\ln S_a(T_j)$ at any two periods T_i and T_j can be obtained using the empirical spectral correlation model.

Spectral Correlation Model

To obtain a knowledge of statistical correlations between spectral accelerations at multiple periods, the Pearson's correlation coefficients are obtained empirically based on a large number of recorded ground motions (Baker and Cornell, 2006a; Baker and Jayaram, 2008).

Given a predicted value $f(m, r, T_j, \boldsymbol{\theta})$ by any set of GMPE for a scenario earthquake, the Pearson's correlation coefficient between the natural logarithmic spectral accelerations $\ln S_a(T_u)$ and $\ln S_a(T_v)$ at any two periods T_u and T_v is given by

$$\rho_{\ln S_a(T_u),\ln S_a(T_v)} = \frac{\sum_{i=1}^{N} [\ln S_a^{(i)}(T_u) - \overline{\ln S_a(T_u)}][\ln S_a^{(i)}(T_v) - \overline{\ln S_a(T_v)}]}{\sqrt{\sum_{i=1}^{N} [\ln S_a^{(i)}(T_u) - \overline{\ln S_a(T_u)}]^2 \sum_{i=1}^{N} [\ln S_a^{(i)}(T_v) - \overline{\ln S_a(T_v)}]^2}}, \tag{3.2.3}$$

where $\ln S_a^{(i)}(T_u)$ and $\ln S_a^{(i)}(T_v)$ are the ith observations of $\ln S_a(T_u)$ and $\ln S_a(T_v)$ from the ith ground motion record, $\overline{\ln S_a(T_u)}$ and $\overline{\ln S_a(T_v)}$ are their sample means, and N is the total number of observations used in the statistical and regression analysis. Using equation (3.2.3), empirical correlation coefficients can be determined from all the observations of $\ln S_a$ between any two periods. For practical use, these correlation coefficients are further fit to analytical predictive equations.

Figure 3.1 shows a contour of correlation coefficients between the horizontal spectral accelerations at any two periods by Baker and Jayaram (2008). Details about this model and the associated predictive equations are given in Appendix A.1.

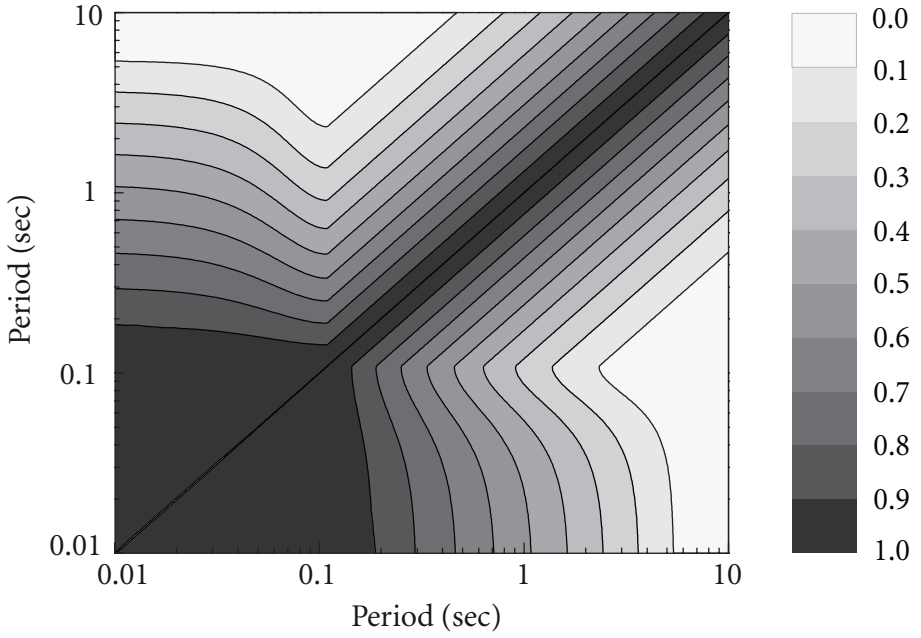

Figure 3.1 Correlation coefficients of spectral accelerations by Baker and Jayaram (2008)

Example Vector-valued PSHA

A joint hazard in terms of spectral accelerations at 0.1 and 1 sec for the hypothetical site shown in Figure 2.6 is evaluated using vector-valued PSHA. The matrix of spectral correlation by Baker and Jayaram (2008) is adopted in determining the conditional joint distribution of spectral accelerations governed by equation (3.2.2), while all other information required in performing scalar PSHA is retained.

A contour of the joint annual probability of exceedance is shown in Figure 3.2. It is seen that the joint probability of spectral accelerations at 0.1 sec and 1 sec exceeding $0.586\,g$ and $0.191\,g$ is 2.3×10^{-5}, which is much smaller than the marginal probability of exceedance 4×10^{-4} from scalar PSHA.

The joint probability density (strictly probability mass when using numerical integration) is shown in Figure 3.3, where a 2-dimensional normality is observed in a log-log scale. For the 2 dimensional case, the differential volume under the density function and above the horizontal axes is the relative likelihood of spectral accelerations taking on specific values. The integral over the entire space is equal to ν (occurrence rate of earthquake).

3.2.2 Fragility Model Considering Multiple Ground motion Parameters

Given a knowledge of joint seismic hazard in terms of multiple GMP, the damage of structures can usually be better predicted. The functional dependency of demand parameter D on k spectral accelerations is given by

$$D = a\cdot S_a^{b_1}(T_1)\cdots S_a^{b_k}(T_k)\cdot\varepsilon,\quad \ln D = \ln a + b_1\cdot\ln S_a(T_1) + \cdots + b_k\cdot S_a(T_k) + \ln\varepsilon. \tag{3.2.4}$$

where $a, b_1, \cdots, b_k$ are the regression parameters, and ε is the random error with a median of unity and standard deviation of δ_ε.

Statistics of $\ln D$, including conditional mean $\mu_{\ln D\,|\,S_a(T_1)=s_1,\cdots,S_a(T_k)=s_k}$ and standard deviation $\sigma_{\ln D\,|\,S_a(T_1)=s_1,\cdots,S_a(T_k)=s_k}$, are obtained from a multivariate regression analysis. Hence, the fragility model can be constructed as

$$P\left\{D>z\,\middle|\,S_a(T_1)=s_1,\cdots,S_a(T_k)=s_k\right\} = 1-\Phi\left(\frac{\ln z-\mu_{\ln D\,|\,S_a(T_1)=s_1,\cdots,S_a(T_k)=s_k}}{\sigma_{\ln D\,|\,S_a(T_1)=s_1,\cdots,S_a(T_k)=s_k}}\right). \tag{3.2.5}$$

3.2.3 Integration for Seismic Risk

Combining vector-valued PSHA given in equation (3.2.1) and the fragility model with multiple GMP given in equation (3.2.5), seismic risk of annual probability of D exceeding z

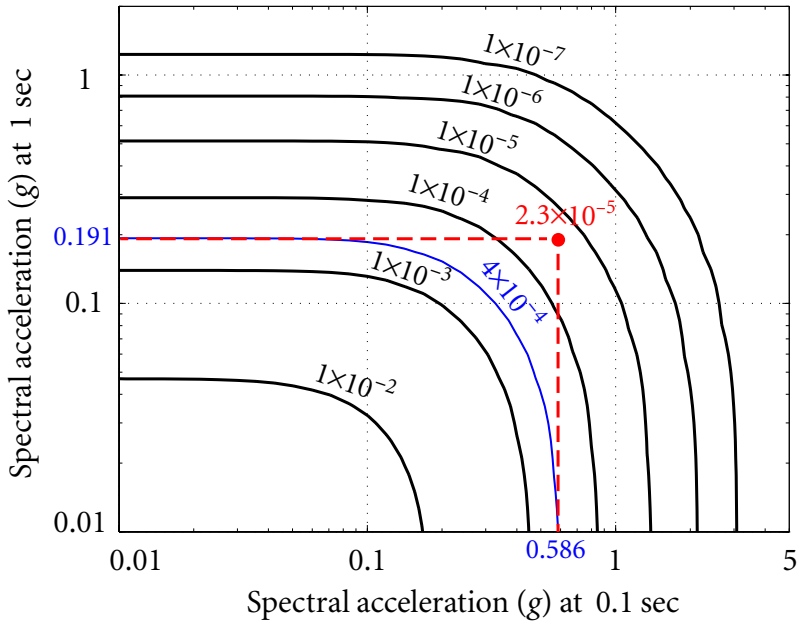

Figure 3.2 Contours of joint hazard for spectral accelerations at 0.1 and 1.0 sec

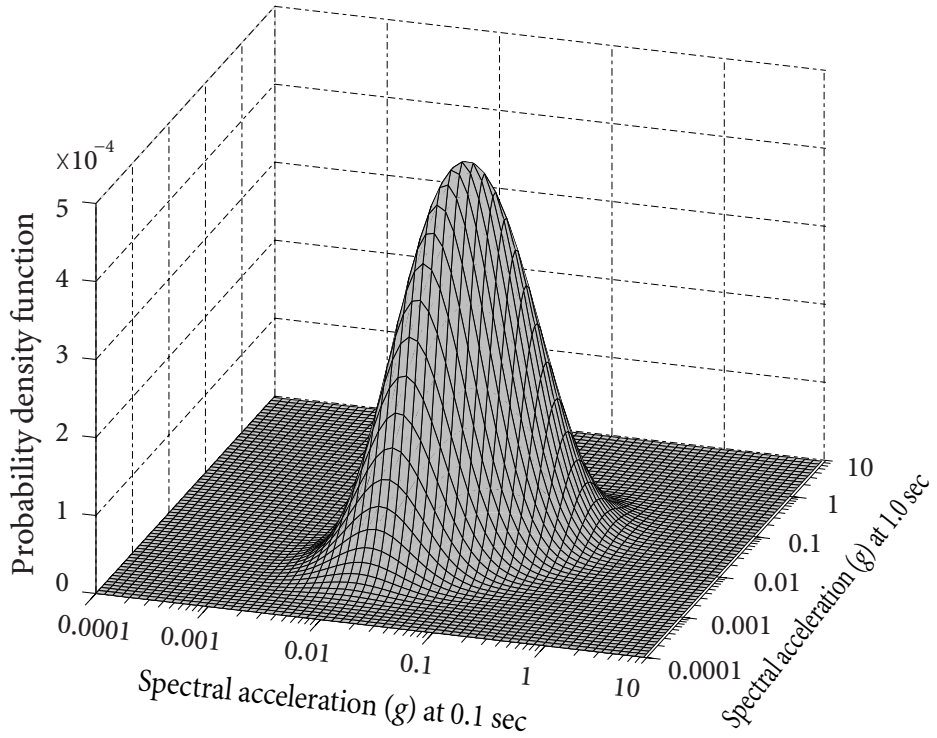

Figure 3.3 Probability density of joint hazard for spectral accelerations at 0.1 and 1.0 sec

is given by

$$\begin{aligned}\lambda_D(z) &= \int_0^\infty \cdots \int_0^\infty \bar{P}\left\{D>z \,\middle|\, S_a(T_1)=s_1,\cdots,S_a(T_k)=s_k\right\} \cdot \frac{\partial^k \lambda_{S_1\cdots S_k}}{\partial s_1 \cdots \partial s_k} \cdot \mathrm{d}s_1 \cdots \mathrm{d}s_k \\ &= \int_0^\infty \cdots \int_0^\infty \bar{P}\left\{D>z \,\middle|\, S_a(T_1)=s_1,\cdots,S_a(T_k)=s_k\right\} \\ &\quad \cdot \sum_{i=1}^{N_S} \nu_i \left\{ \int_r \int_m f_{S_a(T_1)\cdots S_a(T_k)}(s_1\cdots s_k \,|\, m,r)\, f_{M,R}(m,r)\mathrm{d}m\,\mathrm{d}r \right\}_i \mathrm{d}s_1 \cdots \mathrm{d}s_k, \quad (3.2.6)\end{aligned}$$

where $\partial^k \lambda_{S_1\cdots S_k}/\partial s_1 \cdots \partial s_k$ is the joint probability density of multiple spectral accelerations, and $\bar{P}\left\{D>z \,\middle|\, S_a(T_1)=s_1,\cdots,S_a(T_k)=s_k\right\}$ is the fragility model, which can be plotted as a fragility surface for the two-dimensional case, but is difficult to visualize for higher dimensional cases.

Contributing Factors to Computational Complexity

VSRA in equation (3.2.6) involves the extensive vector-valued PSHA and the fragility analysis in a multi-fold integration. Evaluation of this risk equation can be challenging, based on current computational tools, due to the following factors:

(a) Number of seismic sources N_S surrounding the site. Depending on the actual seismic environment at a site, N_S can be quite large. For example, 13 fault segments within the 200 km distance from the site of Diablo Canyon Nuclear Power Plant (DCPP) in coastal California need to be considered. 15 areal sources within 600 km from the site of Montreal in eastern Canada need to be considered (Adams and Halchuk, 2003).

(b) Mesh size of magnitude Δm and earthquake location, which gives the total number of (m,r)-pairs. While $\Delta m = 0.1$ unit is conventionally taken in modern PSHA, the mesh of location can be a little arbitrary, typically ranging from 1 km to 10 km. Note that for the hypothetical site shown in Figure 2.6, mesh size of 0.5 km was adopted due to the small radial distance measured from the site location (approximately 90 km).

(c) Spectral dimension $s_1,\cdots,s_k$ and their discretization $\Delta s_1,\cdots,\Delta s_k$. The dimension considered is based on the desired degree of accuracy in analysis for a particular application, where a multi-dimensional analysis is necessary and desirable. The discretization Δs_k adopted depends on the energy distribution in s_k. Figure 3.4 shows

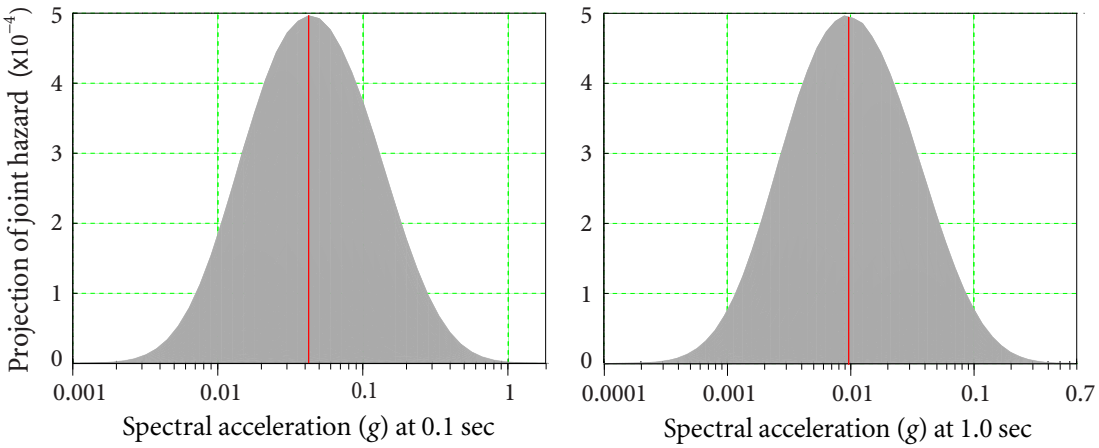

Figure 3.4 Energy distribution in different spectral acceleration dimensions

the energy distributions in 2 spectral dimensions, projected from the 2-D joint hazard (probability density) shown in Figure 3.3. From the central statistics of energy distribution in s_k, proper truncated boundaries in s_k can be specified for computation. In this study, s_j in any dimension is discretized into 66 segments equally spaced in log scale from $0.0001g$ to $10g$, which is satisfactory for numerical integration in most cases.

(d) Evaluation of the multivariate lognormal distribution. This is usually not of primary concern unless the dimension is greater than 4, when Monte Carlo Simulation is typically applied, requiring substantial computational efforts.

(e) Number of threshold values z needed for constructing a smooth risk curve. The total time in analysis increases with the number of thresholds n. Fortunately, by applying the vectorized computing technique using software such as *Matlab*, the total time effort required does not change significantly with n. The effect of this factor can be minimized and neglected.

It can be concluded that the dominant contributing factors to the computational complexity of seismic risk analysis are (a), (b), and (c), i.e., integrating all possible earthquake occurrences in terms of m and r from N_S sources and extracting repetitively hazard in terms of multiple spectral parameters from all possible earthquakes.

The level of computational complexity makes seismic risk analysis very challenging for structural engineers. For practical applications, a computationally efficient approach is necessary.

3.3 Vector-valued Seismic Risk Analysis – A Simplified Approach

In seismic risk and hazard analysis, two fundamental questions are often asked:

1. What level of ground motion contributes most seismic risk?
2. Which event dominates a certain level of ground motion?

The answer to question 1 is discussed in Subsection 3.3.1 and the answer to question 2 is discussed in Subsection 3.3.2. Based on these discussions, a procedure for simplified seismic risk analysis is developed in Subsection 3.3.3, to address the computational issue of standard VSRA.

3.3.1 Dominant Hazard Range for Risk Analysis

Different levels of ground motion usually contribute very differently to the seismic risk. Neither very low nor extremely high level of ground motion contributes significantly to the seismic risk. So what level of ground motion contributes most to seismic risk? To answer this question, let's first look at a risk quantification example.

Figure 3.5 shows the hazard curve and fragility curve required for risk quantification. The hazard curve is developed for spectral acceleration at 1 sec for the hypothetical site shown in Figure 2.6. The fragility curve is developed for a simple structure with a fundamental period of 1 sec. The structure has a median $S_a(T_1)$ capacity $A_m = 0.695\,g$ (50% probability of failure given $S_a(T_1) = 0.695\,g$) with an associated variability $\beta = 0.40$. Procedure of risk calculation is illustrated using Table 3.1.

Table 3.1 shows that seismic risk of this structure is annual probability of failure $P_F = 1.01 \times 10^{-5}$ and that different levels of ground motion contribute differently to seismic risk.

- At low ground motion level ($< 0.237g$), i.e., $\lambda_a > 1 \times 10^{-4}$/year, seismic fragility is very small, hence the risk contribution is not significant.

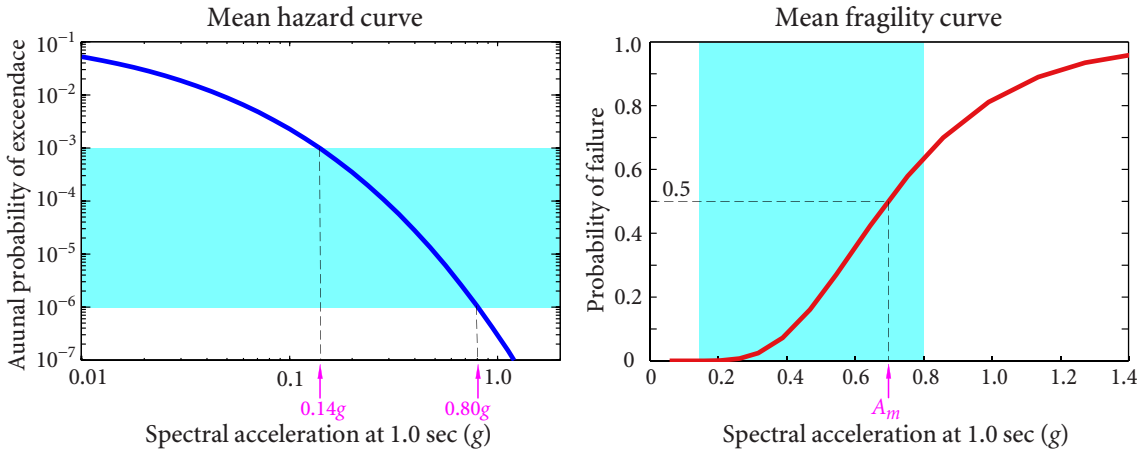

Figure 3.5 Example hazard curve and fragility curve for risk quantification

- At high ground motion level ($>0.911g$), e.g., $\lambda_a < 1\times10^{-6}$/year, the ground motion hazard is too small to make significant risk contribution.
- Ground motion level corresponding to $\lambda_a = 1\times10^{-4}\sim10^{-6}$/year (shaded rows in Table 3.1) contributes over 80% to the seismic risk.

In current seismic design and evaluation practice, structures are usually aimed at a fairly low seismic risk, called "target performance goal" for a given Seismic Design Category (SDC). For example, the code specified target performance goals for SDC 3, 4, and 5 of nuclear structures are aimed at probability of failure of $P_F = 1.0\times10^{-4}\sim1\times10^{-5}$/year (ASCE, 2005).

Given a target risk probability level, the ground motion range in the two adjacent probability decades contributes most to the seismic risk, as the example risk quantification illustrates. Similarly, for target risk level of $P_F = 1\times10^{-4}$/year, the dominant ground motion range is approximately $\lambda_a = 1\times10^{-3}\sim1\times10^{-5}$/year. In general, for any seismically-designed structure aimed at risk level of $P_F = 1\times10^{-4}\sim1\times10^{-5}$/year, the dominant ground motion hazard range should be within $\lambda_a = 1\times10^{-3}\sim1\times10^{-6}$/year. Consider again the aforementioned example, ground motion hazard ranging $\lambda_a = 1\times10^{-3}\sim1\times10^{-6}$/year contributes over 92% to seismic risk $P_F = 1\times10^{-5}$/year.

Hence, it is clear that the objective of the simplified approach is to approximate seismic hazard in the probability range $\lambda_a = 1\times10^{-3}\sim1\times10^{-6}$/year.

Table 3.1 Example risk quantification for target risk goal of $P_F = 1.0 \times 10^{-5}$/year

Acceleration a_i (g)	Exceedance prob. λ_a ($\times 10^{-5}$/year)	C.G. $a_{c.g.,i}$ (g) †	(1) Fragility $P_{F/a_{c.g.,i}}$	(2) Increment $\Delta\lambda(a_i)$ ($\times 10^{-5}$/year)	(1) × (2) ($\times 10^{-5}$/year)	Contribution to risk (%)
0.069	500					
		0.087	0.000000	300	0.0000	0.00
0.106	200					
		0.122	0.000007	100	0.0007	0.07
0.139	100					
		0.158	0.000106	50	0.0053	0.5
0.177	50					
		0.207	0.00121	30	0.0362	3.5
0.237	20					
		0.262	0.00738	10	0.0738	7.3
0.288	10					
		0.316	0.0246	5	0.123	12.1
0.345	5					
		0.388	0.0723	3	0.217	21.4
0.431	2					
		0.467	0.161	1	0.161	15.8
0.504	1					
		0.544	0.271	0.5	0.135	13.3
0.585	0.5					
		0.644	0.424	0.3	0.127	12.5
0.703	0.2					
		0.753	0.579	0.1	0.0579	5.7
0.803	0.1					
		0.857	0.700	0.05	0.0350	3.4
0.911	0.05					
		0.989	0.811	0.03	0.0243	2.4
1.07	0.02					
		1.13	0.890	0.01	0.0090	0.9
1.20	0.01					
		1.27	0.934	0.005	0.0047	0.5
1.34	0.005					
		1.528	0.976	0.004	0.0039	0.4
1.72	0.001					
			≈ 1.0	0.001	0.001	0.1
					$P_F = \sum(1) \times (2) = 1.01 \times 10^{-5}$/year	

† $a_{c.g.,i} = \dfrac{\int_{a_i}^{a_{i+1}} a \cdot \lambda(a) \mathrm{d}a}{\int_{a_i}^{a_{i+1}} \lambda(a) \mathrm{d}a}$ is the center-of-gravity ground motion amplitude between a_i and a_{i+1}.

3.3.2 Seismic Hazard Deaggregation

PSHA determines the seismic hazard at a site by integrating over primary random variables, i.e., magnitude M and source-site distance R, from all seismic sources. The effect of single dominant event on a certain level of ground motion is somewhat blurred. For improved understanding in seismic threat, relative contributions to hazard from different sources or random variables are often studied. This represents a "deaggregation" procedure of equation (2.2.15) and hence is known as seismic hazard deaggregation (SHD) (McGuire, 1995; Bazzurro and Cornell, 1999).

Deaggregation has become a required analysis in the PSHA (USNRC, 2007). It provides information useful for review of the PSHA and insight into sources that most impact the hazard at a particular site. It is also used to select the controlling earthquakes (i.e., m-r pair) at a reference probability, for performing dynamic site response analyses.

To characterize not only the relative hazard contributions from earthquake magnitude m and source-site distance r but also the ground-motion randomness ε in equation (2.2.6), the standard formulation of scalar PSHA given by equation (2.2.15) is extended to

$$\lambda_{s_j} = \sum_{i=1}^{N_S} \nu_i \Big\{ \int_{\varepsilon} \int_{r} \int_{m} P\left\{S_a(T_j) > s_j \,\middle|\, m, r, \varepsilon\right\} f_M(m) f_R(r) f_\epsilon(\varepsilon) \mathrm{d}m \,\mathrm{d}r \,\mathrm{d}\varepsilon \Big\}_i, \tag{3.3.1}$$

where $f_\epsilon(\varepsilon) = (1/\sqrt{2\pi}) \exp(-\varepsilon^2/2)$ represents the standard normal distribution, which is independent of m and r as defined in Subsection 2.2.2, and the first term in the integrand becomes the Heaviside step function

$$P\left\{S_a(T_j) > s_j \,\middle|\, m, r, \varepsilon\right\} = H\Big[S_a(T_j) \,\Big|\, m, r, \varepsilon - s_j\Big] = \begin{cases} 1, & \text{if } S_a(T_j) \,|\, m, r, \varepsilon > s_j, \\ 0, & \text{otherwise,} \end{cases} \tag{3.3.2}$$

where $S_a(T_j) \,|\, m, r, \varepsilon$ is computed from equation (2.2.6).

From equation (3.3.1), relative hazard contributions towards s_j (corresponding to λ_{s_j}) can be calculated. The general procedure of SHD is summarized as follows:

(1) The contribution from all seismic sources to spectral acceleration s_j is deaggregated into smaller intervals $m_{x-1} \leqslant m \leqslant m_x$, $r_{y-1} \leqslant r \leqslant r_y$, and $\varepsilon_{z-1} \leqslant \varepsilon \leqslant \varepsilon_z$ ($1 \leqslant x \leqslant x_N$, $1 \leqslant y \leqslant y_N$, and $1 \leqslant z \leqslant z_N$, in which x_N, y_N, and z_N are the number of intervals divided for m, r, and ε,

respectively), and is given by

$$\lambda_{s_j,x,y,z} = \sum_{i=1}^{N_S} \nu_i \Big\{ \int_{\varepsilon_{z-1}}^{\varepsilon_z} \int_{r_{y-1}}^{r_y} \int_{m_{x-1}}^{m_x} \mathcal{P}\left\{S_a(T_j) > s_j \,\middle|\, m, r, \varepsilon\right\} f_M(m) f_R(r) f_\epsilon(\varepsilon) \mathrm{d}m \,\mathrm{d}r \,\mathrm{d}\varepsilon \Big\}_i. \tag{3.3.3}$$

(2) Dividing the deaggregated probabilities of exceedance $\lambda_{s_j,x,y,z}$ for small m-r-ε intervals by the total probability of exceedance λ_{s_j} to determine the relative hazard contributions from different cubic intervals of m-r-ε. A 4-dimensional histogram of relative hazard contributions against the coordinates of m, r, and ε can be displayed.

(3) From the relative hazard contributions towards s_j, a representative earthquake, in terms of modal or mean values of magnitude m, source-site distance r, and the number of standard deviations ε, can be obtained.

- **Modal earthquake** (bivariate modal values $\hat{m}_j$-$\hat{r}_j$ or triplet $\hat{m}_j$-$\hat{r}_j$-$\hat{\varepsilon}_j$), is the most-likely earthquake towards s_j, corresponding to the cubic interval having the largest hazard contribution. It represents a physically realizable earthquake threat to the site of interest.

- **Mean earthquake** is the (marginal) mean earthquake towards s_j, corresponding to the weighted average values of magnitude $\bar{m}_j$, distance $\bar{r}_j$, and the number of standard deviations $\bar{\varepsilon}_j$, given by (Ni, 2012)

$$\bar{m}_j = \sum_{x=1}^{x_N} \sum_{y=1}^{y_N} \sum_{z=1}^{z_N} \frac{\left(m_{x-1} + m_x\right)}{2} \frac{\lambda_{s_j,x,y,z}}{\lambda_{s_j}}, \tag{3.3.4a}$$

$$\bar{r}_j = \sum_{x=1}^{x_N} \sum_{y=1}^{y_N} \sum_{z=1}^{z_N} \frac{\left(r_{y-1} + r_y\right)}{2} \frac{\lambda_{s_j,x,y,z}}{\lambda_{s_j}}, \tag{3.3.4b}$$

$$\bar{\varepsilon}_j = \sum_{x=1}^{x_N} \sum_{y=1}^{y_N} \sum_{z=1}^{z_N} \frac{\left(\varepsilon_{z-1} + \varepsilon_z\right)}{2} \frac{\lambda_{s_j,x,y,z}}{\lambda_{s_j}}, \tag{3.3.4c}$$

where $\lambda_{s_j,x,y,z}$ and λ_{s_j} are given by equations (3.3.3) and (3.3.1), respectively.

Sometimes it may not be a physically realizable earthquake, but it is more capable of representing the expected hazard and thus preferable for risk communication.

☞ SHD is performed towards a specific s_j (or probability level λ_{s_j}) at a specific period T_j; consequently, any summary statistics obtained are referred to this condition.

Example Seismic Hazard Deaggregation

Consider the hypothetical site shown in Figure 2.6. At three reference probabilities of 50%/50 year, 10%/50 year, and 2%/50 year, 3-dimensional histograms of relative hazard contributions for spectral accelerations at 0.1 and 1.0 sec from various *m*-*r* intervals are shown in Figure 3.6. A uniform *m* interval of 0.5 unit and uniform *r* interval of 10 km are used for identifying the dominant or controlling events.

From the joint *m*-*r* distribution, a widely recognized phenomenon can be observed: small near-field events (from source 1) dominate hazard in short period portion (0.1 sec); large far-field events (from sources 2 and 3) contribute more hazard in long period portion (1.0 sec) (McGuire, 1995; Halchuk and Adams, 2004). Hazard at the site can be either single-source-dominant or multiple-source-dominant, which is period-dependent.

Existing Seismic Hazard Deaggregation Procedures

For seismic hazard analysis, deaggregation procedures have been developed to extract a single controlling earthquake to represent the type of event that contributes to hazard at a given probability λ_{s_j}. It is desirable to recover the "target" spectral acceleration s_j (corresponding to λ_{s_j}) when event parameters are substituted into the GMPE used in PSHA. However, there is no theoretical reason that could support this property; there is bias between the recovered and target s_j values.

McGuire (1995) proposed a deaggregation procedure for obtaining a controlling event that matches the target uniform hazard spectrum (UHS) in major period range of interest. If one source dominates hazard at both 0.1 sec and 1 sec, then one controlling event called beta earthquake, is determined by taking the most-likely m_β and r_β. ε_β is adjusted so that predicted s_j (using triplet m_β-r_β-ε_β and GMPE) matches target s_j at both 0.1 and 1 sec on UHS. If different sources dominate hazard at 0.1 and 1 sec, then two beta earthquakes are determined to represent hazard at 0.1 and 1 sec, respectively. Since the deaggregated ε_β together with m_β and r_β may not necessarily recover target s_j, an adjusted ε_β was used.

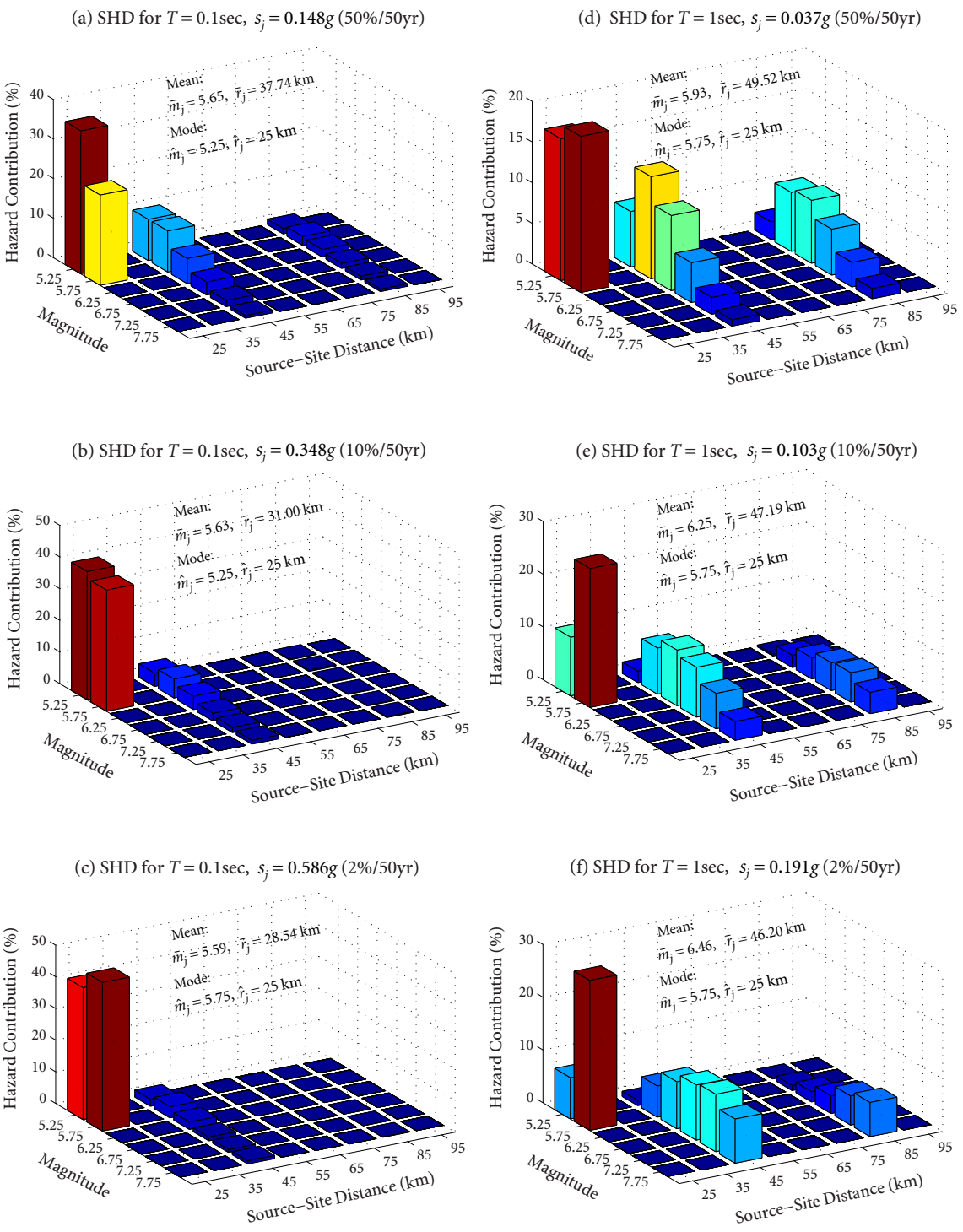

Figure 3.6 Seismic hazard deaggregation for SA at 0.1 and 1 sec at 3 probability levels

Ni *et al.* (2012) proposed another SHD procedure for obtaining a controlling earthquake in terms of magnitude m_C, distance r_C, and occurrence rate ν_C, in a weighted average sense. The controlling earthquake (m_C, r_C, ν_C) describes the expected earthquake threat to the site towards s_j. It has been used for a simplified approach to develop some design spectra (Ni *et al.*, 2012), with reported average relative error of less than 20%. This procedure includes the deaggregation in terms of occurrence rate ν instead of ε, in appreciation of the role that ν plays in the integrative PSHA towards target s_j. m_C and r_C are determined using equations (3.3.4a) and (3.3.4b) and ν_C is determined across all seismic sources using

$$\nu_{\mathrm{C}} = \sum_{i=1}^{N_S} \nu_i \frac{\lambda_{s_j}^{(i)}}{\lambda_{s_j}}, \tag{3.3.5}$$

where $\lambda_{s_j}^{(i)}$ is the hazard contribution from source *i*.

Ni *et al.* (2012) further extended "scalar" SHD based on scalar PSHA into the "vector-valued" case, to determine a controlling event that contributes to a joint hazard of spectral accelerations at multiple periods. By replacing the conditional marginal distribution of spectral acceleration at individual period in equation (2.2.14) by the conditional joint distribution of spectral accelerations at multiple periods in equation (3.2.2), the deaggregated joint hazard in each *m*-*r* interval becomes

$$\lambda_{s_1 \cdots s_k, x, y} = \sum_{i=1}^{N_S} \nu_i \left\{ \int_{r_{y-1}}^{r_y} \int_{m_{x-1}}^{m_x} \mathcal{P}\left\{ S_a(T_1) > s_1, \cdots, S_a(T_k) > s_k \,\middle|\, m, r \right\} f_M(m) f_R(r) \mathrm{d}m \, \mathrm{d}r \right\}_i. \tag{3.3.6}$$

The joint *m*-*r* distribution are then obtained by dividing the probability of exceedance $\lambda_{s_1 \cdots s_k, x, y}$ for various *m*-*r* intervals by the total $\lambda_{s_1 \cdots s_k}$ from equation (3.2.1).

The weighted average values of magnitude, distance, and occurrence rate, which drive seismic hazard towards spectral accelerations $s_1, s_2, \cdots, s_k$ simultaneously, are given by

$$m_{\mathrm{C}} = \sum_{x=1}^{x_N} \sum_{y=1}^{y_N} \frac{(m_{x-1} + m_x)}{2} \frac{\lambda_{s_1 \cdots s_k, x, y}}{\lambda_{s_1 \cdots s_k}}, \tag{3.3.7a}$$

$$r_{\mathrm{C}} = \sum_{x=1}^{x_N} \sum_{y=1}^{y_N} \frac{(r_{y-1} + r_y)}{2} \frac{\lambda_{s_1 \cdots s_k, x, y}}{\lambda_{s_1 \cdots s_k}}, \tag{3.3.7b}$$

$$\nu_C = \sum_{i=1}^{N_S} \nu_i \frac{\lambda^{(i)}_{s_1 \cdots s_k}}{\lambda_{s_1 \cdots s_k}}. \tag{3.3.7c}$$

Figure 3.7 shows vector-valued SHD towards spectral accelerations at 1.0 and 1.0 sec, at marginal probabilities of 50%/50 year and 2%/50 year. Both the joint *m*-*r* distribution and the mean earthquake are somewhere in between the marginal statistics provided by scalar SHD shown in Figure 3.6.

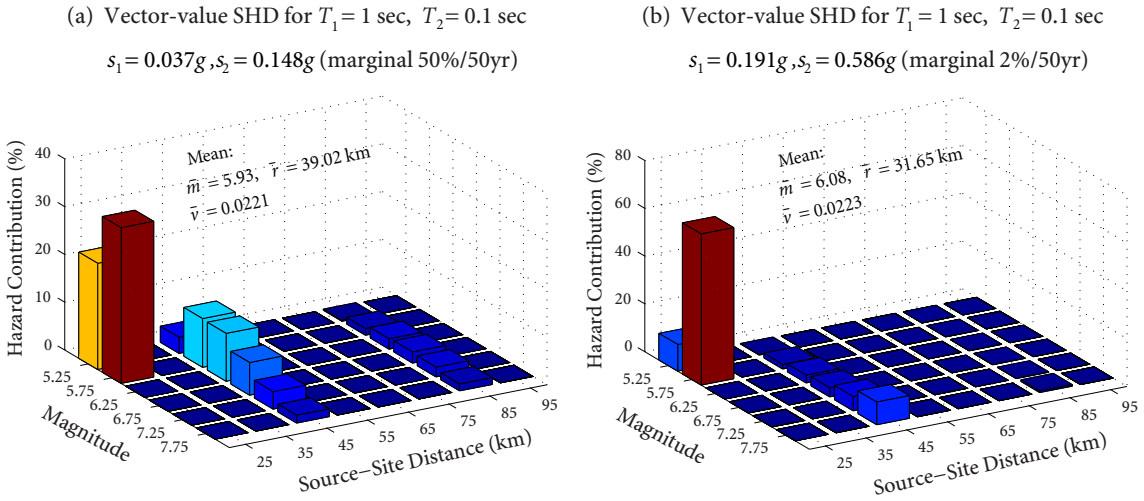

Figure 3.7 Vector-valued seismic hazard deaggregation for SA at 0.1 and 1.0 sec

Due to the integrative nature of PSHA, no single event can fully represent the seismic hazard at a site. In many practical cases, multiple (m, r)-pairs show comparable contributions to to a specific level of hazard. Ground motions generated by earthquakes having different (m, r)-pairs may have quite different frequency content. Considering only one (m, r)-pair is not likely to provide correct ground motion estimate in the entire frequency range (joint hazard). Hence, it is more appropriate to report different (m, r)-pairs along with their relative contributions and make sure that they are properly reflected during structural analysis and design. However, little research has been done here.

In addition, the controlling earthquake extracted from deaggregation may be very different as the reference probability level varies, especially for the long period hazard (e.g., 1 sec), as Figure 3.6 illustrates. It is impossible to extract a single controlling earthquake that induces dominant hazard at the site applicable to all probability levels. This is why U.S.

NRC (2007) recommends that analysis of multiple ground motion levels be used to obtain a more complete understanding of the earthquake characteristics (i.e., mean magnitudes and distances) that contribute to both the high-frequency (5 and 10 Hz) and low-frequency (1 and 2.5 Hz) hazard, than could be obtained from a single ground motion level.

3.3.3 Proposed Procedure for Simplified Seismic Risk Analysis

Since seismic risk analysis integrates over the full range of s_j and different s_j are usually dominated by different earthquakes, it is too simplistic to apply a single controlling earthquake, i.e., (m, r)-pair, for risk analysis. Rather, it is more desirable to identity multiple dominant (m, r)-pairs and reflect their relative contributions. These (m, r)-pairs should collectively recover hazard curve in the probability range $\lambda_a = 1 \times 10^{-3} \sim 1 \times 10^{-6}$/year that contribute most to seismic risk, and hence are called a set of controlling earthquakes.

The mathematical basis for using a set of controlling earthquakes for risk analysis is the mean value theorem of integration.

Mean Value Theorem of Integration

First Mean Value Theorem of Integration: Let $f(x)$ be continuous and integrable on $[a, b]$, there exists $c \in (a, b)$ such that

$$\int_a^b f(x)\mathrm{d}x = f(c)\big(b - a\big),$$

where point $f(c)$ is called the average value of $f(x)$ on $[a, b]$.

Second Mean Value Theorem of Integration: Let $f(x)$ and $g(x)$ be continuous on $[a, b]$. Assume that $g(x) \geqslant 0$ for any $x \in [a, b]$. Then there exists $c \in (a, b)$ such that

$$\int_a^b f(x)\, g(x)\mathrm{d}x = f(c) \int_a^b g(x)\mathrm{d}x,$$

where point $f(c)$ is called the $g(x)$-weighted average of $f(x)$ on $[a, b]$.

Mean Value Theorem of Double Integration: Let $f(x, y)$ be continuous and integrable over a region D with an area of $A(D)$, then there exists a point (x_0, y_0) in D such that

$$\iint_D f(x, y)\mathrm{d}A = f(x_0, y_0)\, A(D).$$

The various Mean Value Theorems of integration imply that integration can be approximated and simplified by using a point value, which could be mean, a weighted-average, or other properly defined values on the domain.

However, approximations of integration may not always be satisfactory in practical cases such as complex functional forms of integrand, wide integration domain, and multi-fold integration. A convenient way of improving approximation is to divide the integration domain into a number of subdomains and apply the Mean Value Theorem in each subdomain. For example, the formula in the Second Mean Value Theorem of Integration is also true for

$$\int_a^b f(x)\,g(x)\mathrm{d}x = f(c_1)\int_a^{b_1} g(x)\mathrm{d}x + f(c_2)\int_{b_1}^{b_2} g(x)\mathrm{d}x + \cdots + f(c_n)\int_{b_{n-1}}^{b_n} g(x)\mathrm{d}x,$$

where $a < b_1 < \cdots < b_n = b$ and $f(c_i)$ is the $g(x)$-weighted average of $f(x)$ on the respective interval $[b_{i-1}, b_i]$. Using multiple weighted average $f(c_i)$ instead of a single $f(c)$ helps improve the approximation.

The risk equation (3.2.6) involves multi-fold integration and complex functional forms of integrand, i.e., GMPE and fragility. A single controlling earthquake, determined in a weighted average sense over the entire m and r domain, does not always provide satisfactory risk approximation (Wang *et al.*, 2013a).

By dividing the integration domain in term of m and r into a number of subdomains, i.e., (M, R)-bins and applying Mean Value Theorem of Integration in each (M, R)-bin, the risk integration can be better approximated. In any (M, R)-bin, the included m-r pairs generate similar ground motions, hence is referred to as a "characteristic" (M, R)-bin.

Proposed Procedure for Simplified VSRA

Based on the aforementioned concepts, a procedure for simplified vector-valued SRA is proposed, as illustrated in Figure 3.8. The core part is to deaggregate a set of controlling earthquakes that dominate seismic hazard at the site for the probability range of interest, based on which standard vector-valued SRA that integrates over all possible earthquake occurrences can be simplified. Successful implementation of this procedure depends on the following steps.

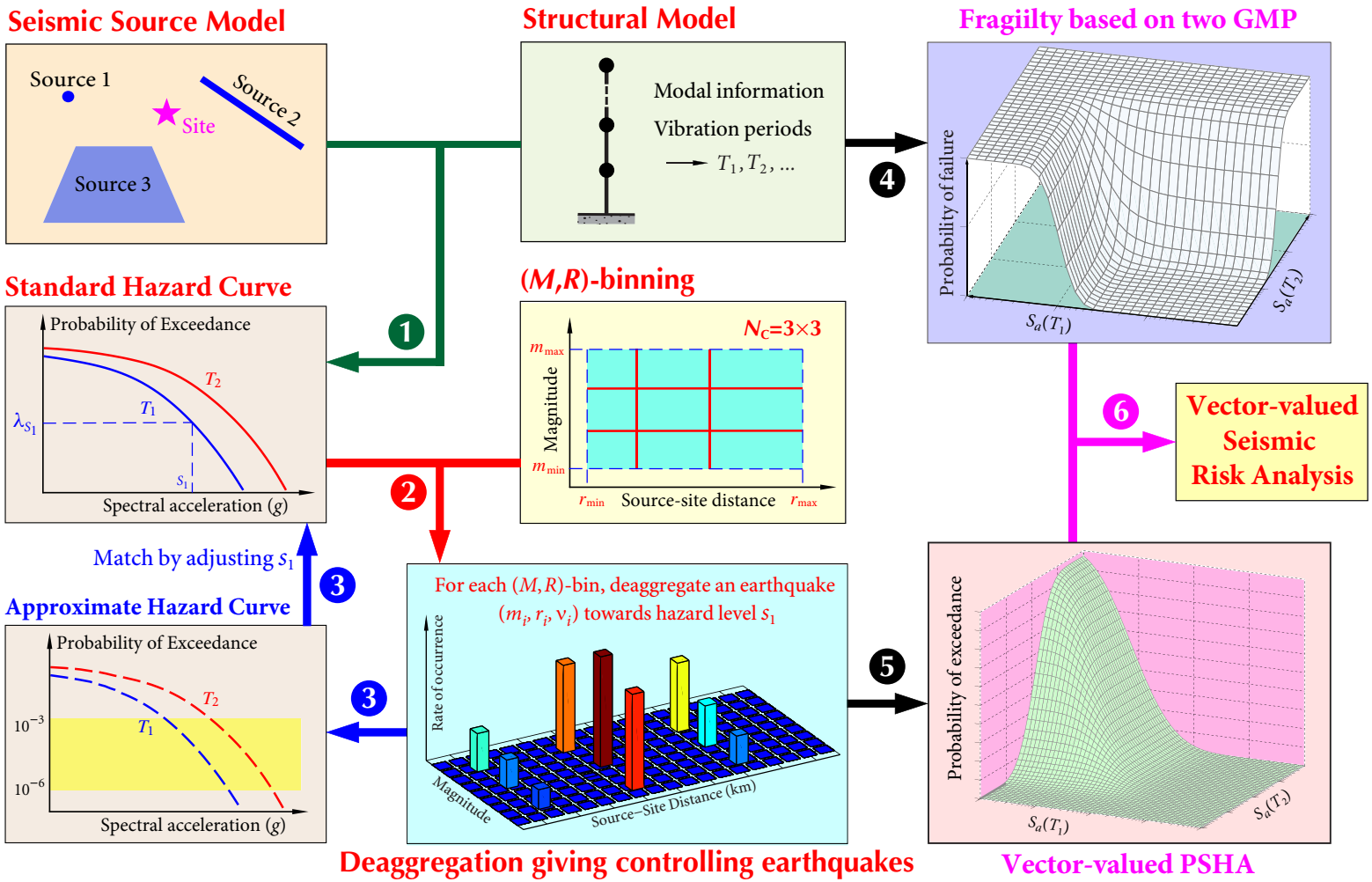

Figure 3.8 Framework of the simplified approach to VSRA

(1) Development of standard hazard curves. PSHA is performed to obtain the hazard curves at a site for spectral accelerations at the vibration periods of the structure, $T_1, T_2, \cdots$. It is based on all possible earthquake occurrences defined by the seismic source model.

(2) (M, R)-binning, which can be achieved by inspection for simple source configurations, or by displaying hazard contributions from (m, r)-pairs for complex source configurations. For the latter, existing SHD procedures presented in Subsection 3.3.2 can be used. From the relative contributions towards s_1, a set of characteristic (M, R)-bins, each showing similar hazard contribution pattern, are determined. Typically, if both M and R are divided into 3 segments

$$M_S = [m_{\min},\, m_1), \quad M_M = [m_1,\, m_2), \quad M_L = [m_2,\, m_{\max}],$$
$$R_S = [r_{\min},\, r_1), \qquad R_M = [r_1,\, r_2), \qquad R_L = [r_2,\, r_{\max}],$$

a set of $N_C = 3 \times 3 = 9$ $(M, R)_i$-bins $(i = 1, 2, \cdots, 9)$ are obtained.

M_S, M_M, and M_L can be interpreted as small, median, and large earthquakes, respectively. Similarly, R_S, R_M, and R_L can be interpreted as near-field, median-field, and far-field earthquakes, respectively. The determination of $(M, R)_i$-bins is dependent on the ranges of M and R, and is adjustable for site-specific applications.

(3) Deaggregation giving a set of controlling earthquakes. For each $(M, R)_i$-bin, determine *locally* the weighted average values of m_{C_i} and r_{C_i}, and determine *globally*, i.e., across all seismic sources, the weighted average value of rate of occurrence ν_{C_i}, by

$$m_{C_i} = \sum_{x=1}^{x_{N_i}} \sum_{y=1}^{y_{N_i}} \frac{(m_{x-1} + m_x)}{2} \cdot \frac{\lambda_{s_1,x,y,(M\text{-}R)_i}}{\lambda_{s_1,(M\text{-}R)_i}}, \tag{3.3.8a}$$

$$r_{C_i} = \sum_{x=1}^{x_{N_i}} \sum_{y=1}^{y_{N_i}} \frac{(r_{y-1} + r_y)}{2} \cdot \frac{\lambda_{s_1,x,y,(M\text{-}R)_i}}{\lambda_{s_1,(M\text{-}R)_i}}, \tag{3.3.8b}$$

$$\nu_{C_i} = \sum_{k=1}^{N_S} \nu_k \cdot \frac{\lambda_{s_1,k,(M\text{-}R)_i}}{\lambda_{s_1}}, \tag{3.3.8c}$$

where $1 \leqslant x \leqslant x_{N_i}$, $1 \leqslant y \leqslant y_{N_i}$, and x_{N_i} and y_{N_i} are respectively the number of (m, r)-pairs belonging to $(M, R)_i$-bin, $\lambda_{s_1,(M\text{-}R)_i}$ is the portion of λ_{s_1} contributed by $(M, R)_i$-bin, $\lambda_{s_1,x,y,(M\text{-}R)_i}$

is hazard contribution from an (m, r)-pair within $(M, R)_i$-bin, λ_{s_1} is the overall annual probability of exceedance of s_1 , ν_k is the rate of occurrence for source k, $\lambda_{s_1,k,(M\text{-}R)_i}$ is the portion λ_{s_1} contributed by $(M, R)_i$-bin from source k.

Note that the hazard level s_1, towards which the deaggregation is performed, should be adjusted so that the approximate hazard curves, based on a set of N_C deaggregated earthquakes, using

$$\lambda_{s_1} \approx \sum_{i=1}^{N_C} \nu_{C_i} \cdot \bar{\mathcal{P}} \left\{ S_a(T_1) > s_1 \,\middle|\, m_{C_i}, r_{C_i} \right\}, \tag{3.3.9}$$

accurately recover the standard curves within probability range $\lambda_a = 1 \times 10^{-3} \sim 1 \times 10^{-6}$/year.

The associated set of deaggregated earthquakes are then the controlling earthquakes that dominate the hazard at the site. Earthquake scenario (m_{C_i}, r_{C_i}) reflects the dominant event in $(M, R)_i$-bin. Rate of occurrence ν_{C_i} reflects the relative contribution by each $(M, R)_i$-bin to the overall hazard λ_{s_j}; consequently, ν_{C_i} is a natural weighting factor for (m_{C_i}, r_{C_i}).

(4) Seismic hazard approximations. Using a set of controlling earthquakes, combined with the probabilistic model of spectral accelerations, PSHA can be simplified.

The overall hazard given by standard PSHA reflects the contributions from all possible (m, r)-pairs weighted by their joint probability density and source-wise occurrence rate ν. Since a set of controlling earthquakes have been determined to dominate seismic hazard at the site in the range of interest, it is therefore reasonable to use them instead of the random variables M and R and occurrence rate ν for simplicity and approximation.

By substituting (m_{C_i}, r_{C_i}) directly into the conditional probability distribution of spectral accelerations in the standard formulation of PSHA, numerical integrations with respect to m and r can be avoided. When multiplied by the rate of occurrence ν_{C_i}, seismic hazard induced by earthquake i (m_{C_i} and r_{C_i}) can be approximated marginally or jointly. Summing up hazard contributions from all N_C earthquakes gives the approximate overall hazard

$$\lambda_{s_1} \approx \sum_{i=1}^{N_C} \nu_{C_i} \cdot \bar{\mathcal{P}} \left\{ S_a(T_1) > s_1 \,\middle|\, m_{C_i}, r_{C_i} \right\}, \tag{3.3.10a}$$

$$\lambda_{s_1,\cdots,s_k} \approx \sum_{i=1}^{N_C} \nu_{C_i} \cdot \bar{\mathcal{P}} \left\{ S_a(T_1) > s_1, \cdots, S_a(T_k) > s_k \,\middle|\, m_{C_i}, r_{C_i} \right\}. \tag{3.3.10b}$$

Note that in equation (3.3.10a) the marginal seismic hazard in terms of spectral acceleration $S_a(T_1)$ at period T_1 is a verified approximation in the primary range of interest. In contrast, in equation (3.3.10b) the joint hazard in terms of spectral accelerations $S_a(T_1), \cdots, S_a(T_k)$ at multiple periods $T_1, \cdots, T_k$ is a less rigorous approximation, which is based on the set of controlling earthquakes deaggregated towards marginal hazard s_1.

In the multivariate probability model of spectral accelerations in equation (3.2.2), the core inputs are the conditional means and standard deviations at individual periods and the spectral correlation matrix. Given the structural vibration periods, the correlation matrix is totally defined and the marginal central statistics become the critical inputs. Hence, the accuracy of joint hazard approximation using equation (3.3.10b) depends on the marginal hazard approximations (3.3.10a) from using a set of controlling earthquakes.

(5) Risk analysis approximations. For seismic risk analysis, fragility model considering spectral accelerations must be incorporated.

In seismic analysis of structures, dynamic response in the first mode is most important. Accordingly, hazard approximation for spectral acceleration $S_a(T_1)$ becomes crucial. Secondary hazard approximation for spectral accelerations $S_a(T_2), \cdots, S_a(T_k)$ can be relatively relaxed, but should be checked. Since the first several modal periods of typical structures is not very apart, using a set of controlling earthquakes deaggregated towards $S_a(T_1)$ is appropriate in most practical cases.

Incorporating the simplification given in equation (3.3.10) with seismic fragility model, simplified seismic risk analysis can be obtained.

For the scalar case,

$$\lambda_D(z) \approx \sum_{i=1}^{N_C} \nu_{C_i} \cdot \int_0^{\infty} \mathcal{P}\left\{D > z \,\middle|\, S_a(T_1) = s_1\right\} \cdot f_{S_a(T_1)}\left(s_1 \,\middle|\, m_{C_i}, r_{C_i}\right) \mathrm{d}s_1 \,. \tag{3.3.11}$$

For the vector-valued case,

$$\lambda_D(z) \approx \sum_{i=1}^{N_C} \nu_{C_i} \cdot \int_0^{\infty} \cdots \int_0^{\infty} \mathcal{P}\left\{D > z \,\middle|\, S_a(T_1) = s_1, \cdots, S_a(T_k) = s_k\right\}$$

$$\cdot f_{S_a(T_1)\cdots S_a(T_k)}\left(s_1 \cdots s_k \,\middle|\, m_{C_i}, r_{C_i}\right) \mathrm{d}s_1 \cdots \mathrm{d}s_k \,. \tag{3.3.12}$$

The most inner two-fold integrations with respect to m and r, which were performed repetitively in equations (2.3.4) and (3.2.6), are now replaced by a set of N_C controlling earthquakes. Hence, computational efforts can be significantly reduced.

Example Application for Hazard Approximation

Before performing simplified risk analysis, let's first look at an example application for hazard approximation. Consider the simple hypothetical site shown in Figure 2.6.

(1) Development of standard hazard curves. Without no information of structure, hazard curves for spectral accelerations (SA) at at 1 sec and 0.1 sec are developed using (2.2.15), as shown in Figures 3.9 and 3.10.

(2) (M, R)-binning. Since seismic sources have M ranging from 5.0 to 8.0 and well-separated R, from around 25 km to 90 km, it is natural and easy to divide M and R into 3 equal segments

$$M_S = [5.0,\ 6.0), \quad M_M = [6.0,\ 7.0), \quad M_L = [7.0,\ 8.0],$$
$$R_S = [0,\ 30), \qquad R_M = [30,\ 60), \qquad R_L = [60,\ 90],$$

which gives a total of 7 characteristic (M, R)-bins (note that $M = [5.0,\ 6.0]$ for source 1).

(3) Deaggregation for controlling earthquakes. Perform deaggregation using equations (3.3.8) for SA at 1 sec and 0.1 sec, respectively, at probabilities of 50%/50yr, 10%/50yr, and 2%/50yr, to obtain 3 sets of deaggregated earthquakes.

Develop approximate hazard curves using equation (3.3.9), for each set of deaggregated earthquakes, as shown in Figures 3.9 and 3.10. By comparison, the most appropriate λ_{s_j} are 50%/50yr for SA at 1 sec and 2%/50yr for SA at 0.1 sec. The corresponding sets of controlling earthquakes are given in Table 3.2. Hazard contributions from characteristic (M, R)-bins, i.e., controlling earthquakes, are shown in Figures 3.11 and 3.12.

It is observed that high probability event (e.g., $\lambda_{s_j} = 50\%/\text{yr}$) could better approximate hazard at long period (1.0 sec), where far-field events could have a significant contribution. In contrast, low probability event (e.g., $\lambda_{s_j} = 2\%/50\text{yr}$) could better approximate hazard at short period (0.1 sec), where far-field events (Source 3) might be too far to matter.

(4) Secondary hazard curve approximations check. It is also interesting to check hazard approximation for $S_a(T_i)$ using a set of controlling earthquakes deaggregated for $S_a(T_j)$, called

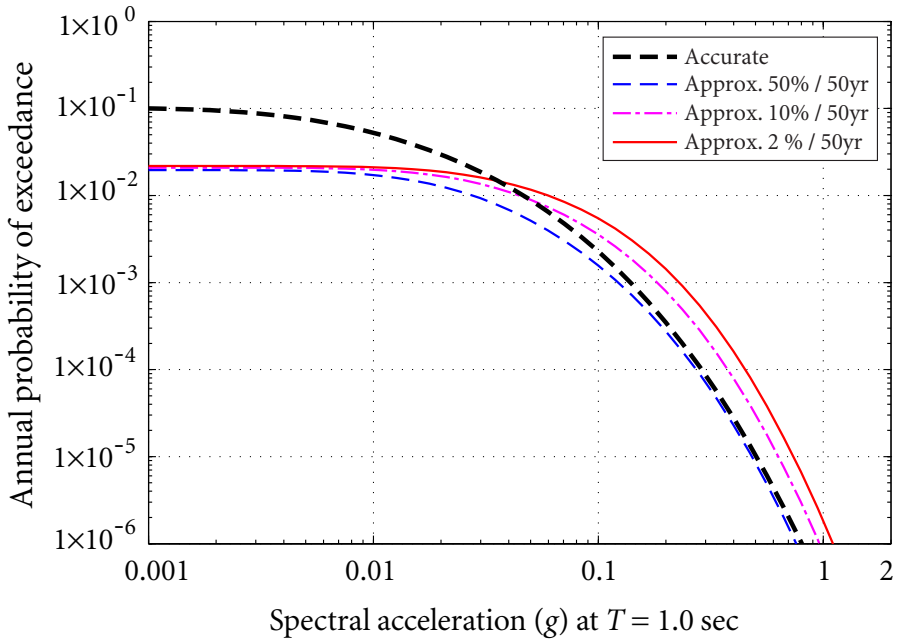

Figure 3.9 Hazard curve approximations for SA at 1 sec using deaggregated earthquakes at 3 probabilities: 50%/50yr, 10%/50yr, and 2%/50yr

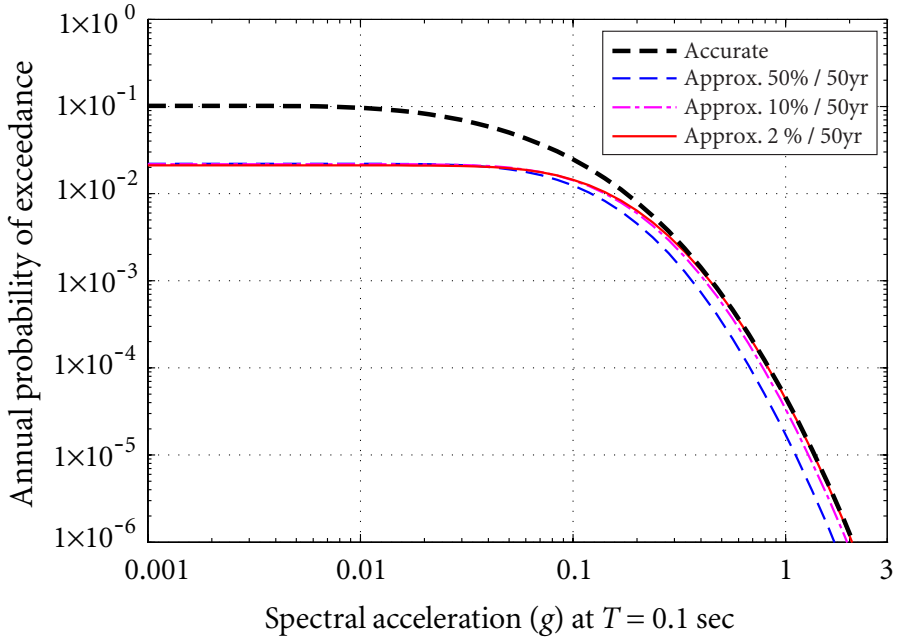

Figure 3.10 Hazard curve approximations for SA at 0.1 sec using deaggregated earthquakes at 3 probabilities: 50%/50yr, 10%/50yr, and 2%/50yr

Table 3.2 Sets of controlling earthquakes deaggregated for two periods

	$S_a(T=1\text{sec})=0.0373g$ (50%/50 yr)			$S_a(T=0.1\text{sec})=0.5855g$ (2%/50 yr)		
i	m_{C_i}	r_{C_i}	ν_{C_i}	m_{C_i}	r_{C_i}	ν_{C_i}
1	5.514	26.108	0.0073	5.516	26.073	0.0177
2	5.592	46.636	0.0058	5.567	46.499	0.0017
3	5.670	84.965	0.0005	5.608	84.420	0.0000
4	6.398	46.672	0.0042	6.393	46.507	0.0010
5	6.448	85.077	0.0007	6.378	84.419	0.0000
6	7.348	46.693	0.0009	7.513	46.544	0.0006
7	7.363	85.164	0.0002	7.643	84.584	0.0000

secondary hazard approximation. Figures 3.13 and 3.14 show secondary hazard approximations between $S_a(T=0.1\,\text{sec})$ and $S_a(T=1\,\text{sec})$ hazard. The set of controlling earthquakes for $S_a(T=0.1\,\text{sec})$ associated with $\lambda_{s_j}=2\%/50$ year provide satisfactory secondary hazard approximation for $S_a(T=1\,\text{sec})$. However, the set of controlling earthquakes for $S_a(T=1\,\text{sec})$ associated with $\lambda_{s_j}=50\%/50$ year do not provide very satisfactory secondary hazard approximation for $S_a(T=0.1\,\text{sec})$. This is due to the large separation of vibration periods 0.1 sec and 1 sec. In case of separation of periods is small, the secondary hazard approximation becomes more accurate.

Remarks

Two primary benefits can be gained from this procedure. The first benefit is the desirable features of a set of N_C controlling earthquakes opposed to a single controlling earthquake:

(1) Better representation of seismic hazard at the site, including a complete description of representative earthquakes from small near-field to large far-field earthquakes.

(2) Better capability of representing seismic hazard in the probability range of interest. Hence, the set-wise "controlling earthquakes" representation is more meaningful.

(3) Natural description of the importance of earthquake scenario (m_{C_i}, r_{C_i}) through ν_{C_i}. This information is very useful in selecting ground motions for dynamic analysis of structures.

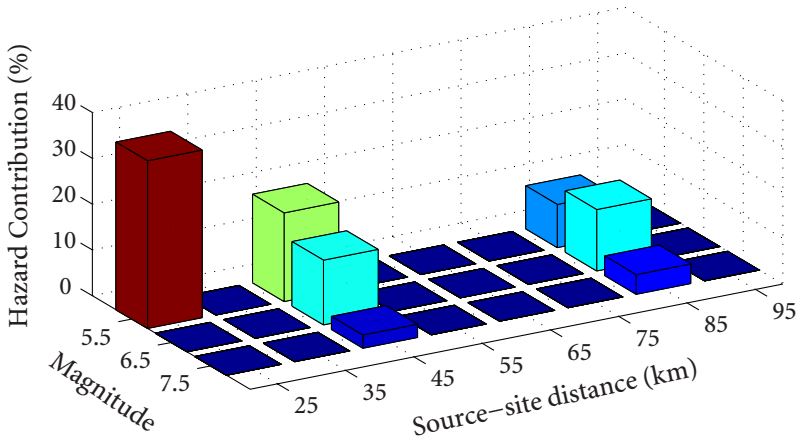

Figure 3.11 Controlling earthquakes for $S_a(T=1\,\text{sec})$ (50%/50 yr)

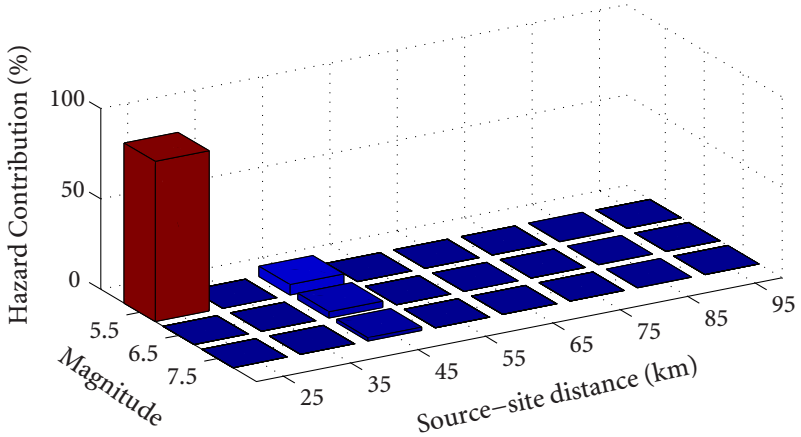

Figure 3.12 Controlling earthquakes for $S_a(T=0.1\,\text{sec})$ (2%/50 yr)

Another benefit is the improved computational efficiency using this simplified approach given in equations (3.3.10), which can be characterized by comparing the number of controlling earthquakes N_C with the total number of (m,r)-pairs N defined by the seismic source model.

- In the seismic source model, mesh size $\Delta m = 0.1$ for magnitude is consistently used, which gives 10 magnitudes for source 1 ($M=[5,6]$), 30 magnitudes for sources 2 and 3 ($M=[5,8]$).
- Mesh size $\Delta l = 0.5$ km is used for line faults, which gives 40 distances for source 1 ($L=20$ km) and 80 distances for source 2 ($L=40$ km). 100 grids for areal source 3 (10 km $\times$ 10 km) are used, giving 100 distances.

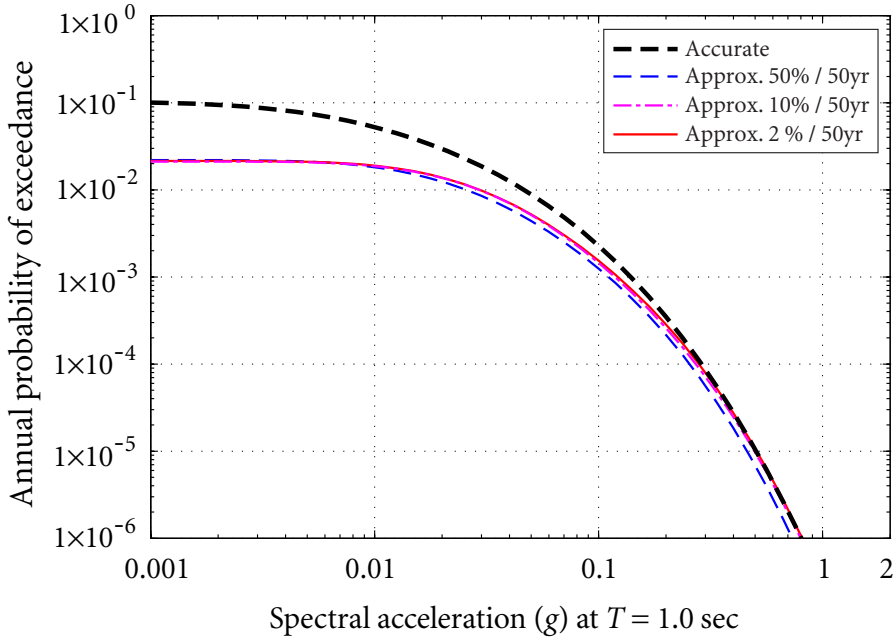

Figure 3.13 Secondary hazard approximation for $S_a(T=1\,\text{sec})$ using the controlling earthquakes for $S_a(T=0.1\,\text{sec})$

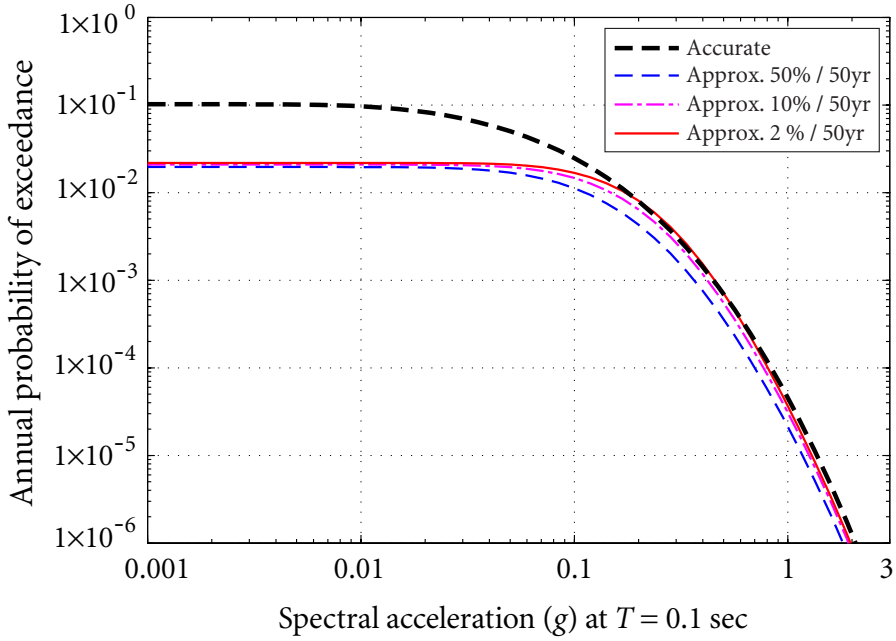

Figure 3.14 Secondary hazard approximation for $S_a(T=0.1\,\text{sec})$ using the controlling earthquakes for $S_a(T=1\,\text{sec})$

- Using this discretization scheme results in $10 \times 40 = 400$ (m, r)-pairs for source 1, $30 \times 80 = 2400$ (m, r)-pairs for source 2, and $30 \times 100 = 3000$ (m, r)-pairs for source 3. Altogether, $N = 5800$ (m, r)-pairs are used in the standard analysis.

- When $N_C = 7$ controlling earthquakes are used in the simplified approach, the computational efficiency is then $N_C/N = 7/5800 = 0.12\%$, which is a significant improvement.

3.4 Numerical Examples

Two numerical examples are presented to illustrate the proposed procedure for simplified seismic risk analysis given in Subsection 3.3.3 and validate its effectiveness. First, the selected target structure is described. Seismic risk analysis is performed for both a hypothetical site and a realistic site in coastal California. Important factors affecting the quality of the simplified approach are discussed through the examples.

3.4.1 20-storey Steel Moment Resisting Frame

Structure configuration

Consider a 20-storey steel moment resisting frame (SMRF) building structure, which was designed as a standard office building situated on stiff soil. Floor plan and elevation of the model building are shown in Figure 3.15, where the shaded area indicates the penthouse location and perimeter moment resisting frames are selected as the structural system. Design loads includes gravity, wind loading, and seismic loading. The buildings were required to conform to a drift ratio limit of $h/400$. Details about the model building, such as column and girder sizes, can be found in the report by Gupta and Krawinkler (1999). Its design is controlled by drift rather than strength requirements; hence the maximum inter-storey drift ratio $\delta_{\max}$ is taken as the damage measure.

Response statistics

The 20-storey SMRF building is very flexible, having a fundamental period $T_1 = 4.0$ sec and the second modal period $T_2 = 1.33$ sec. Its seismic performance has been evaluated using vector-valued PSHA (Bazzurro and Cornell, 2002), based on nonlinear seismic response

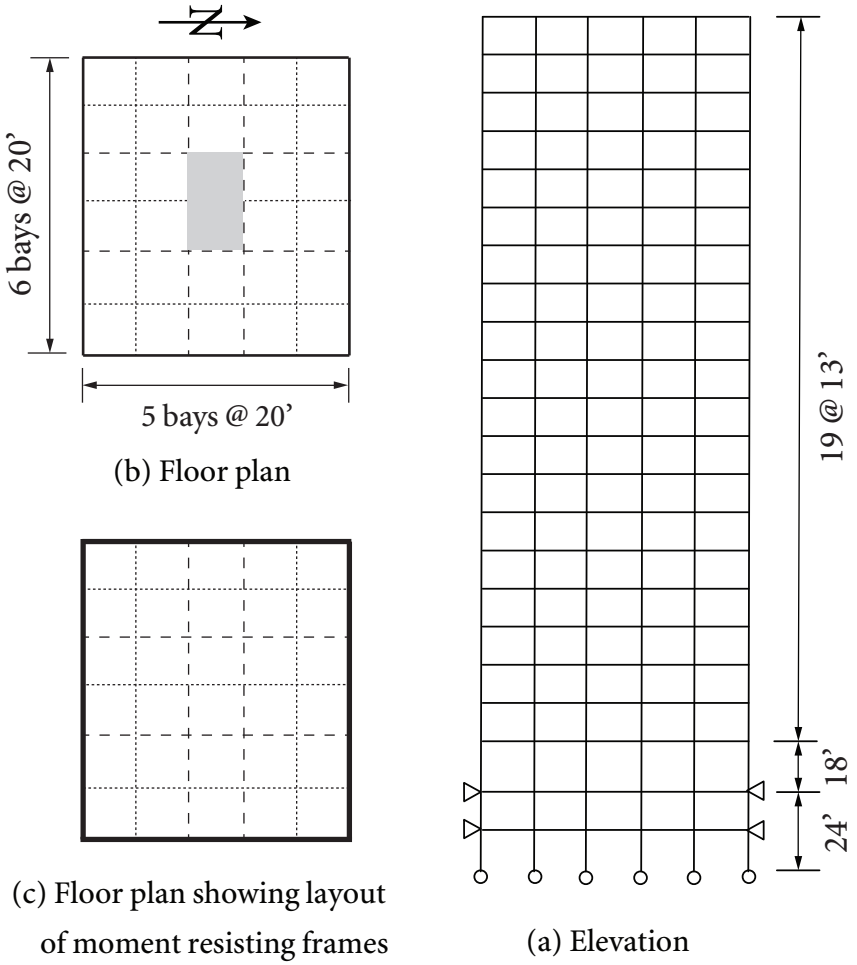

(b) Floor plan

(c) Floor plan showing layout of moment resisting frames

(a) Elevation

Figure 3.15 Floor plans and elevations of 20-storey SMRF model

analyses of running 14 accelerograms recorded on stiff soil in California, with earthquake magnitude m varying from 6.7 to 7.3 and the closest distance to rupture r ranging from 10 km to 30 km.

Table 3.3 gives the response statistics of $\delta_{\max}$ by Bazzurro and Cornell Bazzurro and Cornell (2002), showing that $\delta_{\max}$ is strongly dependent on (2%-damped) S_a at both the first and second vibration periods of the undamaged building, as indicated by the larger R^2. Since a single parameter $S_a(T_1)$ does not provide any spectral shape information induced by all possible (m, r)-pairs from the hazard environment, response statistics based on both $S_a(T_1)$ and $S_a(T_2)$ can more accurately reflect and predict the damage from the hazard environment.

Table 3.3 Statistics of structural responses (Bazzurro and Cornell, 2002)

Mean	Standard error	R^2
$\mu_{\ln \delta_{\max}} = -2.32 + 0.70 \ln S_a(T_1)$	$\sigma_{\ln \delta_{\max}} = 0.37$	0.72
$\mu_{\ln \delta_{\max}} = -2.49 + 0.58 \ln S_a(T_1) + 0.62 \ln S_a(T_2)$	$\sigma_{\ln \delta_{\max}} = 0.23$	0.89

Damage analysis

Different from the forementioned drift limit of $h/400$, a number of allowable drift limits, associated with the damage measure $\delta_{\max}$, following the performance-based approach (ASCE, 2005) can be adopted. For the special SMRF ("special" referring to that the SMRF is expected to withstand significant inelastic deformations under the design ground motion (Asgarian *et al.*, 2012)), seismic design criteria ASCE/SEI 43-05 (2005) specifies four limit states associated with storey drift as defined in Table 3.4.

Table 3.4 Allowable drift limits as a function of limit state for special SMRF

Limit state	LS-A†	LS-B†	LS-C†	LS-D†
Allowable drift limit, $\delta_{\max}$	0.035	0.025	0.010	0.005

† A = Short of collapse, but structural stable, B = Moderate permanent deformation, C = Limited permanent deformation, D = Essentially elastic.

If the four discrete limit states defined in Table 3.4 are used, risk analysis will provide four point values. To provide a continuous risk curve, a damaging spectrum encompassing various drift limits (failure criteria) is adopted in this study.

Fragility analysis

Given the response statistics $\mu_{\ln \delta_{\max}}$ and $\sigma_{\ln \delta_{\max}}$ from Table 3.3, showing the statistical relationships between the damage measure $\delta_{\max}$ and predictor variables $S_a(T_1)$ and $S_a(T_2)$, seismic fragility for any damage state or a single "yes-or-no" failure (by specifying a threshold z for $\delta_{\max}$) can be defined. For a given threshold z, equation (2.3.3) gives a fragility curve of the failure probability against a scalar GMP, and equation (3.2.5) provides a fragility surface of the failure probability against two GMP.

For example, consider LS-A in Table 3.4 defined by $\delta_{\max} = 0.035$. Using response statistics considering $S_a(T_1)$ only in Table 3.3, seismic fragility is given by, using equation (2.3.3)

$$\mathcal{P}\left\{\delta_{\max} > 0.035 \,\middle|\, S_a(T_1)\right\} = 1 - \Phi\left(\frac{\ln(0.035) - [-2.32 + 0.70 \ln S_a(T_1)]}{0.37}\right).$$

Seismic fragility curves for all four limit states are given in Figure 3.16.

Similarly, using the response statistics given two spectral parameters $S_a(T_1)$ and $S_a(T_2)$ in Table 3.3, seismic fragility for LS-A can be obtained using equation (3.2.5)

$$\mathcal{P}\left\{\delta_{\max} > 0.035 \,\middle|\, S_a(T_1), S_a(T_2)\right\} = 1 - \Phi\left(\frac{\ln 0.035 - [-2.49 + 0.58 \ln S_a(T_1) + 0.62 \ln S_a(T_2)]}{0.23}\right),$$

which can be plotted as fragility surface as shown in Figure 3.17.

3.4.2 Seismic Risk Analysis at a Hypothetical Site

Suppose that the 20-storey structure is situated on the hypothetical site shown in Figure 2.6.

Standard Seismic Risk Analysis

In the seismic source model, uniform distribution of focal locations is used for each source. The most widely used truncated Gutenberg-Richter magnitude distribution Gutenberg and Richter (1944); Cosentino and Ficarra (1977) is used, in which $m_{\min} = 5.0$, $m_{\max} = 6.0$, and $\beta = 2.07$ for source 1, $m_{\min} = 5.0$, $m_{\max} = 8.0$, and $\beta = 2.07$ for sources 2 and 3. The mean annual rates ν for sources 1, 2, and 3 are taken as 0.02, 0.03, and 0.05, respectively. Focal depths are all taken as 5 km.

The ground-motion prediction equations (GMPE) by Abrahamson and Silva Abrahamson and Silva (1997) are adopted for obtaining the mean and standard deviation in the conditional probability distribution of spectral acceleration in equation (2.2.14). In the GMPE, parameters are set for rock site, reverse fault, non-hanging wall, and sigma for arbitrary component. The matrix of correlation coefficients by Baker and Jayaram Baker and Jayaram (2008) is used for constructing the joint probability model of spectral accelerations at T_1 and T_2, which gives a correlation coefficient of $\rho_{\ln S_a(T_1), \ln S_a(T_2)} = 0.608$.

By performing scalar PSHA using equation (2.2.15) and 2-D vector-valued PSHA using equation (3.2.1), the hazard curves and hazard surface are given in Figures 3.18 and 3.19.

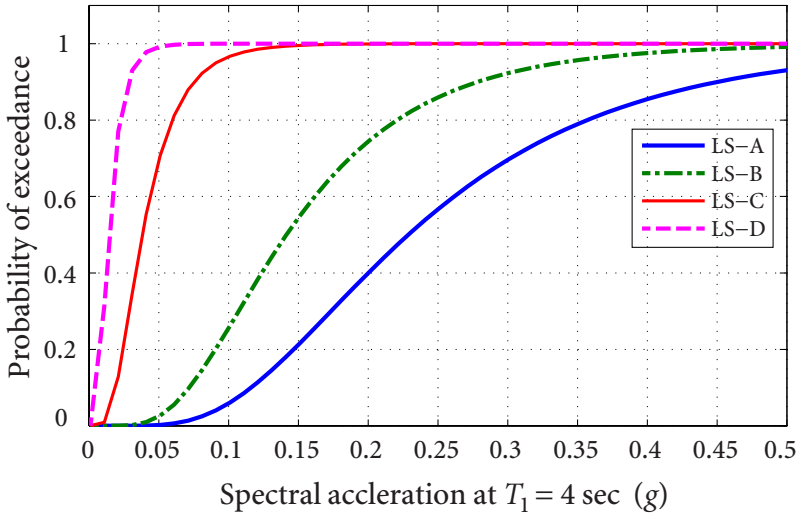

Figure 3.16 Fragility curves for four limit states

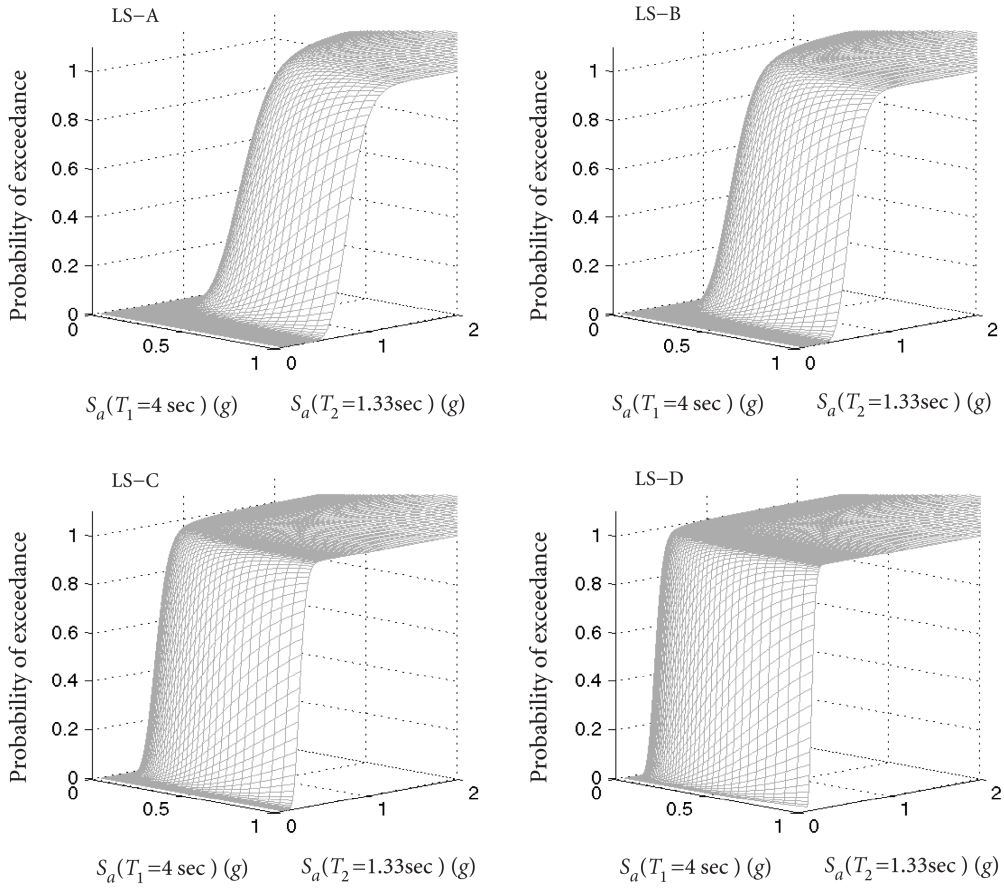

Figure 3.17 Fragility surfaces for four limit states

From the hazard curve for $S_a(T_1)$, the ground motion level s_1 at any reference probability λ_{s_1} can be obtained.

In Figure 3.19 of the cumulative density function for the joint hazard, given spectral acceleration $S_a(T_2)=0.0001g\approx 0g$, hazard for $S_a(T_1)$ is equal to the corresponding hazard curve in Figure 3.18, i.e., $\bar{P}\{S_a(T_1)>s_1 \mid S_a(T_2)=0\}=\bar{P}\{S_a(T_1)>s_1\}$. However, for any non-diminished s_2, the relation $\bar{P}\{S_a(T_1)>s_1 \mid S_a(T_2)=s_2\}<\bar{P}\{S_a(T_1)>s_1\}$ always holds; the joint hazard is smaller.

By performing scalar SRA using equation (2.3.4) and 2-D VSRA using (3.2.6), accurate seismic risk curves are obtained, as shown in Figure 3.20. Note that due to the extensive computational effort, the standard SRA is performed for up to 2-D only. Higher dimensional analyses necessitate access to supercomputers or more tractable numerical schemes, as well as response statistics considering more spectral parameters.

Simplified Seismic Risk Analysis

To perform the simplified approach, the following steps are applied.

(1) (M, R)-binning. Similar to the example application for hazard approximation in Subsection 3.3.3, by dividing M and R into 3 equal segments

$$M_S=[5.0,\ 6.0),\quad M_M=[6.0,\ 7.0),\quad M_L=[7.0,\ 8.0],$$
$$R_S=[0,\ 30),\quad R_M=[30,\ 60),\quad R_L=[60,\ 90],$$

a total of 7 characteristic (M, R)-bins are obtained (note that $M=[5.0,\ 6.0]$ for source 1).

(2) Deaggregation for controlling earthquakes. Perform hazard deaggregation according to equations (3.3.8) towards $S_a(T_1)$ at hazard level s_1 to obtain a set of controlling earthquakes $(m_{C_i}, r_{C_i}, \nu_{C_i})$ $(i=1,2,\cdots,7)$. Based on these earthquakes, approximate hazard curves are developed according to equation (3.3.9) to accurately match the standard hazard curves by adjusting hazard level to $s_1=0.0034\,g$, as shown in Figure 3.21. The set of controlling earthquakes for this hypothetical site are given in Table 3.5.

(3) Perform the simplified SRA using equations (3.3.11) and (3.3.12). The approximate risk curves are shown in Figure 3.22, from which the predicted $\delta_{\max}$ at any risk level can be determined.

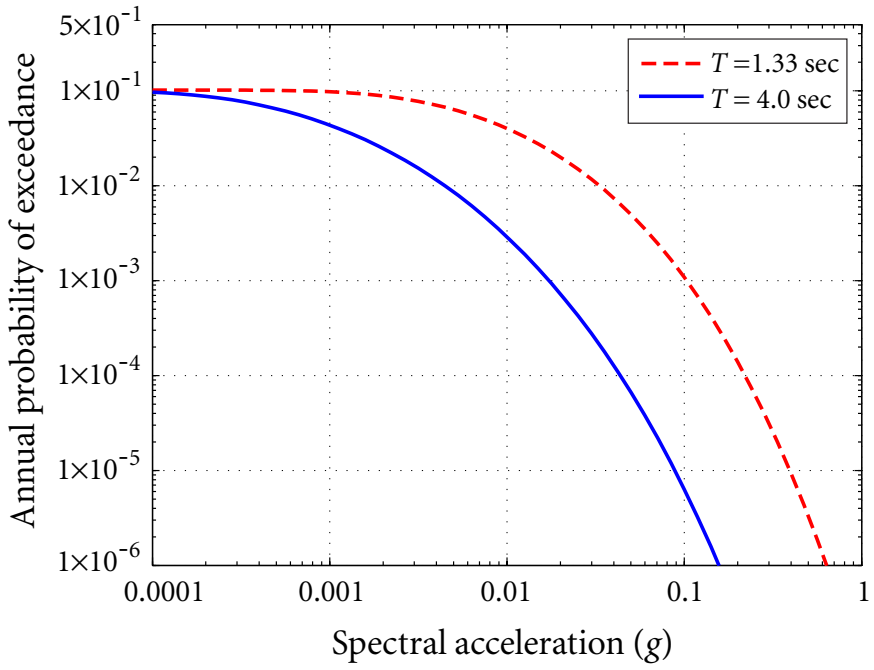

Figure 3.18 Seismic hazard curves for spectral accelerations at 4.0 sec and 1.33 sec

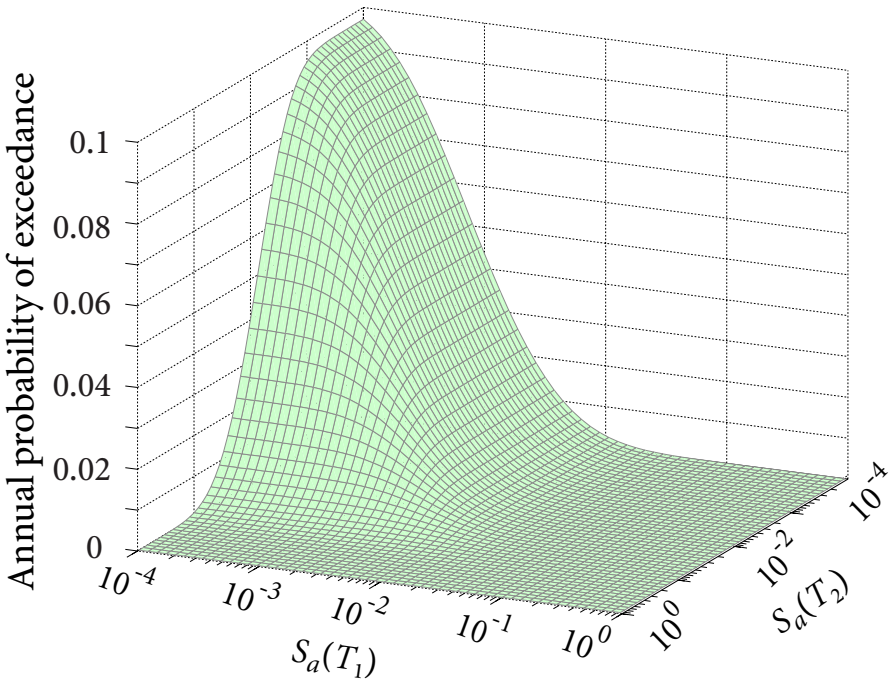

Figure 3.19 Seismic hazard surface for spectral accelerations at 4.0 sec and 1.33 sec

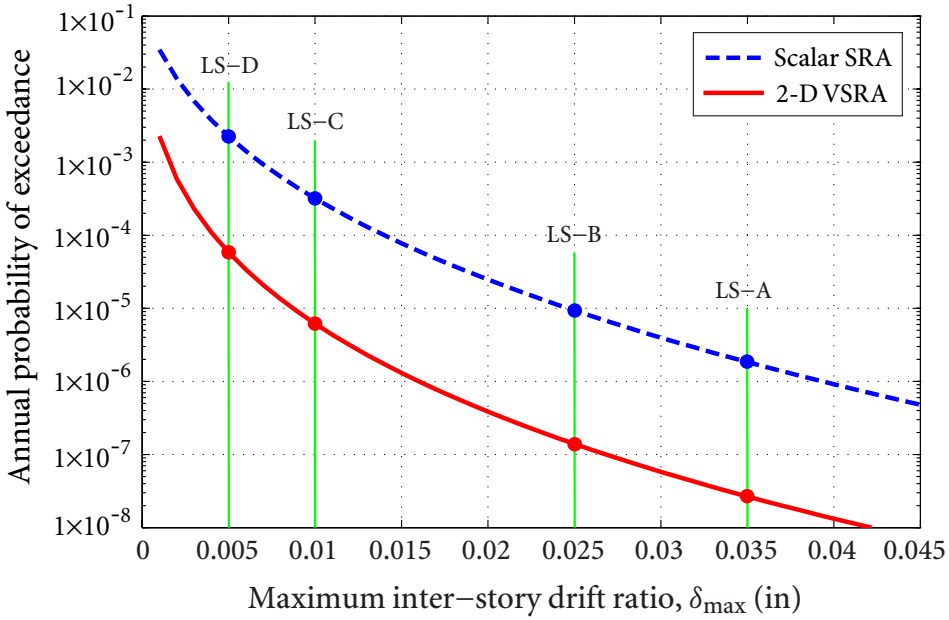

Figure 3.20 Seismic risk curves for the hypothetical site

Table 3.5 The set of controlling earthquakes deaggregated for $S_a(T_1 = 4.0\text{sec})$

$S_a(T_1) = 0.0034\,g$ (50%/50 yr)			
i	m_{C_i}	r_{C_i}	ν_{C_i}
1	5.569	26.111	0.0057
2	5.638	46.651	0.0054
3	5.703	85.031	0.0006
4	6.394	46.681	0.0046
5	6.433	85.125	0.0009
6	7.345	46.696	0.0009
7	7.351	85.184	0.0002

Comparative Analysis

In the proposed procedure for simplified risk analysis, controlling earthquakes are obtained by adjusting s_1, based on which the simplification is established. A suitable s_1 is the most important factor affecting the accuracy of the approach.

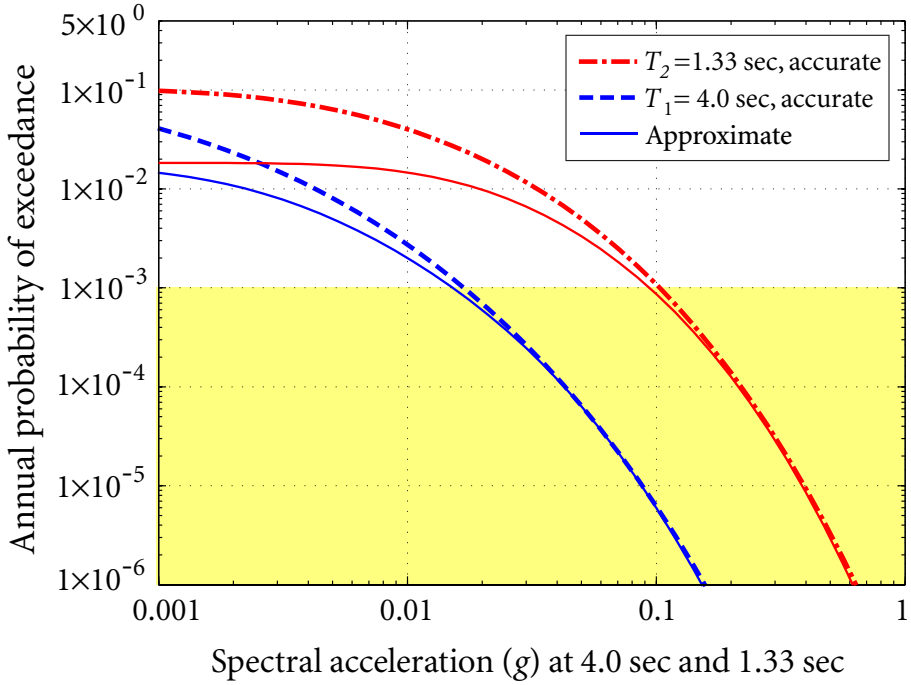

Figure 3.21 Hazard curve approximations for risk analysis at the hypothetical site

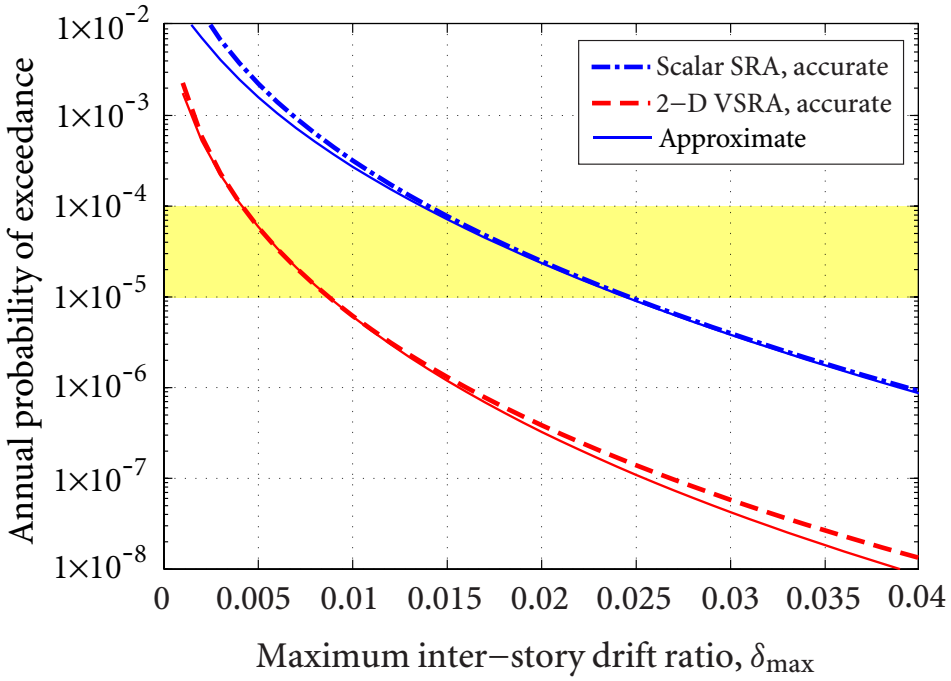

Figure 3.22 Risk curve approximations for 20-storey SMRF at the hypothetical site

1. Accuracy. The relative errors in the predicted $\delta_{\max}$ from applying the simplified approach, governed by equations (3.3.11) and (3.3.12), is evaluated at three risk levels of interest, prescribed by ASCE (2005)

$$\text{Error} = \frac{|\text{Accurate} - \text{Approximate}|}{\text{Accurate}}. \tag{3.4.1}$$

Table 3.6 gives the relative errors, where the largest error is 2.4% for scalar SRA and only 0.4% for 2-D VSRA, showing a high level of accuracy the simplified approach can achieve.

Table 3.6 Computational error

P_F (/year)	Scalar SRA	2-D VSRA
1×10^{-4}	2.4 %	0.0 %
4×10^{-5}	1.4 %	0.4 %
1×10^{-5}	0.8 %	0.0 %

2. **Efficiency**. Similar to the example application for hazard approximation, meshing magnitude with $\Delta m = 0.1$ and earthquake locations by 0.5 km gives a total of $N = 5800$ (m, r)-pairs for the standard analysis. Using a set of $N_C = 7$ controlling earthquakes given in Table 3.5 for the simplified analysis, computational efficiency is $N_C/N = 7/5800 \approx 0.12\%$.

The time costs recorded for standard and simplified risk analyses are compared in Table 3.7. Using the simplified approach, the time costs are reduced to only 0.05%, and 0.065% for scalar and 2-D vector-valued cases, respectively.

Table 3.7 Computational time cost for SRA at a hypothetical site

Computing scheme	Scalar SRA		2-D VSRA	
	Accurate	Approximate	Accurate	Approximate
Time cost	80 sec	0.04 sec	26.9 hour	63 sec

3.4.3 Seismic Risk Analysis at a Realistic Site

The simplified approach is further verified by relocating the 20-storey SMRF building to the site of Diablo Canyon Power Plant (DCPP) in coastal California, as shown in Figure 3.23.

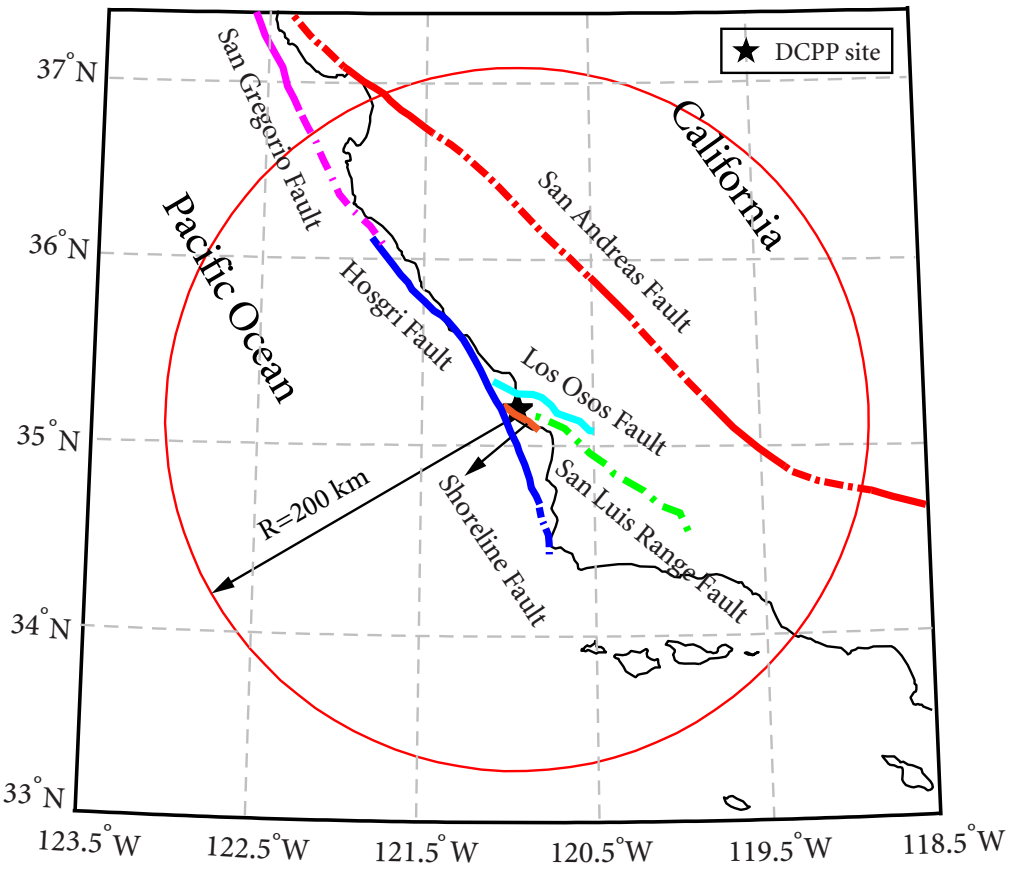

Figure 3.23 Seismic faults surrounding the DCPP site in California

Seismic Source Model

The DCPP site is located at geodetic coordinates [35.212° N, 120.854° W], close to four main faults: Hosgri, Los Osos, San Luis Range, and Shoreline. The closest rupture distances of these faults to the DCPP site are approximately 7.0 km, 8.0 km, 2.5 km, and 0.6 km, respectively. It has been shown that seismic hazard at the DCPP site is dominated by the Hosgri fault (PG&E, 2011). The San Andreas, San Gregorio faults, with closest rupture distances of 77 km and 152 km, respectively, are also considered in this seismic source model. The San Andreas fault is partitioned into a number of segments due to different regional seismicity patterns. Fault segments beyond a radial distance of 200 km from the site are not considered in accordance with the practice in the US national hazard map project (USGS, 2008). All other secondary faults are neglected.

Fault models depend on the fault geometry and slip rate or paleoseismic recurrence rate to establish the locations, sizes, and rates of future earthquakes (USGS, 2008).

The probability distribution of site-source distance $f_R(r)$ can be determined numerically from source configurations. Given the geodetic coordinates of faults and the site, and the assumption of uniform distribution of focal locations along the fault, the site-source distance r and the probability distribution $f_R(r)$ for a fault segment are determined.

The probability distribution $f_M(m)$ for each fault is from the Uniform California Earthquake Rupture Forecast, Version 3 (UCERF3) model (USGS and CGS, 2013), as shown in Figure 3.24. A weighted combination of characteristic and Gutenberg-Richter magnitude-frequency relations are used. This UCERF3 model adopts an approach more derivative than prescriptive, so that the magnitude-frequency relations are no longer assumed. A minimum magnitude $m_{\min} = 5.0$ is consistently used for all faults. In the ranges of $m = [5.0,\ 6.0]$ and somewhere m close to $m_{\max}$, the distribution $f_M(m)$ shows strong characteristic earthquake occurrence. For magnitude range of $m = [6.5,\ m_{\max}]$, the distribution $f_M(m)$ primarily follows the Gutenberg-Richter recurrence law for most faults.

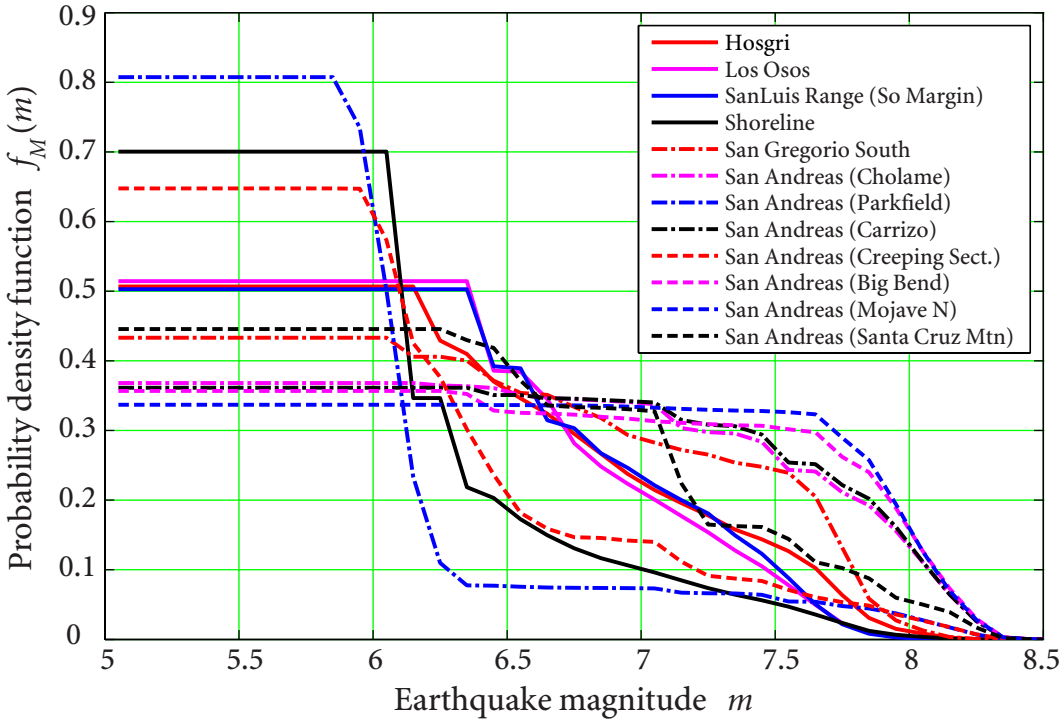

Figure 3.24 Probability density function of earthquake magnitude for 12 fault segments

The mean rate of occurrence $\nu_{m_{\min}}$ for each fault is estimated using the original fault data, e.g., fault seismogenic area A and long-term slip rate $\dot{u}$ (WGCEP, 2003). The general principles used for deriving $\nu_{m_{\min}}$ are given in Appendix A.3 of activity rate.

Table 3.8 summarizes the fault parameters for this seismic source model. Only the fault geometry (including geodetic coordinates, top depth and bottom depth, and average dip) and slip rate are independent parameters. All the rest are dependent, computable parameters. The geometry parameters are obtained from the UCERF3 model (http://pubs.usgs.gov/of/2013/1165/). The fault slip rates are from the USGS database (USGS and CGS, 2006), except that 0.4 for Hosgri Extension fault is from the USGS report (Wills *et al.*, 2008) and that 0.3 for shoreline fault is based on the discussions by Hardebeck (2013). It is noted that the slip rate of 34 mm/yr in most San Andreas fault segments is the maximum slip rate ever found in the U.S. continent. Fault length L can be directly obtained from the geodetic coordinates. The seismogenic area A is obtained using $A = L \times W$, where W is the down-dip width, calculated as (bottom depth−top depth) divided by sine of dip angle. The mean characteristic magnitude $\overline{m}_{\text{char}}$ is obtained by using the empirical magnitude-area scaling relations by Wells and Coppersmith (1994), applicable for all sense types (see Appendix A.3). The mean rate of occurrence ν_{m_0} is computed by invoking conservation of seismic moment, according to the principles given in Appendix A.4. For sense of slip, only the Los Osos and San Luis Range faults are of reverse type, while all the rest are of strike-slip type. All faults are taken as the strike-slip type for simplicity.

Validation of Seismic Hazard Analysis

To perform the PSHA, probability distributions of source-site distance $f_R(r)$ and earthquake magnitude $f_M(m)$, the mean rate of occurrence $\nu_{m_{\min}}$ from the seismic source model are used. The GMPE by Abrahamson and Silva (1997) are adopted to obtain the mean and standard deviation values for the conditional probability distributions of spectral accelerations in equation (2.2.14). Since a relatively high near-surface shear wave velocity ($\sim$1,200 m/s) is estimated at the site (USNRC, 2012a), the generic rock site condition is set in the GMPE.

To validate the self-coded PSHA using software *Matlab*, seismic hazard curves developed using equation (2.2.15) are compared with the public available hazard curves for the Diablo

Table 3.8 Fault parameters used for seismic source models for the DCPP site

No.	Fault (segment) name	Length (km)	Area§ (km^2)	Slip rate (mm/yr)	$\overline{m}_{\text{char}}$ †	$\nu_{m_{\min}}$ ‡	top depth (km)	btm depth (km)	Dip (°)	Endpt N (W)	Endpt S (E)
1	Hosgri	171	1201	2.5	7.4	0.0062	0.0	12.2	80	−121.73; 36.15	−120.75; 34.86
2	Hosgri Extension	29	218	0.4	6.4	0.00021	0.0	7.5	80	−120.75; 34.85	−120.60; 34.69
3	Los Osos	57.9	622	0.5	7.1	0.00095	0.0	12.0	45	−120.99; 35.36	−120.46; 35.12
4	San Luis Range (So margin)	115	893	0.2	7.3	0.00071	0.0	12.0	45	−120.79; 35.18	−119.83; 34.56
5	Shoreline	23	275	0.3	6.5	0.00023	0.0	12.0	90	−120.94; 35.26	−120.74; 35.13
6	San Gregorio (South)	89.9	1080	5.5	7.1	0.0041	0.0	11.6	75	−121.70; 36.15	−122.18; 36.86
7	San Andreas (Cholame)	63	751	34.0	6.9	0.0073	0.0	12	90	−120.30; 35.75	−119.87; 35.31
8	San Andreas (Parkfield)	36.5	372	34.0	6.6	0.015	0.0	10.2	90	−120.56; 36.00	−120.30; 35.75
9	San Andreas (Carrizo)	59	892	34.0	7.0	0.0085	0.0	15.1	90	−119.87; 35.31	−119.40; 34.94
10	San Andreas (Creeping sect)	121	1456	34.0	7.2	0.0520	0.0	12	90	−121.48; 36.80	−120.56; 36.00
11	San Andreas (Big bend)	50	752	34.0	6.9	0.0063	0.0	15.1	90	−119.40; 34.94	−118.89; 34.81
12	San Andreas (Mojave N)	37	557	34.0	6.8	0.0045	0.0	15.1	90	−118.89; 34.81	−118.51; 34.70
13	San Andreas (Santa Cruz mtn)	62.5	955	17.0	7.0	0.0088	0.0	15.0	90	−122.00; 37.18	−121.48; 36.80

§ = Length times Down-dip Width (bottom depth minus top depth divided by sine of dip angle)

† predicted using Wells and Coppersmith (1994) empirical scaling relations given in Appendix A.2

‡ = $\mu\, A\, \dot{u}/\overline{M}_0$, where mean seismic moment $\overline{M}_0 = \int_{m_{\min}}^{m_{\max}} M_0(m)\, f(m) \mathrm{d}m$ (see Appendix A.3 for details)

Canyon site. Figures 3.25-3.28 give the hazard curves developed for PGA and spectral accelerations at 0.2 sec, 1.0 sec, and 4.0 sec, respectively, in comparison with those available from the following sources.

(1) The U.S. Geological Survey (USGS) website provides a convenient hazard curve application tool (http://geohazards.usgs.gov/hazardtool/application.php). Hazard curves for a site can be obtained by inputting the geodetic coordinates, specifying the period of interest and site class (Site class B is specified, corresponding to $V_{30} = 1150$ m/s).

(2) The U.S. NRC's review report (USNRC, 2012a) of the Shoreline Fault report, submitted by the Pacific Gas and Electric Company, provides hazard curves for PGA and spectral accelerations at 0.2 sec and 1.0 sec.

(3) The most recent UCERF3 model for California earthquake forecast (USGS and CGS, 2013) provides supplementary Figures showing hazard curves for the Diablo Canyon site.

Note that those publicly available hazard curves are typically obtained using logic tree analysis to account for the epistemic uncertainty. For example, the UCERF3 model employs 1,440 alternative logic tree branches for this purpose. In contrast, in this study most parameters are taken as mean values and a single set of GMPE model is adopted. In addition, only the important fault sources surrounding the DCPP site are considered.

Looking through Figures 3.25-3.28, it is seen that the calculated hazard curves are not significantly different than other public available curves and that similar trend among hazard curves in each Figure is observed. Since the development of hazard curves is not the focus of this study, the calculated hazard curves are deemed acceptable.

Standard Seismic Risk Analysis

By performing scalar PSHA for this site using equation (2.2.15) for spectral accelerations at $T_1 = 4.0$ sec and $T_2 = 1.33$ sec, seismic hazard curves are developed as shown in Figure 3.29. A correlation coefficient $\rho_{\ln S_a(T_1),\ln S_a(T_2)} = 0.608$ from Baker and Jayaram's model Baker and Jayaram (2008) is obtained.

For the 20-storey SMRF structure, performing the standard SRA using equations (2.2.3) and (3.2.5) yields the accurate risk curves for the scalar and 2-D vector-valued cases as

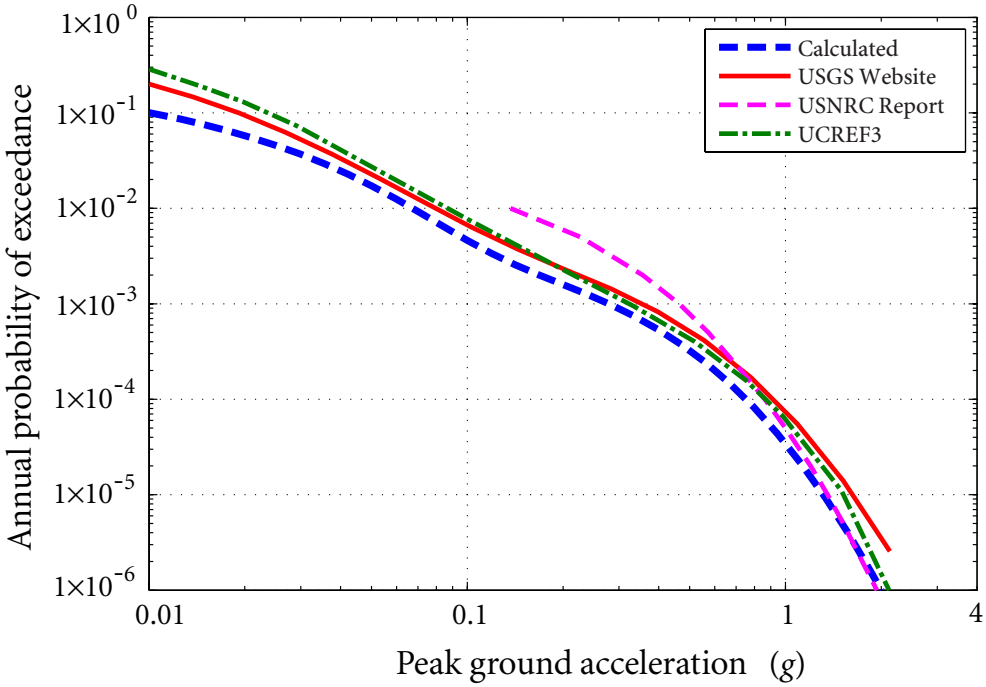

Figure 3.25 Hazard curve for PGA at the DCPP site

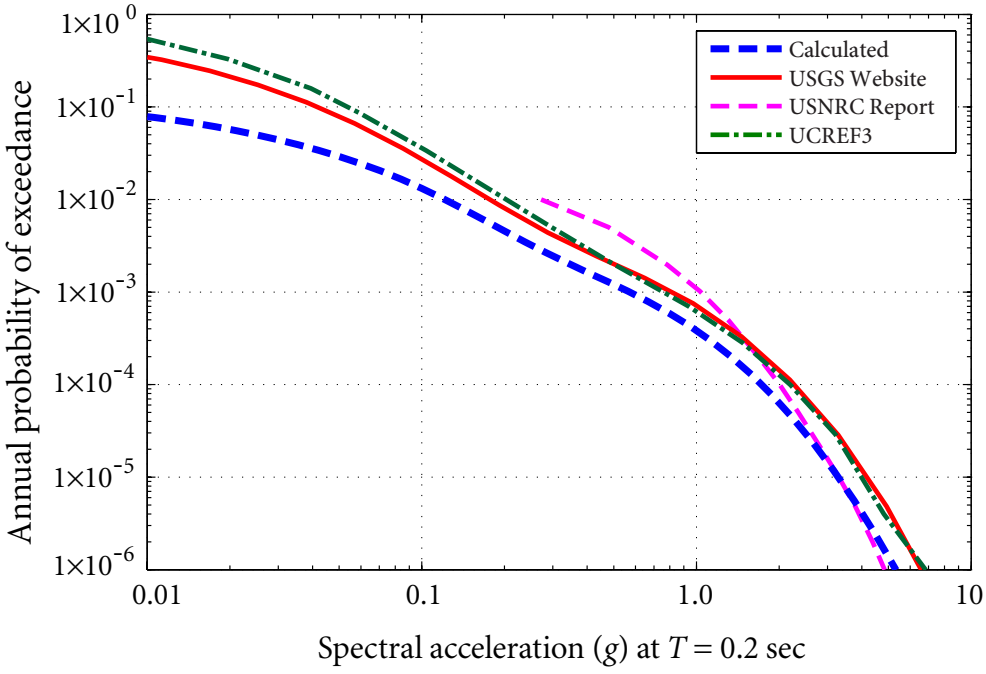

Figure 3.26 Hazard curve for SA at 0.2 sec at the DCPP site

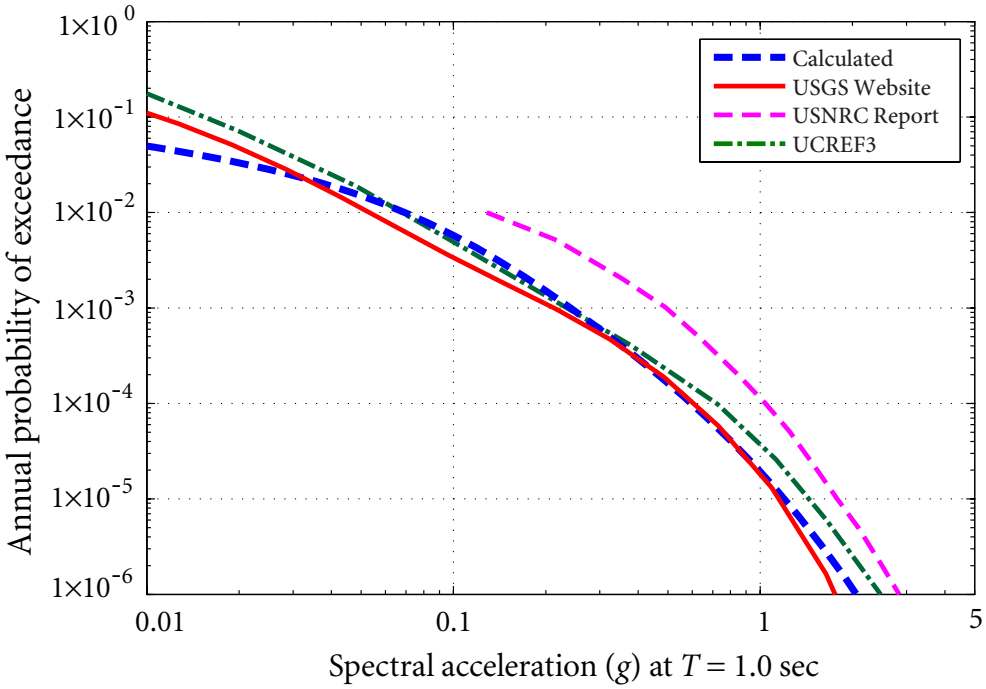

Figure 3.27 Hazard curve for SA at 1.0 sec at the DCPP site

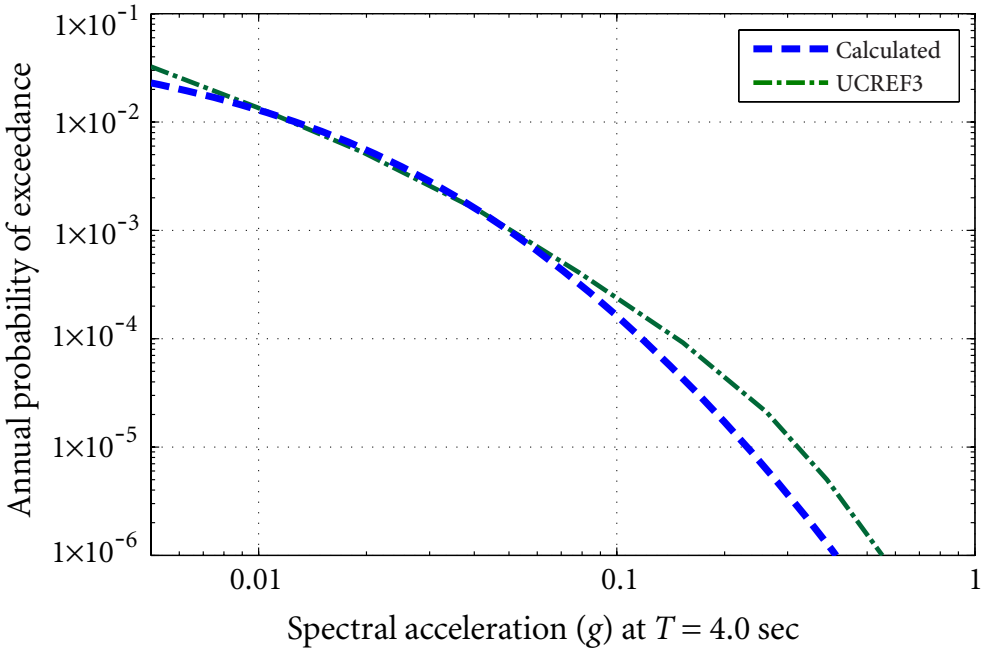

Figure 3.28 Hazard curve for SA at 4.0 sec at the DCPP site

shown in Figure 3.30. It shows that the risk value obtained from the 2-D analysis is approximately only 8% ∼ 10% of that from the scalar analysis.

Simplified Seismic Risk Analysis

(1) (M, R)-binning. Due to the complexity of the DCPP seismic source model, contributions to hazard ($\lambda_s = 10^{-3}$/yr and 10^{-6}/year) from different (m, r)-pairs are displayed in Figure 3.31. At $\lambda_s = 10^{-6}$/year level, seismic hazard is dominated mainly by near-field events, especially those with r less than 10 km; contribution from far-field earthquakes diminishes, especially those with r greater than 110 km. Based on these observations, the following characteristic (M, R)-bins are taken:

$$M_S = [5.0,\ 6.0), \qquad M_M = [6.0,\ 7.0), \qquad M_L = [7.0,\ 8.5],$$
$$R_S = [0,\ 10)\ \text{km}, \qquad R_M = [10,\ 35)\ \text{km}, \qquad R_L = [35,\ 110]\ \text{km},$$

which gives a total of $N_C = 3 \times 3 = 9$ characteristic $(M, R)_i$-bins ($i = 1, 2, \cdots, 9$).

(2) Deaggregation for controlling earthquakes. Using equations (3.3.8), a set of controlling earthquakes $(m_{C_i}, r_{C_i}, \nu_{C_i})$ ($i = 1, 2, \cdots, 9$) are deaggregated towards $S_a(T_1)$ at hazard level s_1 from standard hazard curve. Approximate hazard curves are developed according to equation (3.3.9) to accurately match the standard hazard curves by adjusting $s_1 = 0.040\,g$.

To illustrate the process, let's first perform deaggregation towards s_1 at probability levels $\lambda_s = 2\%/50$ yr, $10\%/50$ yr, and $50\%/50$ yr (corresponding to $s_1 = 0.0724$, 0.0351, 0.0093 g, respectively). Hazard curve approximations for $S_a(T_1)$ and $S_a(T_2)$, based on the corresponding deaggregated earthquakes, are shown in Figures 3.32 and 3.33, respectively. $s_1 = 0.035g$ associated with $\lambda_s = 10\%/50$ yr provides satisfactory hazard approximations. By performing simplified SRA using equations (3.3.11) and (3.3.12), approximate risk curves are shown in Figure 3.34.

Note that both hazard and risk approximations are not optimal; they are on the lower side of accurate curves in the range of interest. By trial, the best approximations are achieved by performing deaggregation towards $s_1 = 0.040\,g$. Table 3.8 gives the controlling earthquakes, and Figures 3.35 and 3.36 shows the hazard curve and risk curve approximations, respectively.

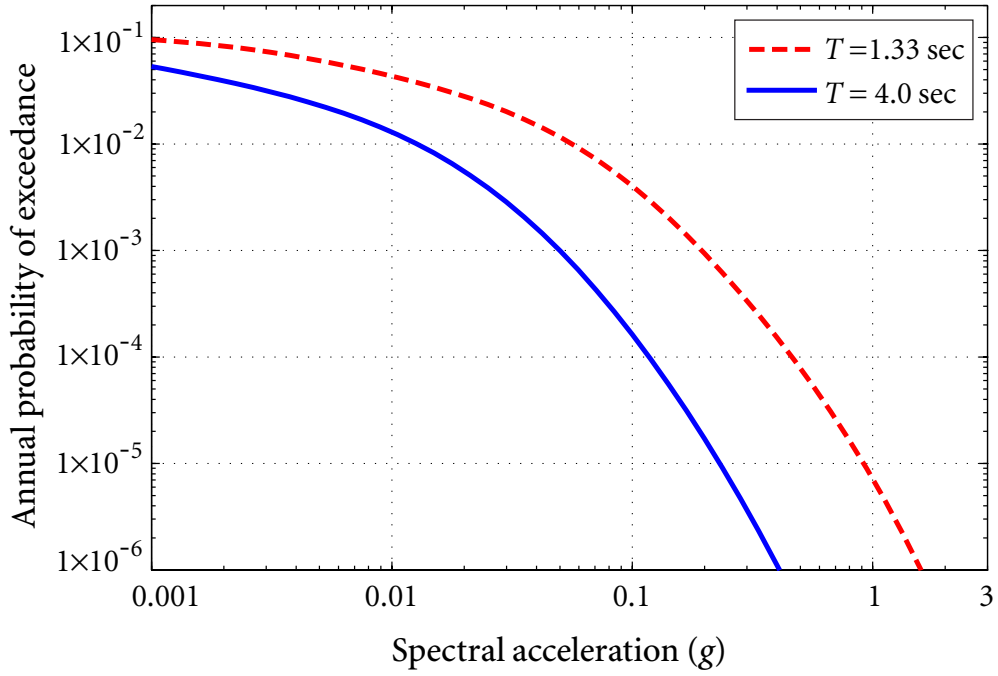

Figure 3.29 Seismic hazard curves for SA at 4.0 and 1.33 sec at the DCPP site

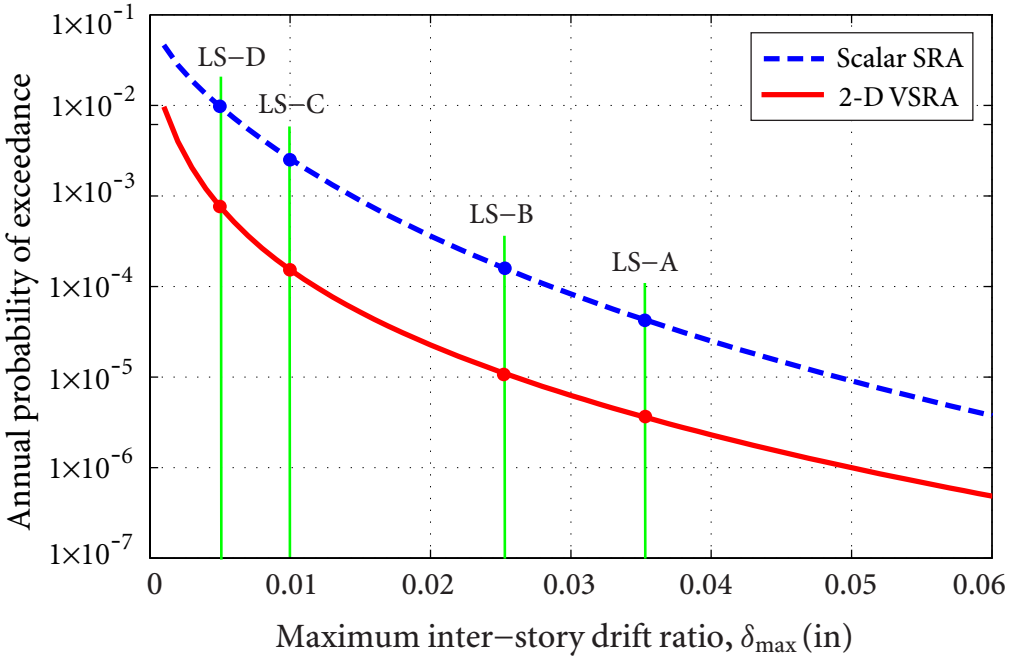

Figure 3.30 Seismic risk curves for the 20-storey SMRF at the DCPP site

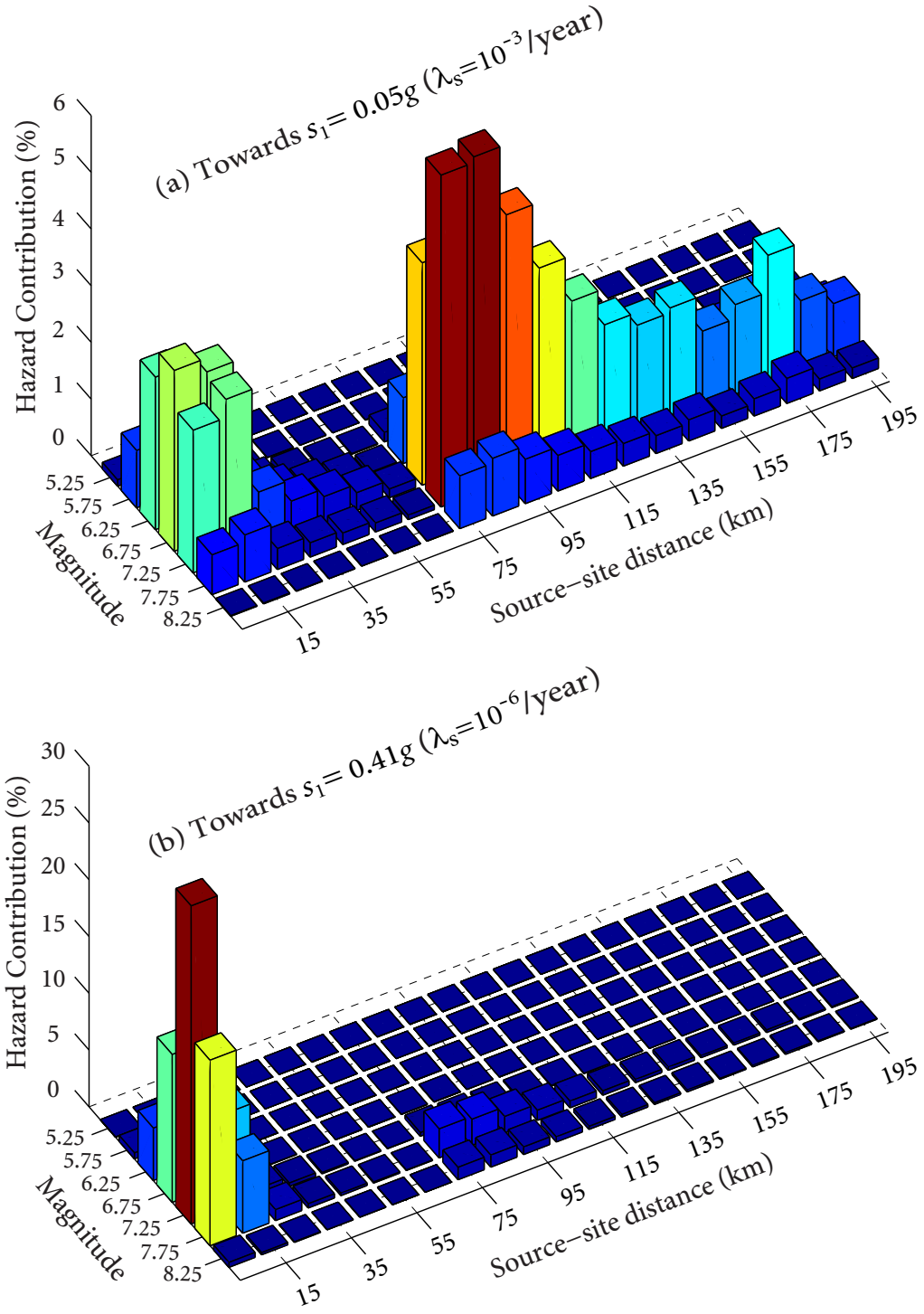

Figure 3.31 Contributions to hazard for $S_a(T_1 = 4\,\text{sec})$ at two probability levels

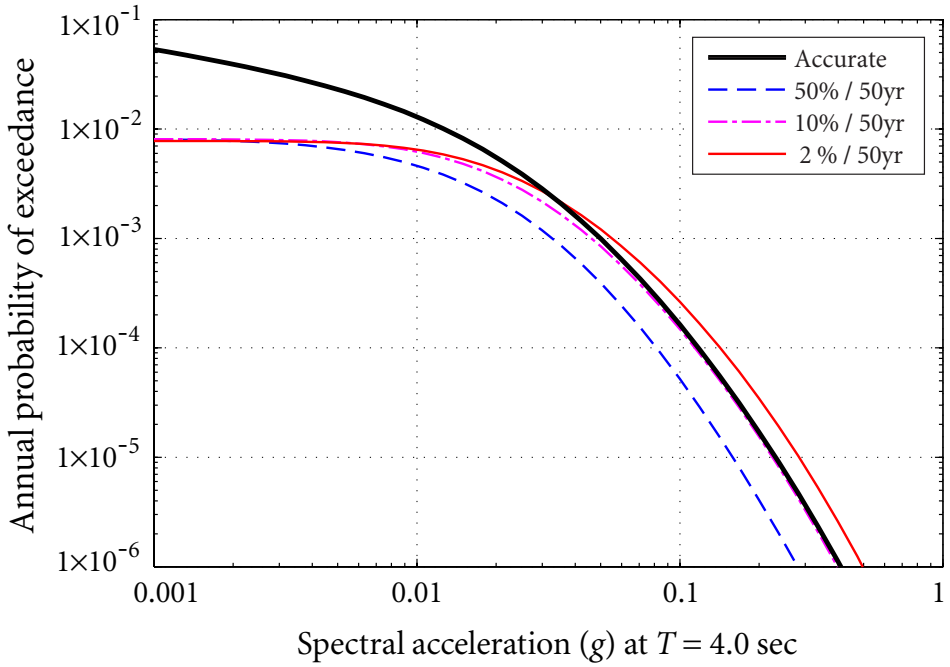

Figure 3.32 Hazard curve approximations for $S_a(T_1)$ achieved by deaggregation towards s_1 at 3 probabilities

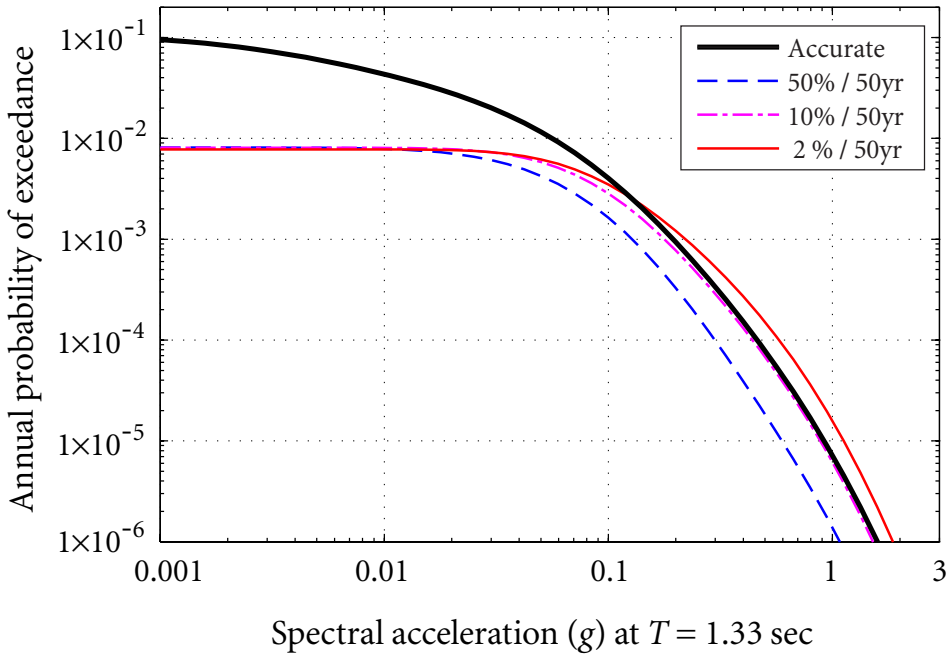

Figure 3.33 Secondary hazard curve approximations for $S_a(T_2)$ achieved by deaggregation towards s_1 at 3 probabilities

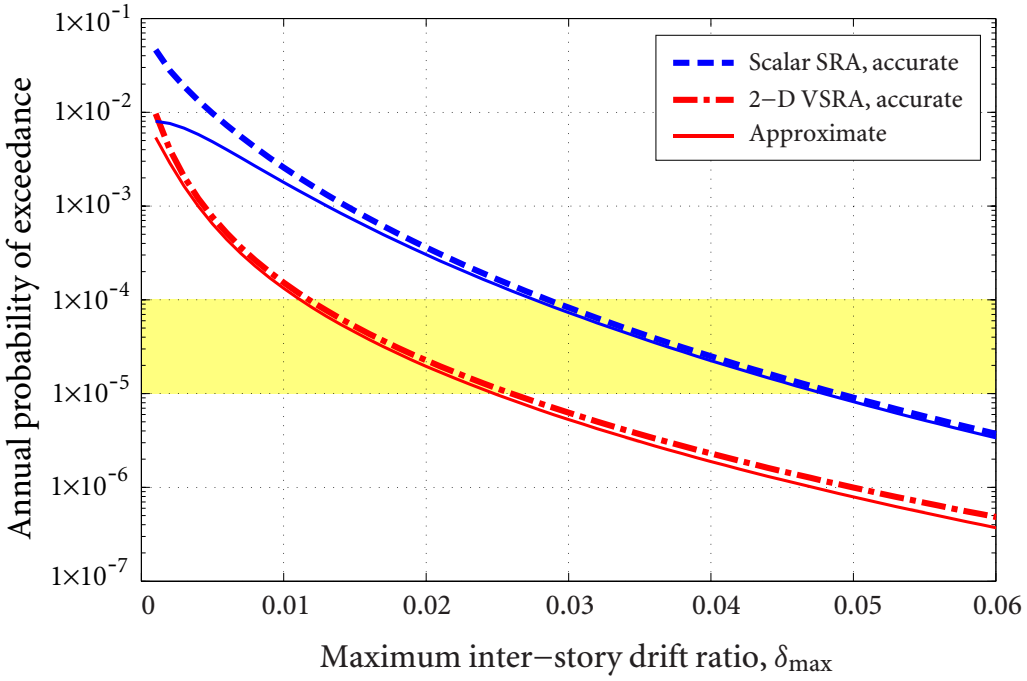

Figure 3.34 Hazard curve approximations achieved by deaggregation towards $\lambda_s = 10\%/50\text{yr}$

Comparative Analysis

Based on the best achievable risk curve approximations shown Figure 3.36, the accuracy and efficiency are discussed as follows.

1. Accuracy. Table 3.10 gives the relative errors in the predicted $\delta_{\max}$ evaluated using equation (3.4.1) at risk levels of interest. The maximum error is only 0.9%; the simplified approach provides excellent approximate results.

2. **Efficiency**. For all 13 fault segments, earthquake locations are meshed with approximately 3.0 km length and magnitude is meshed with 0.1 unit, giving a total number of $N = 8098$ (m, r)-pairs for standard analysis. In the simplified approach, a set of $N_S = 9$ controlling earthquakes are adopted. The time cost is expected to reduce to $9/8098 \approx 0.11\%$. Based on actual records given in Table 3.11, using the simplified approach, the time costs required are reduced to 0.07% and 0.09% for scalar and the 2-D vector-valued cases, respectively.

Comparing Tables 3.7 and 3.11, one notices that the time cost required in standard risk analysis for the DCPP site having $N = 8089$ (m, r)-pairs is even less than that for the

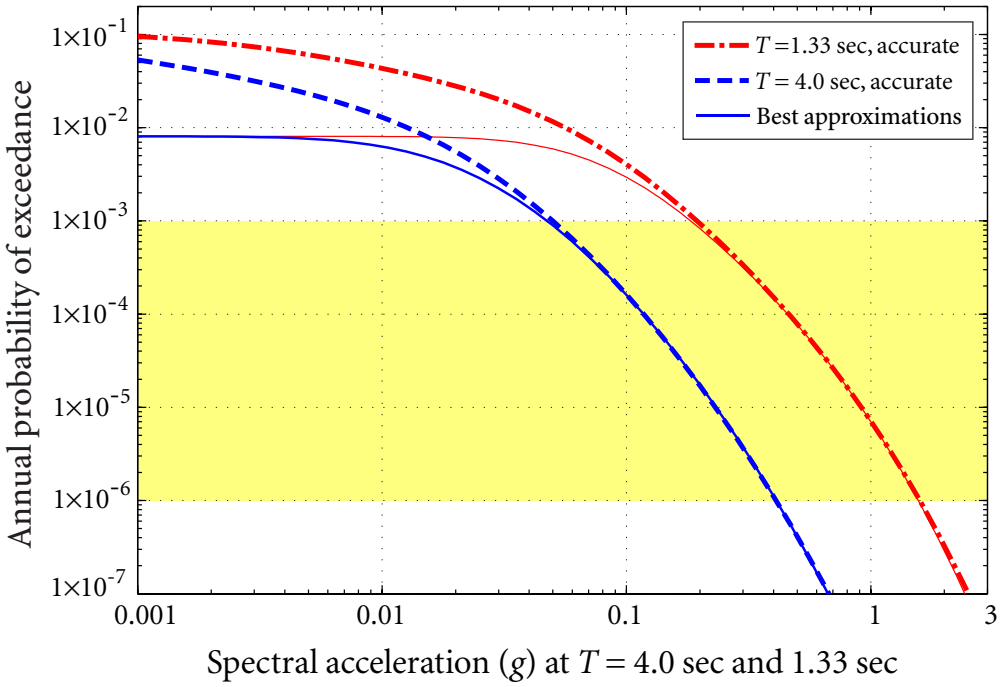

Figure 3.35 Best hazard curve approximations for both $S_a(T_1)$ and $S_a(T_2)$

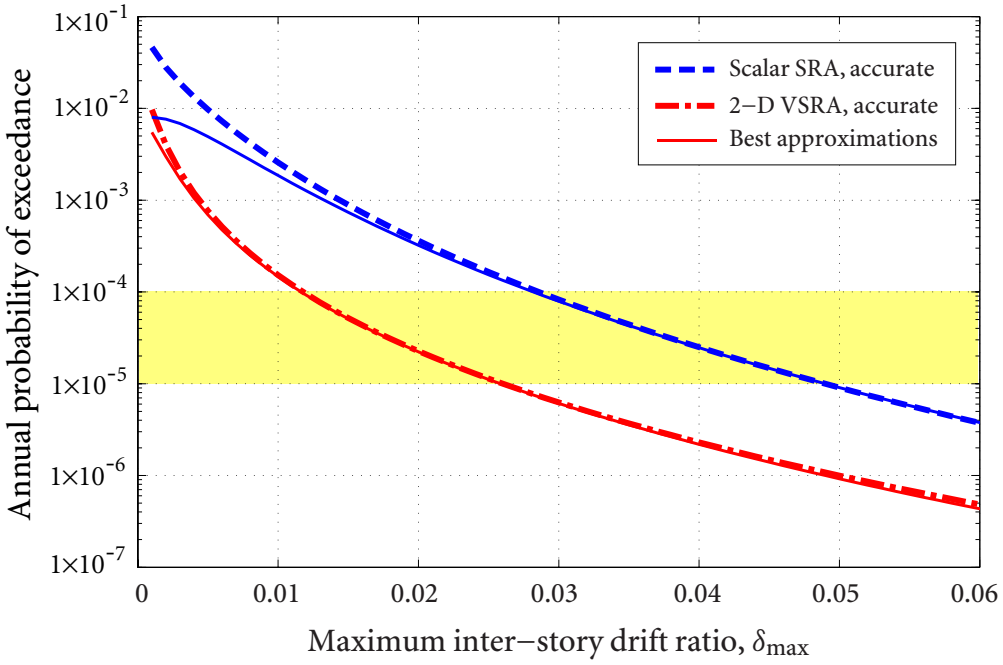

Figure 3.36 Best risk curve approximations for the 20-storey SMRF at DCPP site

Table 3.9 Controlling earthquakes for $S_a(T_1 = 4.0\text{sec})$ at DCPP site

$S_a(T_1) = 0.040\,g$			
i	m_{C_i}	r_{C_i}	ν_{C_i}
1	5.794	4.272	0.0000191
2	5.841	14.053	0.0000076
3	5.890	77.641	0.0000021
4	6.556	6.054	0.0002490
5	6.633	16.616	0.0002500
6	6.763	82.346	0.0004941
7	7.369	6.378	0.0002068
8	7.399	18.800	0.0003693
9	7.694	86.921	0.0064669

Table 3.10 Computational error

P_F (/year)	Scalar SRA	2-D VSRA
1×10^{-4}	0.9 %	0.2 %
4×10^{-5}	0.1 %	0.4 %
1×10^{-5}	0.6 %	0.4 %

Table 3.11 Computational time cost for SRA at the DCPP site

Computing scheme	Scalar SRA		2-D VSRA	
	Accurate	Approximate	Accurate	Approximate
Time cost	73 sec	0.05 sec	25.3 hour	80 sec

hypothetical site having $N = 5800$ (m, r)-pairs. This is due to the different integration schemes adopted. For the hypothetical site, the probability density function of site-source distance $f_R(r)$ is obtained analytically using equation (2.2.1) in a r-loop, whereas for the DCPP site, $f_R(r)$ is obtained numerically using a vectorized computing scheme without an explicit r-loop. Nevertheless, the integration scheme adopted within each example is consistent, without affecting the efficiency (time cost) evaluating.

Discussions

In the above, the best risk curve approximations, using the simplified analysis, are achieved under the following accompanying conditions:

(1) the maximum source-site distance $r_{\max}$ is taken 110 km,

(2) the entire m and r domain is partitioned into 9 (M, R)-bins, using

$$M_S = [5.0\text{–}6.0), \qquad M_M = [6.0\text{–}7.0), \qquad M_L = [7.0\text{–}8.5],$$
$$R_S = [0\text{–}10)\,\text{km}, \qquad R_M = [10\text{–}35)\,\text{km}, \qquad R_L = [35\text{–}110]\,\text{km},$$

(3) hazard level $s_1 = 0.040\,g$ is adjusted for deaggregation, so that hazard curves can be accurately approximated.

Condition (3) is most critical when applying the simplified approach, which has been well-illustrated throughout the examples. Next, to better understand how these conditions, i.e., deaggregation schemes, affect the accuracy of risk approximations, the following three factors regarding conditions (1) and (2) are considered:

1) change of $r_{\max} = 110$ km in condition (2),

2) change of partitioning schemes while maintaining a total of 9 (M, R)-bins,

3) change of the total number of (M, R)-bins based on condition (2).

Table 3.12 lists various deaggregation schemes that fall into three categories corresponding to the three factors to be considered, i.e., $r_{\max}$, (M, R) binning, and the total number of bins N_C. In each scheme, only a single changing factor is investigated as highlighted in the table. The hazard level s_1 is invariably adjusted to achieve the best risk approximations in each scheme, except that in schemes 1b and 3c, suboptimal s_1 are used for other comparison purposes. The base scheme 1a, 2a, and 3a preserves the three conditions that achieve the best rick approximations, as listed at the beginning of discussion. Table 3.12 also summarizes the results obtained by using each scheme, i.e., referring Figure showing risk curve approximation, maximum error for both scalar and 2-D vector-valued SRA, the descriptive accuracy, and the efficiency.

Table 3.12 Comparison of risk approximation results from various deaggregation schemes

Deaggregation scheme					Comparison of results				
No.	r_{max} (km)	(M, R) binning	N_C	Hazard level s_1 (or λ_s)	Figure	Maximum error† (%)		Accuracy§	Efficiency $(\frac{N_C}{N})$
						Scalar case	2-D case		
Base scheme 1a, 2a, 3a	110	$M=[5.0–6.0),\ [6.0–7.0),\ [7.0–8.5]$, $R=[0–10),\ [10–35),\ [35–r_{max}]$ km	3×3	0.040 g	Fig. 3.36	0.9%	0.4%	**Best 1**	0.11 %
1b	110	$M=[5.0–6.0),\ [6.0–7.0),\ [7.0–8.5]$, $R=[0–10),\ [10–35),\ [35–r_{max}]$ km	3×3	0.035 g (10%/50yr)	Fig. 3.34	3.3%	5.2%	Good	0.11 %
1c	200	$M=[5.0–6.0),\ [6.0–7.0),\ [7.0–8.5]$, $R=[0–10),\ [10–35),\ [35–r_{max}]$ km	3×3	0.035 g	Fig. 3.38	2.5%	4.8%	Good	0.11 %
1d	70	$M=[5.0–6.0),\ [6.0–7.0),\ [7.0–8.5]$, $R=[0–10),\ [10–35),\ [35–r_{max}]$ km	3×3	0.055 g	Fig. 3.40	13.6%	12.5%	Bad	0.11 %
2b	110	Trisection of M range, $R=[0–10),\ [10–35),\ [35–r_{max}]$ km	3×3	0.040 g	Fig. 3.42	1.8%	1.4%	**Best 2**	0.11 %
2c	110	$M=[5.0–6.0),\ [6.0–7.0),\ [7.0–8.5]$, Trisection of R range	3×3	0.055 g	Fig. 3.44	2.6%	4.4%	O.K.	0.11 %
2d	110	Trisection of M range, Trisection of R range	3×3	0.055 g	Fig. 3.46	3.7%	4.2%	O.K.	0.11 %
3b	110	$M=[5.0–5.5),\ [5.5–6.0),\ [6.0–6.5)$, $[6.5–7.0),\ [7.0–7.7),\ [7.7–8.5]$, $R=[0–5),\ [5–10),\ [10–22)$, $[22–35),\ [35–72),\ [72–r_{max}]$ km	6×6	0.035 g (10%/50yr)	Fig. 3.48	1.1%	2.0%	**Best 3**	0.44 %
3c			6×6	0.040 g	Fig. 3.50	3.5%	4.0%	Good	0.44 %
3d	110	$M=[5.0–6.5),\ [6.5–8.5]$, $R=[0–15),\ [15–r_{max}]$ km	2×2	0.049 g (5%/50yr)	Fig. 3.52	0.3%	1.7%	Good	0.05 %
3e	110	$M=[5.0–8.5], R=[0–r_{max}]$ km	1×1	0.15 g	Fig. 3.54	1.7%	18.0%	Bad	0.012 %
			1×1	0.20 g		6.9%	8.7%	Bad	0.012 %

† maximum error is obtained among 3 risk levels of $P_F = 1\times10^{-4}$/yr, 4×10^{-5}/yr, and 1×10^{-5}/yr.

§ Accuracy criteria includes both quantitative maximum error and prescriptive general curve trend shown in the referring Figure.

1) Scheme category 1 regarding r_{max} selection

The effect of r_{max} on the risk approximation is characterized. Three different r_{max} values, i.e., 110 km, 200 km, and 70 km, are chosen through schemes 1a to 1d. Scheme 1b characterizes the effect of using suboptimal hazard level s_1, compared to scheme 1a. The following observations can be made:

- The use of $r_{max} = 110$ km (scheme 1a) is important for achieving the best results. This can be selected based on the standard deaggregation plots performed for probability levels within the range of interest.
- Even $r_{max} = 110$ km is used, a suboptimal s_1 selection will not lead to best results (scheme 1b). Using different s_1 will shift the curves away from the best approximation.
- The use of $r_{max} = 200$ km (scheme 1c) can be a natural choice, which can still lead to good results, but it will not give the best results for this DCPP site example, since the curve slopes are slightly modified.
- The use of $r_{max} = 70$ km (scheme 1d) is not valid, since it totally neglects the contribution to hazard from far-field earthquakes, which undesirably modifies the curve slopes substantially.

2) Scheme category 2 regarding (M, R) binning

The effect of (M, R) binning on the risk approximations is characterized. The simplest uniform partitions (i.e., trisections) of M and R are considered against the binning adopted in base scheme 2a. This shows the sensitivity of the approximation with respect to variables of M and R. The following observations are made:

- Trisection of M from 5.0-8.5 (scheme 2b) only slightly affect the best achievable approximation results. The maximum error $< 2\%$ and good curve trend shown in Figure 3.42 indicate that the simplified method is not sensitive to the M binning.
- Trisection of R from 0-110 km (scheme 2c) significantly affects the slope trend of curve approximations. As a result, the maximum error increases and approximations are bad at lower probabilities. Hence, the simplified method is sensitive to the R binning.

- Simultaneous trisections of M and R (scheme 2d) show a little worse results than scheme 2c. The results are still acceptable in the range of interest, beyond which the approximations look poor.

3) Scheme category 3 regarding the number of (M,R)-bins N_C

The effect of the number of (M,R)-bins N_C on risk approximations is investigated. A number of finer and coarser bins compared to $N_C = 9$ bins of base scheme 3a are investigated. Comparisons show that

- Increasing N_C by doubling both M bins and R bins (schemes 3b and 3c) hardly improve the approximations. In scheme 3b, by slightly adjusting s_1, very good risk approximations can be achieved; the maximum error is only 2% and curves maintain good trends. Note that keeping s_1 unchanged increases the maximum error from 0.9% in scheme 3a to 4.0% in scheme 3c; s_1 should be adjusted for each new trial.
- Bisections of both M and R (scheme 3d) also provide very good risk approximations. Since M is not a sensitive factor, the R binning becomes critical. With good R binning, good approximations can be achieved even if $N_C = 4$ only.
- Single M and R bin (scheme 3e) cannot provide good risk approximations, especially for the 2-D SRA case. Seen from Figure 3.54, curve slope trend is bad and the maximum error goes large. Hence, $N_C = 1$ is not recommended for simplified risk analysis.
- In overall, for this particular site, $N_C = 3 \times 3$ can generally provide good approximations. Finer binning hardly improves the approximations, but compromises the efficiency. Coarser $N_C = 2 \times 2$ may be acceptable. However, $N_C = 1 \times 1$ is generally not recommended.

3.5 Conclusions

In this chapter, a simplified approach to Vector-valued Seismic Risk Analysis (VSRA) is developed to achieve computational efficiency without compromising the accuracy.

- Vector-valued Probabilistic Seismic Hazard Analysis (VPSHA), along with the seismic fragility model considering multiple ground-motion parameters, are applied to establish

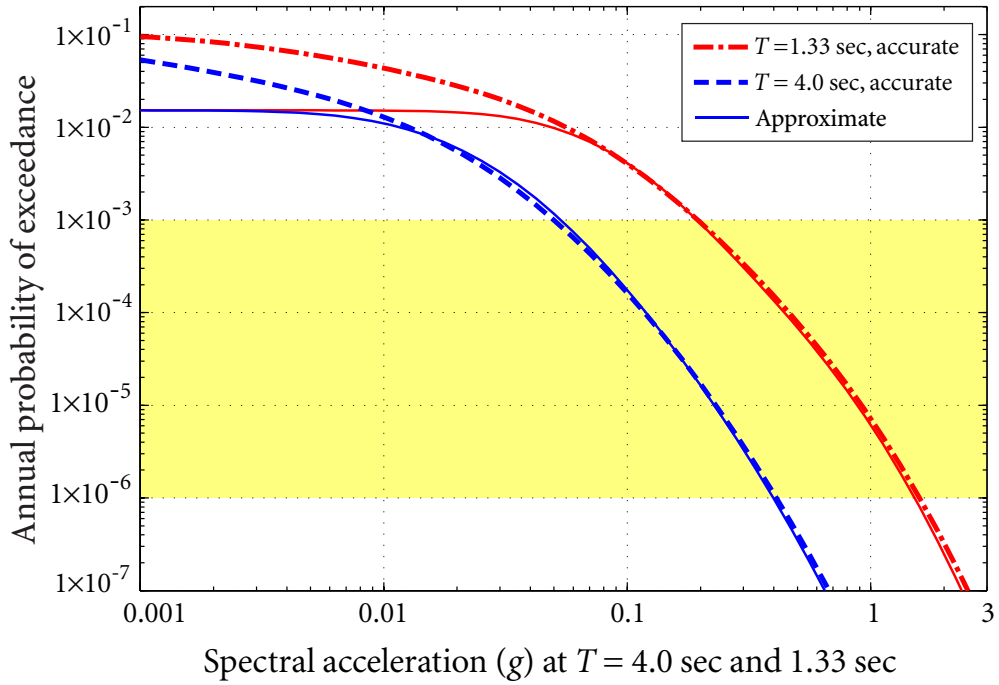

Figure 3.37 Hazard curve approximations using scheme 1c, $r_{max} = 200$ km

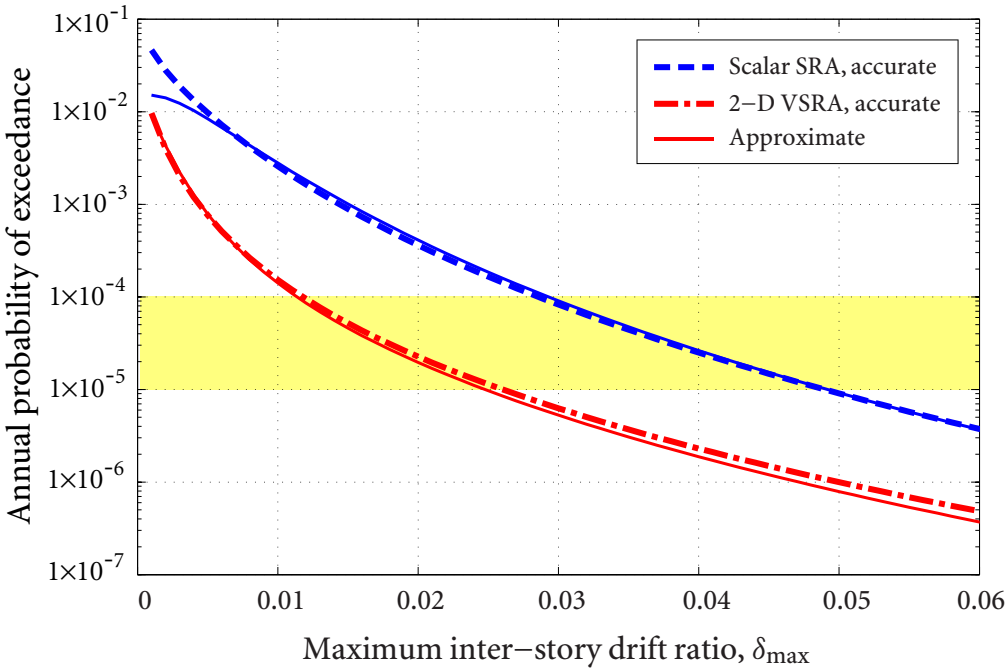

Figure 3.38 Risk curve approximations using scheme 1c, $r_{max} = 200$ km

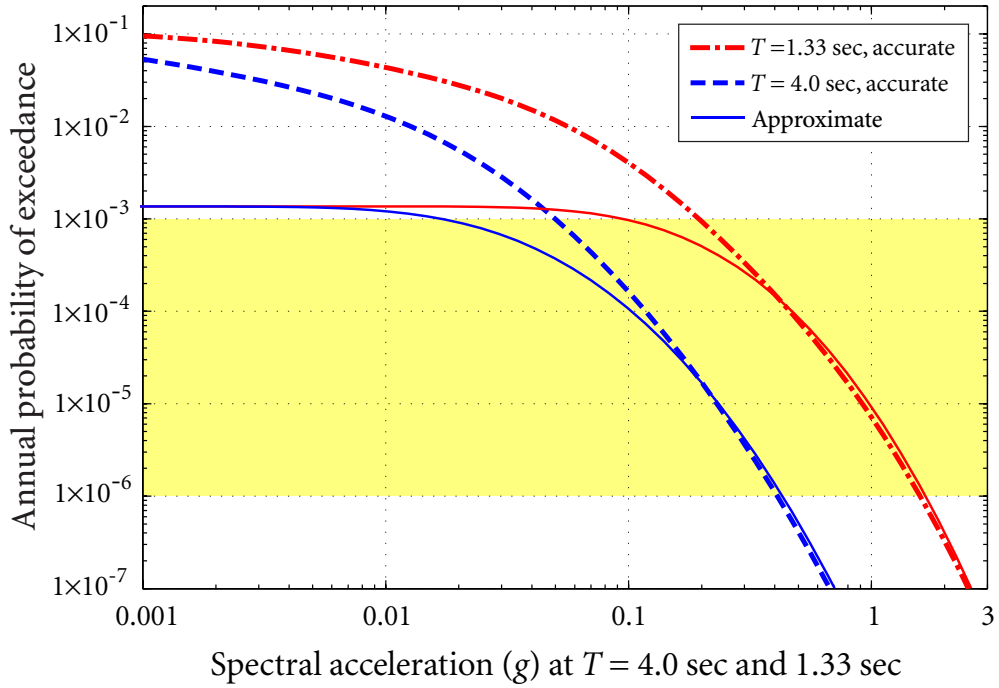

Figure 3.39 Hazard curve approximations using scheme 1d, $r_{max} = 70$ km

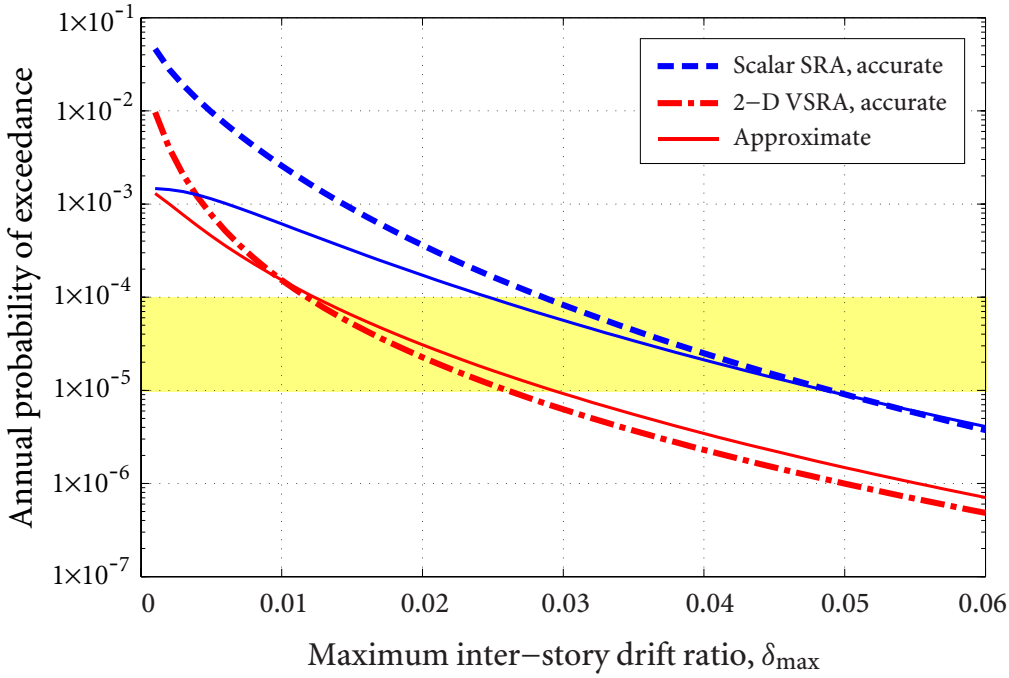

Figure 3.40 Risk curve approximations using scheme 1d, $r_{max} = 70$ km

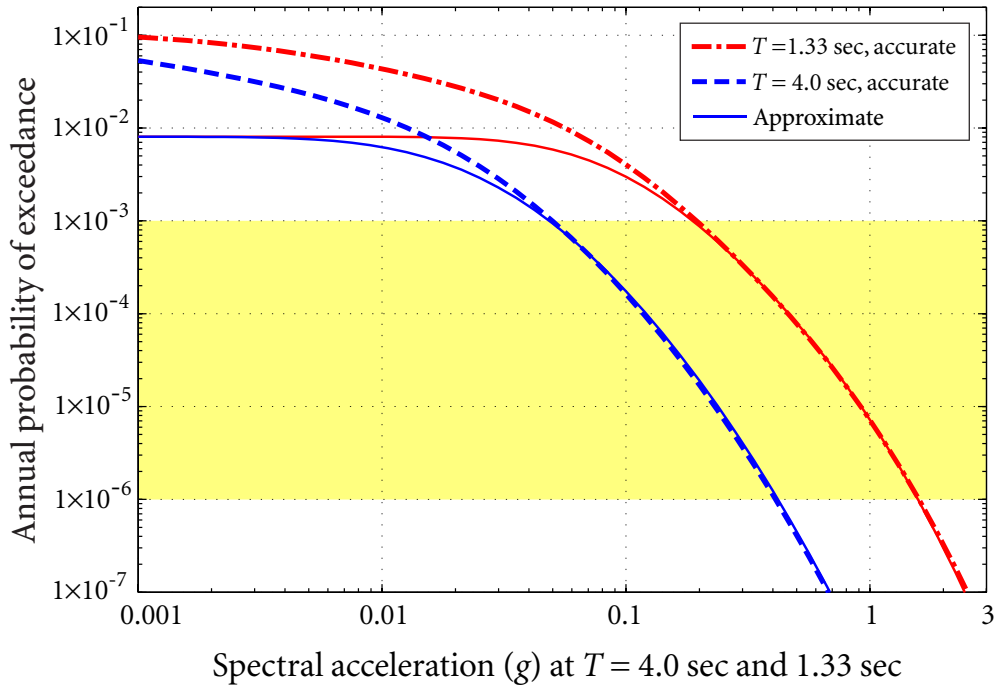

Figure 3.41 Hazard curve approximations using scheme 2b, trisection of M

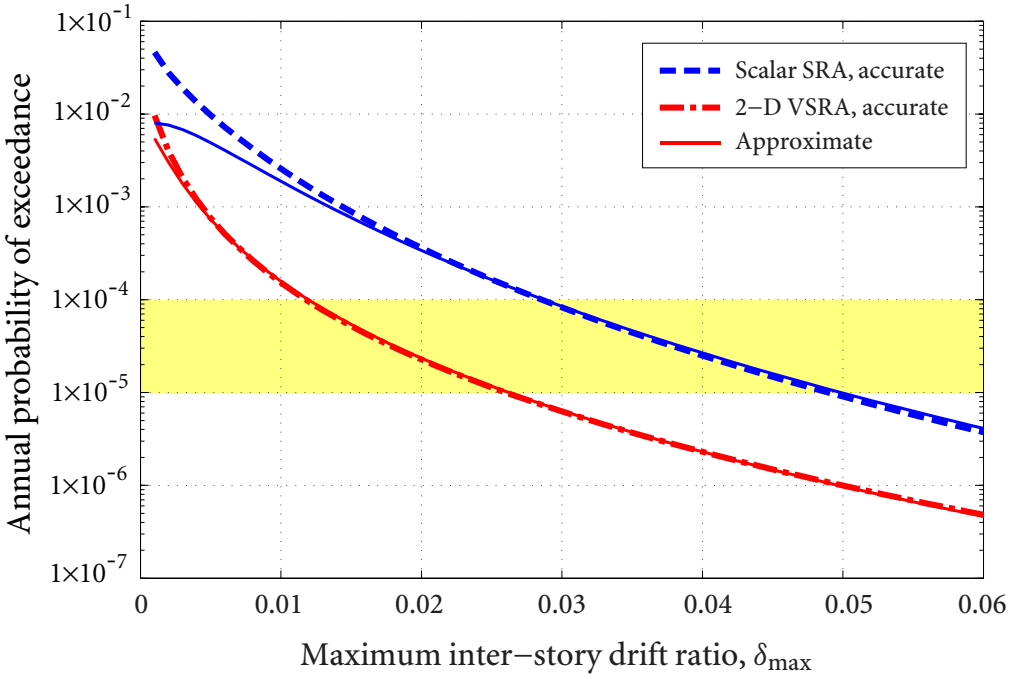

Figure 3.42 Risk curves approximations using scheme 2b, trisection of M

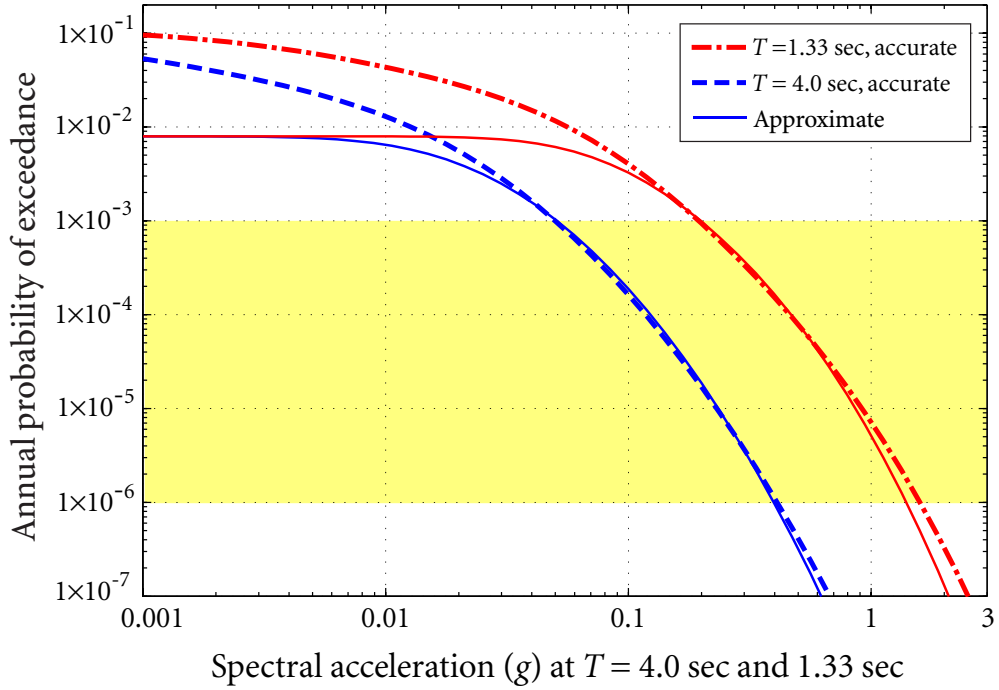

Figure 3.43 Hazard curve approximations using scheme 2c, trisection of R

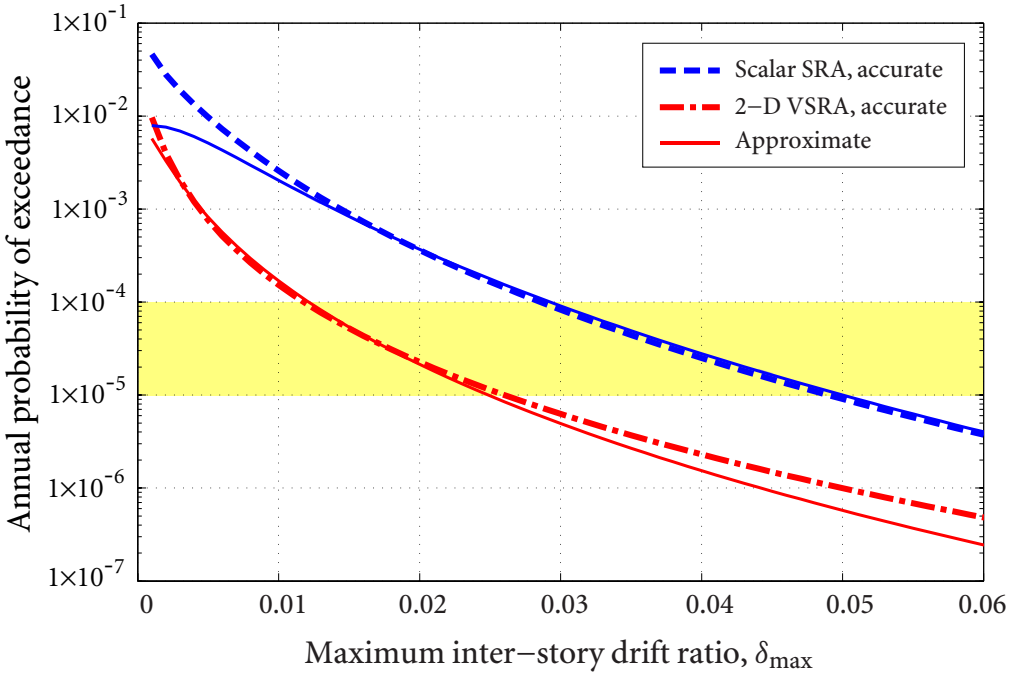

Figure 3.44 Risk curves approximations using scheme 2c, trisection of R

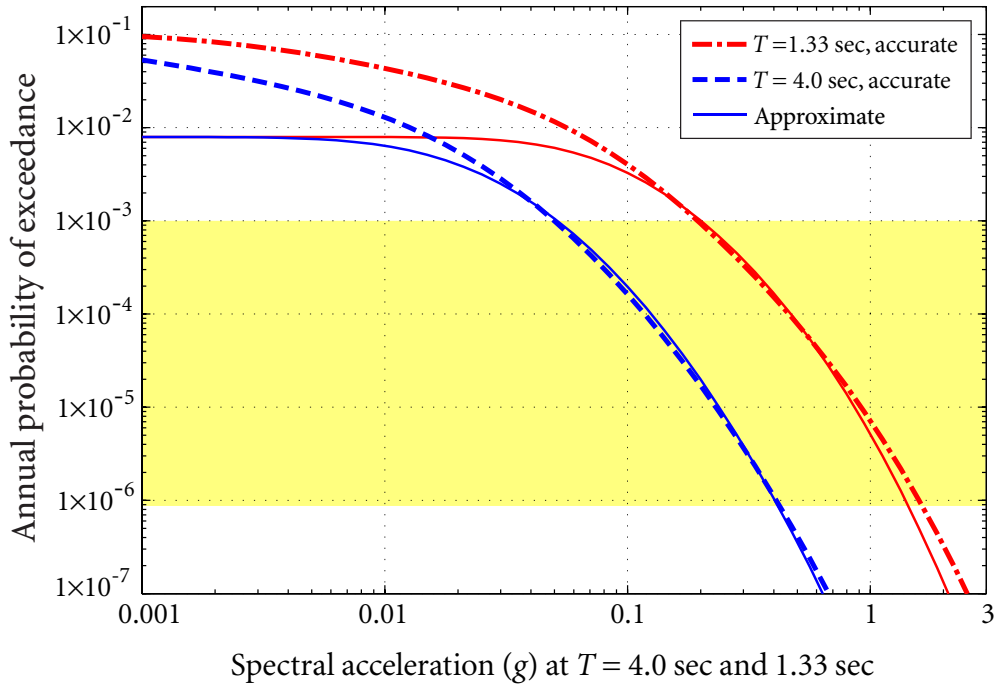

Figure 3.45 Hazard curve approximations using scheme 2d, trisections of both M and R

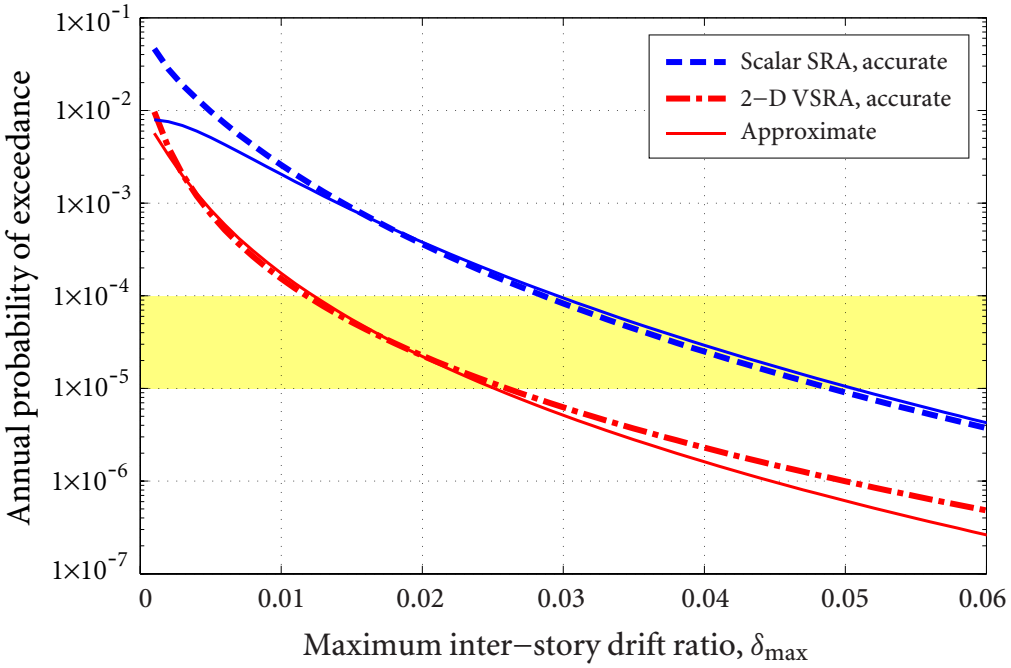

Figure 3.46 Risk curves approximations using scheme 2d, trisections of both M and R

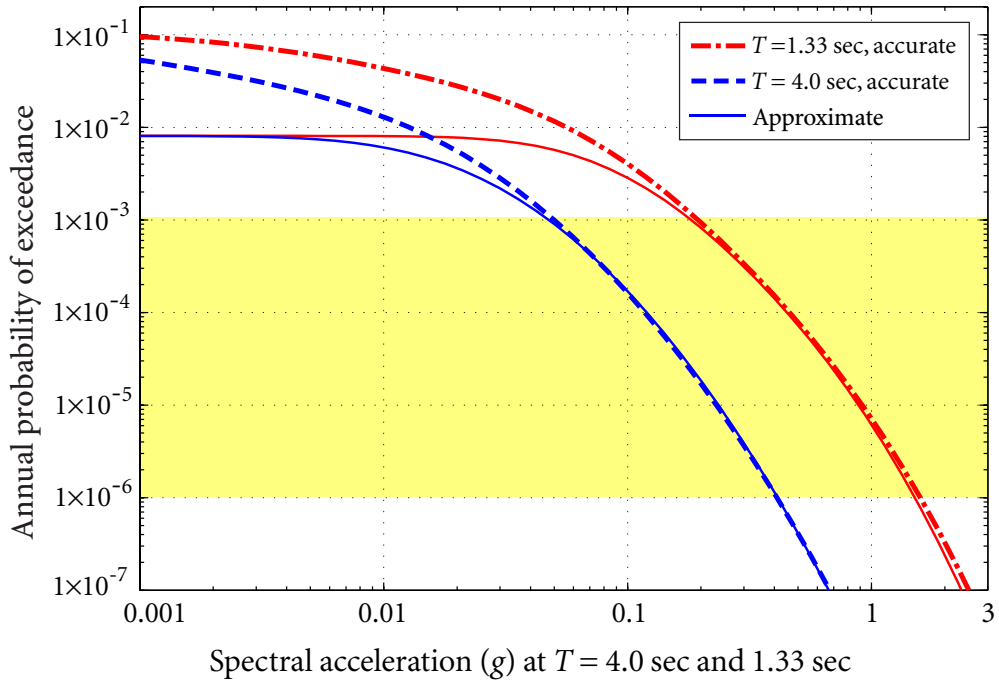

Figure 3.47 Hazard curve approximations using scheme 3b, $N_C = 6 \times 6$ and $s_1 = 0.035\,g$

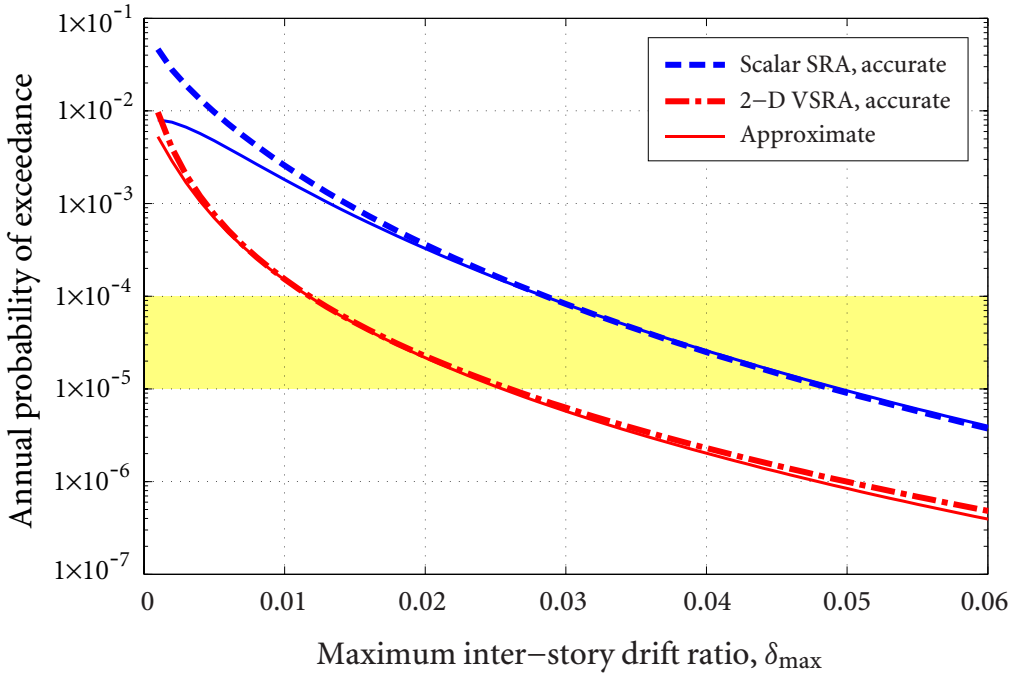

Figure 3.48 Risk curves approximations using scheme 3b, $N_C = 6 \times 6$ and $s_1 = 0.035\,g$

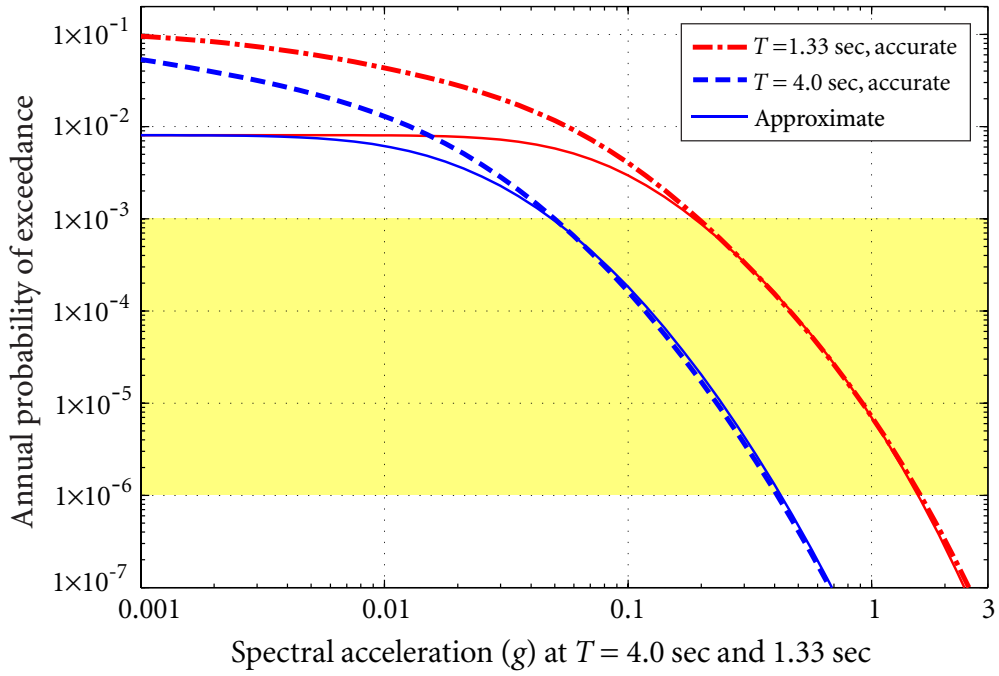

Figure 3.49 Hazard curve approximations using scheme 3c, $N_C = 6 \times 6$ and $s_1 = 0.040\,g$

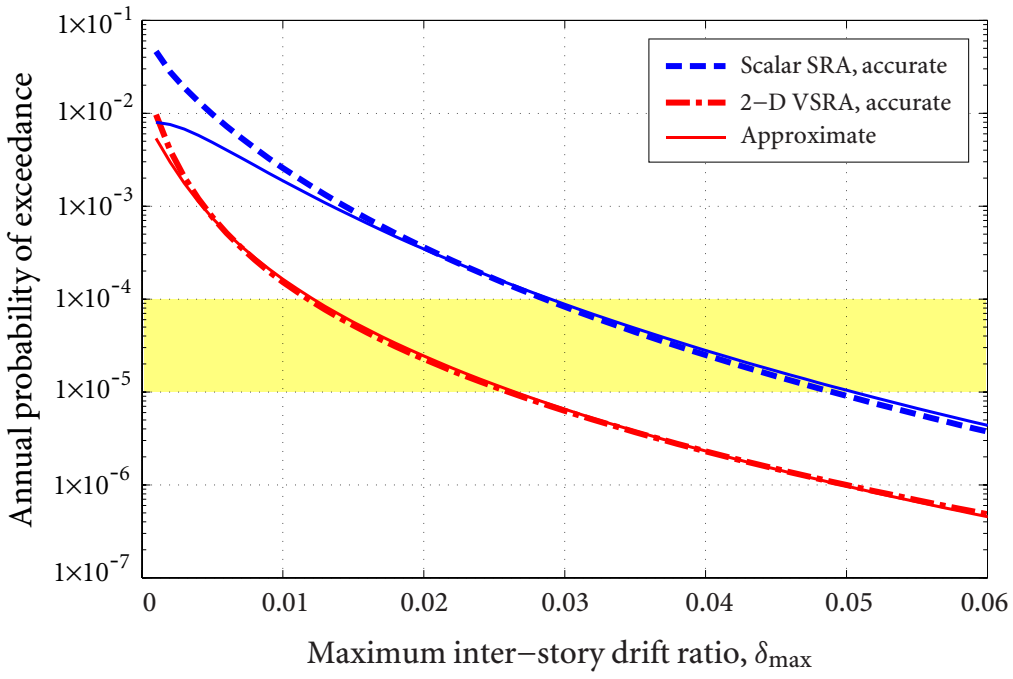

Figure 3.50 Risk curves approximations using scheme 3c, $N_C = 6 \times 6$ and $s_1 = 0.040\,g$

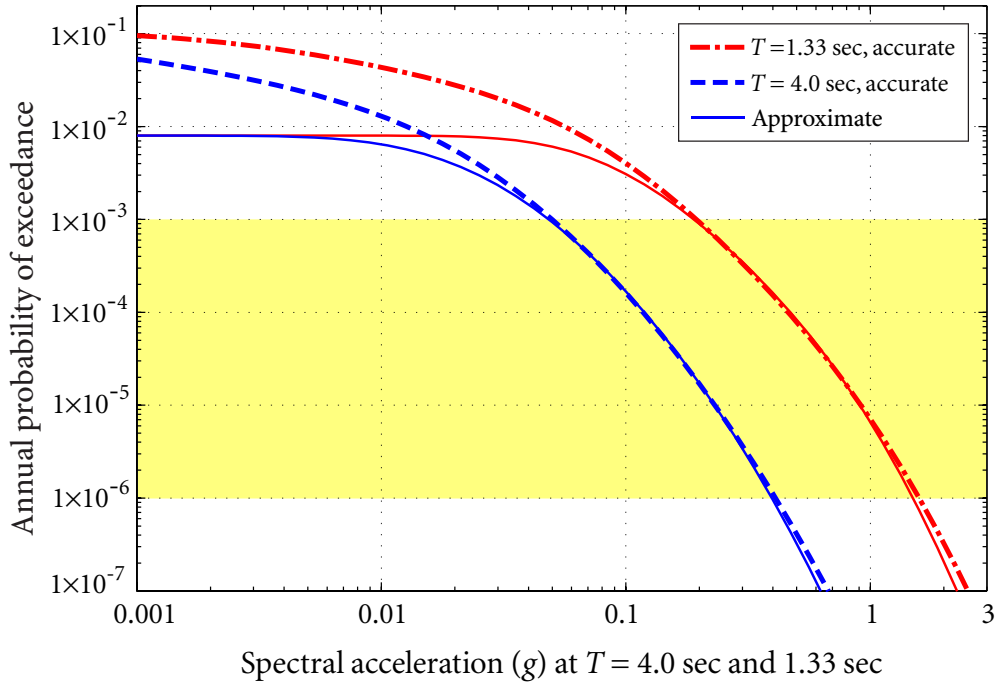

Figure 3.51 Hazard curve approximations using scheme 3d, $N_C = 2 \times 2$

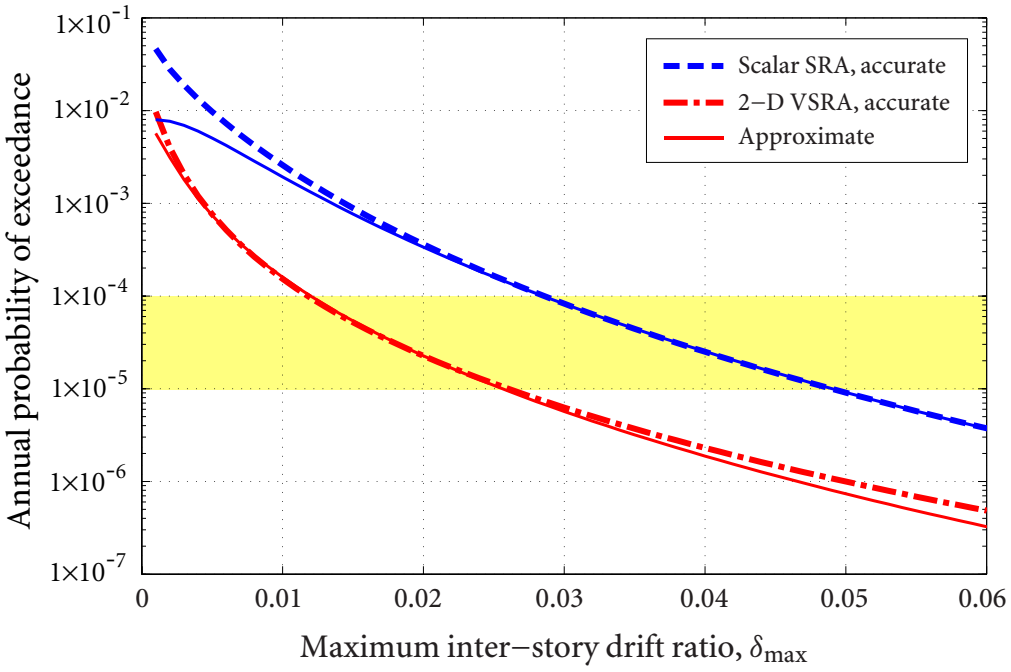

Figure 3.52 Risk curves approximations using scheme 3d, $N_C = 2 \times 2$

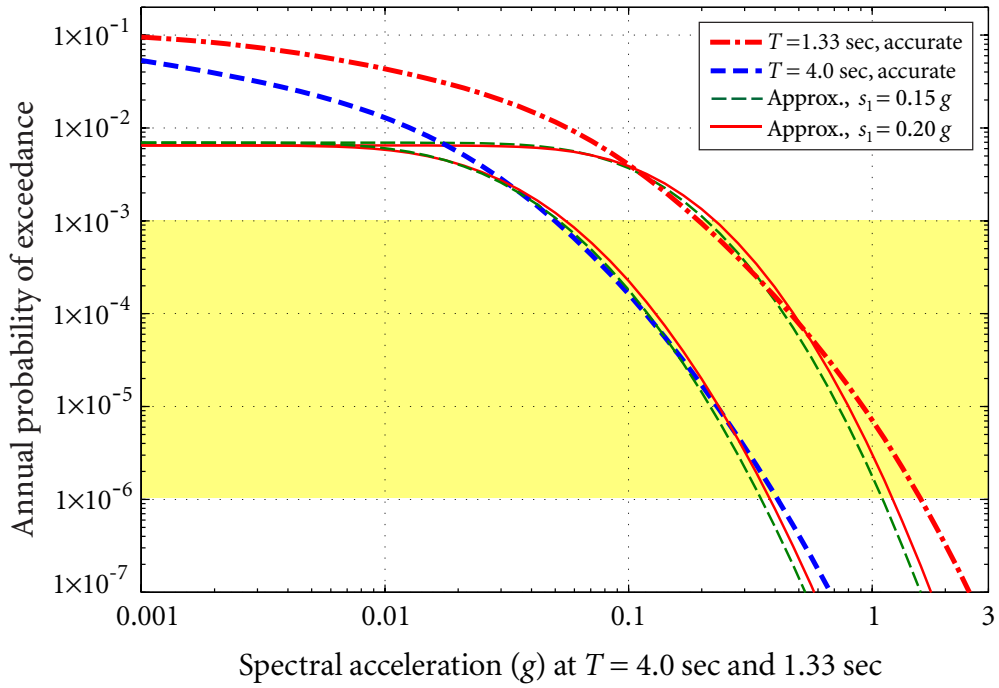

Figure 3.53 Hazard curve approximations using scheme 3e, $N_C = 1 \times 1$

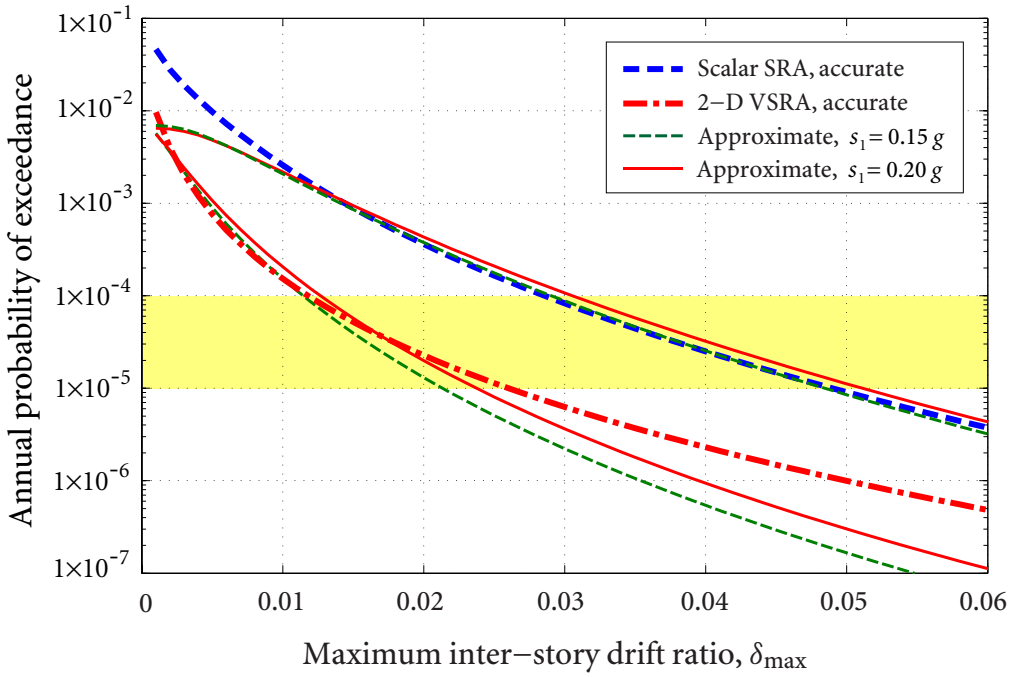

Figure 3.54 Risk curves approximations using scheme 3e, $N_C = 1 \times 1$

a standard VSRA. However, due to the extensive computational effort required for the multiple dimensional cases, VSRA cannot be widely applied in current engineering practice.

- A new seismic hazard deaggregation procedure is proposed to determine a set of controlling earthquakes in terms of magnitude, source-site distance, and occurrence rate. This set of controlling earthquakes represent complete description of seismic hazard at the site and dominant seismic hazard in the probability range of interest.

- A simplified approach to VSRA is developed based on a set of controlling earthquakes. The integration in standard risk analysis with respect to all possible earthquake occurrences, i.e., all $(m,\ r)$-pairs from all N_S sources, are then avoided. Numerical examples show that the simplified approach can provide good risk approximations to standard VSRA. The computational efficiency can be substantially improved with the typical time cost reduced to less than 0.5%.

- It is also demonstrated that this simplified approach can provide best achievable approximations using a typical 3×3 (M, R)-bins, i.e., a total of 9 controlling earthquakes. Finer binning can hardly improve the approximations. Coarser 2×2 (M, R)-bins may be acceptable. 1×1 (M, R)-bin is not recommended for risk approximations.

- In addition, the simplified approach is more sensitive to the R binning than M binning; good R binning helps improve the approximations in most situations.

C H A P T E R 4

Seismic Fragility Analysis for Nuclear Facilities

Seismic fragilities of Structures, Systems, and Components (SSC), representing their seismic capacities and the associated variabilities, are the fundamental ingredient in Seismic Probabilistic Risk Analysis (SPRA) of Nuclear Power Plants (NPP). The objective of fragility analysis is to produce results for SPRA, which are realistic, neither conservative nor optimistic. The quality of seismic fragility analysis directly affects the accuracy of SPRA, hence great care should be taken. There are two popular methods of seismic fragility analysis for nuclear facilities:

(1) The Conservative Deterministic Failure Margin (CDFM) method (EPRI, 1991a), where the HCLPF (*High Confidence of Low Probability of Failure*) capacity is determined first, and the median capacity with an estimated composite variability (typically in the range of 0.3-0.6) is then calculated from the HCLPF;

(2) The Fragility Analysis (FA) method (EPRI, 1994, 2009), where the median seismic capacity is directly estimated using median values for each of the basic variables affecting seismic capacity, and the randomness and uncertainty associated with the median seismic capacity due to basic variables are evaluated.

The CDFM method is a simple deterministic method for evaluating seismic capacity, which can provide efficiency in the overall effort. However, it is an approximate method that

takes into account only the major sources of uncertainty in estimating seismic capacity. In contrast, the FA method is a formal accurate method for evaluating seismic capacity, which considers all sources of uncertainty in a probabilistically rigorous manner. For sites with high seismicity, the FA method should be used (EPRI, 2013).

In this chapter, seismic fragility analysis for nuclear energy facilities is presented. In Section 4.1, the general FA methodology is described. In Sections 4.2 and 4.3, fragility analyses of two significant risk contributors in the plant, the block masonry wall (Wang *et al.*, 2014) and horizontal heat exchanger, are performed, respectively. Results from the FA method and the CDFM method are compared and discussed. This chapter also gives the background for the parametric study presented in Chapter 5.

4.1 Seismic Fragility Analysis Methodology

Not all components in the NPP require the fragility analyses; certain high-capacity components may be screened-out of the list based on qualification documents and walkdown screening. For those screened-in components, fragility analysis is required.

Fragility analysis involves the estimation of conditional probability of failure of a SSC for a given ground motion level. The general procedure of performing fragility analysis is illustrated in Figure 4.1, which includes the following steps.

1. The governing failure mode of a SSC must be clearly defined.
2. Fragility parameters, including median seismic capacity A_m and logarithmic standard deviations reflecting randomness β_R and uncertainty β_U in capacity, need to be evaluated for this failure mode.

    (1) By introducing an overall factor of safety F against a reference earthquake A_{Ref}, all relevant factors affecting F are identified and evaluated.

    (2) The effect of each single factor on the overall F are combined to determine the fragility parameters A_m, β_R, and β_U, using certain procedure of analysis.

3. Using fragility parameters, fragility curves of conditional probabilities against GMP a are then developed.

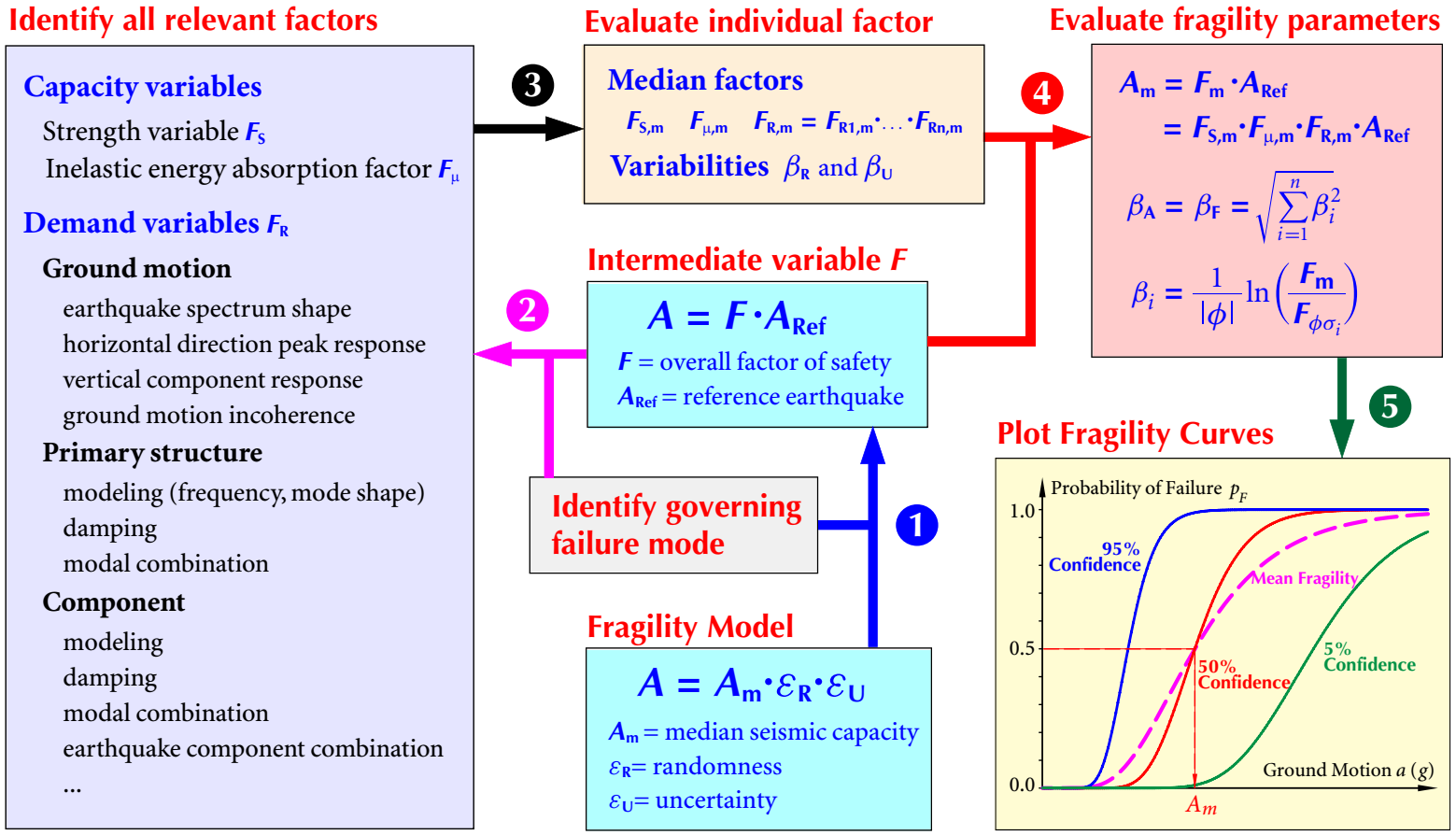

Figure 4.1 Procedure of performing seismic fragility analysis

4.1.1 Definition of Seismic Fragility

Kennedy *et al.* (1980); Kennedy and Ravindra (1984) conducted seismic fragility studies of NPP and developed a semi-empirical method of fragility analysis that has been widely used in nuclear energy industry for the past thirty years.

Define the ground motion capacity A of a SSC as its capacity to withstand the seismic hazard, i.e., the ground acceleration a beyond which seismic response of the SSC would result in its structural or functional failure. Seismic fragility of a SSC is the cumulative distribution function of capacity. Given any ground motion hazard, the probability of failure, i.e., capacity < hazard, can be calculated as

$$P_F(a) = \mathcal{P}\{A < a\} = F_A(a). \tag{4.1.1}$$

4.1.2 Seismic Fragility Model

The ground motion capacity A is modeled as the product of three variables

$$A = A_m \, \varepsilon_R \, \varepsilon_U, \tag{4.1.2}$$

where A_m is the best estimate of median ground motion capacity, ε_R is the random variable representing the inherent *randomness* (aleatory uncertainty) about the capacity, and ε_U is the random variable representing the *uncertainty* (epistemic uncertainty) in estimating A_m due to lack of knowledge. ε_R and ε_U are usually taken to be lognormal random variables with unit median and logarithmic standard deviations β_R and β_U, respectively.

For purpose of seismic risk analysis, the uncertainty in seismic fragility needs to be expressed in terms of a range of failure probabilities for a given ground acceleration a. Seismic fragility for a given a, at confidence level Q, can be derived as (Kennedy and Ravindra, 1984)

$$p_{F,Q}(a) = \mathcal{P}\{A < a \,|\, Q\} = \Phi\left[\frac{\ln(a/A_m) + \beta_U \Phi^{-1}(Q)}{\beta_R}\right]. \tag{4.1.3}$$

The confidence levels Q are often taken as several discrete values, such as 5%, 50%, and 95%; equation (4.1.3) then gives a family of fragility curves.

Fragility can also be expressed in terms of the composite variability β_C, without separating randomness and uncertainty, as

$$p_F(a) = P(A < a) = \Phi\left[\frac{1}{\beta_C} \ln\left(\frac{a}{A_m}\right)\right], \quad \beta_C = \sqrt{\beta_R^2 + \beta_U^2} \tag{4.1.4}$$

which provides a single composite fragility curve or mean fragility curve. In a SPRA, the composite fragility curve is conventionally used for integrating hazard to risk.

As an example, suppose the fragility parameters for a SSC be $A_m = 0.87g$, $\beta_R = 0.25$, and $\beta_U = 0.35$, a family of fragility curves with different confidence levels and a composite fragility curve are developed using equations (4.1.3) and (4.1.4), as shown in Figure 4.2.

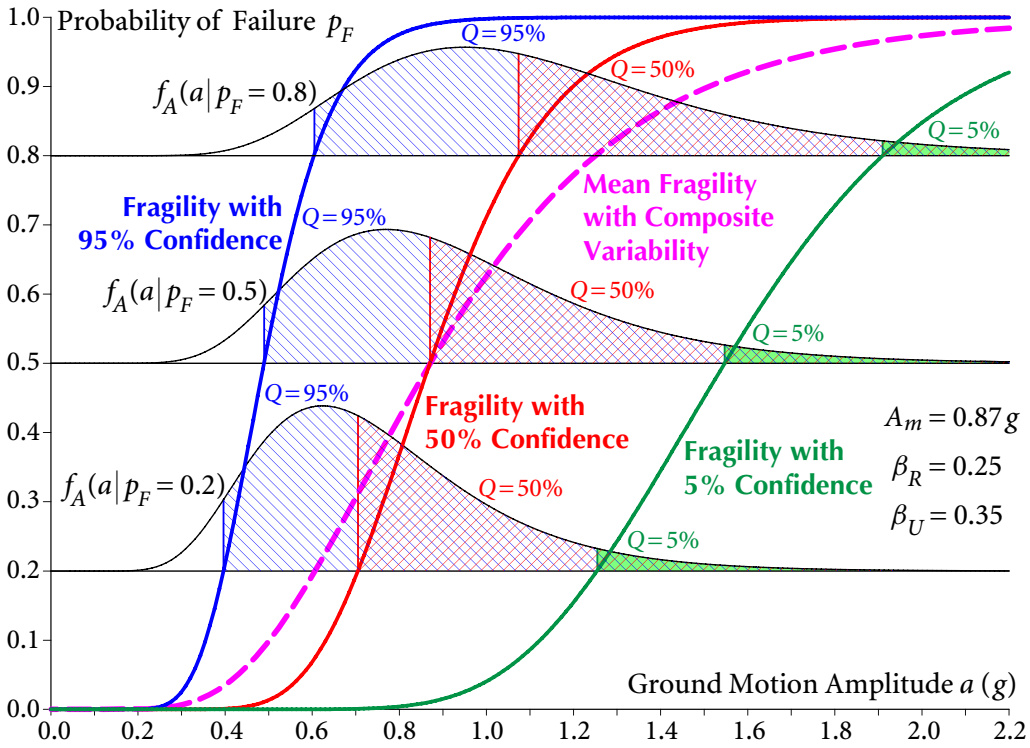

Figure 4.2 Example fragility curves

Bayesian Interpretation of Seismic Fragility

When parameter estimation involves multiple levels/sources of uncertainty, hierarchical Bayesian model is advocated for interpreting and combining all sources of uncertainty

(Gelman *et al.*, 2013). In the following, seismic fragility is derived in a Bayesian format to combine clearly the two sources of uncertainty in estimating A (Wang *et al.*, 2013b).

Given that ground motion capacity A follows the lognormal distribution: $A \sim LN(\alpha, \beta^2)$, hence $Y = \ln A$ follows the normal distribution

$$Y \sim N(\alpha, \beta^2), \quad \text{or} \quad Y = \alpha + R, \text{ where } R \sim N(0, \beta_R^2) \tag{4.1.5}$$

where α is also uncertain, and has its own distribution

$$\alpha = \alpha_Y + U, \text{ where } U \sim N(0, \beta_U^2). \tag{4.1.6}$$

Combining equations (4.1.5) and (4.1.6), one has

$$Y = \alpha_Y + U + R \sim N(\alpha_Y, \beta_U^2 + \beta_R^2), \tag{4.1.7}$$

which corresponds to the composite fragility. α_Y is the logarithm of A_m in equation (4.1.2), and $(\beta_U^2 + \beta_R^2)$ are the two sources of uncertainty combined.

If more than the composite fragility is of interest, from equation (4.1.6) one has

$$\alpha = \alpha_Y + s \cdot \beta_U, \tag{4.1.8}$$

where $s \sim N(0, 1)$ is a standard normal random variable characterizing the epistemic uncertainty in estimating α_Y. Associating s with confidence level Q in the sense that

$$\Phi(s_q) = 1 - Q, \quad s_q = \Phi^{-1}(1-Q) = -\Phi^{-1}(Q), \tag{4.1.9}$$

one has

$$Y \,|\, \beta_R \sim N(\alpha_Y + \beta_U \cdot s_q,\ \beta_R^2) = N(\alpha_Y - \beta_U \cdot \Phi^{-1}(Q),\ \beta_R^2) \tag{4.1.10}$$

Seismic fragility is then given by

$$p_{F,q} = P\{Y < y\} = P\{\alpha_Y + \beta_U \cdot s_q < y\} = \Phi\left[\frac{y - \alpha_Y - \beta_U \cdot s_q}{\beta_R}\right]. \tag{4.1.11}$$

where aleatory and epistemic uncertainties are separated. Noting that $y = \ln a, \alpha_Y = \ln A_m$, and $s_q = -\Phi^{-1}(Q)$, equation (4.1.11) is essentially the same as equation (4.1.3).

It is seen that the Bayesian method provides a sound provision for combining different sources of uncertainty in a mathematically rigorous manner.

For a specific failure probability p_F and confidence level Q, solving equation (4.1.11) gives

$$y^{q,p} = \alpha_Y + \beta_U \cdot s_q + \beta_R \cdot s_p, \quad \text{or} \tag{4.1.12a}$$

$$a^{q,p} = A_m \cdot \mathrm{e}^{(\beta_U \cdot s_q + \beta_R \cdot s_p)}, \tag{4.1.12b}$$

where $s_p = \Phi^{-1}(p_F)$. Equation (4.1.12) clearly shows how two types of uncertainty are propagated in estimating the ground acceleration a for a failure probability p_F and confidence level Q, as shown in Figure 4.2 for $p_F = 0.2, 0.5$, and 0.8.

HCLPF Capacity

In Seismic Margin Assessment (SMA), efforts are frequently made to determine the HCLPF capacity of a SSC, which is defined as the ground acceleration a corresponding to the 5% probability of failure ($p_F = 0.05$) with 95% confidence ($Q = 0.95$) on the fragility curve.

Substituting $p_F = 0.05$ and $Q = 0.95$ into equation (4.1.12b) gives the HCLPF capacity

$$A_{\text{HCLPF}} = A_m \, \mathrm{e}^{(\beta_R + \beta_U)\Phi^{-1}(0.05)} = A_m \, \mathrm{e}^{-1.645(\beta_R + \beta_U)}. \tag{4.1.13}$$

For the special case when $\beta_R = \beta_U$ and $\beta_C = \sqrt{\beta_R^2 + \beta_U^2} = \sqrt{2}\beta_R$, equation (4.1.13) becomes

$$\begin{aligned} A_{\text{HCLPF}} &= A_m \, \mathrm{e}^{-1.645 \times 2\beta_R} = A_m \, \mathrm{e}^{-1.645 \times \sqrt{2} \times \sqrt{2}\beta_R} = A_m \, \mathrm{e}^{-2.326 \times \sqrt{2}\beta_R}, \\ &= A_m \, \mathrm{e}^{\Phi^{-1}(0.01)\beta_C}, \quad \Phi^{-1}(0.01) = -2.326. \end{aligned} \tag{4.1.14}$$

- When $\beta_R = \beta_U$, equation (4.1.14) is exact, i.e., HCLPF capacity can be obtained either by using $p_F = 0.05$ from the fragility curve with 95% confidence ($Q = 0.95$) or by using $p_F = 0.01$ from the composite fragility curve.
- When $\beta_R \neq \beta_U$, equation (4.1.14) is not exact; it is acceptable as an approximation in practice when $0.5 \leqslant \beta_R / \beta_U \leqslant 2$.

  Figure 4.3 shows the fragility curve with 95% confidence level and the composite fragility curve. The HCLPF capacity obtained using the two fragility curves are, respectively, 0.324 g and 0.320 g, the difference between which is negligible.

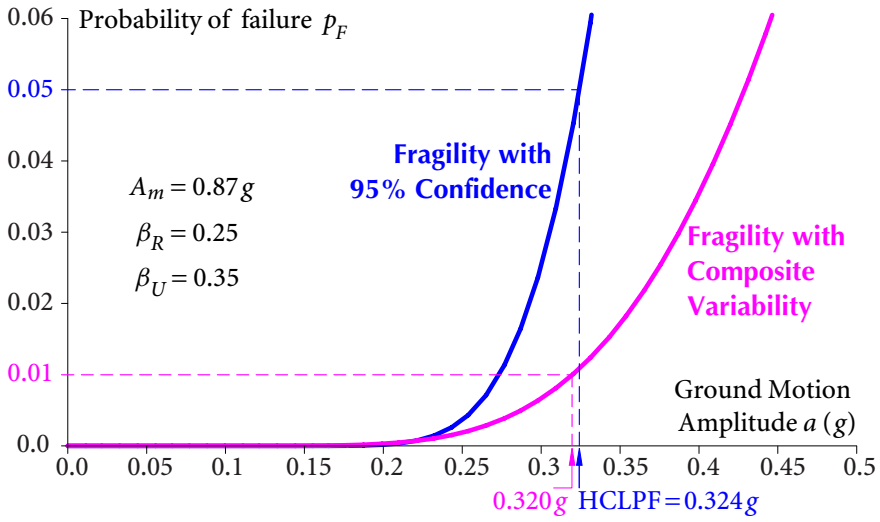

Figure 4.3 HCLPF capacity on fragility curves

4.1.3 Failure Modes

For fragility analysis, the first step is to develop a clear understanding of the possible failure modes of a SSC. Identification of possible failure modes is often based on the analyst's experience and judgment. In addition, review of plan design criteria, qualification reports, previous fragility studies, earthquake experience data are all useful resources.

It is usually possible to identify the most likely (governing) failure mode of a SSC caused by an earthquake by observations during walkdown or by reviewing the equipment design. In this case, only this failure mode needs to be considered in fragility analysis. Otherwise, multiple possible failure modes should be evaluated, and lowest capacity failure mode is the governing failure mode for fragility analysis.

Nuclear structures housing safety systems usually have a large margin of safety against total collapse. Their seismic capacities are generally governed by functional failures. For example, functional failures may occur when structures deform sufficiently large to interfere with the operability of safety-related equipment attached thereon or fracture sufficiently so that equipment attachment fails.

Individual components are more vulnerable to failure in an earthquake, so their fragilities are of more interest. Significant seismic risk contributors to the plant include electrical cabinets, tanks, diesel generators, block walls, heat exchangers, and etc (EPRI, 2000).

4.1.4 Estimation of Fragility Parameters

Development of seismic fragility curves for a SSC involves mainly the determination of fragility parameters: (1) median ground motion capacity A_m, and (2) the logarithmic standard deviations β_R and β_U, or β_C.

In estimating the fragility parameters, it is more convenient to work with an intermediate variable F, called the *factor of safety*. The ground motion capacity A is then estimated by the factor of safety F multiplied to a reference level earthquake A_{Ref}:

$$A = F \cdot A_{\text{Ref}}. \tag{4.1.15}$$

Hence, the median factor of safety F_m can be directly related to the median ground motion capacity A_m by

$$A_m = F_m \cdot A_{\text{Ref}}. \tag{4.1.16}$$

The logarithmic standard deviations of F, representing inherent randomness and uncertainty, are identical to those of A.

The factor of safety F is evaluated through various factors affecting the capacity and response factors of safety

$$F = F_{\text{S}} \cdot F_{\mu} \cdot F_{\text{R}}, \tag{4.1.17}$$

where

1. F_{S} = strength factor, representing the ratio of ultimate strength to seismic demand calculated for A_{Ref}, given by
$$F_{\text{S}} = \frac{S - P_{\text{N}}}{P_{\text{T}} - P_{\text{N}}}, \tag{4.1.18}$$
where S is the static strength of component for a specific failure mode, P_{N} is the demand due to normal operating load. P_{T} is the demand against total load, and $P_{\text{T}} - P_{\text{N}}$ is the portion of demand calculated for A_{Ref}.
2. F_{μ} = inelastic energy absorption factor, reflecting the conservatism in assessing capacity beyond elastic limit due to ductility. F_{μ} is generally a function of system ductility ratio μ. Kennedy and Ravindra (1984) suggested that

   (a) For *brittle and functional failure modes*, median value of F_{μ} is taken to be 1.0.

(b) For *ductile failures modes* of equipment responding in the amplified region of the design spectrum (2-8 Hz),

$$F_\mu = \varepsilon\sqrt{2\mu - 1}, \tag{4.1.19}$$

where $\varepsilon \sim LN(1.0,\ \beta_U^2)$ considers the error in equation (4.1.19), where β_U ranges from 0.02 to 0.10 (increasing with the ductility ratio).

(c) For *rigid equipment*,

$$F_\mu = \varepsilon\, \mu^{0.13}, \tag{4.1.20}$$

where ε is the same as that in equation (4.1.19).

3. F_{R} = response factor, reflecting the conservatism in calculating the demand. In case when equipment or component fragility is evaluated, both response factor of primary structure F_{RS} and response factor of equipment F_{RE} must be evaluated.

   The structure response factor F_{RS} is evaluated based on the response characteristics of the structure at the location of equipment support. Thus, variables pertinent to structural response analyses used to generate the floor spectra for equipment design are the only variables of interest for equipment fragility, which includes spectral shape, damping, modelling, and soil-structure interaction.

   The equipment response factor F_{ES} is the ratio of equipment response calculated in the design to the realistic equipment response. When dynamic analysis procedure is used, the important variables affecting equipment response include quantification method, spectral shape, modelling, damping, and combinations of modal responses and earthquake components.

   Hence, the response factor F_{R} is given by

$$F_{\mathrm{R}} = F_{\mathrm{RS}} \cdot F_{\mathrm{RE}} = (F_{\mathrm{SA}} \cdot F_\delta \cdot F_{\mathrm{M}} \cdot F_{\mathrm{SS}}) \cdot (F_{\mathrm{QM}} \cdot F_{\mathrm{SA}} \cdot F_\delta \cdot F_{\mathrm{M}} \cdot F_{\mathrm{MC}} \cdot F_{\mathrm{EC}}), \tag{4.1.21}$$

   where

   (a) F_{QM} = factor of qualification method. If the equipment is quantified by dynamic analysis, then the median factor $F_{\mathrm{QM},m} = 1.0$ and $\beta_R = \beta_U = 0$.

(b) F_{SA} = factor associated with spectral shape of ground response spectra or floor response spectra. If the median spectral shape is used, then its median $F_{SA,m} = 1.0$. Otherwise, conservatism against the median shape needs to be characterized.

(c) F_M = modelling factor due to modelling assumptions. If the dynamic model of structure or equipment is deemed adequate to predict the seismic response, a median of $F_{M,m} = 1.0$ can be expected.

(d) $F_{\delta,m}$ = damping factor considering the difference in actual damping and design damping for structure or equipment. EPRI-CR-103959 (1994) recommended some median damping values for various types of structures and equipment common in nuclear power plants. Using these recommended medians, $F_{\delta,m} = 1.0$ is appropriate.

(e) F_{MC} = modal combination factor. Using the "*Square-Root-of-the-Sum-of-the-Squares*" (SRSS) combination rule, the response is median centered, $F_{MC,m} = 1.0$.

(f) F_{EC} = factor for earthquake component combination. Besides the SRSS, the "100-40-40" rule is also an acceptable method for combining responses from three principle earthquake components, using which the equipment response is believed to be median centered, i.e., $F_{EC,m} = 1.0$.

(g) F_{SS} = factor accounting for soil-structure interaction. If fixed-base analysis is performed, $F_{SS} = 1.0$ can be assumed, without any variability.

EPRI-CR-103959 (1994) provides guidelines for estimating the variabilities for each of the basic capacity and demand variables, which were mainly based on available test results, theoretical derivations, and engineering judgments. For each basic variable affecting the factor of safety, the randomness β_R and uncertainty β_u should be estimated separately.

4.1.5 Procedure of Fragility Analysis

For each of the parameters affecting capacity and response factors of safety, the median and variabilities are estimated, as described in Subsection 4.1.4. These estimates need to

be combined to obtain the overall median factor of safety F_m and variabilities β_R and β_U, required to define the fragility curves.

Suppose that the factor of safety or scale factor F in equation (4.1.15) can be expressed as a function of the basic demand and capacity variables X_i, $i=1,2,\ldots,n$,

$$F = F(\mathbf{X}) = F(X_1, X_2, \ldots, X_n). \tag{4.1.22}$$

An example of equation (4.1.22) is the factor of safety given in equation (4.1.17).

Expanding F in Taylor series about the mean values $\bar{\mathbf{X}} = (\bar{X}_1, \bar{X}_2, \ldots, \bar{X}_n)$ of variables $\mathbf{X} = (X_1, X_2, \ldots, X_n)$ gives

$$\begin{aligned} F(\mathbf{X}) &= \sum_{k=0}^{\infty} \frac{1}{k!} \left[(X_1 - \bar{X}_1) \frac{\partial}{\partial X_1} + (X_2 - \bar{X}_2) \frac{\partial}{\partial X_2} + \cdots + (X_n - \bar{X}_n) \frac{\partial}{\partial X_n} \right]^k F \Big|_{\bar{\mathbf{X}}} \\ &= F(\bar{\mathbf{X}}) + \sum_{i=1}^{n} \frac{\partial F}{\partial X_i}\Big|_{\bar{\mathbf{X}}} (X_i - \bar{X}_i) + \frac{1}{2} \sum_{i=1}^{n} \sum_{j=1}^{n} \frac{\partial^2 F}{\partial X_i \partial X_j}\Big|_{\bar{\mathbf{X}}} (X_i - \bar{X}_i)(X_j - \bar{X}_j) + \cdots . \end{aligned} \tag{4.1.23}$$

Taking expected value of equation (4.1.23) yields the mean factor of safety

$$\bar{F} = F(\bar{\mathbf{X}}) + \sum_{i=1}^{n} \frac{\partial F}{\partial X_i}\Big|_{\bar{\mathbf{X}}} \mathrm{E}\big[X_i - \bar{X}_i\big] + \frac{1}{2} \sum_{i=1}^{n} \sum_{j=1}^{n} \frac{\partial^2 F}{\partial X_i \partial X_j}\Big|_{\bar{\mathbf{X}}} \mathrm{E}\big[(X_i - \bar{X}_i)(X_j - \bar{X}_j)\big] + \cdots . \tag{4.1.24}$$

Assuming that the variables $X_i, i=1,2,\ldots,n,$ are uncorrelated, one has

$$\mathrm{E}\big[(X_i - \bar{X}_i)(X_j - \bar{X}_j)\big] = \begin{cases} \mathrm{E}\big[(X_i - \bar{X}_i)^2\big] = \mathrm{Var}(X_i) = \sigma_{X_i}^2, & i = j, \\ 0, & i \neq j, \end{cases}$$

where σ_{X_i} is the standard deviation of variable X_i, and equation (4.1.24) becomes

$$\bar{F} = F(\bar{\mathbf{X}}) + \frac{1}{2} \sum_{i=1}^{n} \frac{\partial^2 F}{\partial X_i^2}\Big|_{\bar{\mathbf{X}}} \sigma_{X_i}^2 + \cdots . \tag{4.1.25}$$

From equations (4.1.23) and (4.1.25), the variance of F can be obtained

$$\mathrm{E}\big[(F - \bar{F})^2\big] = \mathrm{E}\left[\left\{ \sum_{i=1}^{n} \frac{\partial F}{\partial X_i}\Big|_{\bar{\mathbf{X}}} (X_i - \bar{X}_i) + \cdots \right\}^2 \right] = \sum_{i=1}^{n} \left(\frac{\partial F}{\partial X_i} \right)^2 \Big|_{\bar{\mathbf{X}}} \mathrm{E}\big[(X_i - \bar{X}_i)^2\big] + \cdots,$$

i.e.,

$$\sigma_F^2 = \sum_{i=1}^{n} \left(\frac{\partial F}{\partial X_i} \right)^2 \Big|_{\bar{\mathbf{X}}} \sigma_{X_i}^2 + \cdots . \tag{4.1.26}$$

Variables X_i are usually modelled as lognormally distributed random variables, i.e., $X_i \sim LN(X_{i,m}, \beta_{X_i}^2)$. Its mean value $\bar{X}_i$, median $X_{i,m}$, standard deviation σ_{X_i}, and logarithmic standard deviation β_i are related as follows

$$\bar{X}_i = X_{i,m}\, \mathrm{e}^{\beta_{X_i}^2/2}, \tag{4.1.27a}$$

$$\mathrm{COV}_i = \sqrt{\mathrm{e}^{\beta_{X_i}^2} - 1}, \tag{4.1.27b}$$

$$\sigma_{X_i} = \mathrm{COV}_i \cdot \bar{X}_i, \tag{4.1.27c}$$

Similarly, the median F_m and logarithmic standard deviation β of the factor of safety F can be obtained from the mean value $\bar{F}$ and standard deviation σ_F:

$$\mathrm{COV}_F = \frac{\sigma_F}{\bar{F}}, \tag{4.1.28a}$$

$$\beta_F = \sqrt{\ln\left(\mathrm{COV}_F^2 + 1\right)}, \tag{4.1.28b}$$

$$F_m = \bar{F}\, \mathrm{e}^{-\beta^2/2}. \tag{4.1.28c}$$

Depending on how many terms are kept in equations (4.1.25) and (4.1.26), one has the following second-moment methods.

Second-Moment First-Order Method

From equations (4.1.25) and (4.1.26), taking

$$\bar{F} = F(\bar{\mathbf{X}}), \quad \sigma_F^2 = \sum_{i=1}^{n} \left(\frac{\partial F}{\partial X_i} \right)^2 \Bigg|_{\bar{\mathbf{X}}} \sigma_{X_i}^2, \quad \bar{\mathbf{X}} = (\bar{X}_1, \bar{X}_2, \ldots, \bar{X}_n), \tag{4.1.29}$$

gives the Second-Moment First-Order method.

Second-Moment Second-Order-Mean Method

From equations (4.1.25) and (4.1.26), taking

$$\bar{F} = F(\bar{\mathbf{X}}) + \frac{1}{2} \sum_{i=1}^{n} \frac{\partial^2 F}{\partial X_i^2} \Bigg|_{\bar{\mathbf{X}}} \sigma_{X_i}^2, \quad \sigma_F^2 = \sum_{i=1}^{n} \left(\frac{\partial F}{\partial X_i} \right)^2 \Bigg|_{\bar{\mathbf{X}}} \sigma_{X_i}^2, \tag{4.1.30}$$

gives the Second-Moment Second-Order-Mean method.

☞ *A second-order formulation can be derived for the standard deviation, but it offers very little benefit and is unreasonably complex. Therefore, the second-order procedure is recommended only when calculating the mean.*

Approximate Second-Moment Method

In the approximate second-moment method, the median capacity F_m is obtained by using median values $X_{i,m}$ for all the basic variables X_i in a deterministic analysis:

$$F_m = F(\mathbf{X}_m) = F\big(X_{1,m}, X_{2,m}, \ldots, X_{n,m}\big). \tag{4.1.31}$$

The logarithmic standard deviation for randomness β_R and uncertainty β_U are obtained by using the square-root-of-sum-of-squares (SRSS) rule:

$$\beta_F = \sqrt{\sum_{i=1}^{n} \beta_i^2}\,, \tag{4.1.32}$$

where β_i represents the part of the final β-value due to the effect of variability in the ith basic variable, and is obtained from

$$\beta_i = \frac{1}{|\phi|} \ln\!\left(\frac{F_m}{F_{\phi\sigma_i}}\right), \tag{4.1.33}$$

where $F_{\phi\sigma_i}$ is the scale factor applied to the reference earthquake input to reach failure when the ith variable X_i is set at the ϕ-standard-deviation level, while all other variables are kept at their median levels. The parameter ϕ is usually set at 1 on the side of the median that leads to the lower capacity:

- Demand variables are increased by evaluating at median-plus-one-standard-deviation level, i.e., $\phi = 1 \implies X_i = X_{i,m}\, e^{\beta_{X_i}}$.
- Capacity variables are decreased by setting at median-minus-one-standard-deviation level, i.e., $\phi = -1 \implies X_i = X_{i,m}\, e^{-\beta_{X_i}}$.

In this method, for each basic variable X_i, the mean is assumed to be the same as the median, and standard deviation is set equal to the logarithmic standard deviation times the median, i.e.,

$$\bar{X}_i \approx X_{i,m} \quad \text{and} \quad \sigma_{X_i} \approx \beta_{X_i} \cdot X_{i,m} \tag{4.1.34}$$

are used instead of equations (4.1.27a) and (4.1.27c).

Similarly, the same approximations are made for the factor of safety

$$F_m = F(\mathbf{X}_m), \quad \sigma_F^2 = \sum_{i=1}^{n} \left(\frac{\partial F}{\partial X_i}\bigg|_{\bar{\mathbf{X}}} \beta_{X_i} \cdot X_{i,m} \right)^2, \quad \beta = \frac{\sigma_F}{F_m}, \tag{4.1.35}$$

This assumption may be slightly conservative, depending on the effect on the median capacity from the relative variability of the underlying basic variable.

For fragility analysis, this method is easy to use and has been tested to produce very acceptable results for the following equation forms of basic variables (EPRI, 1994):

(1) $F = X_1 \cdot X_2 \cdot X_3$, (2) $F = X_1 + X_2 + X_3$, (3) $F = X_1 \cdot X_2 / X_3$,
(4) $F = (X_1 + X_2)/X_3$, (5) $(F \cdot X_1)^{X_3} + (F \cdot X_2)^{X_3} = 1.0$.

As an example application of the approximate second-moment method, consider the following simple equation form

$$Y = X_1 + X_2,$$

where $X_1 \sim LN(X_{1,m},\ \beta_{X_1})$ and $X_2 \sim LN(X_{2,m},\ \beta_{X_2})$ are lognormal random variables.

Using equation (4.1.35), the approximate median and β become

$$Y_m = X_{1,m} + X_{2,m},$$
$$\beta = \sqrt{\left(\frac{X_{1,m}}{X_{1,m}+X_{2,m}}\beta_{X_1}\right)^2 + \left(\frac{X_{2,m}}{X_{1,m}+X_{2,m}}\beta_{X_2}\right)^2} = \sqrt{\beta_1^2 + \beta_2^2}.$$

Letting $X_1 \sim LN(2,\ 0.3)$ and $X_2 \sim LN(3,\ 0.4)$ yields

$$Y_m = 2 + 3 = 5,$$
$$\beta = \sqrt{\left(\frac{2}{2+3}(0.3)\right)^2 + \left(\frac{3}{2+3}(0.4)\right)^2} = \sqrt{0.12^2 + 0.24^2} = 0.268. \tag{4.1.36}$$

Equation (4.1.33) provides a simplified approach to determine β_i, easy to use when equation form of $F(\mathbf{X})$ is complicated. Using equation (4.1.33) and letting $\phi = -1$ give

$$F_{1\sigma_1} = X_{1,-1\sigma} + X_{2,m} = 2 \times e^{-0.3} + 3 = 4.341,$$
$$F_{1\sigma_2} = X_{1,m} + X_{2,-1\sigma} = 2 + 3 \times e^{-0.4} = 3.820,$$

$$\beta_1 = \frac{1}{|-1|}\ln\left(\frac{5}{4.341}\right) = 0.11, \quad \beta_2 = \frac{1}{|-1|}\ln\left(\frac{5}{3.820}\right) = 0.22,$$
$$\beta = \sqrt{\beta_1^2 + \beta_2^2} = \sqrt{0.11^2 + 0.22^2} = 0.246,$$

which is only slightly different than 0.268 provided by equation (4.1.36).

Having obtained the fragility parameters A_m, β_R, and β_U, seismic fragility of a SSC is completely defined. The concept of developing seismic fragility is further presented by the following two examples.

4.2 Fragility Analysis of the Block Masonry Wall

4.2.1 Background

The block masonry wall, a commonly used fire barrier or partition in nuclear power plants, is fairly vulnerable to failure under an earthquake. It is frequently considered as ''safety-related'' in the sense that its failure could affect a safety system or equipment. Block masonry walls have been identified as governing components for plant risk and HCLPF, hence their evaluation and retrofit are often required (EPRI, 2000).

Configuration

Figure 4.4 shows a lightly reinforced non-load bearing block wall, constructed using 8 inch masonry units. It is assumed that the wall is simply supported at top and bottom, considering that supporting elements do not possess sufficient stiffness to transfer the wall moments into the supports. The wall has a height L of 11 feet and a nominal thickness of 8-inch (t is actually equal to 7.625 inches). It is fully grouted, with #4 bar reinforcement at 16 inch spacing located at mid-depth of the wall section. The wall weight is estimated to be 83.5 pounds per square foot (psf) of wall surface.

Governing failure mode

The primary loads imposed on the block masonry wall are due to seismic events. Seismic capacity of such block wall is usually governed by the out-of-plane bending failure. The maximum deformation/drift limit and structural integrity of the wall should be secured such that the operability of safety-related system is not in jeopardy.

Previous test results (Hamid *et al.*, 1989) showed that this type of wall exhibits substantial nonlinear drift capability under cyclic loading and that the effective frequency is lowered due to the drift. However, severe pinching phenomenon of the hysteretic loop for the centrally-

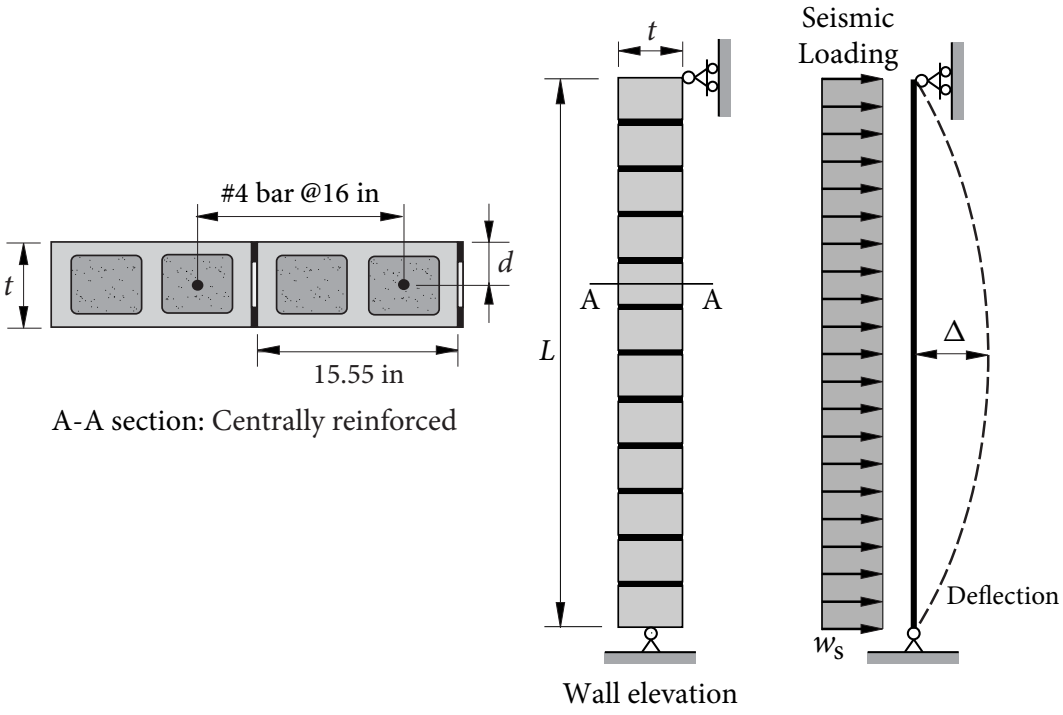

Figure 4.4 Block masonry wall

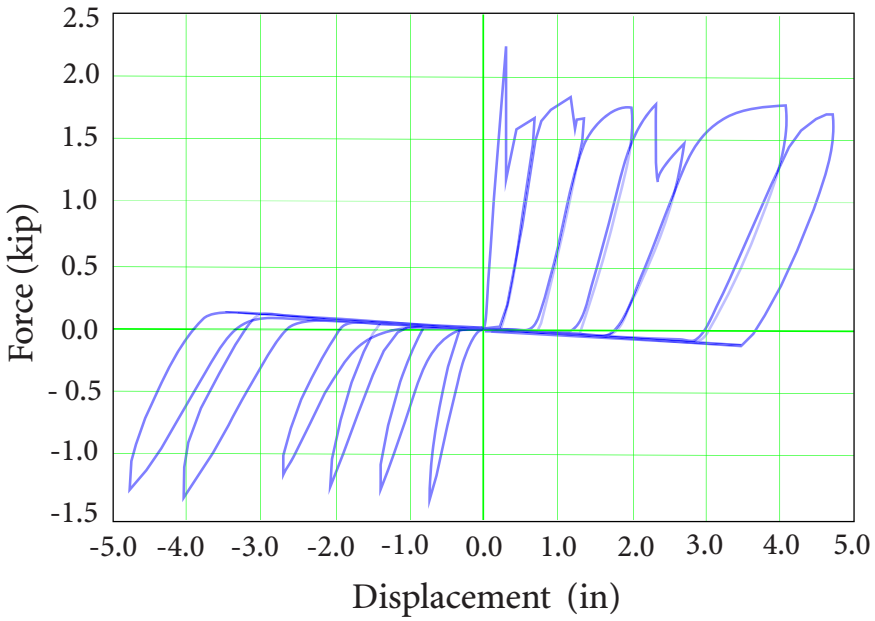

Figure 4.5 Hysteretic loop of centrally-reinforced block masonry wall

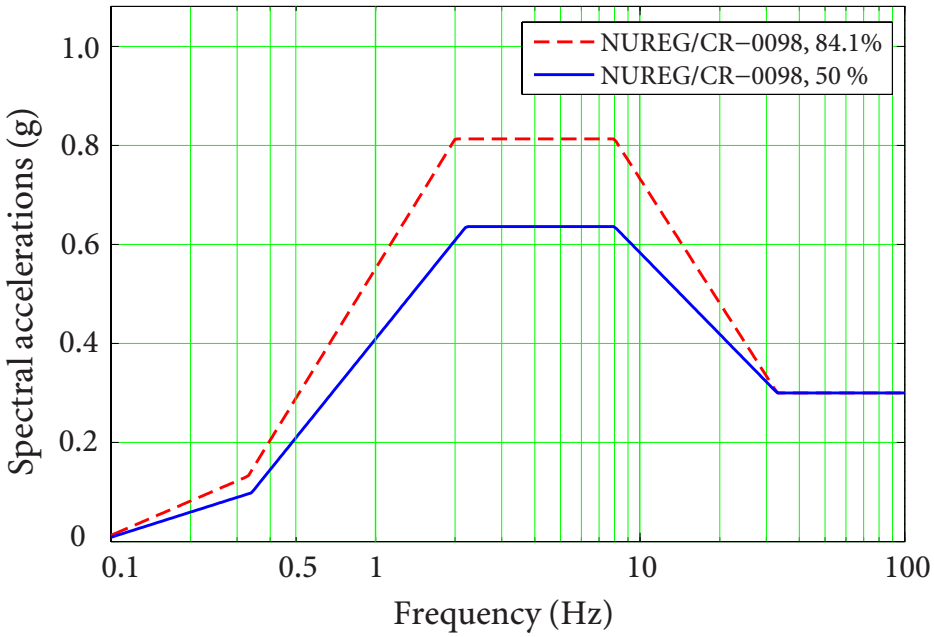

Figure 4.6 Reference ground response spectra

reinforced walls was observed under cyclic loading (see Figure 4.5), so that negligible inelastic energy absorption capability can be assumed, i.e., $F_\mu = 1.0$.

Seismic input

The block masonry wall is mounted on floor-3 of a 6.58 Hz primary structure on a rock site, hence is subjected to the horizontal floor response spectra (FRS) generated from a reference ground response spectrum (GRS). The reference GRS is chosen as the 5%-damped NUREG/CR-0098 median rock spectrum (1978) anchored to 0.30g PGA, as shown in Figure 4.6, in each of the horizontal directions. The vertical GRS is assumed to be 2/3 of the horizontal GRS over the entire frequency range. It is also assumed that the hazard curve is defined in terms of the 5%-damped average PGA of the two horizontal directions.

Figure 4.7 shows the FRS generated using a direct spectra-to-spectra method based on Duhamel's integral and modal analysis, as described in Section 5.2.3. The FRS $S_n(f_0, \zeta_0)$ on floor-n of a primary structure at oscillator frequency f_0 corresponding to damping ratio ζ_0 is governed by equation (5.2.1). The information required for generating the FRS includes only the modal information of the primary structure and the damping values for

primary structure and secondary system. Since the primary structure is founded on a rock site, a fixed-base analysis is performed. Its basic modal information is given in Figure 4.8. For primary structure, the median damping is estimated to be 5% in all vibration modes, i.e., $\zeta_k = \zeta_s = 5\%$ $(k = 1, \cdots, 4)$. For the block wall, the median damping is 6% and the minus-one-standard-deviation (-1σ) damping is 4%, i.e., $\zeta_0 = \zeta_c = 6\%$ or 4%.

4.2.2 Basic Variables

The median and the associated variabilities of all basic demand and capacity variables are provided in Table 4.1 and 4.2, respectively. These values are based on the recommendations given in report EPRI-TR-103959 (EPRI, 1994) and other supporting reports. Definition and evaluation of these factors are given in Appendix A.5.

4.2.3 Static Capacity Analysis

Static capacity of the block wall can be estimated from its "best-estimate" moment strength and the strength reduction due to P-Δ effect within the inelastic drift limit.

"Best-estimate" Moment Strength

The theoretical ultimate moment strength according to the established principles is calculated first. Conservatism in the calculated strength against the actual strength needs to be considered to obtain the best-estimate moment strength.

Take unit wall width ($b = 1.0$ in) in the analysis. For lightly-reinforced, non-load bearing masonry wall, ultimate moment strength M_{u}' is given by (Cl-3.3.5.4 commentary, MSJC-11)

$$M_{\mathrm{u}}' = \big(A_s \cdot f_y\big)\big(d - \frac{a}{2}\big) = \big(0.0123 \times 46.4\big)\big(3.812 - \frac{0.300}{2}\big) = 2.090 \left(\frac{\text{kip-in}}{\text{in}}\right), \quad (4.2.1a)$$

$$a = \frac{A_s \cdot f_y}{0.80\, f_{\mathrm{m}}'\, b} = \frac{0.0123 \times 46.4}{0.80 \times 2.38 \times 1.0} = 0.300\,\text{in}, \quad (4.2.1b)$$

where A_s=0.0123 in^2/in is the steel area per unit width over wall section, $d = t/2 = 3.812$ in is the depth from the compressive surface to rebar center, and a is the depth of the equivalent compression stress block.

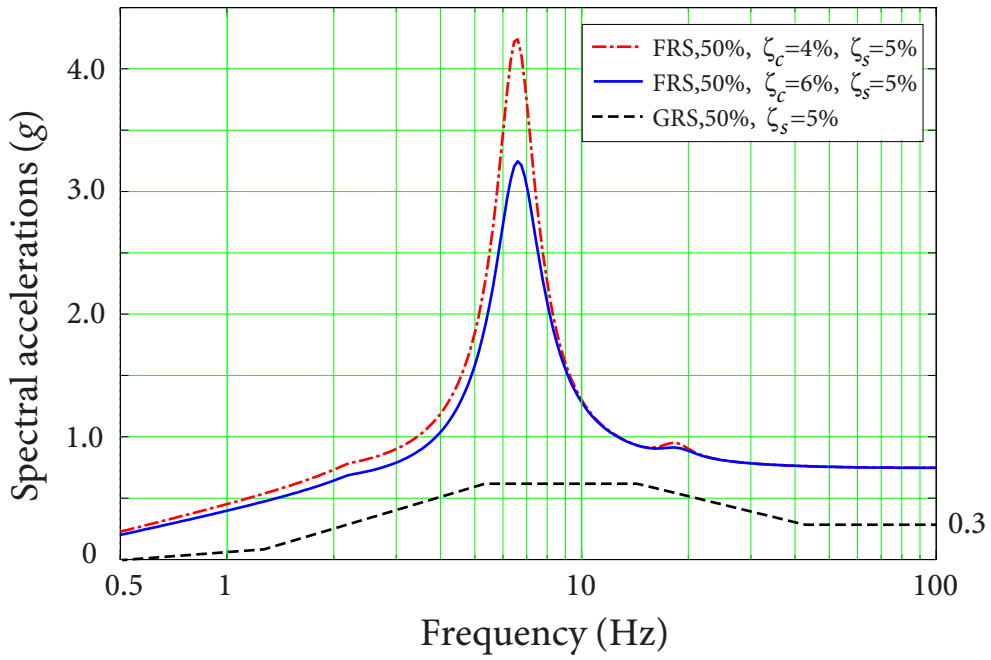

Figure 4.7 Floor response spectra

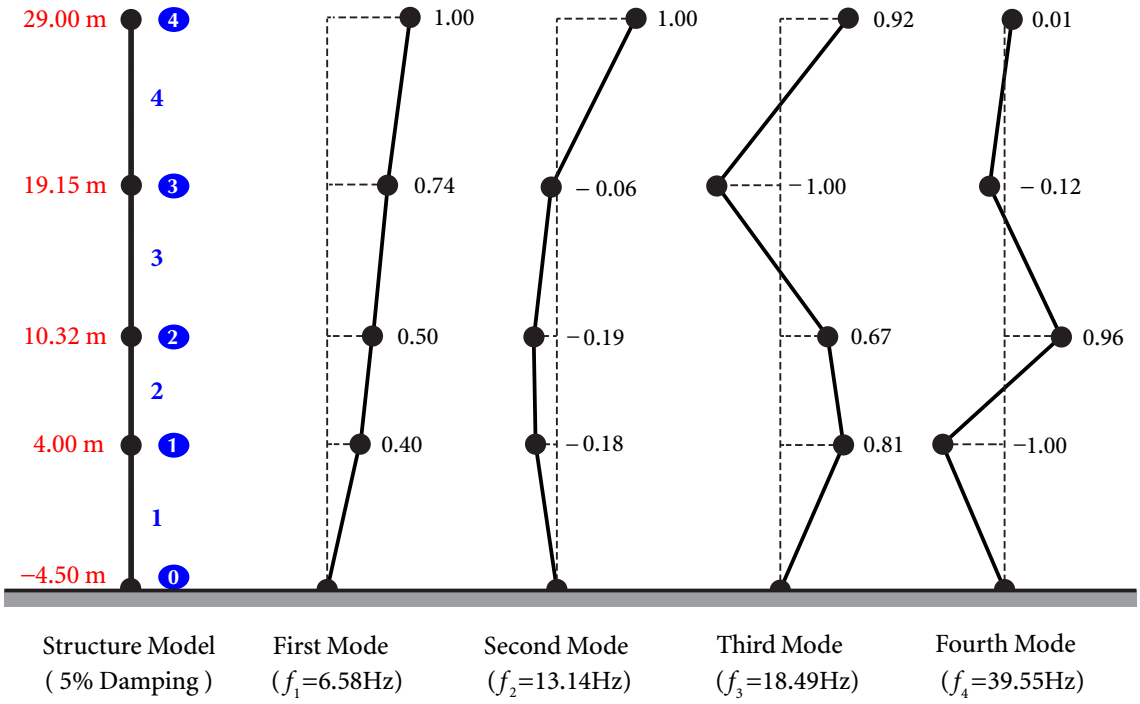

Figure 4.8 Modal information of primary structure

Table 4.1 Basic demand variables for block masonry wall

Factor	Median	β_R	β_U
Ground Motion			
Earthquake response spectrum shape	1.0	0.20	0.215
Horizontal direction peak response	1.0	0.13	–
Vertical component response	1.0	–	–
Ground motion incoherence	0.97	–	0.017
Primary structure			
Damping	0.05 (median)	–	0.03 (-1σ)
Frequency	1.0	–	0.15
Mode Shape	1.0	–	0.10
Torsional Coupling	1.0	–	0.0
Mode Combination	1.0	0.10	–
Block wall			
Quantification Method	1.0	–	0.0
Damping	0.06 (median)	–	0.04 (-1σ)
Frequency	1.0	–	0.10
Mode shape	1.0	–	0.05
Mode combination	1.0	0.05	–

Table 4.2 Basic capacity variables for block masonry wall

Factor	Median	β_U	Nominal
Masonry compressive strength f'_{m}	2376 psi	0.12	1950 psi
Steel yield strength f_y (Grade 40)	46.4 ksi	0.09	40.0 ksi

Model Uncertainty

In fragility analysis, model uncertainty considering possible errors in code equation and construction must be evaluated.

Based on available test results for measured strength of similar masonry wall members reported by Hamid *et al.* (1989), the equation error factor against the MSJC-11 code equations is evaluated to be (details is given in Appendix A.6)

$$\text{Median } F_{\text{eqn}} = 1.034 \quad \text{and} \quad \beta_{\text{eqn}} = 0.105.$$

From careful inspection and some reasonable assumptions, the factor considering error in rebar placement is given by

$$\text{Median } F_{\text{l}} = 1.0 \quad \text{and} \quad \beta_{\text{l}} = 0.071.$$

"Best-estimate" of drift capability

Under seismic loading, if seismic demand on the wall exceeds moment strength, the wall will begin to drift inelastically. Such behaviour is acceptable as long as the drift is within a permissible limit. The drift is defined by the ratio Δ/L of midheight displacement Δ to the wall height L. It will impose a secondary moment on the wall, i.e., P-Δ effect, hence lowers its seismic capacity. In capacity analysis, drift capability must be incorporated.

Only a limited amount of test data exists for defining the permissible drift limit of masonry wall under cyclic loading. Table 4.3 summarizes the cyclic test results on out-of-plane drift capability of seven walls by Hamid *et al.* (1989), in which $\rho = A_s/d$ is the steel ratio, $c = a/0.85$ is the depth from the compressive flanges to the neutral axis, and Δ_u is the ultimate drift corresponding to the onset of significant strength degradation. All walls were simply supported at top and bottom with $L = 117.5$ in.

The ultimate drift ratio Δ_u/L ranges from a low value of 2.7% for wall W7 (with the largest c/d ratio of 0.375) up to 6.8% for W5 (with the smallest c/d ratio of 0.136). Previous studies on concrete beams and slabs showed that Δ_u/L should be inversely proportional to c/d, at least for large L/d ratios. This conclusion also appears to hold for the masonry walls summarized in Table 4.3, for which

$$\left(\frac{\Delta_u}{L}\right)(c/d) \geqslant 0.009. \tag{4.2.2}$$

Table 4.3 Displacement capability data of masonry walls

Wall	d (in)	ρ (%)	$\frac{c}{d}$	$\frac{L}{d}$	Δ_u (in)	$\frac{\Delta_u}{L}$	$\frac{\Delta_u}{L}\cdot\frac{c}{d}$	$\frac{\text{Measured}}{\text{Predicted}^\dagger}$
W2	2.81	0.455	0.201	41.8	5.65	0.0481	0.0097	1.07
W3	2.81	0.455	0.215	41.8	4.80	0.0409	0.0088	0.98
W5	2.81	0.291	0.136	41.8	7.94	0.0676	0.0092	1.02
W7	2.81	0.892	0.375	41.8	3.16	0.0269	0.0101	1.12
W11	2.81	0.455	0.231	41.8	6.18	0.0526	0.0122	1.35
W13	2.26	0.362	0.227	52.0	8.35	0.0711	0.0161	1.79
W14	3.82	0.483	0.217	30.8	4.80	0.0409	0.0089	0.99

† The predicted value is obtained using equation (4.2.5).

It is suggested that the "best-estimate" of out-of-plane drift capability can be approximated by

$$\left(\frac{\Delta_u}{L}\right) = \frac{0.009}{(c/d)} F_{C(L/d)} \leqslant 0.07, \quad F_{C(L/d)} = \frac{(L/d)}{30} \leqslant 1.0, \tag{4.2.3}$$

where $F_{C(L/d)}$ is a correction factor for L/d ratio less than 30.

For the block wall problem, $c = \frac{a}{0.85} = \frac{A_s f_y}{0.85^2 \times f'_m} = \frac{0.0123 \times 46.4}{0.85^2 \times 2.38} = 0.333$, $\frac{c}{d} = \frac{0.333}{3.812} = 0.087$, $\frac{L}{d} = \frac{132}{3.812} = 34.6 \geqslant 30$, $F_{C(L/d)} = 1.0$, and $\left(\frac{\Delta_u}{L}\right) = \frac{0.009}{0.087} \times 1.0 = 0.103 \geqslant 0.07$. Hence, the drift capability is finally given by

$$\left(\frac{\Delta_u}{L}\right) = 0.07, \quad \text{or} \quad \Delta_u = 9.24 \text{ in.} \tag{4.2.4}$$

Static S_a Capacity Considering Permissible Drift

The total moment acting on the wall is due to both seismic loading and the drift. Assume that the wall weight tributary to the midheight is the upper half weight, acting approximately on the section corresponding to 2/3 midheight displacement Δ. The midheight moment M_o on the wall can be determined using statics. Figure 4.9 shows the free body diagrams for determining M_o, where

First, the horizontal force H_T at top T is found by summing moments about B

$$+\curvearrowleft \sum M_B = 0; \quad H_T \cdot L - \frac{1}{2} w_S L^2 - \frac{P_w}{2} \times \frac{2\Delta}{3} \times 2 = 0. \implies H_T = \frac{1}{2} w_S L + \frac{2}{3L} P_w \Delta.$$

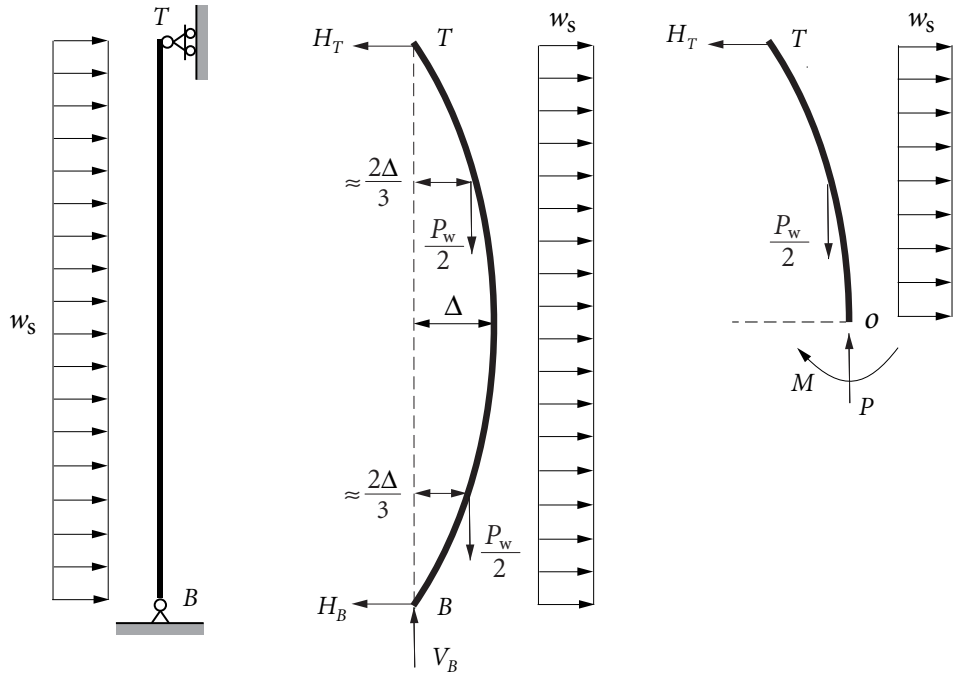

Figure 4.9 Block wall free body diagrams

w_S = Seismic loading intensity acting on the wall per unit width ($= W/g \times S_a$),

H_T = Horizontal support reaction at top T,

H_B , V_B = Support reactions at bottom B ,

P_w = Wall weight per unit width($= W \times L$),

Δ = Midheight displacement of the wall under seismic loading.

Next, M_o is solved by summing moments about midheight o and substituting H_T

$$+\curvearrowleft \sum M_o = 0; \quad H_T \cdot \frac{L}{2} + \frac{P_w}{2} \times \frac{\Delta}{3} - \frac{1}{2} w_S \left(\frac{L}{2}\right)^2 - M_o = 0.$$

$$\Longrightarrow \; M_o = H_T \cdot \frac{L}{2} + \frac{P_w \Delta}{6} - \frac{1}{8} w_S L^2 = \frac{1}{8} w_S L^2 + \frac{1}{2} P_w \Delta \, .$$

Substituting $P_w = W \times L$ and $w_S = (W/g) \times S_a$ into the above equation gives

$$M_o = \frac{W L^2}{8\, g} \cdot S_a + \frac{W L}{2} \cdot \Delta \, . \tag{4.2.5}$$

According to the strength design method, the moment resultant M_o shall not exceed the moment strength M_u. By equating the maximum moment M_o to its "best-estimate"

ultimate moment strength M_u, static capacity of the block wall $S_{a,C}$ can be obtained as

$$S_{a,C} = \left\{ \frac{8\,M_u}{W\,L^2} - 4\left(\frac{\Delta}{L}\right) \right\} g = \left\{ \frac{8 \times (2.160 \times 10^3)}{83.5 \times 11^2} - 4\left(\frac{\Delta}{L}\right) \right\} g$$
$$= \left(1.71 - 4\,\frac{\Delta}{L}\right) g\,. \tag{4.2.6}$$

Note that $S_{a,C}$ decreases from 1.71 g to 1.43 g as drift $\frac{\Delta}{L}$ increases from 0.0 to limit 0.07.

4.2.4 Demand Analysis

Demand analysis of the block wall mainly involves the determination of vibration frequency. Prior to reaching the code-specified nominal moment strength, the wall behaves approximately as an elastic structure with an elastic frequency. As the drift goes inelastic, the wall exhibits nonlinear behavior with a lowered effective frequency.

Elastic Demand

The elastic frequency f of the block masonry wall should be estimated based on the effective moment of inertia I_e and the Elasticity modulus of masonry E_m, using (EPRI, 1991a)

$$f = \frac{1}{2\,\pi}\sqrt{\frac{g}{\Delta}} = \frac{1}{2\,\pi}\sqrt{\frac{384\,(E_m\,I_e)\,g}{5\,W\,L^4}}\,, \tag{4.2.7}$$

where $\Delta = \frac{5\,W\,L^4}{384\,E_m\,I_e}$ is the static deflection at the mid-span of a simply-supported uniform beam member with horizontal span L, Elasticity modulus E_m, and effective moment of inertia I_e, subjected to uniformly distributed load with intensity W (assuming $w_S = W$).

The effective moment of inertia I_e, which recognizes the reduction in the net moment of inertia I_n over the wall cross section due to cracking, is given by

$$I_e = I_n\left(\frac{M_{cr}}{M_a}\right)^3 + I_{cr}\left[1 - \left(\frac{M_{cr}}{M_a}\right)^3\right] \leqslant I_n\,, \qquad \text{(Eqn. 1-1, MSJC-11)}$$

where M_a is the applied out-of-plane moment, M_{cr} and I_{cr} are the cracking moment and moment of inertia of the cracked cross section, respectively (I_{cr} is conservatively assumed to be applied over the entire wall height L). Hence, to determine elastic frequency f, relevant quantities M_{cr}, I_n, I_{cr}, and M_a need to be obtained first.

Cracking moment strength: M_{cr} is obtained using the uncracked section analysis, where the use of gross moment of inertia I_g is usually permitted. For wall section per unit width ($b = 1$ in) with thickness $t = 7.625$ in, the gross moment of inertia I_g, section modulus S, and the cracking moment strength M_{cr} are given by, respectively,

$$I_g = b\,t^3/12 = 36.94\,\frac{\text{in}^4}{\text{in}}, \quad S = I_g/d = 9.69\,\frac{\text{in}^3}{\text{in}}, \quad \text{and } M_{cr} = S \times f_t = 1.58\frac{\text{kip-in}}{\text{in}},$$

where modulus of rupture $f_t = 163$ ksi is given by the Table method using MSJC-11 code.

Net moment of inertia: I_n is a physical sectional property and can be found in design tables (NCMA, 2007). For the fully-grouted 8 in masonry unit with grout spacing of 16 in,

$$I_n = 378.6\,\frac{\text{in}^4}{\text{ft}} \quad \text{or} \quad 31.55\,\frac{\text{in}^4}{\text{in}}, \qquad \text{(Table3, TEK 14-01B, NCMA)}$$

which is about 85% of $I_g = 36.94\,\text{in}^4/\text{in}$ of the gross section.

Cracked section moment of inertia: I_{cr} is evaluated using cracked section analysis, resorting to the concept of transformed section (assuming that flexural tension is resisted by reinforcement alone; the flexural tensile strength of masonry is neglected). The MSJC-11 code provides a set of equations for calculating I_{cr}, which showed good agreements with test results of similar masonry walls. The modulus ratio n of steel to masonry, the depth c of compressive fiber over wall section, and I_{cr} are given by, respectively,

$$\begin{aligned}
n &= E_s/E_m = 29.0/1.755 = 16.52, \\
c &= \frac{A_s\,f_y}{0.64\,f'_{\text{m}}\,b} = \frac{0.0123 \times 46.4}{0.64 \times 2.38 \times 1} = 0.394\,\text{in}, && \text{(Eqn. 3-32, MSJC-11)} \\
I_{cr} &= n\,A_s(d-c)^2 + \frac{b\,c^3}{3} && \text{(Eqn. 3-31, MSJC-11)} \\
&= 16.52 \times 0.0123 \times (3.812 - 0.394)^2 + \frac{1 \times 0.394^3}{3} = 2.395\left(\frac{\text{in}^4}{\text{in}}\right).
\end{aligned}$$

Applied moment: M_a is assumed to be equal to the nominal moment strength, given by

$$M_a = \big(A_s f_y\big)\big(d - \frac{a}{2}\big) = \big(0.0123 \times 40\big)\big(3.812 - \frac{0.315}{2}\big) = 1.80\left(\frac{\text{kip-in}}{\text{in}}\right),$$

$$\text{where } \; a = \frac{A_s f_y}{0.80\,f'_{\text{m}}\,b} = \frac{0.0123 \times 40}{0.80 \times 1.95 \times 1} = 0.315\,\text{in}.$$

Having obtained the relevant quantities, the effective moment of inertia I_e is given by

$$I_e = I_n\Big(\frac{M_{cr}}{M_a}\Big)^3 + I_{cr}\Big[1 - \Big(\frac{M_{cr}}{M_a}\Big)^3\Big] \qquad \text{(Eqn. 1-1, MSJC-11)}$$
$$= 31.55\Big(\frac{1.58}{1.80}\Big)^3 + 2.13\Big[1 - \Big(\frac{1.58}{1.80}\Big)^3\Big] = 22.15 \leqslant 31.55\,\frac{\text{in}^4}{\text{in}}.$$

The elastic frequency f is then determined to be

$$f = \frac{1}{2\,\pi}\sqrt{\frac{384\,(E_m\,I_e)\,g}{5WL^4}} = \frac{1}{2\,\pi}\sqrt{\frac{384\,(1.755\times10^6\times22.15)\,386}{(5\times83.5)\,(11^4)\,12^2}} = 12.9\,\text{Hz}. \qquad (4.2.8)$$

☞ *In determining the elastic frequency (at a low stress level), the combined use of code specified f_t (i.e., for obtaining M_{cr}) and the best-estimate of M_u (i.e., use M_u as M_a) is not recommended, since it will give a very conservative I_e that lowers the elastic frequency.*

Finally, median elastic demand $S_{a,D}$ is obtained by using median FRS S_a^F given in Figure 4.7 (in solid line), multiplied by a factor of 0.97 that considers the incoherence reduction (see Table 4.1)

$$S_{a,D} = S_a^F(12.9\,\text{Hz},\ \zeta_c = 6\%)\times0.97 = 0.95\,g. \qquad (4.2.9)$$

Note that FRS used in fragility analysis can be raw, without frequency shifting or broadening.

Effective Nonlinear demand

Nonlinear demand on the wall drifting in the inelastic range changes due to the following two phenomena: (1) lowered effective frequency, (2) increased effective damping.

One approach to determine the nonlinear demand is the "*equivalent linear elastic procedure*" (EPRI, 1994), which approximates the average reduced stiffness (or frequency) and average increased damping occurred during the nonlinear response cycles by using the secant stiffness as the minimum effective stiffness. Using this procedure, the nonlinear demand can be directly obtained using the elastic response spectrum.

The secant frequency f_s, corresponding to inelastic drift Δ and the associated static capacity $S_{a,C}$, is given by

$$f_s = \frac{1}{2\,\pi}\sqrt{\frac{1.5\,S_{a,C}}{\Delta}}\,. \qquad \text{(Eqn. R-23, EPRI-NP-6041)}$$

For the block masonry wall, deformed up to ultimate drift $\Delta_u = 9.24$ in, with static capacity $S_{a,C} = 1.43\,g$, f_s is determined to be

$$f_s = \frac{1}{2\pi}\sqrt{\frac{1.5\,S_{a,C}}{\Delta_u}} = \frac{1}{2\pi}\sqrt{\frac{1.5\,(1.43\times 386)}{9.24}} = 1.51 \text{ Hz}, \tag{4.2.10}$$

which is much smaller than the elastic frequency $f = 12.9$ Hz.

Nonlinear time history analyses of similar masonry walls, using severely pinched hysteretic loops, shows that seismic demand could be accurately approximated by treating them as pseudo-elastic walls with effective frequency $f_e = f_s$ and effective damping $\zeta_e = 6\%$ (EPRI, 1991a). Hence, the effective nonlinear demand (considering incoherence reduction) is given by

$$S_{a,D} = S_a^F(f_s\,, \zeta_e = 6\%) \times 0.97, \tag{4.2.11}$$

which can be obtained by reading the FRS shown in Figure 4.7.

4.2.5 Median Seismic Capacity

The strength factor F_S, representing the Capacity/Demand ratio, is given by

$$F_S = \frac{S_{a,C}}{S_{a,D}}\,.$$

Since both static capacity $S_{a,C}$ and seismic demand $S_{a,D}$ are functions of wall drift Δ, for any problem in general, a maximum F_S should be found within the limits of elastic drift (at $f = 12.9$ Hz) and the maximum inelastic drift (at $f_s = 1.51$ Hz). Table 4.4 provides example calculations for some selected drifts Δ/L, showing that

(a) As wall drift increases, seismic demand $S_{a,D}$ first increases rapidly then decreases first rapidly then slowly, whereas static capacity $S_{a,C}$ decreases slowly.

(b) The minimum F_S is found to be 0.54, when seismic demand is maximum.

(c) The maximum F_S is found to be 2.79, corresponding to $\frac{\Delta}{L} = 7\%$, which is the maximum credit that can be taken within the drift limit.

☞ *The maximum F_S is usually found at the frequency boundaries. However, for the major inelastic drifts ranging from 1% to 7%, unless the demand is decreasing faster than static capacity is decreasing, no more credit can be taken from allowing additional inelastic drift.*

Table 4.4 Strength factor as a function of wall drift ratio

Drift ratio	Δ	Frequency	Demand	Capacity	F_S
(Δ/L)	(in)	f or f_s (Hz)	$S_{a,D}\,(g)$	$S_{a,C}\,(g)$	
Elastic	–	12.9	0.95	1.71	1.79
0.43%	0.53	6.61	3.13	1.69	0.54
1%	1.32	4.31	1.12	1.67	1.49
3%	3.96	2.43	0.69	1.59	2.31
5%	6.60	1.83	0.58	1.51	2.59
7%	9.24	1.51	0.51	1.43	2.79

Noting that $F_\mu = 1.0$, the median seismic capacity of the block wall is finally given by

$$A_m = F_S \cdot F_\mu \cdot \text{PGA} = 2.79 \times 1.0 \times 0.3 = 0.84\,g \text{ pga}.$$

4.2.6 Logarithmic Standard Deviations

The approximate second-moment procedure, presented in Subsection 4.1.5, is used to quantify the effect of uncertainty in each single variable on the uncertainty in A_m. Table 4.5 gives the results and some special notes are given below.

The input β_U value for structure damping is obtained from the 5%-damped (median) and 3%-damped (-1σ) GRS

$$\beta_U = \frac{1}{1}\ln\left(\frac{S_a(6.6\text{Hz}, \zeta = 3\%)}{S_a(6.6\text{Hz}, \zeta = 5\%)}\right) = \frac{1}{1}\ln\left(\frac{2.46 \times 0.3g}{2.12 \times 0.3g}\right) = 0.15.$$

where the S_a values are from the reference GRS (NUREG/CR-0098 median rock spectrum), where 2.12 and 2.46 are, respectively, the amplifications factors for the 5%- and 3%-damped median spectral shapes normalized to 1.0 g PGA.

The input β_U value for structure frequency is essentially zero since the peak plateau of GRS is flat in the vicinity of the fundamental frequency 6.6 Hz of the structure.

The input β_U value for equipment damping is obtained by using the 6%-damped (median) and 4%-damped (-1σ) FRS of floor-3 shown in Figure 4.6. By evaluating the slopes on the two FRS in the $\pm 1\sigma$ secant frequency ($0.9 f_s = 1.36$ Hz, $1.1 f_s = 1.66$ Hz) of the block

Table 4.5 Logarithmic standard deviations for demand and capacity parameters

Variable	Parameter at $1\sigma^{\dagger}$	F_S	β_R	β_U
Base Case		2.79		
Ground Motion				
Earthquake response spectrum shape	$S_{a,D}\,e^{0.20}$ $S_{a,D}\,e^{0.215}$	2.29	0.20	0.215
Horizontal direction peak response	$S_{a,D}\,e^{0.13}$	2.45	0.13	—
Ground motion incoherence	$S_{a,D}\,e^{0.017}$	2.75	—	0.017
Primary structure				
Damping	$S_{a,D}\,e^{0.15}$	2.40	—	0.15
Frequency	$S_{a,D}\,e^{0.0}$	2.79	—	0.0
Mode Shape	$S_{a,D}\,e^{0.10}$	2.53	—	0.10
Mode Combination	$S_{a,D}\,e^{0.10}$	2.53	0.10	—
Block wall demand				
Damping	$S_{a,D}\,e^{0.13}$	2.45	—	0.13
Frequency	$S_{a,D}\,e^{0.12}$	2.47	—	0.12
Mode shape	$S_{a,D}\,e^{0.05}$	2.66	—	0.05
Mode combination	$S_{a,D}\,e^{0.05}$	2.66	0.05	—
Block wall capacity				
Equation error F_{eqn}	$F_{\text{eqn}}\,e^{-0.10}$	2.57	—	0.08
Rebar error F_{l}	$F_{\text{l}}\,e^{-0.07}$	2.64	—	0.06
Steel strength f_y	$f_y\,e^{-0.09}$	2.61	0.07	—
Masonry strength f'_{m}	$f'_{\text{m}}\,e^{-0.12}$	2.78	0.004	—
		Combined	0.273	0.350

† $+1\sigma$ for demand variables; -1σ for capacity variables.

wall in the semi-log scale, one has

$$k_{6\%} = \frac{0.565 - 0.494}{\ln 1.66 - \ln 1.36} = 0.36, \quad k_{4\%} = \frac{0.642 - 0.561}{\ln 1.66 - \ln 1.36} = 0.41.$$

Since the two slopes $k_{6\%}$ and $k_{6\%}$ for the 6%- and 4%-damped FRS are fairly close to each other in the vicinity of $f_s = 1.51$ Hz, then the β_U value for damping is simply given by

$$\beta_U = \frac{1}{1} \ln\left(\frac{S_a^F(1.51\text{Hz}, 4\%)}{S_a^F(1.51\text{Hz}, 6\%)}\right) = \frac{1}{1} \ln\left(\frac{0.602\,g}{0.530\,g}\right) = 0.128.$$

Otherwise, if the 6%- and 4%-damped FRS were not quite parallel to each other, it is more accurate to find an average value where the β_U values at each frequency in the vicinity of the secant frequency are weighted by the lognormal density function of the frequency

$$\bar{\beta}_U = \int_0^\infty p(f_s)\, \frac{1}{1} \ln\left(\frac{S_a^F(f_s, 4\%)}{S_a^F(f_s, 6\%)}\right) \mathrm{d}f_s\,,$$

where $p(f_s)$ = lognormal density function of secant frequency, LN(1.51 Hz, 0.10).

The $\beta_U = 0.12$ for evaluating the effect of component frequency is obtained from the FRS amplitudes close to the secant frequency. Since the block wall is located on the primary structure, a combined β_U (0.18) accounting for uncertainties of primary structure frequency (0.15) and block wall frequency (0.10) is used. Hence,

$$\beta_U = \frac{1}{1} \ln\left(\frac{S_a^F(1.51 \times \mathrm{e}^{0.18}\text{Hz}, 4\%)}{S_a^F(1.51\text{Hz}, 6\%)}\right) = \frac{1}{1} \ln\left(\frac{0.598\,g}{0.530\,g}\right) = 0.12.$$

For the capacity variables, the static capacity equations derived in Section 4.2.3 are summarized below

$$S_{a,C} = \left\{\frac{8\,M_u}{W\,L^2} - 4\left(\frac{\Delta}{L}\right)\right\} g\,,$$

$$M_u = F_{\text{eqn}} \cdot F_{\text{l}} \cdot \left(A_s f_y\right)\left(d - \frac{a}{2}\right), \quad a = \frac{A_s f_y}{0.80\, f'_{\text{m}}\, b}\,.$$

Combining these equations gives

$$S_{a,C} = \left\{\frac{8\,M_u}{W\,L^2} - 4\left(\frac{\Delta}{L}\right)\right\} g = \left\{\frac{8\,F_{\text{eqn}} \cdot F_{\text{l}} \cdot \left(A_s f_y\right)\left(d - \frac{A_s f_y}{1.60\, f'_{\text{m}}\, b}\right)}{W\,L^2} - 4\left(\frac{\Delta}{L}\right)\right\} g\,.$$

It shows that static capacity $S_{a,C}$ is a nonlinear function of lognormal random variables F_{eqn}, F_{l}, f_y, and f'_{m}. Note that $\frac{\Delta}{L} = 0.07$, where the maximum F_S is obtained, is considered as a constraint on defining $S_{a,C}$, thus its uncertainty is not to be propagated. In addition, due to the nonlinearity and the constraint term in the $S_{a,C}$ equation, uncertainties in F_{eqn}, F_{l}, f_y,

and f'_{m} will propagate very differently. For example, through propagation, the uncertainty $\beta_U = 0.12$ for f'_{m} contributes only slightly (0.004) to the uncertainty in A_m.

Finally, fragility parameters of the block masonry wall are given by

$$A_m = 0.84\,g \text{ PGA}, \quad \beta_R = 0.27, \quad \beta_U = 0.35 \quad (\beta_C = 0.444).$$

Using equations (4.1.3) and (4.1.4), fragility curves for confidence levels $Q = 5\%$, 50%, and 95%, and for the composite variability are developed, as shown in Figure 4.10.

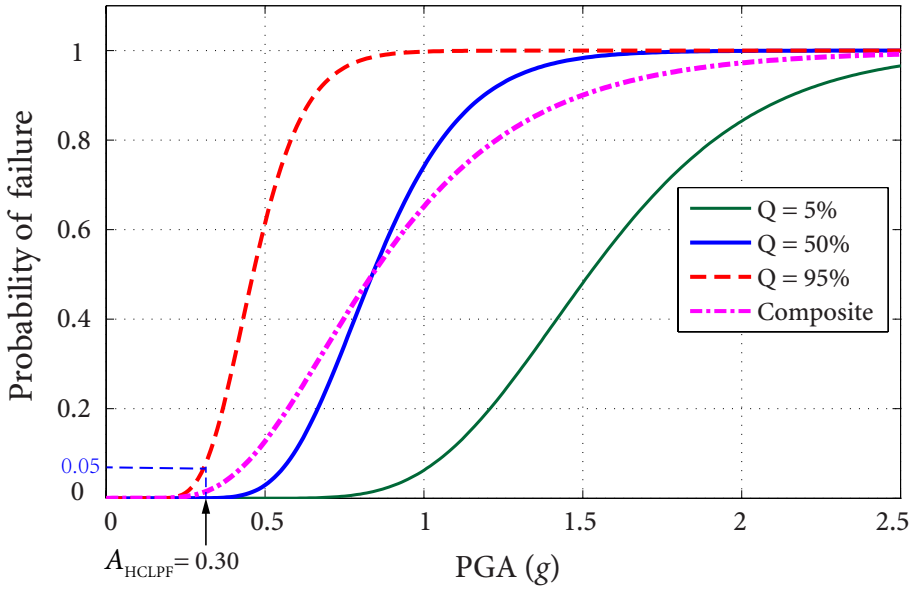

Figure 4.10 Fragility curves for the block wall

The HCLPF capacity A_{HCLPF}, corresponding to the 5% probability of failure with 95% confidence on the fragility curve, is determined using equation (4.1.13)

$$A_{\mathrm{HCLPF}} = A_{5\%}^{95\%} = A_m\, \mathrm{e}^{-1.645(\beta_R+\beta_U)} = 0.84\, \mathrm{e}^{-1.645(0.27+0.35)} = 0.30 \text{ PGA}. \qquad (4.2.12)$$

4.2.7 CDFM-Calculated Capacity

For comparison, the CDFM capacity given by the CDFM method is also evaluated. In the CDFM method, specific degree of conservatism is intensionally introduced in steps where significant parameter uncertainty exists, e.g., using conservative earthquake response spectral shape for demand analysis and using nominal strength and strength reduction factor for static capacity analysis. Less significant factors are neglected.

(1) For seismic input, the reference GRS shape defined at the 84% non-exceedance probability (NEP) level should be used instead of the median shape. This is the factor contributing the largest conservatism in demand estimate. Additional conservatism from less important demand factors is not needed; median-centered response is targeted by using median-centered damping and structural modelling parameters.

(2) Material strengths should be defined at approximately the 95% exceedance probability (EP) from test data. Otherwise, code-specified minimum strengths should be used. For brittle failures, material strengths should be defined at about the 98% EP.

(3) Strength capacity equations are usually defined at about the 84% EP, by using a strength reduction factor ϕ. For brittle failures, additional conservatism should be provided, aiming at about the 98% EP.

(4) The inelastic energy absorption factor considers the conservatism due to system ductility. For ductile failures and linear analysis, use 80% of computed seismic stress in capacity evaluation or perform nonlinear analysis and go to the 95% exceedance ductility levels.

The combination of the conservative seismic input, median centered response, and a conservative strength prediction is supposed to give a HCLPF.

Seismic Input

The reference GRS is chosen as the 5%-damped NUREG/CR-0098 84.1% amplified shape anchored to 0.30 g PGA (see Figure 4.6). The horizontal FRS corresponding to the median damping $\zeta_c = 6\%$ of block wall is shown in Figure 4.11.

Static Capacity Analysis

The nominal material strengths, given in Table 4.2, equation factor ϕ_{CDFM}, and the CDFM drift limit are applied to determine the CDFM static S_a capacity.

CDFM Moment Strength: using nominal strengths (about 95% EP), the depth of compressive block and the nominal moment strength are given by

$$a = \frac{A_s f_y}{0.80\, f'_{\text{m}}\, b} = \frac{0.0123 \times 40}{0.80 \times 1.95 \times 1.0} = 0.315\,\text{in}, \qquad \text{(C3.3.5.4, MSJC-11)}$$

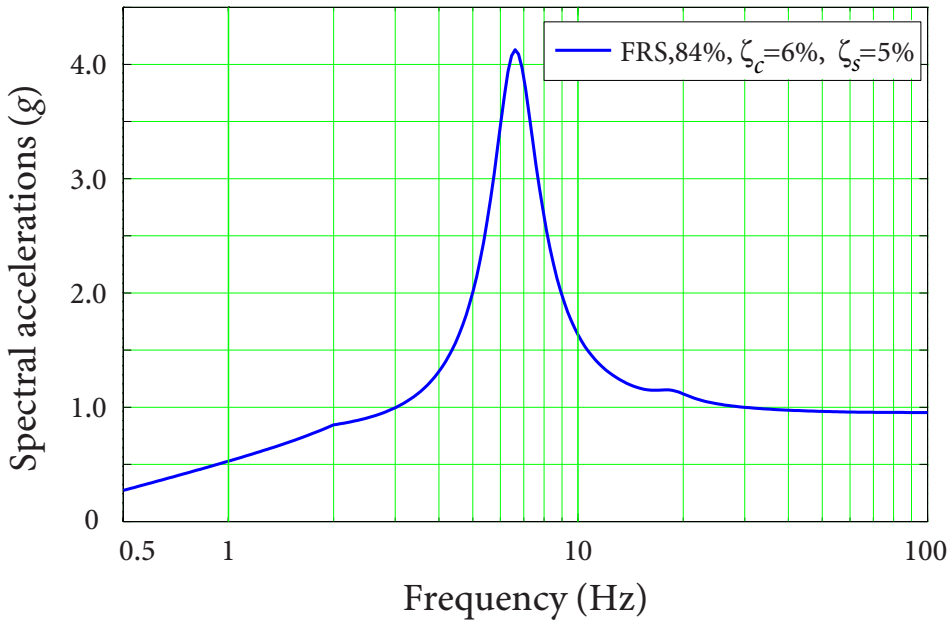

Figure 4.11 Floor response spectrum for CDFM capacity evaluation

$$M_u = \left(P_u/\phi + A_s f_y\right)\left(d - \frac{a}{2}\right) \qquad \text{(C3.3.5.4, MSJC-11)}$$
$$= \left(0/0.9 + 0.0123 \times 40\right)\left(3.812 - \frac{0.315}{2}\right) = 1.798\left(\frac{\text{kip-in}}{\text{in}}\right),$$

where $P_u = 0$ corresponds to non-loading bearing condition for the block wall.

A strength reduction factor ϕ_{CDFM}, considering errors in equation and rebar placement, must be applied. As discussed in Section 4.2.3, the equation factor is defined by: $F_{\text{eqn}} = 1.145 \times 0.90 = 1.031$, $\beta_{\text{eqn}} = 0.105$. For the rebar placement factor, $\beta_{\text{l}} = 0.07$. Hence, the strength reduction factor ϕ_{CDFM}, defined at about the 84% EP, is given by

$$\phi_{\text{CDFM}} = F_{\text{eqn}}\, \text{e}^{-\sqrt{\beta_{\text{eqn}}^2 + \beta_{\text{l}}^2}} = 1.031 \times \text{e}^{-\sqrt{0.105^2 + 0.07^2}} = 0.908.$$

The CDFM moment capacity is then given by

$$M_{\text{CDFM}} = \phi_{\text{CDFM}} \cdot M_u = 0.908 \times 1.798 = 1.633 \frac{\text{kip-in}}{\text{in}}. \qquad (4.2.13)$$

CDFM Drift capability: the CDFM permissible drift limit should be set at about the 95% confidence limit. Due to the large uncertainty existed for the out-of-plane drift capability of masonry walls, a rather large factor of 1.75 is judged to be appropriate for obtaining the

CDFM permissible drift limit from the "best-estimate" value

$$\left(\frac{\Delta_u}{L}\right)_{\text{CDFM}} = \frac{0.009/1.75}{(c/d)} F_{C(L/d)} \leqslant \frac{0.07}{1.75} = 0.04.$$

For the example problem, $(c/d) = 0.35/3.812 = 0.092$, $(L/d) = 132/3.812 = 34.6 \geqslant 30$, $F_{C(L/d)} = 1.0$. Hence,

$$\left(\frac{\Delta_u}{L}\right)_{\text{CDFM}} = 0.04, \quad \text{or} \quad \Delta_u = 5.28 \text{ in.}$$

Inferred from the 95% confidence level and a factor of 1.75, the underlying variability about the drift limit is $\beta_{(\Delta_u/L)} = \frac{1}{1.645} \ln\left(\frac{1.75}{1}\right) = 0.34$.

Static S_a Capacity Considering Permissible Drift: By equating the CDFM moment strength M_{CDFM} given by equation (4.2.13) to the maximum moment resultant M_o given by equation (4.2.5), static $S_{a,C}$ capacity is obtained as

$$\begin{aligned} S_{a,C} &= \left\{\frac{8\,M_u}{W\,L^2} - 4\left(\frac{\Delta}{L}\right)\right\} g = \left\{\frac{8 \times (1.633 \times 10^3)}{83.5 \times 11^2} - 4\left(\frac{\Delta}{L}\right)\right\} g \\ &= \left(1.29 - 4\,\frac{\Delta}{L}\right) g. \end{aligned}$$

Static $S_{a,C}$ capacity decreases from 1.29 g to 1.13 g as drift $\frac{\Delta}{L}$ goes from 0.0 to limit 0.04.

Demand Analysis

Elastic Demand: The wall behaves approximately elastically prior to reaching the CDFM moment strength. The elastic frequency f is estimated similarly to that in the FA method.

Three of four relevant quantities for evaluating f, including cracking moment strength $M_{cr} = 1.58 \frac{\text{kip-in}}{\text{in}}$, net moment of inertia $I_n = 31.55\ \frac{\text{in}^4}{\text{in}}$, and cracked section moment of inertia $I_{cr} = 2.395\ \frac{\text{in}^4}{\text{in}}$ are the same as those obtained in FA method in Subsection 4.2.4.

Only the applied moment M_a is assumed to be equal to the CDFM moment strength $M_{\text{CDFM}} = 1.633 \frac{\text{kip-in}}{\text{in}}$, which results in a larger effective moment of inertia I_e in CDFM

$$\begin{aligned} I_e &= I_n\left(\frac{M_{cr}}{M_a}\right)^3 + I_{cr}\left[1 - \left(\frac{M_{cr}}{M_a}\right)^3\right] \qquad \text{(Eqn. 1-1, MSJC-11)} \\ &= 31.55\left(\frac{1.58}{1.63}\right)^3 + 2.40\left[1 - \left(\frac{1.58}{1.63}\right)^3\right] = 28.67 \leqslant 31.55\ \frac{\text{in}^4}{\text{in}}, \end{aligned}$$

Hence, the elastic frequency f is determined to be

$$f = \frac{1}{2\pi}\sqrt{\frac{384\,(E_m\,I_e)\,g}{5WL^4}} = \frac{1}{2\pi}\sqrt{\frac{384\,(1.755\times10^6\times28.67)\,386}{(5\times83.5)\,(11^4)\,12^2}} = 14.7\text{ Hz}.$$

Effective Nonlinear demand: When seismic demand exceeds the CDFM moment capacity, the wall begins to drift inelastically with a lowered frequency and an increased damping. Using the equivalent linear elastic procedure (EPRI, 1994), the secant frequency f_s of the wall in the extreme deformed shape is given by

$$f_s = \frac{1}{2\pi}\sqrt{\frac{1.5\,S_{a,C}}{\Delta_u}} = \frac{1}{2\pi}\sqrt{\frac{1.5\,(1.13\times386)}{5.28}} = 1.77\text{ Hz}.$$

The effective nonlinear demand of block masonry wall can be determined using the elastic FRS S_a^F, at effective frequency $f_e = f_s$ with effective damping $\zeta_e = 6\%$

$$S_{a,D} = S_a^F(f_s,\ \zeta_e = 6\%).$$

Strength Factor and the CDFM Capacity

A maximum strength factor $F_S = S_{a,C}/S_{a,D}$ should be found within elastic response (at $f = 14.7$ Hz) and inelastic response (at $f_s = 1.77$ Hz). To considers the effect of frequency uncertainty of structure on wall seismic demand, $\pm15\%$ frequency shifting on the reference FRS is applied to introduce additional conservatism. The principle is to increase seismic demand, leading to a smaller strength factor. The shifted frequencies, seismic demand, and strength factors are given in Table 4.6.

The maximum F_S is found to be 1.33 when drift limit $\frac{\Delta_u}{L} = 4\%$ is realized. Noting that $F_\mu = 1.0$, the CDFM capacity of the block masonry wall is then given by

$$C_{\text{CDFM}} = F_S \cdot F_\mu \cdot \text{PGA} = 1.33\times1.0\times0.3 = 0.40g\text{ PGA}.$$

4.2.8 Comparison of Results

1. Comparison of the HCLPF capacity

For the example block masonry wall, the FA method gives a HCLPF capacity $A_{\text{HCLPF}} = 0.30\,g$ PGA. While the CDFM method provides a CDFM capacity $C_{\text{CDFM}} = 0.40\,g$, which is

Table 4.6 Strength factor as a function of drift level for block wall in CDFM method

Drift ratio (Δ/L)	u (in)	Frequency (Hz)		Demand	Capacity	F_S
		f or f_s	±15% range	$S_{a,D}(g)$	$S_{a,C}(g)$	
Elastic	—	14.7	12.47+	1.29	1.29	1.00
0.33%	0.43	6.61	6.61	4.13	1.28	0.31
0.5%	0.66	5.32	6.12–	3.66	1.27	0.35
1%	1.32	3.73	4.29–	1.46	1.25	0.86
2%	2.64	2.60	2.99–	0.99	1.21	1.22
3%	3.96	2.08	2.40–	0.89	1.17	1.31
4%	5.28	1.77	2.04–	0.85	1.13	1.33

about 35% larger than the HCLPF; $C_{\text{CDFM}} \approx A_{\text{HCLPF}}$ does not always hold. This is mainly due to the large uncertainty ($\beta_C = 0.444$) existed in estimating median seismic capacity A_m, as captured using the FA method.

1. The FA method is a more accurate method in evaluating seismic capacity, as it takes into account of variability in all important factors affecting seismic capacity in a probabilistically rigorous manner.
2. The CDFM method is an approximate method, which considers only some of the most significant factors contributing to variability in seismic capacity. Hence, it should not be used for determining the HCLPF capacity when large parameter variability exists (e.g., $\beta_C > 0.40$), since it is likely to provide overly optimistic results.

2. Comparison of Seismic Risk

In case of a formal seismic probabilistic risk analysis (SPRA), the FA method can provide more accurate results. Considering a site of Diablo Canyon Nuclear Power Plant in California as an example. Convolution of hazard curve for PGA shown in Figure 4.12 (USNRC, 2012a) and the composite fragility curve shown in Figure 4.10, using equation (4.2.14), leads to seismic risk of block wall failure at this site as $p_F = 3.44 \times 10^{-4}$ per year.

$$P_F = -\int_0^\infty P_F(a) \cdot \frac{\mathrm{d}H(a)}{\mathrm{d}a}\,\mathrm{d}a, \tag{4.2.14}$$

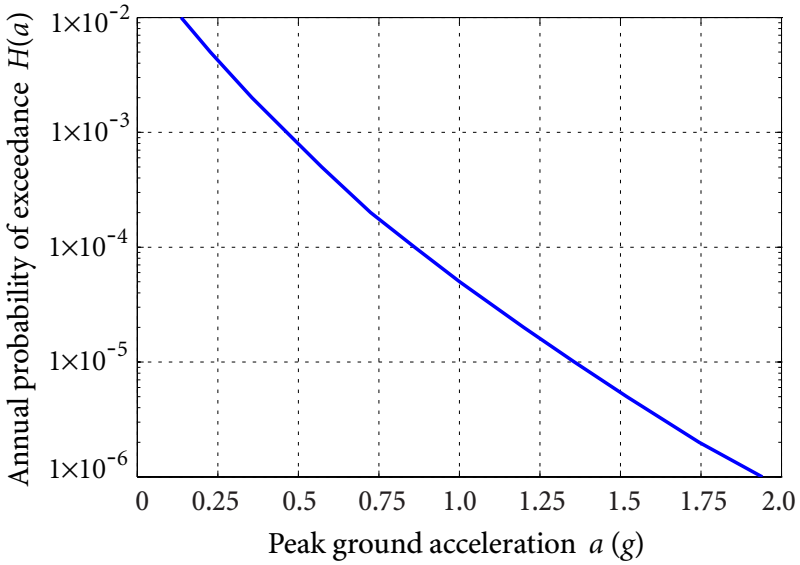

Figure 4.12 Seismic hazard curve for PGA at the DCPP site

where a = a specific PGA level, $P_F(a)$ = conditional probability of failure given a, $H(a)$ = annual probability of exceedance of a.

In contrast, using the CDFM method, first the CDFM capacity of 0.40 g needs to be combined with an estimated β_C to generate a composite fragility curve, which is then convoluted with hazard curve to obtain seismic risk. Table 4.7 gives the risk obtained for typical β_C values ranging from 0.3 to 0.6 and the inferred A_m. It is seen that

1. Regardless of the β_C used, the CDFM-calculated risk is always smaller than that obtained using the formal fragility analysis.
2. The CDFM method provides A_m estimates relatively larger than the actual value. This is due to the lognormal assumption of A_m, where parameter uncertainty β_C has an influential impact on the tail region values.

4.3 Fragility Analysis of the Horizontal Heat Exchanger

4.3.1 Background

In nuclear power plants, heat exchanger is used to transfer heat produced by nuclear reaction to drive steam turbines for electricity production. The heat exchanger has been identified

Table 4.7 Comparison of risk from the FA and the CDFM methods

	A_m (g)	β_C	HCLPF (g)	Risk ($\times 10^{-4}$/yr)
FA method	0.84	0.444	0.30	3.44
CDFM method	0.80	0.3	0.40	2.47
	1.01	0.4		1.57
	1.28	0.5		1.12
	1.62	0.6		0.88

as one of the governing components for the overall plant risk (EPRI, 2000). In addition, anchorage failure governing the seismic capacity of heat exchanger is a common failure mode for many nuclear facilities.

Construction Details

Figure 4.13 shows the details of the horizontal heat exchanger and Table 4.8 lists the properties. It has a diameter of 8 ft = 96 in, length of 30 ft = 360 in, and is supported by equally spaced saddles. Each saddle is secured to the concrete floor by three sets of 2 cast-in-place anchor bolts. Two of the saddle base plates have slotted holes, allowing the thermal expansion of the tank in the longitudinal direction. Each saddle has four stiffener plates to increase the rigidity of the heat exchanger in the longitudinal direction. A total weight of W = 110 kips is estimated for the exchanger. The connecting piping is relatively light, and its weight is included in W = 110 kips. The heat exchanger is located at the ground surface on a rock site, and will be subjected to the tri-directional excitations during seismic events.

Potential Failure Modes

From SPRA fragility estimates, it has been concluded that the lowest capacity failure modes are from anchorage or component supports (EPRI, 1991a). Assume that the heat exchanger itself was designed to be seismically robust. The capacity of the connection of the saddles to the heat exchanger is relatively high and this potential failure mode is not considered further. Only the following failure modes regarding the anchorage and support are considered:

(1) steel failure of the anchor bolt,

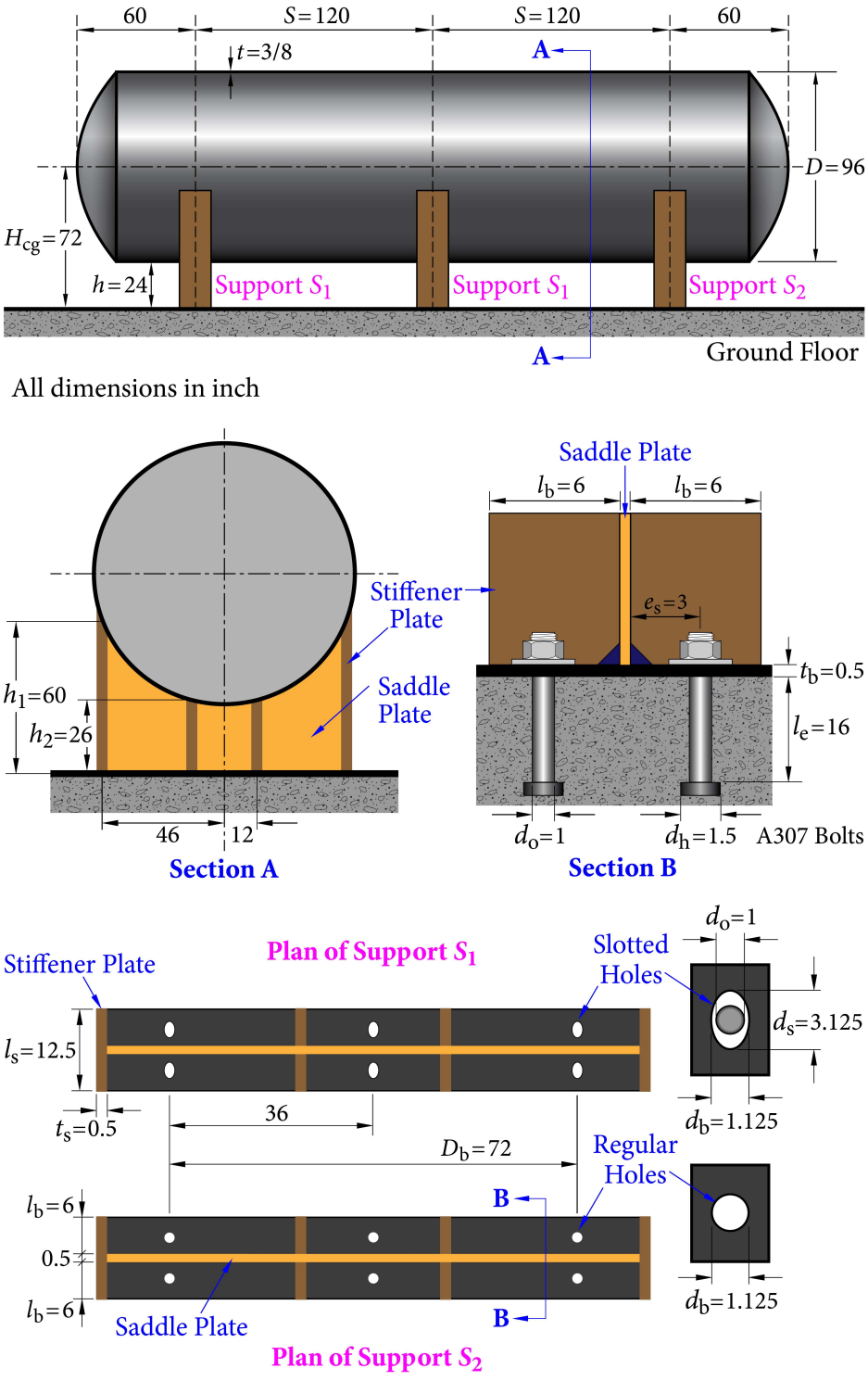

Figure 4.13 Example heat exchanger

Table 4.8 Deterministic properties of heat exchanger

Property	Variable	Value
Heat Exchanger Tank		
Diameter	D	96 in
Length	L	360 in
Floor to bottom tank	h	24 in
Height to center of gravity	H_{cg}	72 in
Shell thickness	t	3/8 in
Weight	W	110 kip
Saddle Supports (ASTM A36)		
Base plate thickness	t_b	0.5 in
Anchor bolt hole diameter	d_b	1-1/8 in
Saddle plate to edge of base plate	l_b	6 in
Distance between outside bolts in base plate	D_b	72 in
Weld leg dimension	t_w	1/4 in
Stiffener width	l_s	12.5 in
Stiffener height (outside pair)	h_1	60 in
Stiffener height (inside pair)	h_2	26 in
Stiffener thickness	t_s	0.5 in
Number of supports	NS	3
Anchor Bolts (ASTM A307)		
Bolt diameter	d_o	1 in
Head diameter	d_h	1-1/2 in
Embedment length	l_e	16 in
Area through bolt	A_{gross}	0.7854 in^2
Area through threads	A_{net}	0.6057 in^2
Eccentricity from bolt centerline to saddle plate	e_s	3 in
Number of anchor bolt locations at each saddle	NL	3
Number of anchor bolts at each location	NB	2
Modulus of Elasticity (steel)	E	29×10^3 ksi
Modulus of Rigidity (steel)	G	11.2×10^3 ksi

(2) anchorage failure of the anchor bolt in the concrete,

(3) bending failure of the support base plate,

(4) weld connection failure between base plate and saddle plate.

Seismic Input

The reference GRS input in each of the horizontal directions is chosen as the NUREG/CR-0098 median shape anchored to 0.3*g* PGA (see Figure 4.6). The vertical GRS is assumed to be 2/3 of the horizontal GRS over the entire frequency range. It is also assumed that the hazard curves are defined in terms of the 5%-damped average spectral acceleration (i.e., 5–10 Hz) in the two horizontal directions.

4.3.2 Basic Variables

The basic demand and capacity variables for fragility analysis are given in Tables 4.9 and 4.10, respectively.

Earthquake response spectrum shape

To minimize the potential uncertainty, an *average spectral acceleration parameter* is used, where the frequency range (i.e., 5–10 Hz) should reflect the frequencies of the component that dominate the seismic risk,

$$S_{a,\text{avg}}(5\text{-}10) = \sqrt{S_a(5) \cdot S_a(10)} = \sqrt{0.649 \times 0.594} = 0.62\,g.$$

Since earthquake forces in the longitudinal direction (with a fundamental frequency of about 8 Hz) controls, according to Table 3-2 of EPRI-TR-103959, $\beta_U = 0.0$ and $\beta_R = 0.20$ are taken, where 0.20 is the average of 0.18 and 0.22.

Horizontal direction peak response

For the anchorage that fails in a shear-tension interactive fashion, this variable has a unit median, according to Table 3-2 of EPRI-TR-103959. This is a randomness variability, hence $\beta_U = 0.0$. β_R is between 0.12 and 0.14, hence their average $\beta_R = 0.13$ is taken.

Vertical component response

Both randomness and uncertainty exist for the vertical response. However, since the vertical earthquake component has only a minor effect on the final fragility parameters, it

Table 4.9 Basic demand variables for heat exchanger fragility analysis

Factor	Median	β_R	β_U
Ground Motion			
Earthquake response spectrum shape	1.0	0.20	0
Horizontal direction peak response	1.0	0.10	–
Vertical component response	1.0	0.34	–
Heat exchanger			
Frequency	1.0	–	0.10
Damping	5%	–	3.5%
	(median)	–	(-1σ)
Mode shape	1.0	–	0.05
Mode combination	1.0	0.05	–
Direction combination	100-40-40 rule	abs. sum 2.3σ	–

Table 4.10 Basic capacity variables for heat exchanger fragility analysis

Factor	Median	β_U
Steel (ASTM A36, A307)		
Yield strength σ_y	44 ksi	0.12
Ultimate strength σ_u	64 ksi	0.06
Concrete		
Compressive strength f'_c	6120 psi	0.12
Weld		
Tensile strength of electrode	$1.1F_{\text{EXX}}$ §	0.05
Anchor Bolt		
Tension T_{ST}	$\phi A_{\text{net}}\sigma_{u,m}$ †	0.13
Shear V_{ST}	$0.62\,A_{\text{net}}\sigma_{u,m}$	0.10
Friction coefficient for shear friction capacity of concrete μ	1.0	0.24

§ $F_{\text{EXX}} = 60$ ksi is the code nominal tensile strength for weld material.

† $\phi = 0.9$ is the notch reduction and reduction due to accidental loading.

is treated as all randomness for simplicity. From Table 3-2 of EPRI-TR-103959, $\beta_R = 0.25$ is taken as the average of 0.22 and 0.28, $\beta_U = 0.23$ is taken as the average of 0.20 and 0.26. Lumping them together yields $\beta_R = \sqrt{0.25^2 + 0.23^2} = 0.34$.

Since a response spectrum analysis is conducted, no "time history analysis" variable is required. Also, since the heat exchanger is founded on a rock site, no contribution from SSI and building response variables are expected.

Frequency, mode shape, and modal combination

Since the heat exchanger is a simple structure that responds primarily in the fundamental modes in each earthquake direction, the median factors associated with these variables are assumed to be unity. According to the recommendations, given in Chapter 3 of EPRI-TR-103959, $\beta_U = 0.10$ for the frequency variable, $\beta_U = 0.05$ for the mode shape variable, and $\beta_R = 0.05$ for the modal combination variable are taken.

Damping

According to Table 3-8 of EPRI-TR-103959, the median damping for the horizontal heat exchanger is taken to be 5% and the -1σ damping is taken as 3.5%.

Direction combination

Note that the shear force in the longitudinal direction dominates the capacity of this heat exchanger. Since only the two horizontal earthquake components affect the shear force, the absolute sum of the three components is assumed to be at the +2.3σ level, according to Section 3 of EPRI-TR-103959.

Strength variables

The basic capacity variables for static strength analysis are given according to the potential failure modes. The nominal values X_n, median values X_m, and the associated β_U satisfy $X_n = X_m \, e^{-1.645\beta_U}$, which implies that X_n is defined at the 95% confidence level.

Tensile strength of electrode

F_{EXX} = electrode classification number (= code nominal strength in ksi). For base metal A36 with thickness less than 3/4 in, if matching filler metal 60 ksi Electrode is used, a median strength $1.1F_{EXX}$ and $\beta_U = 0.05$ are taken approximately.

Strength equations for bolt

The strength formulas for tension and shear, listed in Table 4.10, are based primarily on test results (Kulak *et al.*, 1987, 2001). The associated variabilities are determined in an SRSS manner considering comprehensively the uncertainties in material, equation, and fabrication (refer to Table 3-10 of EPRI-TR-103959).

4.3.3 Demand Analysis

The heat exchanger is a relatively simple component, which primarily responds to the first mode in each earthquake direction. First, the fundamental frequency and the associated spectral acceleration in each direction need to be determined, then the tension and shear demands in the highest stressed anchor bolt are evaluated using statics.

Frequency in the longitudinal direction of the heat exchanger

The fundamental frequency f_{L} in the longitudinal direction is controlled by bending in the end saddle support S_2 about the weak axis. This is the only support that resist shear force, since the bolt holes for the other two supports are elongated in the longitudinal direction to allow thermal expansion of the heat exchanger. Due to the squat configuration of this component and the long distance between outside bolts, it is unlikely that stretching in the anchor bolts will significantly affect the frequency in this direction. Hence, the fundamental frequency of this single degree-of-freedom system is given by

$$f_{\mathrm{L}} = \frac{1}{2\pi}\sqrt{\frac{k_{\mathrm{s}}}{m}} = \frac{1}{2\pi}\sqrt{\frac{k_{\mathrm{s}}\, g}{W}}, \tag{4.3.1}$$

where k_{s} is the stiffness of one saddle support (S_2), and W is the weight (m is the mass) of the heat exchanger.

Assume that the stiffeners have the equivalent boundary condition of a fixed connection at the tank and a pinned connection at the base plate. Since the stiffener is a deep beam, it is modelled as a Timoshenko beam to take into account both bending and shear deformations (Figure 4.14). From the Timoshenko beam theory, the tip displacement $w(0)$ of the beam is given by

$$w(0) = \frac{PL^3}{3EI} + \frac{PL}{\kappa AG}, \tag{4.3.2}$$

where A is the cross-section area of the beam, E is the Young's modulus, G is the shear modulus, I is the second moment of area, and κ is the Timoshenko shear coefficient, where $\kappa = 1$ for an ideal I beam and 5/6 for the rectangular cross-section.

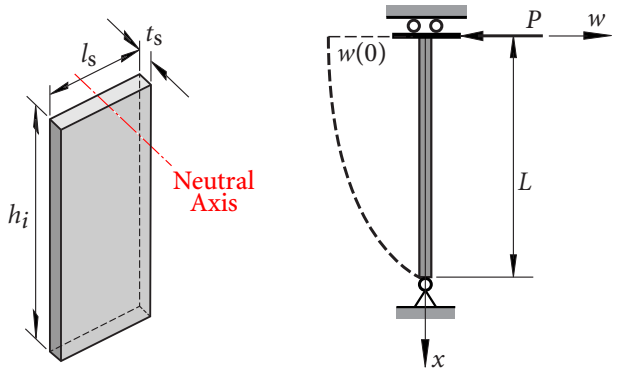

Figure 4.14 Stiffness of a stiffener plate

For the heat exchanger,

$$A_s = t_s l_s = 0.5 \times 12.5 = 6.25 \text{ in}^2, \quad I_s = \frac{t_s l_s^3}{12} = \frac{0.5 \times 12.5^3}{12} = 81.38 \text{ in}^4.$$

The stiffness of support S_2, considering two stiffeners of height h_1 and two of height h_2, is

$$\begin{aligned} k_s &= \frac{2}{\frac{h_1}{\kappa A_s G} + \frac{h_1^3}{3EI_s}} + \frac{2}{\frac{h_2}{\kappa A_s G} + \frac{h_2^3}{3EI_s}} \\ &= \frac{2}{\frac{60}{\frac{5}{6} \times 6.25 \times 11.2 \times 10^3} + \frac{60^3}{3 \times 29 \times 10^3 \times 81.38}} \\ &\quad + \frac{2}{\frac{26}{\frac{5}{6} \times 6.25 \times 11.2 \times 10^3} + \frac{26^3}{3 \times 29 \times 10^3 \times 81.38}} \\ &= 746.4 \frac{\text{kips}}{\text{in}}. \end{aligned}$$

The fundamental frequency in the longitudinal direction is, from equation (4.3.1),

$$f_L = \frac{1}{2\pi} \sqrt{\frac{746.4 \times 386.4}{110}} = 8.15 \text{ Hz}. \tag{4.3.3}$$

Frequency in the transverse direction of the heat exchanger

In this direction, the heat exchanger is much stiffer and the flexibility is controlled principally by the flexibility in the bolts. Suppose that the tank rocks back and forth about an effective length equal to distance D_b between the outside saddle anchor bolts, the fundamental frequency f_T in the transverse direction, due to the bolt flexibility, is

$$f_T = \frac{1}{2\pi}\sqrt{\frac{k_\theta\, g}{I_\theta}}, \tag{4.3.4}$$

where k_θ is the transverse rotational stiffness, and I_θ is the rotational inertia about the axis passing through the outside bolt pair.

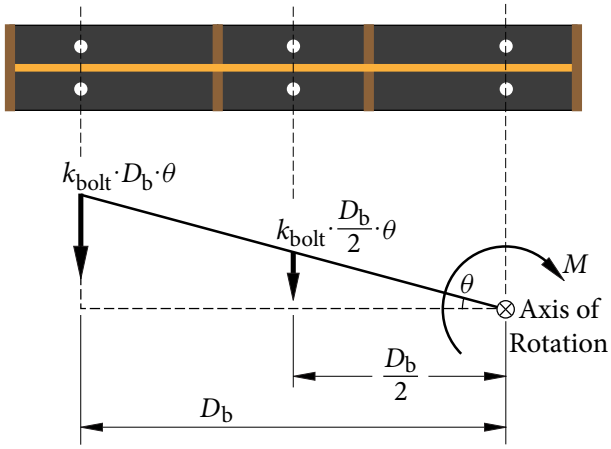

Figure 4.15 Rotational vibration in the transverse direction

Introducing a rotation θ (Figure 4.15), the moment required to balance the resisting forces from the anchor bolts is

$$M = \mathrm{NS}\cdot\mathrm{NB}\cdot\left[(k_{bolt}\cdot D_b\cdot\theta)\cdot D_b + \left(k_{bolt}\cdot\frac{D_b}{2}\cdot\theta\right)\cdot\frac{D_b}{2}\right], \quad k_{bolt} = \frac{EA_{gross}}{l_e}. \tag{4.3.5}$$

The transverse rotational stiffness is

$$\begin{aligned} k_\theta &= \frac{M}{\theta} = \mathrm{NS}\cdot\mathrm{NB}\cdot k_{bolt}\cdot\frac{5}{4}D_b^2 \\ &= 3\times 2\times\frac{29\times 10^3\times 0.7854}{16}\times\frac{5}{4}\times 72^2 = 5.53\times 10^7 \text{ kips-in.} \end{aligned} \tag{4.3.6}$$

Note that the mass moment of inertia of a circular cylinder about its central axis is $\frac{1}{8}mD^2$, where m is the mass and D is the diameter. The mass (weight) moment of inertia of the heat

exchanger tank about the axis of rotation is obtained by applying the parallel axis theorem (see Figure 4.15)

$$I_\theta = I_\theta + W \cdot d^2 = \frac{1}{8} WD^2 + W \left\{ H_{\text{cg}}^2 + \left(\frac{D_{\text{b}}}{2} \right)^2 \right\}$$
$$= \frac{1}{8} \times 110 \times 96^2 + 110(72^2 + 36^2) = 8.40 \times 10^5 \text{ kips-in}^2. \tag{4.3.7}$$

Hence, the fundamental frequency in the transverse direction due to the flexibility in the anchor bolts is, from equation (4.3.4),

$$f_{\text{T}} = \frac{1}{2\pi} \sqrt{\frac{5.53 \times 10^7 \times 386.4}{8.40 \times 10^5}} = 25.4 \text{ Hz}. \tag{4.3.8}$$

☞ The rasing of the center of gravity of the heat exchanger as it rocks about the outside bolt is not significant and is not included in the analysis.

Frequency in the vertical direction

In the vertical direction, the heat exchanger is very stiff. The frequency of the shell translating vertically between supports exceeds 100 Hz and the frequency of the system, where only the bolt and saddle flexibility are considered, exceeds 33 Hz. Thus, the frequency at which the response spectrum returns to the PGA is used for the vertical direction, i.e.,

$$f_{\text{V}} = 33 \text{ Hz}. \tag{4.3.9}$$

Tri-directional seismic excitations

Since the heat exchanger is located on the ground, seismic excitations in terms of spectral accelerations at the fundamental frequencies in the three directions can be obtained from the reference median GRS at 5% damping, as given in Table 4.11.

Responses of critical anchor bolt from three directions

In the longitudinal direction, the tank is subjected to an inertia force equal to the product of its weight W and the spectral acceleration $S_a(f_{\text{L}})$, as shown in Figure 4.16. The inertia force is then transferred to the supports, exerting tension and shear forces on the anchors bolts, where the shear force will be evenly distributed in the anchor bolts of Support 2 only.

Table 4.11 Tri-directional seismic excitations for heat exchanger

Direction	Frequency (Hz)	S_a (g)
Longitudinal	8.15	0.63
Transverse	25.4	0.36
Vertical	33	$2/3 \times 0.30 = 0.20$

In the transverse direction, the seismic loading due to transverse excitation is also transferred to the supports, exerting tension and shear forces in the anchor bolts, as shown in Figure 4.17. Shear force is distributed by anchor bolts of all the supports evenly.

In the vertical direction, the inertial force of the tank due to seismic vertical excitation is transferred to the support as pure tension force, without shear force.

Denote spectral accelerations at the longitudinal, transverse, and vertical vibration frequencies of the heat exchanger as a_{L}, a_{T}, and a_{V}. The force equations and final values for tension and shear in the critical anchor bolts, due to tri-directional seismic excitations and gravity load W, can be determined using statics, as given in Table 4.12.

Table 4.12 Force equations and values for tension and shear in the critical anchor bolt

Direction	Tension		Shear	
	Equation	Value	Equation	Value
Longitudinal	$N_{\mathrm{L}} = \dfrac{W \cdot a_{\mathrm{L}} \cdot H_{\mathrm{cg}}}{\mathrm{NL} \cdot \mathrm{NB} \cdot (2S + S/2)}$	2.78 kips	$V_{\mathrm{L}} = \dfrac{W \cdot a_{\mathrm{L}}}{\mathrm{NL} \cdot \mathrm{NB}}$	11.58 kips
Transverse	$N_{\mathrm{T}} = \dfrac{W \cdot a_{\mathrm{T}} \cdot H_{\mathrm{cg}}}{\mathrm{NB} \cdot \mathrm{NS} \cdot (D_{\mathrm{b}} + \frac{1}{4} D_{\mathrm{b}})}$	5.31 kips	$V_{\mathrm{T}} = \dfrac{W \cdot a_{\mathrm{T}}}{\mathrm{NL} \cdot \mathrm{NB} \cdot \mathrm{NS}}$	2.21 kips
Vertical	$N_{\mathrm{V}} = \dfrac{W \cdot a_{\mathrm{V}}}{\mathrm{NL} \cdot \mathrm{NB} \cdot \mathrm{NS}}$	1.22 kips	V_{V}	0
Dead load	$N_{\mathrm{DL}} = \dfrac{-W}{\mathrm{NL} \cdot \mathrm{NB} \cdot \mathrm{NS}}$	−6.11 kips	V_{DL}	0

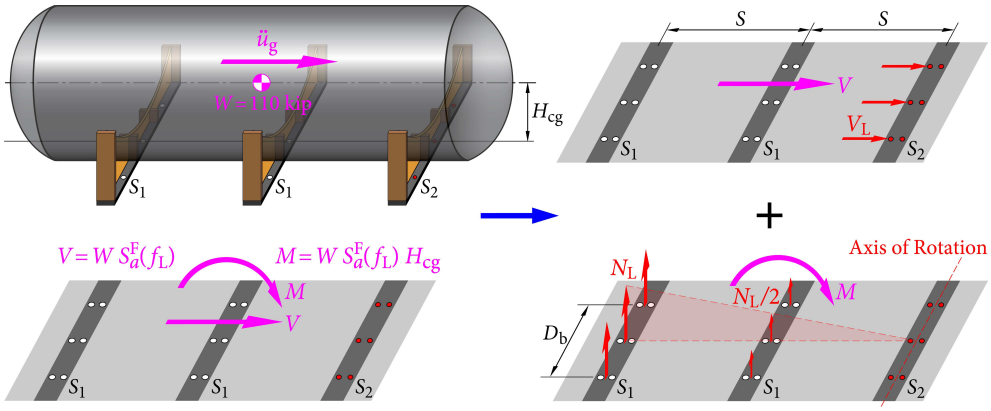

Figure 4.16 Forces due to longitudinal excitation

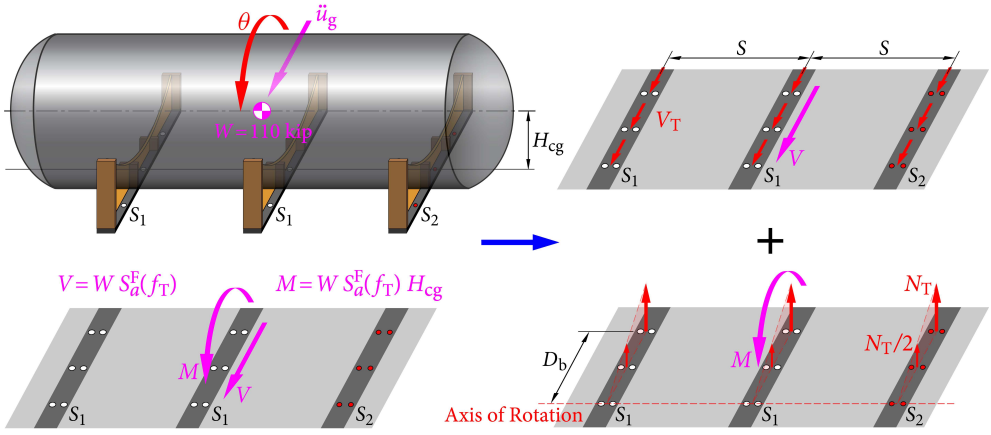

Figure 4.17 Forces due to transverse rocking

Maximum demand on the critical anchor bolt

The maximum forces on the critical anchor bolt can be approximated by using the 100-40-40 percent combination of the maximum responses from three earthquake directions (USNRC, 2006). It is obvious that the vertical direction will not control, only the following two cases are considered.

- When the longitudinal direction controls

$$N_{long} = N_L + 0.4\, T_T + 0.4\, T_V = 5.39\,\text{kips},$$
$$V_{long} = \sqrt{V_L^2 + (0.4\, V_T)^2} = 11.61\,\text{kips}.$$

- When the transverse direction controls

$$T_{\text{tran}} = T_{\text{T}} + 0.4\,T_{\text{L}} + 0.4\,T_{\text{V}} = 6.91\,\text{kips},$$
$$V_{\text{tran}} = \sqrt{V_{\text{T}}^2 + (0.4\,V_{\text{L}})^2} = 5.13\,\text{kips}.$$

4.3.4 Capacity Analysis

Median capacity for each potential failure mode needs to be determined, using static strength formulas from design codes or textbooks. To obtain the actual median capacity, the conservatism against the code-calculated strength needs to be characterized, usually resorting to test results or further research.

Table 4.13 summarizes the capacities evaluated for the four failure mode categories. Detailed analyses are provided in Appendix **??**.

Table 4.13 Summary of equivalent anchor bolt capacities

Failure Mode	Equivalent Capacities (kips)	
	Shear	Tension
Anchor bolt steel	**24.03**	34.89
Pullout		48.06
Concrete capacity		
cone failure	240.0	385.4
shear friction	34.89	
Base plate bending		26.76
Fillet weld base plate to saddle plate		88.19

Comparing the capacities in Table 4.13 with the maximum demand on the critical anchor bolts, it is clear that the anchor bolt steel failure (in shear) will control

$$V_{\text{ST}} = 24.03 \text{ kips}, \qquad N_{\text{ST}} = 34.89 \text{ kips}, \tag{4.3.10}$$

and that the earthquake forces in the longitudinal direction

$$V_{\text{long}} = 11.58 \text{ kips}, \qquad N_{\text{long}} = 5.28 \text{ kips}, \tag{4.3.11}$$

will control the factor of safety against the reference earthquake.

4.3.5 Strength Factor and the Median Seismic Capacity

Anchor bolt failure is usually defined in a tension-shear interaction relation. Based on a large number of shear-tension test data, EPRI-NP-5228-SL (see EPRI, 1991b, pg.2-95) recommends a shear-tension-interaction formulation for expansion bolts and cast-in bolts. The results are plotted in terms of N/N_m and V/V_m in a simple bilinear form as shown in Figure 4.18, where N_m and V_m are the bolt tension and shear capacities in the absence of combined loading:

$$\frac{N}{N_m} = 1.0, \qquad \text{for} \quad \frac{V}{V_m} \leqslant 0.3, \tag{4.3.12a}$$

$$0.7\,\frac{N}{N_m} + \frac{V}{V_m} = 1.0, \quad \text{for} \quad 0.3 < \frac{V}{V_m} \leqslant 1.0. \tag{4.3.12b}$$

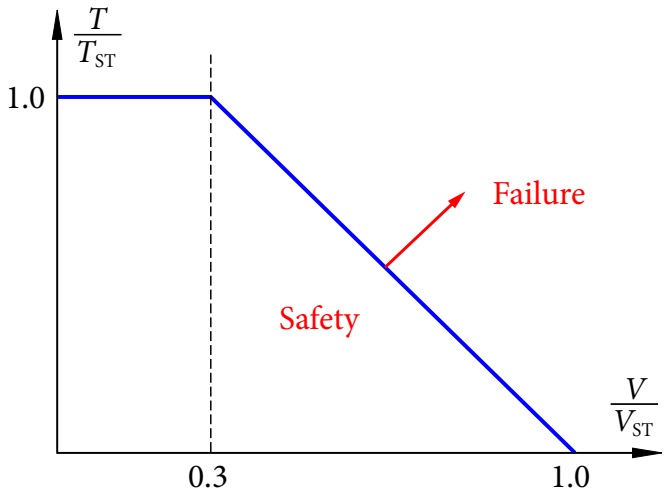

Figure 4.18 Bilinear interaction of bolt tension and shear

From equations (4.3.12), the strength factors F_S for the two regions shown in Figure 4.18, i.e., pure tension region and shear/tension region, are

$$F_{S1} = \frac{T_{ST} - T_{DL}}{T_{long}}, \tag{4.3.13a}$$

$$F_{S2} = \frac{V_{ST} - 0.7\left(\dfrac{V_{ST}}{T_{ST}}\right)T_{DL}}{V_{long} + 0.7\left(\dfrac{V_{ST}}{T_{ST}}\right)T_{long}}. \tag{4.3.13b}$$

The final strength factor F_S is taken as the minimum of the two factors

$$F_S = \min(F_{S1}, F_{S2}). \tag{4.3.14}$$

Substituting values into these equations gives

$$F_{S1} = \frac{34.89 - (-6.11)}{5.28} = 7.77,$$

$$F_{S2} = \frac{24.03 - 0.7 \times \dfrac{24.03}{34.89} \times (-6.11)}{11.58 + 0.7 \times \dfrac{24.03}{34.89} \times 5.28} = 1.91,$$

$$F_S = \min(F_{S1}, F_{S2}) = 1.91.$$

Thus, the capacity is controlled by combined shear and tension with the shear force at $1.91 \times \frac{11.58}{24.03} = 92.0\%$ of its capacity. Because of the relatively large demand-to-capacity ratio for the shear force, the failure tends to be non-ductile with negligible inelastic energy absorption; thus take $F_\mu = 1.0$ and the scale factor or factor of safety is $F = F_S F_\mu = 1.91$.

When the averaged spectral acceleration between 5 and 10 Hz is used as the ground motion parameter and the bilinear shear-tension interaction relation is used, the median capacity of the heat exchanger is given by

$$A_m = F_S \cdot F_\mu \cdot S_{a,\text{avg}}(5\text{–}10\,\text{Hz}) = 1.91 \times 0.62g = 1.18\, g\, S_{a,\text{avg}}.$$

4.3.6 Logarithmic Standard Deviations

The *Approximate Second-Moment Method* presented in Subsection 4.1.3 can be applied to obtain the uncertainties β_R and β_U for the median capacity due to variabilities in the basic variables, which are given in Table 4.14.

Finally, the seismic fragility of heat exchanger in terms of $S_{a,\text{avg}}$ can be totally defined by

$$A_m = 1.18\, g\, S_{a,\text{avg}}, \qquad \beta_R = 0.24, \qquad \beta_U = 0.15.$$

4.3.7 CDFM-calculated Capacity

According to the philosophy of the CDFM method, specific degree of conservatism is intensionally introduced in the most significant contributors to the variability of seismic capacity. Less significant factors will be neglected.

Table 4.14 Logarithmic standard deviations for demand and capacity parameters

Variable	Parameter at 1σ	F_S	β_R	β_U
Base Case		1.91		
Ground Motion				
Earthquake response spectrum shape anchored to average SA	$S_a(f_L)\,e^{0.20}$ $S_a(f_T)\,e^{0.20}$	1.57	0.20	–
Horizontal direction peak response	$S_a(f_L)\,e^{0.13}$ $S_a(f_T)\,e^{-0.13}$	1.71	0.11	–
Vertical component response	$S_a(f_V)\,e^{0.34}$	1.90	0.00	–
Equipment				
Frequency	$S_a(f_T)\,e^{0.05}$	1.90	–	0.01
Damping	$S_a(f_L)\,e^{0.11}$ $S_a(f_T)\,e^{0.02}$	1.72	–	0.10
Modal shape	$S_a(f_L)\,e^{0.05}$ $S_a(f_T)\,e^{0.05}$	1.82	–	0.05
Modal combination	$S_a(f_L)\,e^{0.05}$ $S_a(f_T)\,e^{0.05}$	1.82	–	0.05
Earthquake component combination	Abs. Sum at 2.3σ	1.68	0.06	–
Capacity	$V_{ST}\,e^{-0.10}$ $N_{ST}\,e^{-0.13}$	1.74	–	0.09

Seismic Input

The reference GRS is chosen as the NUREG/CR-0098 84.1% amplified spectral shape at 5% damping anchored to 0.30 *g* PGA (see Figure 4.6). Seismic inputs to the heat exchanger in each of the horizontal directions is taken as the reference GRS, while the vertical input is 2/3 of the horizontal input over the entire frequency range.

CDFM Demand Analysis

The fundamental frequencies of the heat exchanger are the same as those obtained in Section 4.3.3

$$f_{\mathrm{L}} = 8.15 \text{ Hz}, \quad f_{\mathrm{T}} = 25.4 \text{ Hz}, \quad \text{and } f_{\mathrm{V}} = 33 \text{ Hz}.$$

From the 84% GRS given in Figure 4.6, the spectral accelerations are found to be

$$a_{\mathrm{L}} = 0.81\ g, \quad a_{\mathrm{T}} = 0.81\ g, \quad \text{and} \quad a_{\mathrm{V}} = 0.20\ g.$$

Using the equations given in Table 4.12, the directional responses are determined as

$$V_{\mathrm{L}} = \frac{W \cdot a_{\mathrm{L}}}{\mathrm{NL} \cdot \mathrm{NB}} = \frac{110 \times 0.801}{3 \times 2} = 14.69 \text{ kips},$$

$$N_{\mathrm{L}} = \frac{W \cdot a_{\mathrm{L}} \cdot H_{\mathrm{cg}}}{\mathrm{NL} \cdot \mathrm{NB} \cdot \left(2S + \frac{1}{2}S\right)} = \frac{110 \times 0.801 \times 72}{3 \times 2 \times \frac{5}{2} \times 120} = 3.52 \text{ kips}.$$

$$V_{\mathrm{T}} = \frac{W \cdot a_{\mathrm{T}}}{\mathrm{NL} \cdot \mathrm{NB} \cdot \mathrm{NS}} = \frac{110 \times 0.360}{3 \times 2 \times 3} = 2.20 \text{ kips},$$

$$N_{\mathrm{T}} = \frac{W \cdot a_{\mathrm{T}} \cdot H_{cg}}{\mathrm{NB} \cdot \mathrm{NS} \cdot \left(D_{\mathrm{b}} + \frac{1}{4}D_{\mathrm{b}}\right)} = \frac{110 \times 0.360 \times 72}{2 \times 3 \times \frac{5}{4} \times 72} = 5.28 \text{ kips}.$$

Since it was identified that the longitudinal direction controls, the maximum demand in the critical anchor bolt in the longitudinal direction is obtained using the 100-40-40 combination rule

$$\begin{aligned} N_{\text{long}} &= 1.0 \times N_{\mathrm{L}} + 0.4 \times N_{\mathrm{T}} + 0.4 \times N_{\mathrm{V}} \\ &= 1.0 \times 3.52 + 0.4 \times 5.28 + 0.4 \times 1.22 = 6.13 \text{ kips}. \end{aligned}$$

$$V_{\text{long}} = \sqrt{V_{\mathrm{L}}^2 + (0.4\ V_{\mathrm{T}})^2} = \sqrt{14.69^2 + (0.4 \times 0.88)^2} = 14.71 \text{ kips}.$$

Compared to the median value from the FA method, the tension and shear forces have increased about 16% and 25%, respectively.

CDFM Static Capacity

From Table 4.10, the uncertainty β_U about the bolt strength is 0.13 for tension and 0.10 for shear. Since the bolt steel failure in tension and shear is non-ductile, according to the philosophy of the CDFM method, an additional safety factor of 1.33 is introduced

besides the 98% non-exceedance probability of material strength. Hence, the CDFM static capacities for the bolt steel failure are

$$N_{\text{ST, CDFM}} = \frac{N_{\text{ST},m}\mathrm{e}^{-2.0537\beta_{\text{tension}}}}{1.33} = \frac{34.89\mathrm{e}^{-2.0537\times 0.13}}{1.33} = 20.09\,\text{kips},$$
$$V_{\text{ST, CDFM}} = \frac{V_{\text{ST},m}\mathrm{e}^{-2.0537\beta_{\text{shear}}}}{1.33} = \frac{24.03\mathrm{e}^{-2.0537\times 0.10}}{1.33} = 14.72\,\text{kips},$$

Compared to the median capacities obtained from the FA method, the capacities are reduced by 42% in shear strength and 38% in shear strength.

Strength Factor and the CDFM Capacity

Using equations (4.3.13) and (4.3.14), the strength factor is obtained as

$$F_{\text{S1}} = \frac{N_{\text{ST, CDFM}} - N_{\text{DL}}}{N_{\text{long}}} = \frac{20.09 - (-6.11)}{6.13} = 4.28.$$

$$F_{\text{S2}} = \frac{V_{\text{ST, CDFM}} - 0.7\,\dfrac{V_{\text{ST, CDFM}}}{N_{\text{ST, CDFM}}}N_{\text{DL}}}{V_{\text{long}} + 0.7\,\dfrac{V_{\text{ST, CDFM}}}{N_{\text{ST, CDFM}}}N_{\text{long}}} = \frac{14.72 - 0.7\times\frac{14.72}{20.09}\times(-6.11)}{14.71 + 0.7\times\frac{14.72}{20.09}\times 6.13} = 1.00.$$

$$F_{\text{S}} = \min(F_{\text{S1}}, F_{\text{S2}}) = 1.00.$$

The CDFM capacity of the heat exchanger in terms of $S_{a,\text{avg}}$ is

$$C_{\text{CDFM}} = F_{\text{S}}\cdot F_{\mu}\cdot S_{a,\text{avg}} = 1.00\times 1.0\times 0.62g\,S_{a,\text{avg}} = 0.62g\,S_{a,\text{avg}}. \tag{4.3.16}$$

4.3.8 Comparison of Results

The HCLPF capacity A_{HCLPF} from the FA method can be obtained using equation (4.1.13)

$$A_{\text{HCLPF}} = A_{5\%}^{95\%} = A_m\,\mathrm{e}^{-1.645(\beta_R+\beta_U)} = 1.18\,\mathrm{e}^{-1.645(0.24+0.15)} = 0.62g\,S_{a,\text{avg}}.$$

which happens to be the same as the CDFM capacity $C_{\text{CDFM}} = 0.62g\,S_{a,\text{avg}}$, provided by the CDFM method.

This example shows the case when the CDFM method can capture almost all basic variable that have significant effect on seismic capacity, the CDFM capacity will be very

close to the HCLPF value obtained using the FA method. Hence, if proper variability β_C values are estimated, the realistic fragility (including median capacity A_m) can be recovered using the simple CDFM method. When combined with hazard curve, a realistic seismic risk value can also be obtained.

4.4 Summary

In this Chapter, seismic fragility analyses of two commonly used components in nuclear power plant, the block masonry wall and horizontal heat exchanger, are presented. Fragility results from the formal probabilistic Fragility Analysis method are compared to those from the simple Conservative Deterministic Failure Margin method.

- The FA method is a more accurate method in evaluating seismic capacity, as it takes account of variability in all important factors affecting seismic capacity in a probabilistically rigorous manner; whereas the CDFM method is an approximate method, which considers only some of the most significant factors affecting the variability of seismic capacity.
- In cases when the CDFM method can capture almost all basic variables that have significant effect on seismic capacity, the CDFM capacity will be very close to the HCLPF capacity from the FA method, i.e., $C_{\text{CDFM}} \approx A_{\text{HCLPF}}$. This is true for the horizontal heat exchanger example. Combined with a properly estimated variability β_C, the simple CDFM method can provide realistic fragility and risk estimates.
- However, this is not always the case; $C_{\text{CDFM}} \approx A_{\text{HCLPF}}$ does not always hold. When large variability exists (e.g., $\beta_C > 0.40$), the simple CDFM method cannot capture all sources of uncertainty in evaluating seismic capacity and usually provides overly optimistic results. Also, it gives inaccurate fragility and risk estimates. This is the case for the block masonry wall example.

CHAPTER 5

Parametric Evaluation of Seismic Capacity for Nuclear Facilities

5.1 Background

Seismic capacity evaluation of Structures, Systems, and Components (SSC) is an important task in both the seismic probabilistic risk analysis (SPRA) and seismic margin assessment (SMA) for nuclear energy facilities. There has been an increasing demand worldwide on accurate evaluation of seismic capacity of safety-related SSC, especially after the 2011 Tohoku Japan earthquake.

Compared to primary structures, which usually have a large safety margin against the reference earthquake, secondary structures mounted thereon are more vulnerable to failure under an earthquake. Seismic evaluation of secondary structures, as illustrated in Figure 5.1, involves such comprehensive tasks as structural modelling, seismic response analysis of primary structure, generation of floor response spectrum (FRS), static strength estimate and seismic demand analysis of secondary structure.

Two popular methods can be used for evaluating seismic capacity of nuclear energy facilities (NUREG, 1985; EPRI, 2013): the Fragility Analysis (FA) method and the Conservative Deterministic Failure Margin (CDFM) method. The seismic capacity evaluation process using both methods are similar, e.g., factors of safety are determined against a reference earthquake A_{ref}, the concepts in each method are quite different.

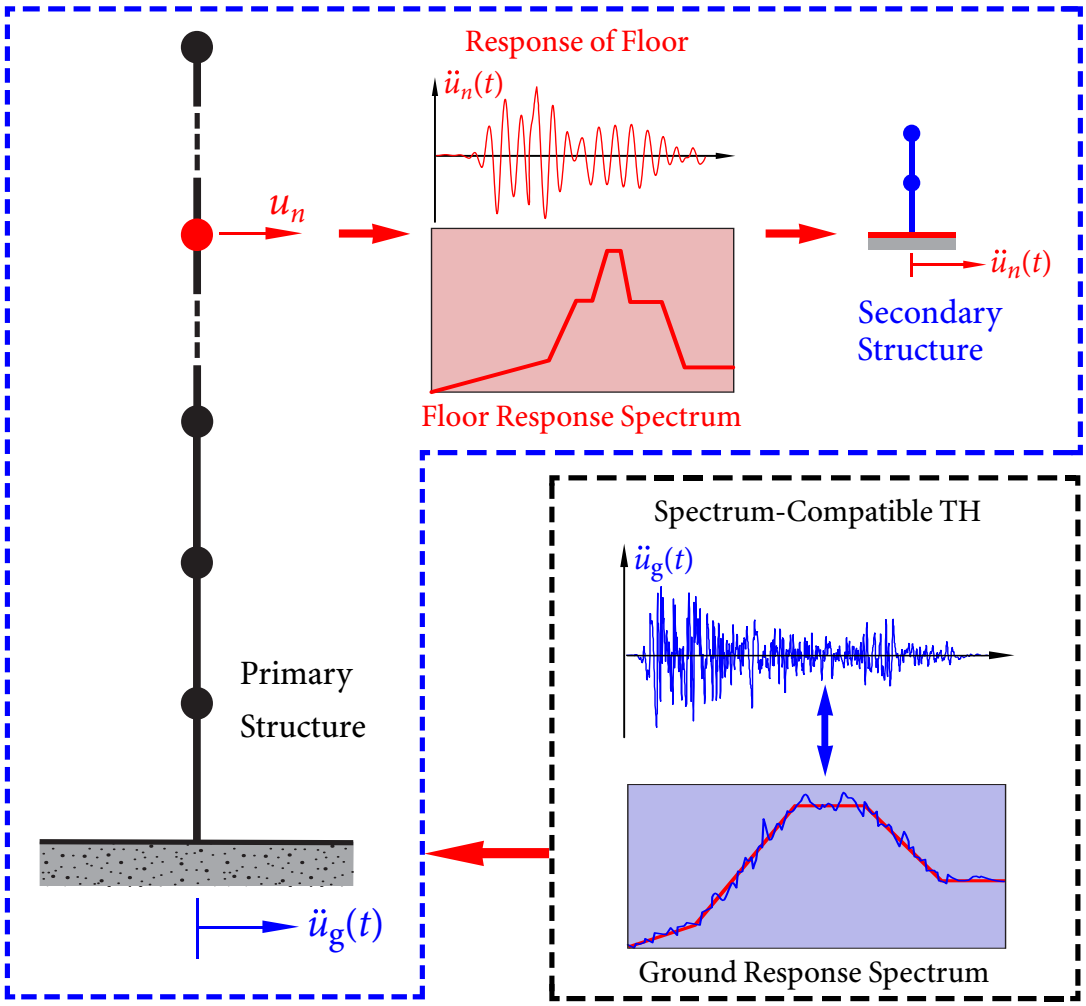

Figure 5.1 Seismic evaluation of secondary structures

The FA method is a probabilistic method as part of SPRA, which determines the median seismic capacity A_m by using median values for all basic variables affecting seismic capacity. The CDFM method is a simple deterministic method following the design-analysis procedure, which evaluates the CDFM capacity by intensionally introducing conservatism in steps where significant parameter uncertainty exists. However, it is an approximate method that captures only the most important sources of parametric uncertainty.

In case for high seismicity sites or for dominant seismic risk contributors, the FA method is recommended (EPRI, 2013). This study is focused on the evaluation of median seismic capacity A_m.

In practice, due to the variation in seismological environment, the site-specific reference earthquake at one site often shows a very different spectral shape than that at another. Seismic capacity estimates of the same SSC, obtained following the current evaluation procedures (EPRI, 1991a, 1994, 2009), can be very inconsistent for different sites. For example, seismic capacity of a diesel generator grounded at the Darlington site in Canada might be quite different from that at the Qinshan site in China. In addition, using different ground motion parameter (GMP) also leads to different levels of inconsistency.

This inconsistency is conceptually undesirable and has caused problems in seismic evaluation process. In a SPRA, fragility analysis is an independent task from hazard analysis, which by definition implies that seismic capacity of a SSC should be consistent given the ground acceleration level. Hence, to better interpret the results and guide engineering practice, all possible factors affecting the inconsistency of seismic capacity estimates need to be investigated. Proper GMP should be selected to facilitate more consistent estimates. Figure 5.1 shows that there are four possible factors to be investigated:

(1) The input ground response spectrum (GRS) shapes, which represent the diverse seismological environments and variation in local site conditions.

(2) Primary structures that generate FRS for secondary structures mounted thereon.

(3) Dynamic characteristics of secondary structures that may affect seismic responses.

(4) GMP that are used to define the seismic capacity.

In this Chapter, a parametric study is performed to evaluate how these factors affect the inconsistency of A_m. The scope of this parametric study is described in Section 5.2. The parametric study is performed in Section 5.3 and general conclusions are drawn. Two realistic applications are presented in Section 5.4 to validate the parametric study.

5.2 Scope of the Parametric Study

Table 5.1 summarizes the scope of the parametric study, which covers a broad and realistic range of important input parameters for seismic capacity evaluation. Details about each input parameter are described in this Section.

Table 5.1 Scope of the parametric study

Input parameter		Description	Details
1	**GRS shape**	3 median spectral shapes (50% percentile) all anchored to PGA = 0.3 g	1) R.G. 1.60 median shape 2) NUGER/CR-0098 median shape 3) UHS median shape (Memphis, TN)
2	**Primary structure**	4 stick-model type structures having different fundamental frequency f_1	1) S-1 (f_1=3.0 Hz) 2) S-2 (f_1=5.6 Hz) 3) S-3 (f_1=10.5 Hz) 4) S-4 (f_1=15.0 Hz)
3	**Secondary structure**	201 simple structures having different dynamic characteristics	1) frequency f_0 ranges from 1-100 Hz, 2) one-mode- or multi-mode-dominant
4	**GMP**	3 popular parameters	1) PGA 2) $S_a(f_1)$ and 3) $S_{a,\text{avg}}$(3-8)†

† $S_{a,\text{avg}}$ is an average spectral acceleration over a frequency range

5.2.1 Input Ground Response Spectra

The GRS is used to represent a reference earthquake, which can be fully defined by three elements (EPRI, 2013): (1) the PGA, which specifies the ground shaking level of interest, (2) spectral shape, which reflects the frequency content of an earthquake, and (3) the control point, where the earthquake is applied, i.e., on rock or a soil layer.

Spectral shape depends primarily on the seismological environment at the site, including seismic source configurations and variations in seismicity parameters. It might also depend on the procedure of earthquake spectrum development. The site-specific Uniform Hazard Spectrum (UHS) (ASCE, 2005), derived from standard PSHA, shows a wider-band spectral shape than the Newmark Design Spectrum (NUREG, 1978), developed from statistical studies of actual earthquake records.

For nuclear engineering applications, whenever possible, a site-specific spectral shape is always preferred; otherwise, when site-specific data is not adequate, the median Newmark spectral shape, referred to as the "standard shape", can be used (EPRI, 1994).

Figure 5.2 shows three median (50% percentile) spectral shapes (all anchored to 0.3g PGA). They are chosen for this study because of their potential use by design and review institutes and a wide coverage of seismological environment. Using these median spectral shapes in seismic capacity evaluation, hidden conservatism can be avoided.

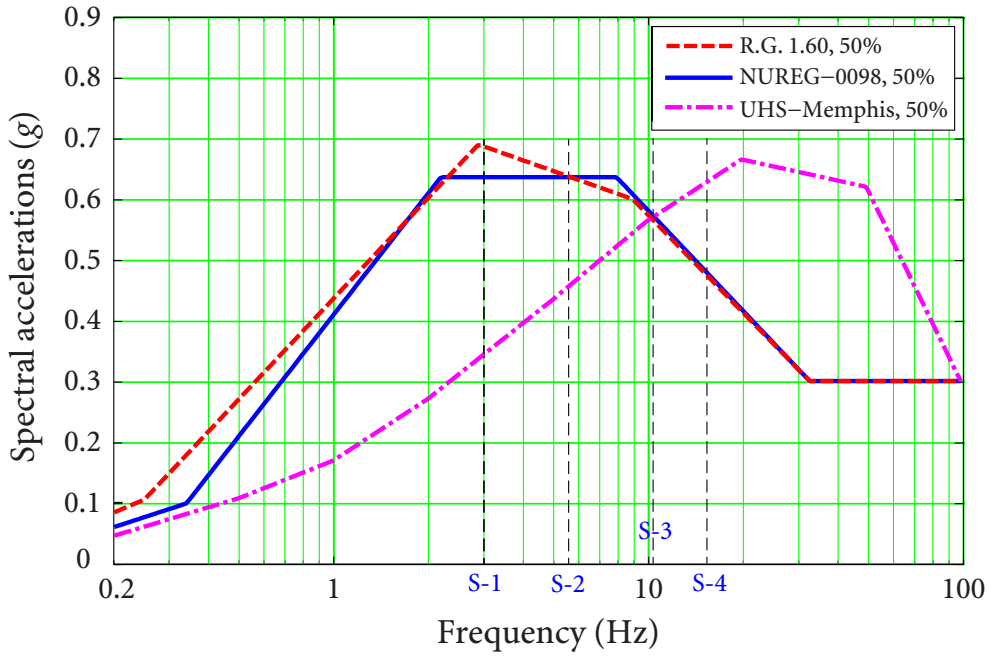

Figure 5.2 Three chosen median spectral shapes

1. The Regulatory Guide (R.G.) 1.60 median spectral shape (USNRC, 1973). Developed statistically from past strong ground motions, it has been widely used for designing and reviewing many of the existing nuclear power plants throughout the world. In this study, the median rather than the 84% spectral shape is used.
2. The NUREG/CR-0098 median standard shape (NUREG, 1978). It has been widely used for seismic analysis in many engineering sectors. It is probably considered as the best-estimate of ground-motion characteristics for the Western United States (WUS), reflecting the empirical strong motion database.
3. The median UHS shape for Memphis, Tennessee (Silva *et al.*, 1999). Developed from standard PSHA, this median UHS shape shows typical ground-motion characteristics for the Central and Eastern United States (CEUS) sites.

These spectral shapes have the following features:

(a) Only slight difference exists between the R.G. 1.60 and NUREG/CR-0098 median spectral shapes, which are both based on statistical studies of strong-motion records in the WUS. Hence they are called Newmark-type spectra.

(b) The UHS for Memphis in the CEUS has a significantly different spectral shape from Newmark-type spectra. It exhibits much stronger high-frequency ground motions and much weaker low-frequency ground motions.

(c) At frequency of 10.5 Hz, they have nearly the same ground motion intensity.

5.2.2 Primary Structures

Nuclear structures usually have a very stiff box-type concrete construction, with walls 2-3 feet thick and have a foundation of thick base mat. Depending on the function of the structure and foundation material (i.e., soil, rock, or hard rock), the fundamental frequency of these structures can range from 3-15 Hz, with a typical value less than 10 Hz (EPRI, 2007). Nuclear structures are not expected to respond significantly to high-frequency ground motions.

In this study, the primary structure is constructed based on an internal structure of a typical reactor building (Li *et al.*, 2005). The original internal structure is completely symmetric in both horizontal directions and has been modelled as a 4-DOF system. Table 5.2 gives the model parameters. The Young's modules of concrete $E = 40$ GPa. Due to symmetry, a planer model can be reasonably used for structural analysis. Modal analysis of the original planer model gives a fundamental frequency $f_1 = 5.3$ Hz.

Table 5.2 Basic parameters of the original structural model

Node†	Mass ($\times 10^3$kg)	Beam element†	Length (m)	Moment of inertia (m^4)
1	5710	1	8.50	5720
2	5970	2	6.32	8160
3	6750	3	8.83	8160
4	1270	4	9.85	325

† Refer to Figure 4.8 for node and beam element numbers

By varying the model parameters, four primary structures are so constructed that their fundamental frequencies f_1 are equal to 3.0, 5.6, 10.5, and 15.0 Hz, respectively, which cover the typical frequency range of nuclear structures. They also represent different possible cases of structural frequency relative to GRS shapes, as shown in Figure 5.2. The basic

modal information of these primary structures is provided in Table 5.3. For simplicity, 5% damping ratios are assumed for all vibration modes, i.e., $\zeta_k = 5\%$ for $k = 1, \cdots, 4$.

5.2.3 Floor Response Spectra

Under seismic excitations, primary structures generate locally amplified FRS as the actual maximum base excitations for secondary systems. Both the time history method (USNRC, 1978) and the direct spectra-to-spectra (S2S) method (see e.g., Singh, 1975) can be used for generation of FRS (ASCE, 1998). In this study, a direct S2S method based on Duhamel's integral and modal analysis is applied. Using this method, FRS is expressed as a function of GRS input and basic modal information of primary structure, as provided in Table 5.3.

Consider an oscillator with natural frequency f_0 and damping ratio ζ_0 mounted on the nth floor of an N-DOF structural system, which has natural frequencies of f_k and damping ratios ζ_k $(k = 1, \cdots, N)$. The FRS of floor-n $S_n(f_0, \zeta_0)$ is obtained by combining the ground's motion $S_{\mathrm{A}}(f_0, \zeta_0)$ and structure's motion $S_{\mathrm{A}}(f_k, \zeta_k)$, using the SRSS combination rule, as

$$S_n^2(f_0, \zeta_0) = \Big[\sum_{k=1}^{N} \Gamma_k \phi_{nk} \cdot \mathrm{AF}_{0,k} \cdot S_{\mathrm{A}}(f_0, \zeta_0)\Big]^2 + \sum_{k=1}^{N} \Big[\Gamma_k \phi_{nk} \cdot \mathrm{AF}_{S,k} \cdot S_{\mathrm{A}}(f_k, \zeta_k)\Big]^2, \quad (5.2.1)$$

where

- $\Gamma_k =$ modal participation factor of mode k and $\phi_{nk} =$ kth modal displacement of floor-n. It is noted that $\sum_{k=1}^{N} \Gamma_k \phi_{nk} = 1$.

- $S_{\mathrm{A}}(f_0, \zeta_0)$ represents the ground's motion and $S_{\mathrm{A}}(f_k, \zeta_k)$ represents the structure's motion, both coming from the GRS as shown in Figure 5.3 (assuming $\zeta_0 = \zeta_k = 5\%$).

- $\mathrm{AF}_{0,k}$ and $\mathrm{AF}_{S,k}$ are modal amplification factors of ground's motion $S_{\mathrm{A}}(f_0, \zeta_0)$ and structure's motion $S_{\mathrm{A}}(f_k, \zeta_k)$, respectively. They can be plotted as functions of the frequency ratio $r_k = f_0/f_k$ and damping ratios ζ_0 and ζ_k, as shown in Figure 5.4 (for $0.1 \leqslant r_k \leqslant 10$ and $\zeta_0 = \zeta_k = 5\%$). Mathematically, $\mathrm{AF}_{0,k} = \sqrt{A_k^2 + B_k^2}$ and $\mathrm{AF}_{S,k} = \sqrt{C_k^2 + D_k^2}$, where A_k, B_k, C_k, and D_k are given by

Table 5.3 Basic modal information of four primary structures

Structure	Mode k	Frequency f_k (Hz)	Modal displacements ϕ_{nk}				Participation factor Γ_k	Modal contribution factor $\Gamma_k \phi_{nk}$			
			floor-1	floor-2	floor-3	floor-4		floor-1	floor-2	floor-3	floor-4
S-1	1	3.0	−0.0003	−0.0004	−0.0006	−0.0012	−1455.8	0.50	0.62	0.86	1.68
	2	5.2	−0.0004	−0.0005	−0.0005	0.0011	−641.2	0.28	0.33	0.32	−0.72
	3	10.6	−0.0007	−0.0005	0.0008	−0.0002	−239.0	0.16	0.12	−0.19	0.04
	4	21.5	−0.0008	0.0008	−0.0001	0.0000	−71.2	0.06	−0.06	0.01	−0.00
S-2	1	5.6	−0.0006	−0.0007	−0.0010	−0.0017	−935.78	0.54	0.67	0.93	1.62
	2	10.1	0.0007	0.0008	0.0007	−0.0019	350.48	0.25	0.28	0.24	−0.66
	3	19.2	0.0011	0.0008	−0.0013	0.0003	146.26	0.16	0.11	−0.19	0.047
	4	38.8	−0.0013	0.0013	−0.0002	0.0000	−44.72	0.06	−0.06	0.01	−0.00
S-3	1	10.5	−0.0008	−0.0010	−0.0015	−0.0027	−606.50	0.51	0.63	0.89	1.61
	2	18.9	−0.0011	−0.0013	−0.0012	0.0026	−248.81	0.28	0.31	0.29	−0.65
	3	37.0	−0.0016	−0.0012	0.0020	−0.0004	−95.50	0.16	0.11	−0.19	0.04
	4	74.8	−0.0020	0.0021	−0.0003	0.0000	−29.08	0.06	−0.06	0.01	−0.00
S-4	1	15.0	−0.0016	−0.0020	−0.0027	−0.0032	−433.32	0.71	0.87	1.15	1.38
	2	36.1	−0.0017	−0.0016	0.0004	0.0072	−80.20	0.14	0.13	−0.03	−0.58
	3	47.8	0.0019	0.0012	−0.0027	0.0041	48.82	0.09	0.06	−0.13	0.20
	4	91.5	−0.0029	0.0029	−0.0005	0.0001	−20.55	0.06	−0.06	0.01	−0.00

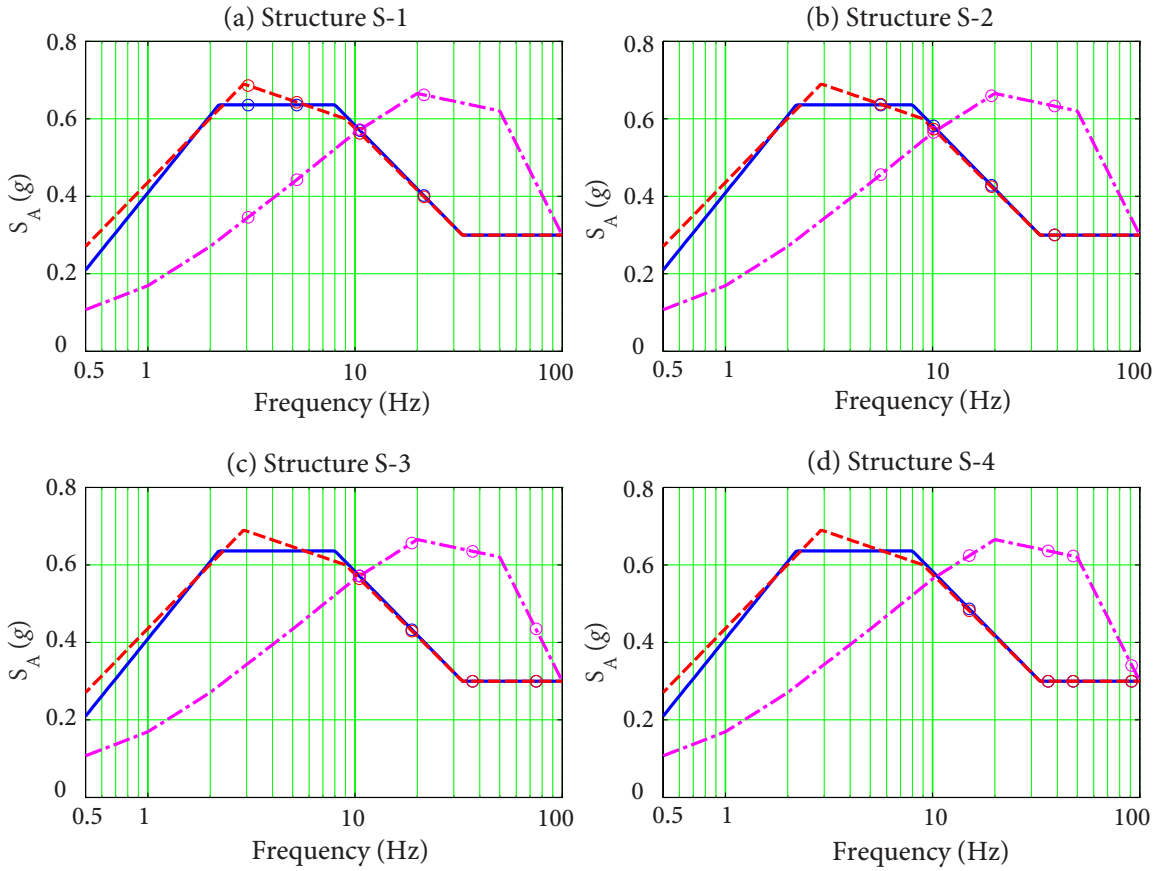

Figure 5.3 Ground's motion $S_A(f_0, \zeta_0)$ in the entire frequency range (lines) and structure's motion $S_A(f_k, \zeta_k)$ at modal frequencies of primary structure (circles), for all 4 primary structures

$$\begin{cases} A_k = \dfrac{-r_k^2 - 2\zeta_0\zeta_k r_k + 2\zeta_0^2 r_k^2 + \zeta_k^2 + 1}{\psi_k}, & B_k = \dfrac{-2r_k(\zeta_k - \zeta_0 r_k)}{\psi_k}, \\ C_k = \dfrac{r_k^2(r_k^2 - 2\zeta_0\zeta_k r_k + \zeta_k^2 - 1)}{\psi_k}, & D_k = \dfrac{2r_k^2(\zeta_k - \zeta_0 r_k)}{\psi_k}, \\ \psi_k = (r_k^2 - 2\zeta_0\zeta_k r_k + \zeta_k^2 - 1)^2 + 4(\zeta_k - \zeta_0 r_k)^2. \end{cases}$$

For analytical analysis, it is important that the spectrum ordinates be computed at natural frequencies sufficiently close to produce accurate response spectra (USNRC, 1978). In this study, a number of 301 frequencies, equally spaced in log-scale from 0.1 to 100 Hz, are used to generate FRS for all four primary structures, as shown in Figures 5.5-5.8 (shown from 0.5 to 100 Hz).

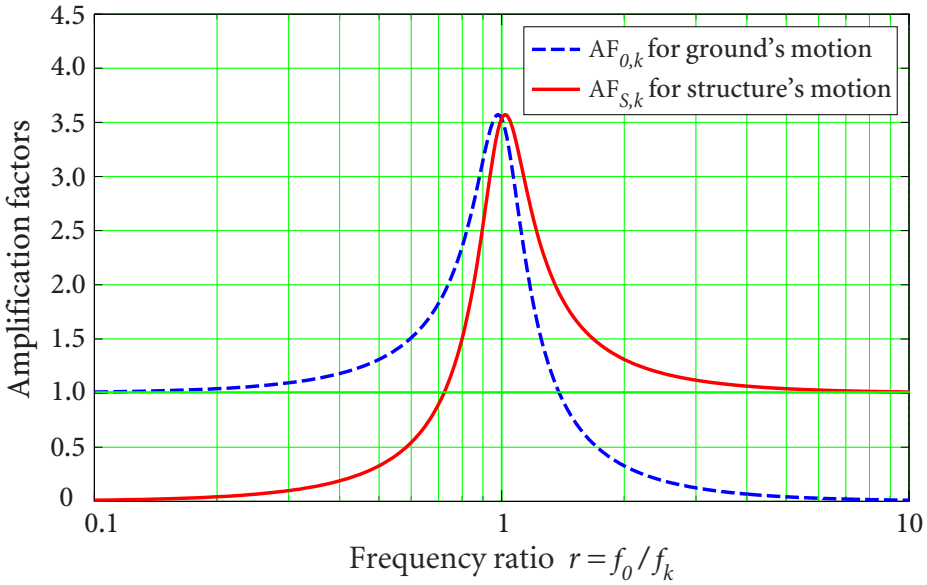

Figure 5.4 Modal amplification factors ($\zeta_0 = \zeta_k = 5\%$)

5.2.4 Secondary Structures

Secondary structures mounted on primary structures are usually stiffer, having fundamental frequencies ranging from 5-40 Hz and can be more vulnerable to high-frequency ground motions (EPRI, 2007). Seismic demand leading to their failures is closely related to their dynamic characteristics.

(1) **Number of significant modes**. A sufficient number of modes should be included to accurately estimate the seismic demand. Relative contribution of modal response to the total response should be calibrated. When only one-mode response is significant, a SDOF model can be used, which is common for nuclear applications. Otherwise, a MDOF model should be used to capture responses of all significant modes.

(2) **Combination of tri-directional responses**. When the total seismic demand is governed primarily by one horizontal earthquake component, responses in other two earthquake directions can be neglected. For example, the in-plane flexure demand of shear walls (EPRI, 1991a). Otherwise, tri-directional responses need to be combined to estimate the total demand (USNRC, 2006). For example, the tension and shear demands of anchor bolts.

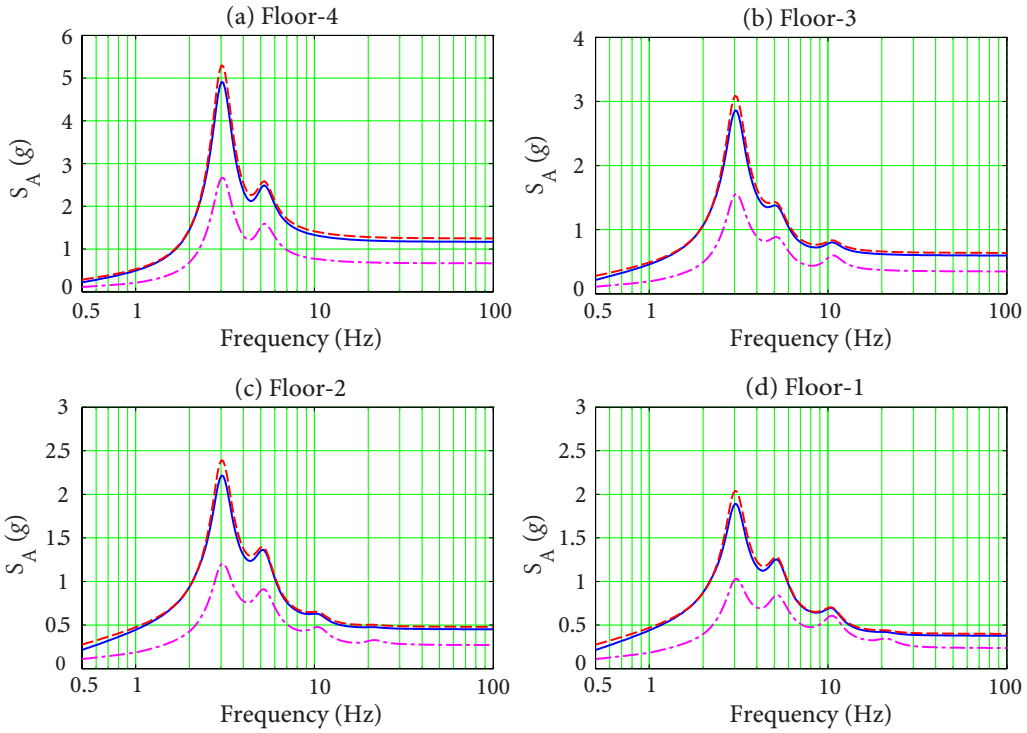

Figure 5.5 Floor response spectra for structure S-1

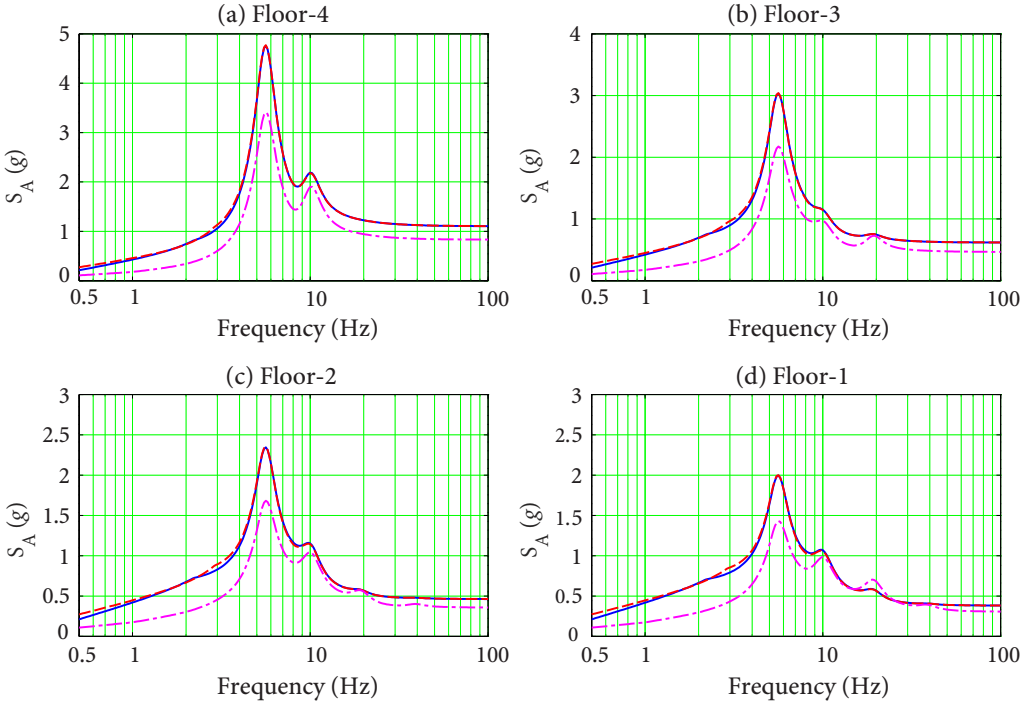

Figure 5.6 Floor response spectra for structure S-2

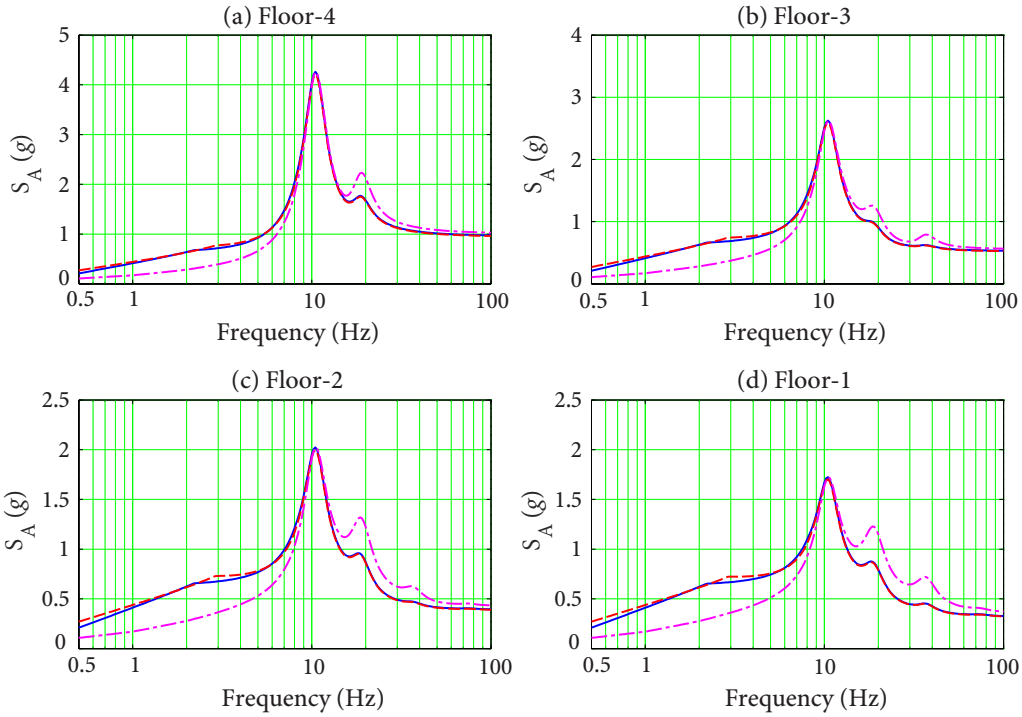

Figure 5.7 Floor response spectra for structure S-3

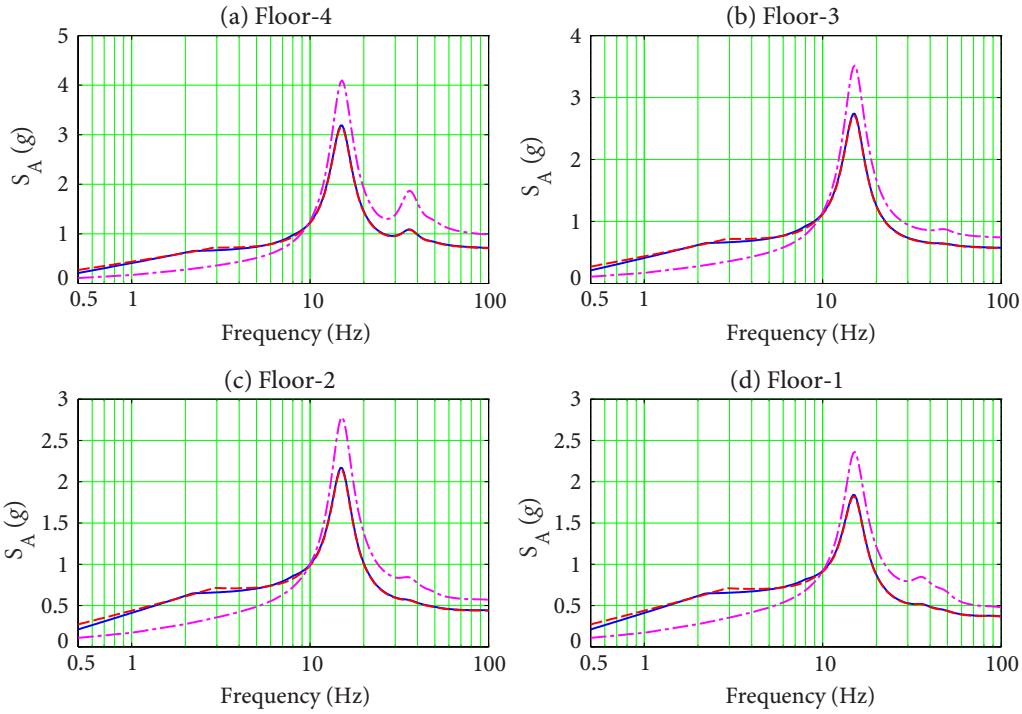

Figure 5.8 Floor response spectra for structure S-4

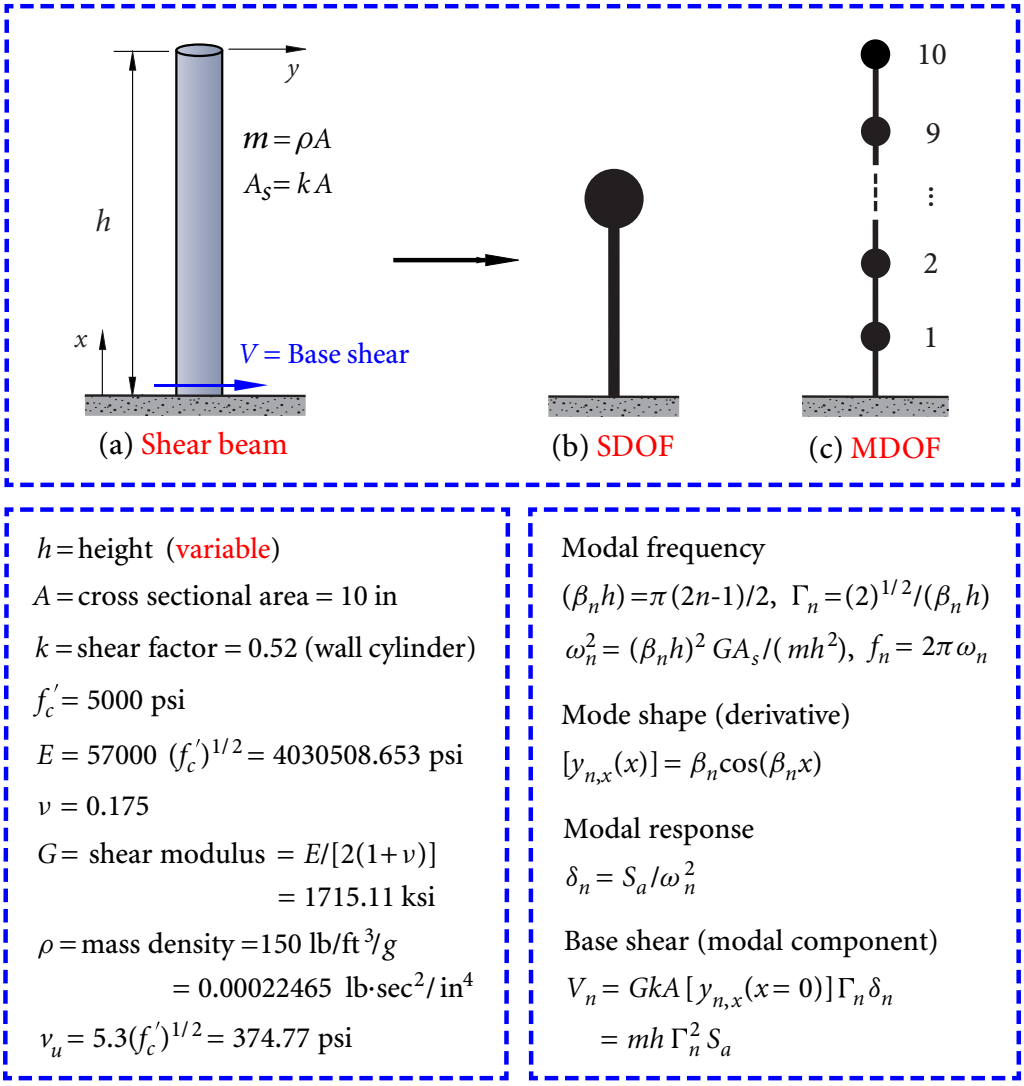

Figure 5.9 Uniform shear beam models, material properties, analytic formulas of modal information and response components

Without losing generality, the uniform shear beam shown in Figure 5.9 is adopted as the secondary structure. It was used in the study of high-frequency ground motion issues for typical CEUS sites (EPRI, 2007). Its desirable features include: (1) it is a simple structure governed by the base shear failure, (2) its modal information is of analytic form, which allows an accurate assessment of the modal base shear components. Suppose that it is a cylinder beam of pure concrete construction. Its geometry, material properties, and analytic formulas of modal information and base shear components are provided in Figure 5.9.

Using the shear beam, effects of various dynamic characteristics can be evaluated. Both the SDOF and MDOF models (first 10 modes) are used for seismic demand analysis. Necessary modifications are made to emphasize its possible dynamic characteristics. For illustration, a number of 201 shear beams are generated with fundamental frequencies equally spaced in log-scale from 1-100 Hz.

5.2.5 Ground Motion Parameters

A GMP needs to be selected for defining seismic capacity, which should be consistent with that used in hazard analysis. Three popular choices for nuclear applications are:

1. **Peak Ground Acceleration (PGA)**. It describes how hard the earth shakes in an earthquake at a given site. PGA can be realistically applied when the SSC is relatively rigid and responds primarily to the high-frequency ground motions.
2. **Spectral Acceleration (SA)**. SA at the fundamental frequency of a SSC $S_a(f_1)$ describes the maximum force that an earthquake exerts on the SSC having a frequency of f_1; it captures the frequency content of ground motion that the SSC primarily responds to and has been a more popular choice than PGA.
3. **Average SA over a frequency range**. $S_{a,\text{avg}}$ is often used to minimize the effect of ground motion uncertainty on evaluating seismic capacity, or to capture responses from several significant modes (Bianchini *et al.*, 2009). In general, the most amplified region on GRS, e.g., from 3-8.5 Hz, is a typical frequency range that dominates the plant risk (see PG&E, 2011, Chap. 6). In this study, average SA over 3-8 Hz is adopted, which is the most amplified region on Newmark-type spectra (see Figure 5.2).

In the following, seismic capacity defined in terms of PGA, S_a, and $S_{a,\text{avg}}$ are referred to as PGA capacity, $S_a(f_1)$ capacity, and $S_{a,\text{avg}}$ capacity, respectively.

5.3 Parametric Study of the Uniform Shear Beam

The static base shear strength V_c of the shear beam is given by the product of cross-sectional shear area A_S and the allowable shear stress ν_u (see Figure 5.9)

$$V_c = A_S \times \nu_u = 0.52 \times \pi \left(\frac{10}{2}\text{in}\right)^2 \times 374.77\ \text{psi} = 1.531 \times 10^4\ \text{lb} = 15.31\ \text{kip}.$$

Its modal participation factors Γ_n are found to be 0.90, 0.30, 0.18, 0.129, 0.10, and 0.082 for the first six modes, showing that it will respond primarily to the first several vibration modes. Since modal frequencies are well separated ($f_n/f_1 = 1, 3, 5, Cdots$), the SRSS rule can be applied to combine the modal responses.

Since the shear failure of pure concrete beam is brittle, no credit can be taken from the inelastic energy absorption factor, hence $F_\mu = 1.0$. For the chosen median GRS shapes, the primary/secondary structural system located on rock site, analyzed using reasonable structural models and median damping ratios, and response components combined using the SRSS or "100-40-40" rule, all the demand variables affecting seismic capacity have median factors equal to unity, i.e., $F_{R_i,m} = 1.0$. Hence, the most significant factor affecting the median seismic capacity A_m is the strength factor F_S, which is the focus of this study.

5.3.1 Idealized SDOF Model

Suppose to begin that the secondary structure is a linear oscillator with frequency f_0. This can be achieved by specifying beam height h and setting $\Gamma_1 = 1$ and $\Gamma_n = 0$ for $n = 2, 3, \cdots$. Seismic capacity of the beam can increase substantially as its frequency increases (structure becomes stiffener) (EPRI, 2007). Since the consistency of seismic capacity is of interest, beam height h is set constant and beam frequency is varied directly. This allows the resulting seismic capacities to stay in the same order.

For each possible combination of the input parameters defined in Table 5.1, median seismic capacity A_m is evaluated using the FA method. Figures 5.10-5.13 illustrate the capacities for each SDOF beam model (by frequency) on all four primary structures. In each Figure, results are given for three GRS shapes, four floors, and three capacities (denoted as Tri-Capacity). The inconsistency patterns shown in Figures 5.10-5.13 are complicated, but in general, it shows that:

- The difference of seismic capacities A_m against the two Newmark-type spectra (R.G. 1.60 and NUREG/CR-0098 spectra) are fairly small regardless of the GMP used.
- Only the difference of seismic capacities A_m against the Newmark-type spectra and the UHS for the CEUS site can be large.

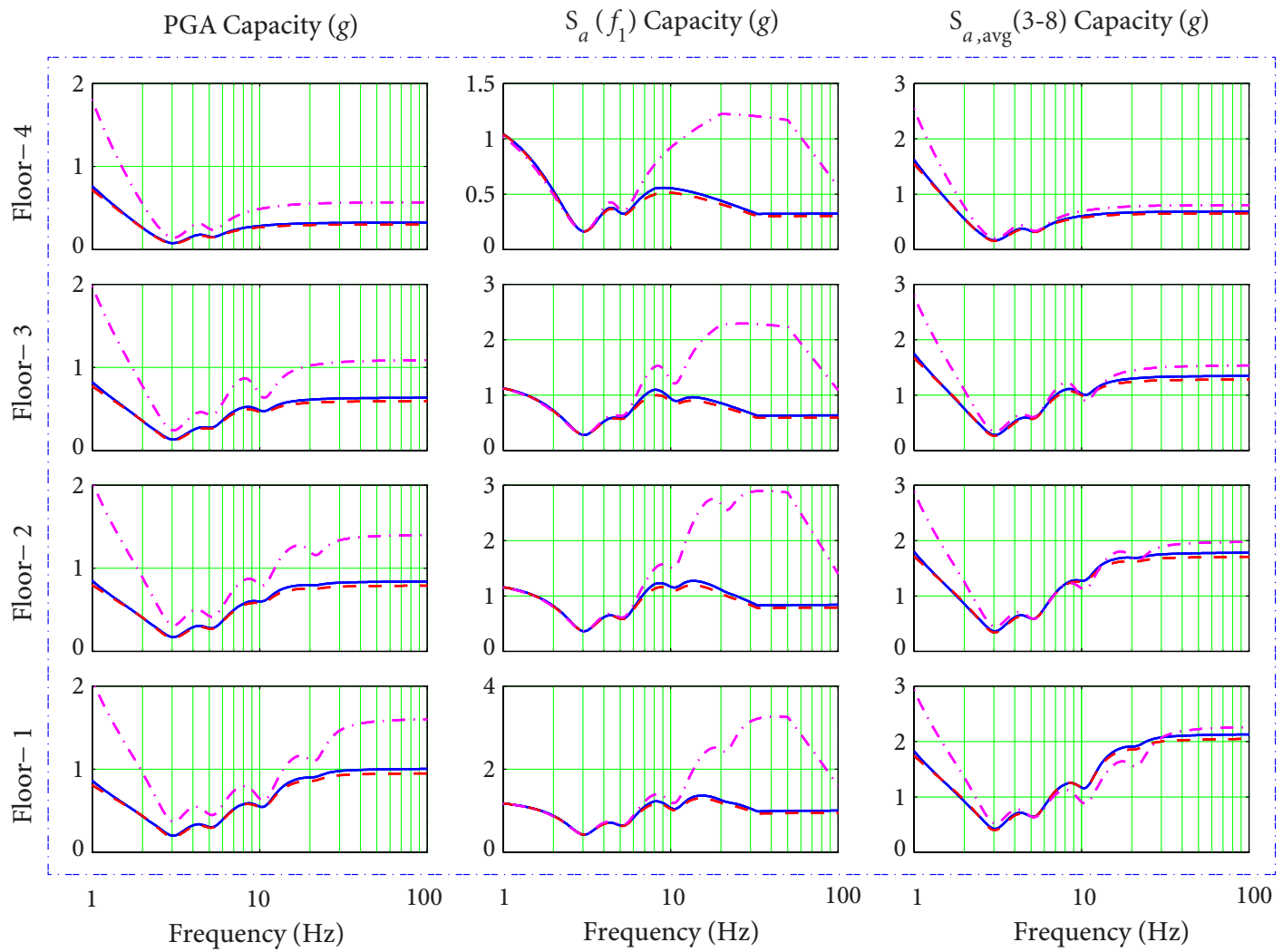

Figure 5.10 Median seismic capacity of the SDOF beam model in structure S-1

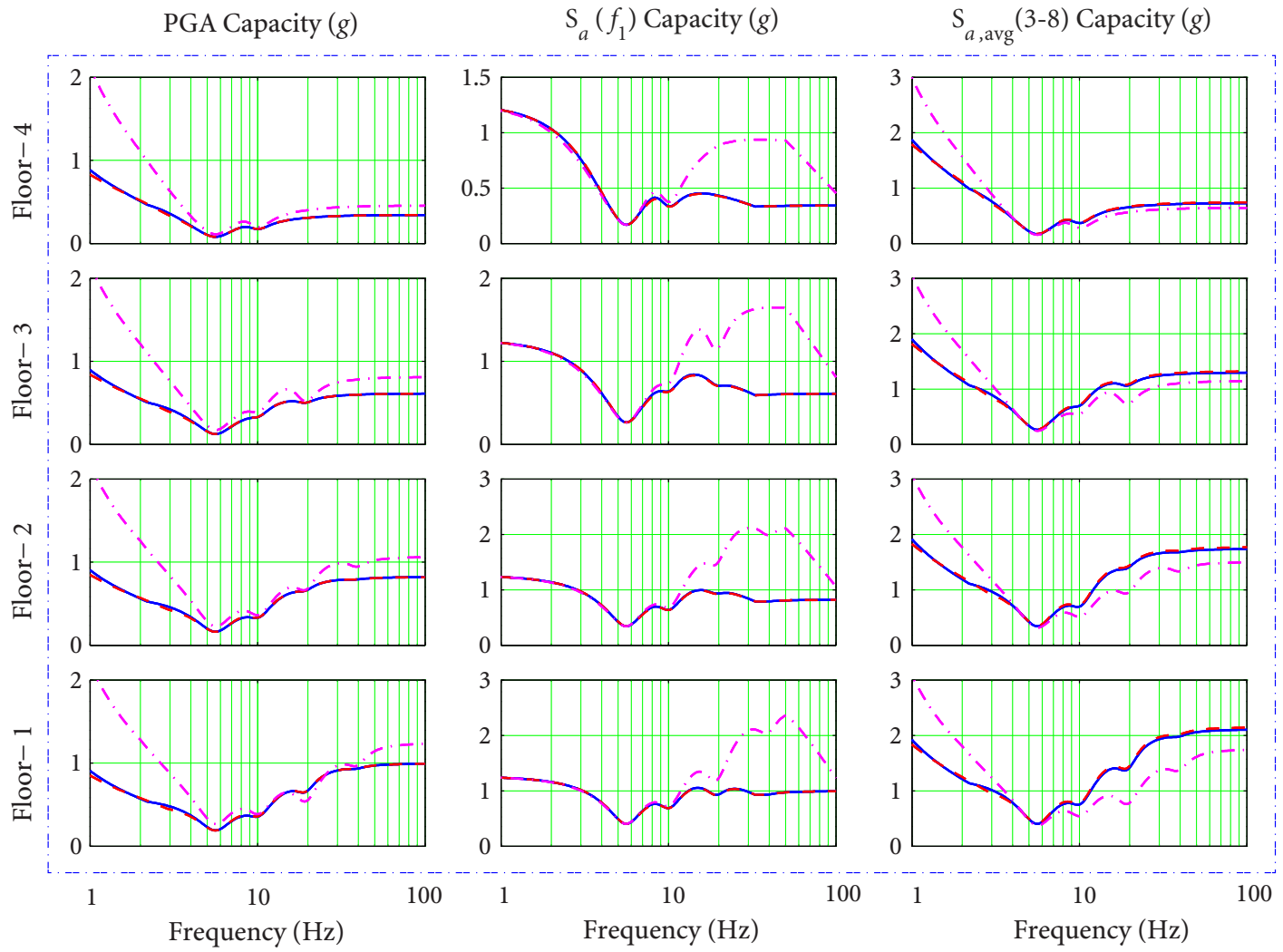

Figure 5.11 Median seismic capacity of the SDOF beam model in structure S-2

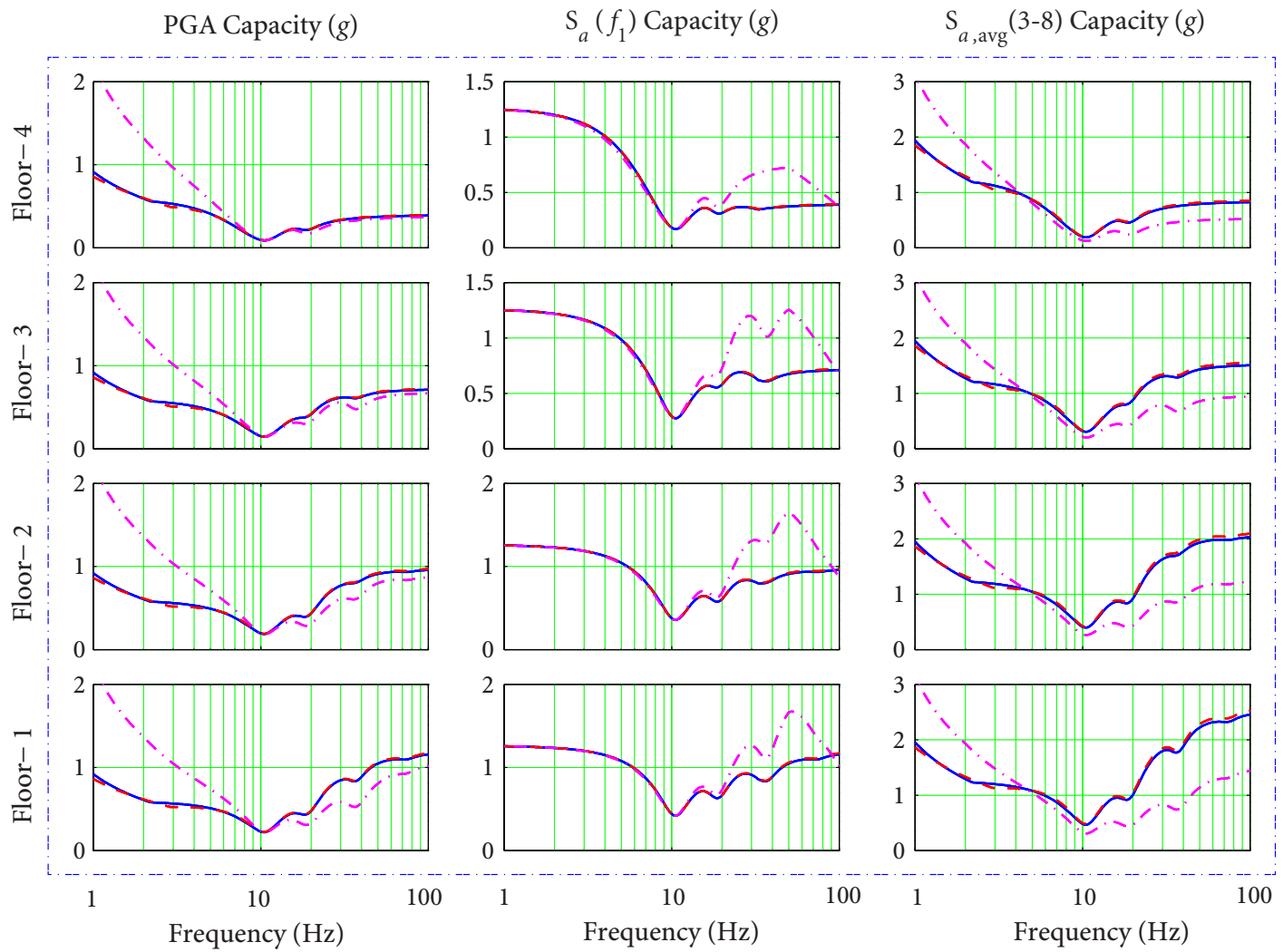

Figure 5.12 Median seismic capacity of the SDOF beam model in structure S-3

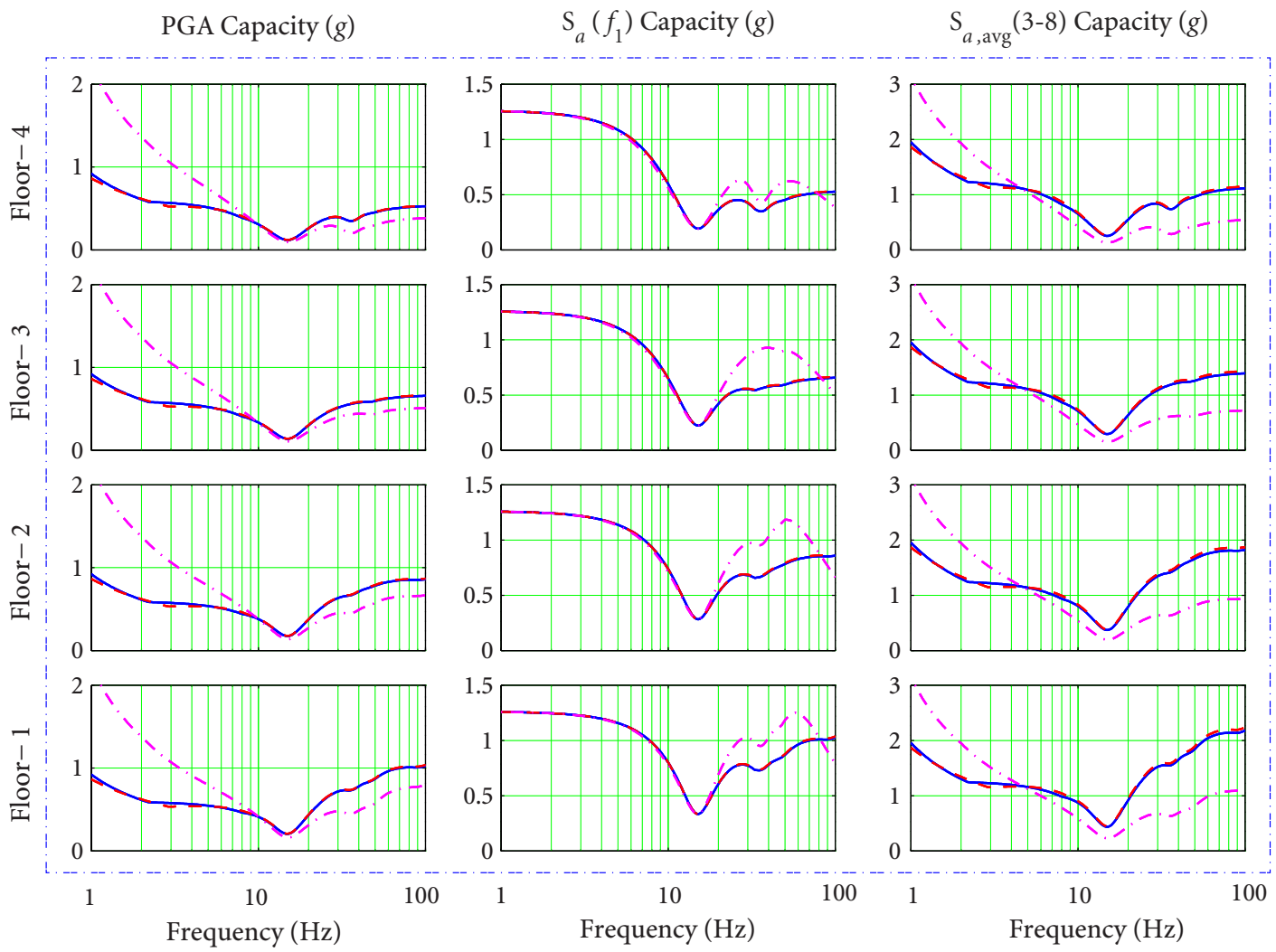

Figure 5.13 Median seismic capacity of the SDOF beam model in structure S-4

Analytic Derivations

To better understand the factors affecting the consistency of seismic capacity, analytic derivations can be resorted to. Denote S_a^G and S_a^F as spectral accelerations of GRS and FRS, respectively. The median seismic capacity A_m for the SDOF model is given by

(1) PGA Capacity

$$A_m = \frac{V_c}{V_d} \cdot F_\mu \cdot \text{PGA} = \frac{(k\,A)\cdot v_u}{(\rho\,A\,h)\cdot S_a^F(f_0)} \times 1.0 \times \text{PGA} = \frac{0.3\,k\,v_u}{\rho\,h} \cdot \frac{1}{S_a^F(f_0)} = \frac{0.3\,k\,v_u}{\rho\,h} \cdot \frac{1}{\text{FRS}}.$$

(2) $S_a(f_0)$ Capacity

$$A_m = \frac{V_c}{V_d} \cdot F_\mu \cdot S_a^G(f_0) = \frac{(k\,A)\cdot v_u}{(\rho\,A\,h)\cdot S_a^F(f_0)} \times 1.0 \times S_a^G(f_0) = \frac{k\,v_u}{\rho\,h} \cdot \frac{S_a^G(f_0)}{S_a^F(f_0)} = \frac{k\,v_u}{\rho\,h} \cdot \frac{1}{\text{AF}}.$$

where $\text{AF} = \dfrac{S_a^F(f_0)}{S_a^G(f_0)} = \dfrac{\text{FRS}}{\text{GRS}}$ is the amplification factor at frequency f_0.

(3) $S_{a,\text{avg}}$(3-8) Capacity

$$A_m = \frac{V_c}{V_d} \cdot F_\mu \cdot S_{a,\text{avg}}^G = \frac{(k\,A)\cdot v_u}{(\rho\,A\,h)\cdot S_a^F(f_0)} \times 1.0 \times S_{a,\text{avg}}^G = \frac{k\,v_u}{\rho\,h} \cdot \frac{S_{a,\text{avg}}^G}{\text{FRS}}.$$

where $S_{a,\text{avg}}^G = 0.636g$, $0.647g$, and $0.423g$ for the NUREG/CR-0098, R.G. 1.60, and UHS-Memphis spectra, respectively.

☞ While parameters k, v_u, ρ, h are constants for a given SDOF model, the degree of consistency in capacity estimates A_m is primarily governed by $\frac{1}{\text{FRS}}$ and $\frac{1}{\text{AF}}$, where $\text{FRS} = S_n(f_0, \zeta_0)$ is defined in equation (5.2.1) and given in Figures 5.5-5.8.

Amplification factor AF_n of floor-n is obtained by dividing the FRS by the GRS

$$\text{AF}_n^2(f_0, \zeta_0) = \Big[\sum_{k=1}^{N} \Gamma_k\,\phi_{nk} \cdot \text{AF}_{0,k}\Big]^2 + \sum_{k=1}^{N} \Big[\Gamma_k\,\phi_{nk} \cdot \text{AF}_{S,k} \cdot \frac{S_\text{A}(f_k, \zeta_k)}{S_\text{A}(f_0, \zeta_0)}\Big]^2. \qquad (5.3.1)$$

Figures 5.14-5.17 shows the AF, corresponding to the FRS shown in Figures 5.5-5.8.

General Observations

From equations (5.2.1) and (5.3.1), and FRS and AF plots, some observations are made.

- The differences in both the FRS and AF shapes result from the difference in GRS shapes. The modal contribution factor $\Gamma_k\,\phi_{nk}$ and modal AF terms $\text{AF}_{0,k}$ and $\text{AF}_{S,k}$ multiplied to the GRS are the same for a given primary structure.

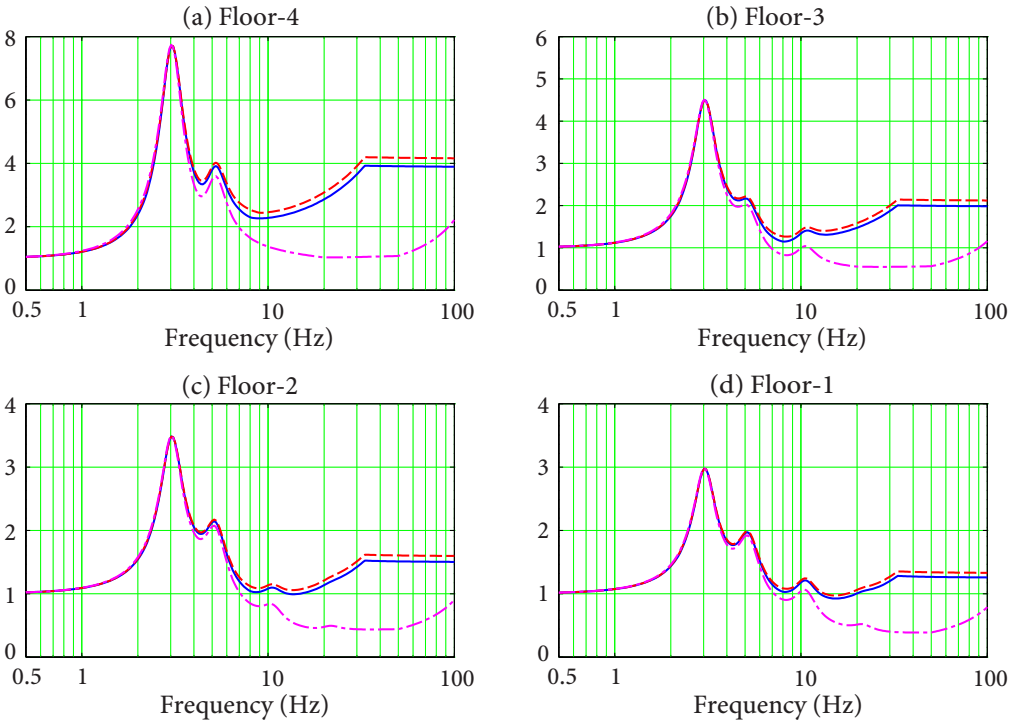

Figure 5.14 Amplification factors of FRS for structure S-1

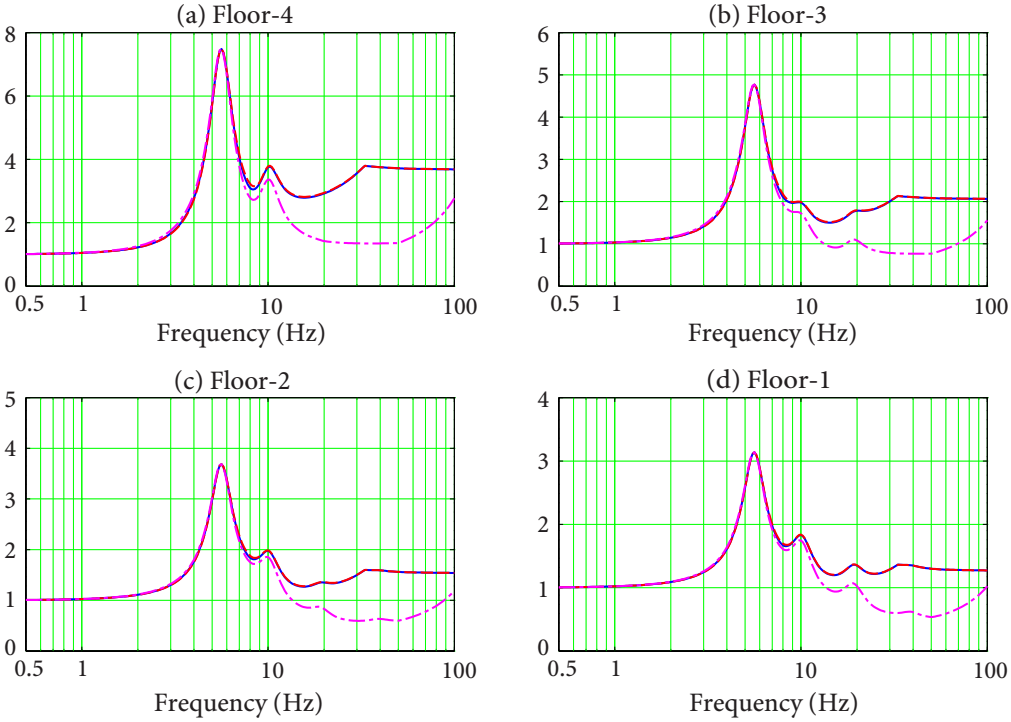

Figure 5.15 Amplification factors of FRS for structure S-2

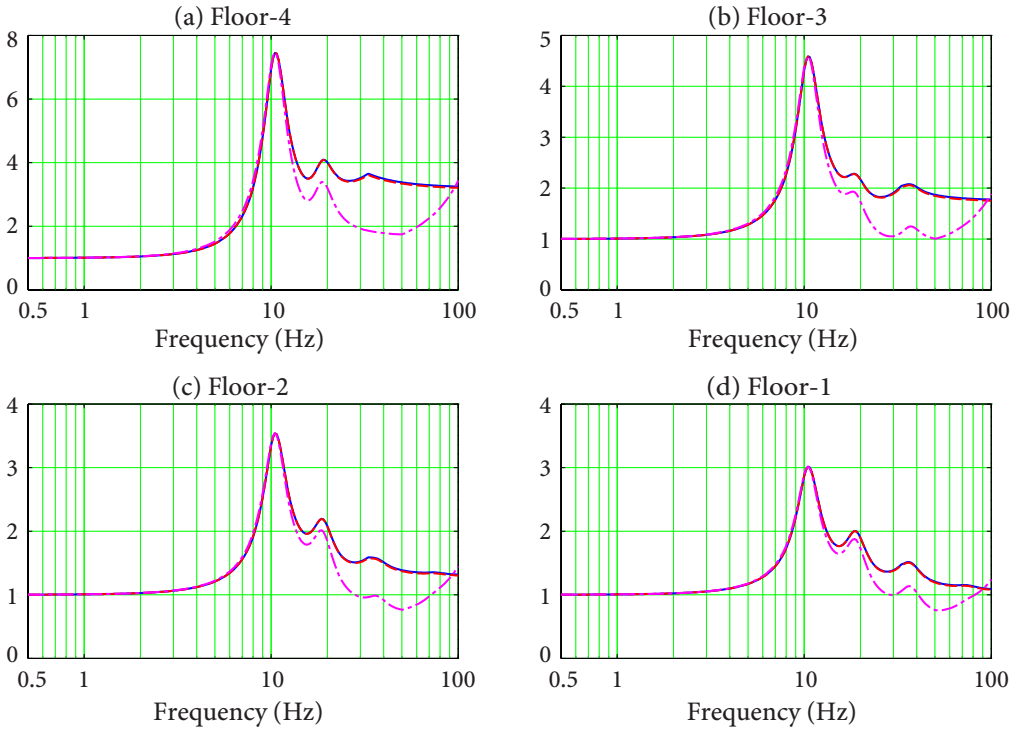

Figure 5.16 Amplification factors of FRS for structure S-3

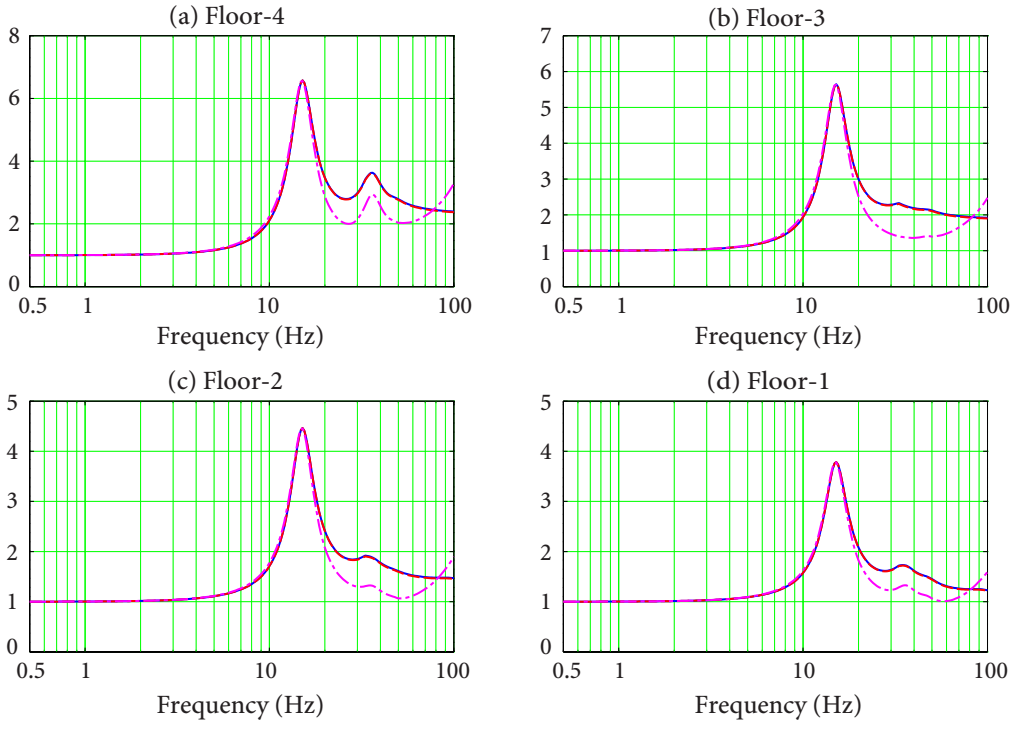

Figure 5.17 Amplification factors of FRS for structure S-4

- The difference in FRS shapes can be characterized from the two terms in equation (5.2.1). The first term contributes most to FRS amplitudes at low frequency portion ($f_0 \leqslant f_1$), where $\mathrm{AF}_{0,k} \to 1.0$ and $\mathrm{AF}_{S,k} \to 0$, which reflects mainly the difference in ground's motion $S_\mathrm{A}(f_0, \zeta_0)$. The second term contributes most to FRS amplitudes at high frequency portion ($f_0 > f_k$), where $\mathrm{AF}_{0,k} \to 0$ and $\mathrm{AF}_{S,k} \to 1.0$, which reflects mainly the difference in structure's motion $S_\mathrm{A}(f_k, \zeta_k)$, especially of mode $k = 1$.

- The difference in AF shapes can be characterized from the two terms in equation (5.3.1). The first term contributes most to AF values at frequency portion $f_0 \leqslant f_1$, which is constant. The second term, involving a frequency-dependent ratio $S_\mathrm{A}(f_k, \zeta_k)/S_\mathrm{A}(f_0, \zeta_0)$, affects AF values at frequency portion $f_0 > f_k$. General shapes of this ratio are given in Figure 5.18 for modal frequencies of structure S-2. The inconsistency of AF (see Figure 5.15) for $f_0 > f_k$ results mainly from mode $k = 1$.

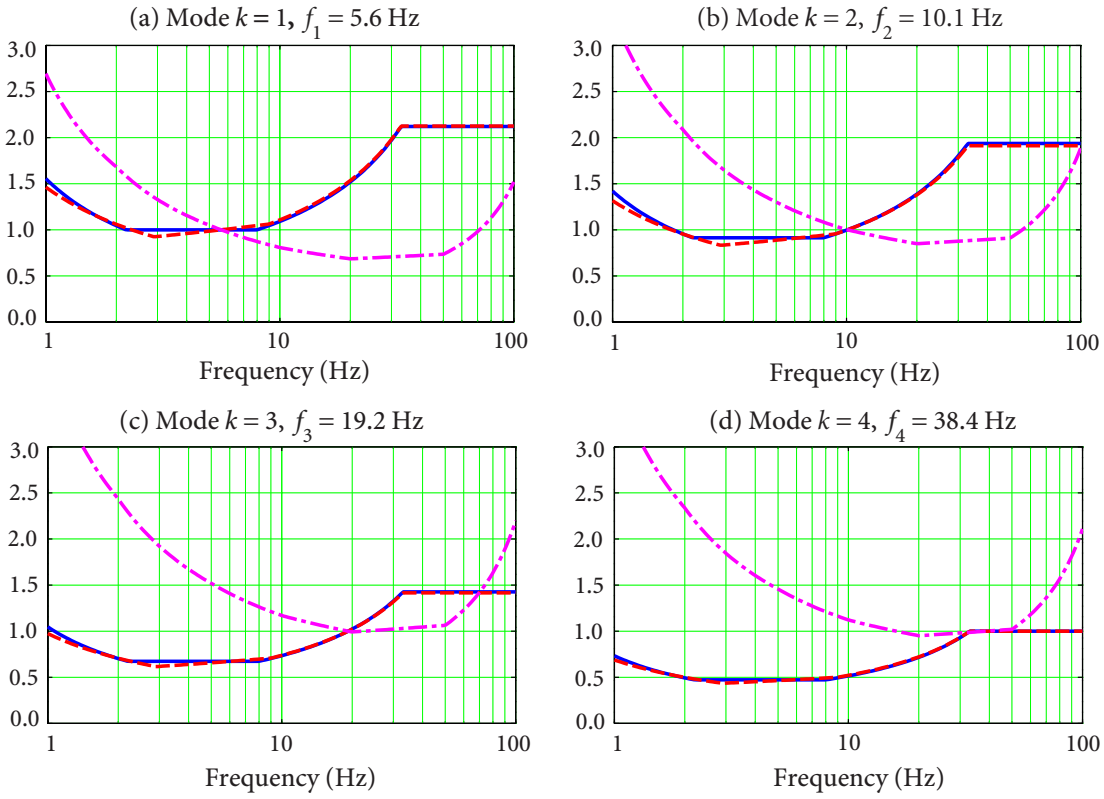

Figure 5.18 $S_\mathrm{A}^2(f_k, \zeta_k)/S_\mathrm{A}^2(f_0, \zeta_0)$ ratios of mode $k = 1, 2, 3, 4$ for primary structure S-2

Case-by-case Analysis

For any particular case of concern, a detailed case-by-case analysis can be performed. In the following, the effect of changing a single factor on seismic capacity is investigated.

1. Change of GRS Shape. By changing GRS shapes, $S_{\mathrm{A}}(f_0, \zeta_0)$ and $S_{\mathrm{A}}(f_k, \zeta_k)$ in equations (5.2.1) and (5.3.1) become variables. Consider floor-4 of structure S-3 ($f_1 = 10.5$Hz). The associated FRS, AF, and seismic capacities A_m are given in Figure 5.19(a).

1. The consistency of Tri-capacity depends primarily on the consistency of FRS and AF.

   ❧ PGA capacity is inversely proportional to FRS. At frequency portion $f_0 < f_1$, it can be highly inconsistent due to the difference in ground's motion. At frequency portion $f_0 > f_1$, its consistency depends on structure's motion $S_{\mathrm{A}}(f_k, \zeta_k)$ ($k = 1, \cdots, 4$), especially $k = 1$.

   ❧ $S_{a,\mathrm{avg}}$(3-8) capacity is also inversely proportional to FRS. It is also scaled by a spectrum-specific parameter $S_{a,\mathrm{avg}}$(3-8), which are close for two Newmark-type spectra (0.647g, 0.636g), but is 1/3 smaller for UHS-Memphis (0.423g). The combined effect of FRS and $S_{a,\mathrm{avg}}$(3-8) on A_m, however, is case-dependent.

   ❧ $S_a(f_0)$ capacity is inversely proportional to AF, which is always quite consistent at frequency $f_0 < f_1$, but can be highly inconsistent at frequency

2. The difference in FRS shapes at low frequency portion is mainly due to the differences in GRS shapes. The difference in FRS shapes at high frequency portion is significantly influenced by GRS amplitudes $S_{\mathrm{A}}(f_1, \zeta_1)$ at the fundamental frequency f_1 of structure S-3. Since $S_{\mathrm{A}}(f_1 = 10.5\,\mathrm{Hz}, \zeta_1)$ amplitudes of the three GRS are close, the FRS remain consistent from f_1 onward close to f_2, where inconsistency is introduced by the difference in $S_{\mathrm{A}}(f_2 = 18.9\,\mathrm{Hz}, \zeta_2)$ of the three GRS. In addition, equation (5.3.1) shows that modal contribution factor $\Gamma_2 \cdot \phi_{4,2}$ also affects the inconsistency. In case when $\Gamma_2 \cdot \phi_{4,2}$ is small, the inconsistency vanishes.

3. AF shapes at low frequency portion are fairly consistent. In contrast, they are highly inconsistent at high frequency portion, which is due to the ratios $S_{\mathrm{A}}(f_k, \zeta_k)/S_{\mathrm{A}}(f_0, \zeta_0)$ shown in Figure 5.18. For frequency $f_1 < f_0 < f_2$, the inconsistency due to ratio $S_{\mathrm{A}}(f_1, \zeta_1)/S_{\mathrm{A}}(f_0, \zeta_0)$ is partially reduced by $S_{\mathrm{A}}(f_2, \zeta_2)/S_{\mathrm{A}}(f_0, \zeta_0)$ after modal com-

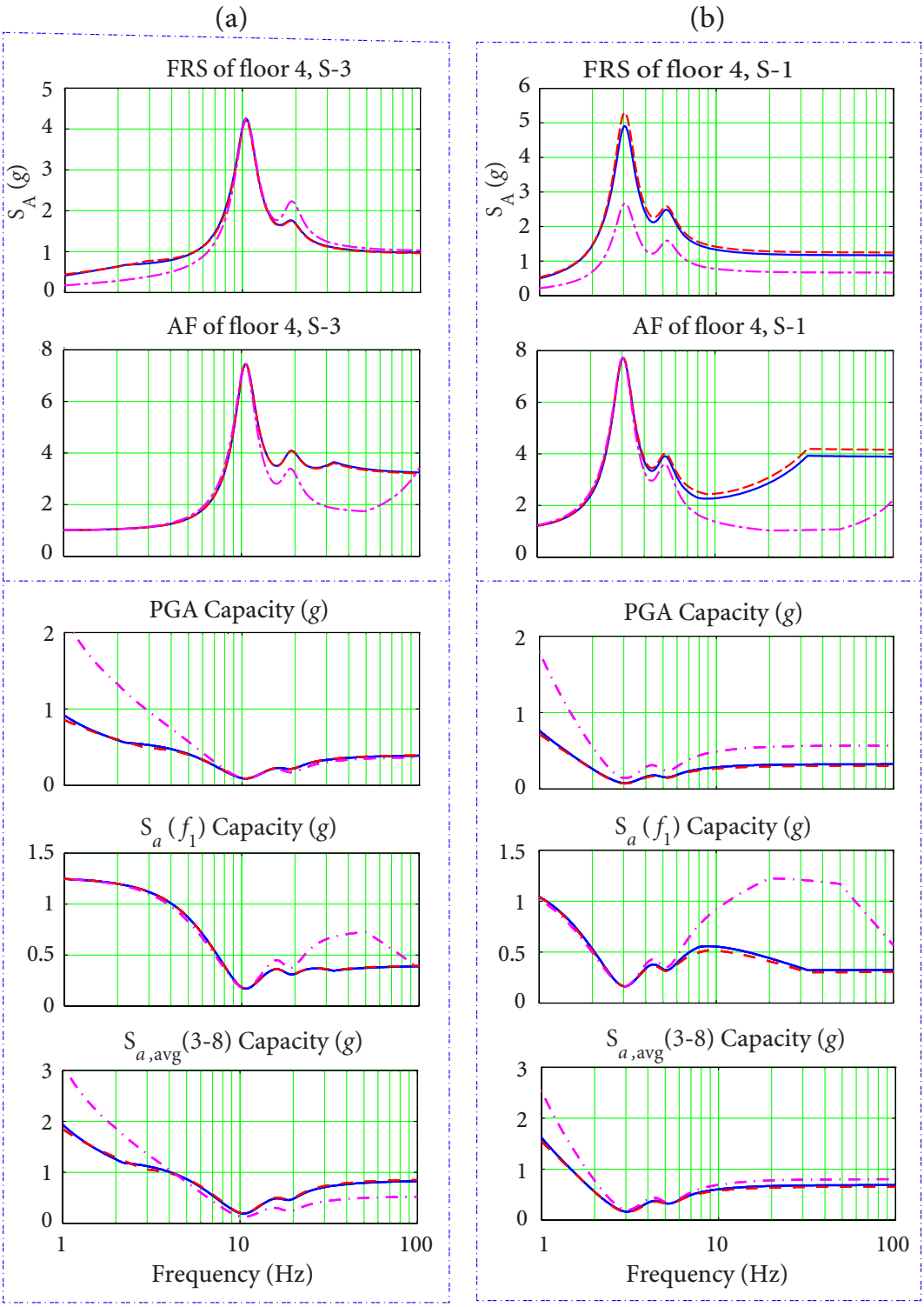

Figure 5.19 FRS, AF, Seismic capacity plots for primary structures S-1 and S-3

bination, because of the inverse order of ratios associated with three GRS. For frequency $f_0 > f_2$, the inconsistency due to $S_A(f_1, \zeta_1)/S_A(f_0, \zeta_0)$ is strengthened by $S_A(f_2, \zeta_2)/S_A(f_0, \zeta_0)$, because of the same order of ratios $S_A(f_k, \zeta_k)/S_A(f_0, \zeta_0)$ $(k = 1, 2)$ associated with the GRS. Mode participation factors of higher modes are usually too small to matter, hence is not discussed further. The consistency observed at 100 Hz, is dominated by the consistency of $S_A(f_1, \zeta_1)/S_A(f_0, \zeta_0)$ of the three GRS.

2. Change of Primary Structure. By changing primary structures, $\Gamma_k \phi_{nk}$, $AF_{0,k}$, $AF_{S,k}$, and $S_A(f_k, \zeta_k)$ become variables. Consider floor-4 of structures S-3 and S-1 as example. The associated FRS, AF, and seismic capacities are shown in Figure 5.19(a) and (b), respectively. Since A_m depends primarily on FRS and AF shapes, analyses are focused on them only.

1. Characteristics of FRS shapes:

- At frequency portion $f_0 < f_1$, since the difference in FRS shapes depends primarily on ground's motion (GRS shapes), change of structure has insignificant effect. For example, the weakest UHS gives the weakest FRS, regardless of primary structure.
- In the vicinity of $f_0 = f_1$, ground's motion equals structure's motion; they equally affect the FRS. The difference in FRS amplitudes reflects the difference in GRS amplitudes, which can be clearly seen from the main peaks of FRS.
- At frequency portion $f_0 > f_1$, the difference in FRS shapes is dominated by structure's motion $S_A(f_1, \zeta_1)$. The FRS from UHS in Figure 5.19(b) is always weaker than those from Newmark-type spectra. It explains why regular nuclear structures, having fundamental frequency less than 10 Hz, are not supposed to respond significantly to high-frequency ground motions for CEUS sites; hence the stiffer, high-frequency equipment or components mounted thereon are not significantly affected.

2. Characteristics of AF shapes:

- At frequency portion $f_0 < f_1$ and in the vicinity of $f_0 = f_1$, AF is highly consistent regardless of the primary structure. This is because the first term in equation (5.3.1) is constant for a given primary structure.
- At frequency portion $f_0 > f_1$, AF can be highly inconsistent and is strongly affected by primary structure. As seen from the second term in equation (5.3.1), the consistency

of AF is governed by the ratio $S_{\mathrm{A}}(f_k,\zeta_k)/S_{\mathrm{A}}(f_0,\zeta_0)$, which is structure-dependent. By changing primary structures, these ratios change significantly. As can be inferred from Figure 5.18, the ratio $S_{\mathrm{A}}(f_1,\zeta_1)/S_{\mathrm{A}}(f_0,\zeta_0)$ for structure S-1 with $f_1=3.0$ Hz is more inconsistent than for structure S-3 with $f_1=10.5$ Hz. In addition, modal combination partially reduces the inconsistency of AF in frequency range f_1–f_2, but strengthens the inconsistency at frequency portion $f_0>f_2$.

In the above, the simplest type of secondary structure, a linear oscillator, has been evaluated as a natural starting point. Further improvements for more complex secondary structures are looked forward next.

5.3.2 Idealized MDOF Model

Suppose that the uniform shear beam is represented by a linear MDOF model. For illustrating the principles, it is further assumed that the SRSS approximation is exact. Denote f_i^0 as the ith modal frequency of a secondary structure to distinguish from the frequency f_k of a primary structure. The $S_a(f_1^0)$ seismic capacity formula for an N-DOF model can be derived as below (derivation in terms of other GMP is similar and not given)

$$A_m=\frac{V_c}{V_d}\cdot F_\mu\cdot S_a^G(f_1^0)=\frac{A_S\cdot v_u}{\sqrt{\sum_{i=1}^{N}\left(\rho\,A\,h\,\Gamma_i^2\,S_a^F(f_i^0)\right)^2}}\cdot 1.0\cdot S_a^G(f_1^0)=\frac{k\,v_u\,S_a^G(f_1^0)}{\rho\,h\sqrt{\sum_{i=1}^{N}\left(\Gamma_i^2\,S_a^F(f_i^0)\right)^2}}$$

$$=\frac{k\,v_u\,S_a^G(f_1^0)}{\rho\,h\,\Gamma_1^2\,S_a^F(f_1^0)\sqrt{1+\left(\frac{\sum_{i=2}^{N}\Gamma_i^2\,S_a^F(f_i^0)}{\Gamma_1^2\,S_a^F(f_1^0)}\right)^2}}=\frac{k\,v_u}{\rho\,h\cdot\mathrm{AF}}\cdot\frac{1}{\Gamma_1^2\sqrt{1+\left(\frac{\sum_{i=2}^{N}\Gamma_i^2\,S_a^F(f_i^0)}{\Gamma_1^2\,S_a^F(f_1^0)}\right)^2}}.$$

It shows an additional fractional term about higher-mode contribution in seismic capacity formula for the N-DOF model. Additional inconsistency beyond that due to AF can be introduced through this fractional term. Noting that the sum of all modal participation factors Γ_i^2 ($i=1,2,\cdots$) is equal to 1.0 in an SRSS sense, $\Gamma_i^2\cdot S_a^F(f_i)$ represents the response of the ith mode. Hence, this term calibrates the responses of higher modes relative to the fundamental mode. Only when higher modes make a comparatively strong contribution to the total demand V_d, additional inconsistency introduced can be significant.

To evaluate the effect of this fractional term on the inconsistency of seismic capacity, three cases are considered. Suppose that the shear beams are mounted on structure S-2.

1. 10-DOF Model with Original Modal Participation Factors

Consider the first 10 modes of the original shear beam model in response analysis. For the large participation factor $\Gamma_1 = 0.90$, higher-mode responses should be insignificant.

The resulting seismic capacities are shown in Figure 5.20, which are slightly larger than those from the SDOF model shown in Figure 5.11. This is because the inclusion of higher-mode responses $\Gamma_i^2 \cdot S_a^F(f_i^0)$ actually leads to lower seismic demand, hence larger seismic capacities.

Inconsistency pattern, however, remains the same. Additional inconsistency will be introduced only if $S_a^F(f_i^0)$ amplitudes associated with higher-mode responses differ from each other. The only additional inconsistency, clearly seen in Figure 5.20, is for $f_1^0 \approx 1/3 f_1$, where the second mode response is strongly contributed by different peak FRS amplitudes.

2. Multiple Significant Modes

Manually assign modal participation factors as $\Gamma_{1-10} = [0.6\ 0.6\ 0.38\ 0.28\ 0.18\ 0.12\ 0.08\ 0.05\ 0.03\ 0.02]$, which gives 4 significant modes with the first two modes being equally significant. This leads to the case when higher-mode responses make a strong contribution to the total seismic demand.

The resulting seismic capacities are given in Figure 5.21. Tri-Capacity against Newmark-type spectra and UHS-Memphis show noticeable inconsistency in a wide frequency range; the consistent part previously observed from the SDOF model is greatly impaired. This is because the relative higher-mode to first-mode responses, from Newmark-type spectra and UHS-Memphis, are very different in the entire frequency range considered. This difference along with strong higher-mode contribution result in additional inconsistency of seismic capacities. Note that for the resonance case of $f_1^0 = f_1$, since modal response $\Gamma_1^2 \cdot S_a^F(f_1^0)$ is likely to dominate the total response, the additional inconsistency is relatively small.

Improved consistency of $S_{a,\text{avg}}(f_1\text{-}f_2)$ capacity at frequency portion $f_1^0 < f_1$ is observed, which is due to modal combination, i.e., the additional inconsistency cancels out the original

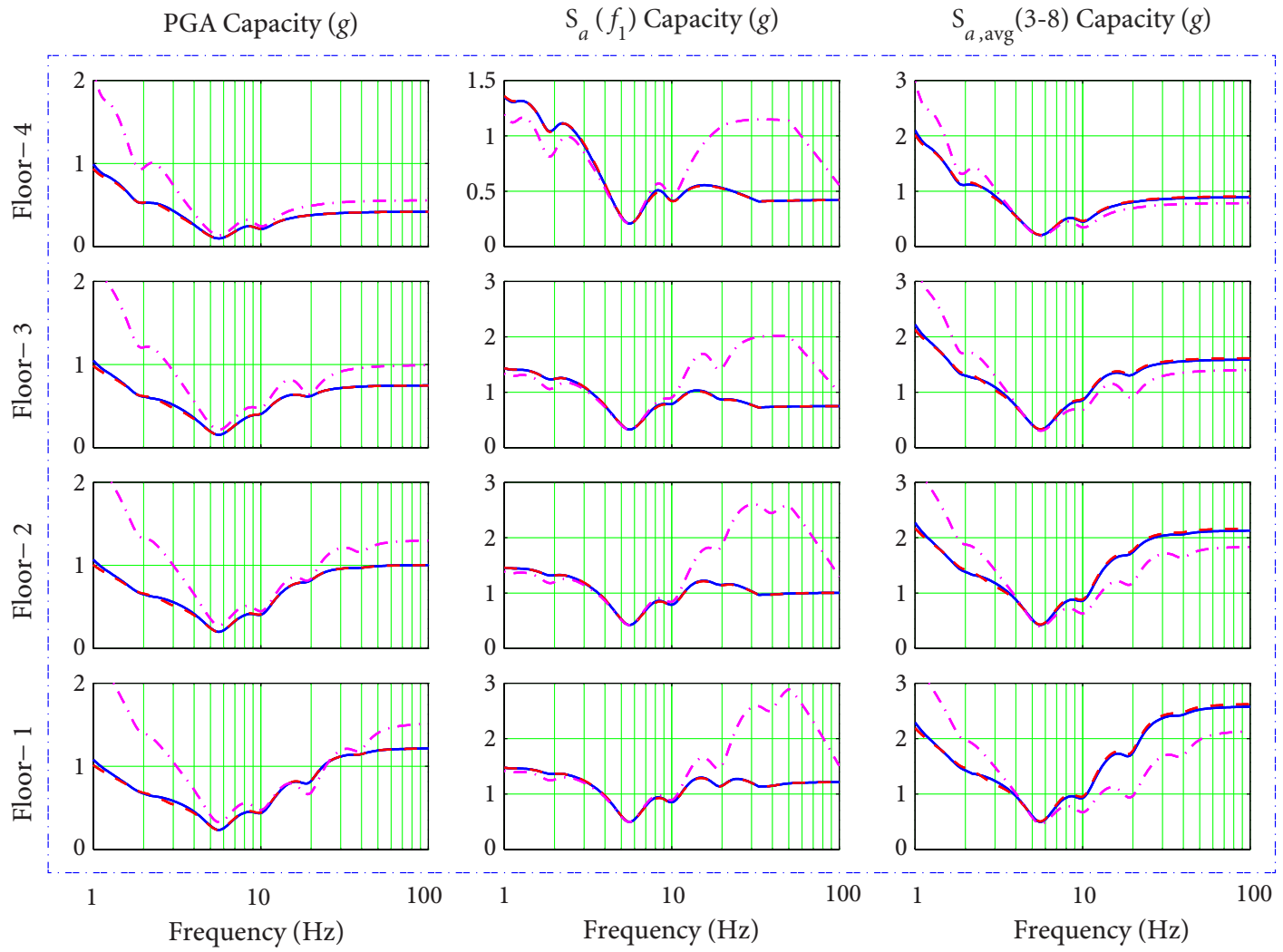

Figure 5.20 Tri-Capacity of the original 10-DOF beam model on structure S-2

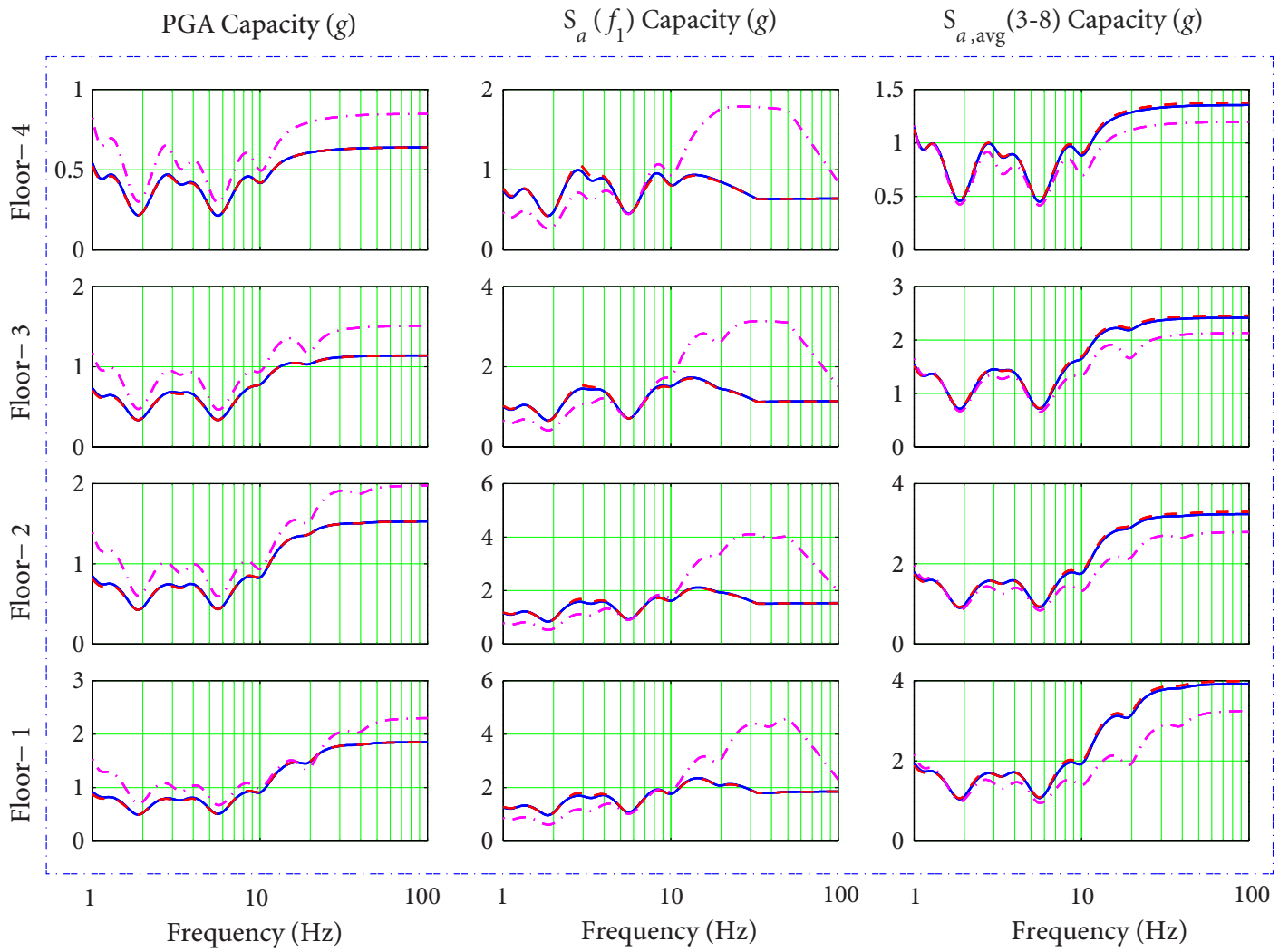

Figure 5.21 Tri-Capacity of 10-DOF beam model on structure S-2, with designated Γ_n =[0.6 0.6 0.38 0.28 0.18 0.12 0.08 0.05 0.03 0.02]

inconsistency from GRS shapes. Conversely, strengthened inconsistency of $S_{a,\text{avg}}(f_1\text{-}f_2)$ capacity at frequency portion $f_1^0 > f_1$ is observed, which is due to the larger higher-mode contribution from the UHS.

It has shown that for multi-mode-dominant secondary structures, factors affecting the consistency of seismic capacities are complex, requiring a case-by-case analysis.

3. Directional Response Combination

For the original shear beam model, consider combination of three earthquake components. In each of the horizontal earthquake directions, maximum shear response is obtained by combining modal responses using the SRSS combination rule. Due to symmetry of the cylinder shear beam, two horizonal responses are equal, i.e., $V_{d,\text{H1}} = V_{d,\text{H2}}$. Suppose that the vertical response does not contribute to the base shear. Combining directional responses using the "100-40-40" combination rule gives the total base shear demand

$$V_d = \sqrt{V_{d,\text{H1}}^2 + (0.4 \cdot V_{d,\text{H2}})^2} = 1.08 V_{d,\text{H1}},$$

which implies that the resulting Tri-Capacity are simply scaled by a factor of $1/1.08 = 0.93$. The consistency makes no difference to the case considering one horizontal response only.

5.3.3 Conclusions and Recommendations from Parametric Study

Factors affecting consistency of seismic capacities for SDOF linear structure

- PGA capacity varies with $\frac{1}{\text{FRS}}$.
- $S_a(f_0)$ capacity varies with $\frac{1}{\text{AF}}$.
- $S_{a,\text{avg}}$(3-8) capacity varies with $\frac{1}{\text{FRS}}$ and is scaled by $S_{a,\text{avg}}$(3-8).

GRS shapes, primary structures, and secondary structures are all factors affecting the differences of FRS and AF, hence affecting the consistency of seismic capacity. Their influences on FRS and AF can be described in a frequency-dependent manner.

Influence on FRS from ground's motion $S_{\text{A}}(f_0, \zeta_0)$ and structure's motion $S_{\text{A}}(f_k, \zeta_k)$

Denote f_0 as the oscillator frequency and f_1 as the fundamental frequency of primary structure.

- When $f_0 < f_1$, the difference in FRS shapes is primarily influenced by ground's motion $S_A(f_0, \zeta_0)$ (GRS shapes). The influence of structure's motion (point GRS amplitudes $S_A(f_1, \zeta_1)$) is insignificant.
- When $f_0 \approx f_1$ (resonance portion), ground's motion $S_A(f_0, \zeta_0)$ is equal to structure's motion $S_A(f_1, \zeta_1)$. They both influence significantly the difference in FRS shapes.
- When $f_0 > f_1$, the influence of ground's motion $S_A(f_0, \zeta_0)$ diminishes and that of structure's motion $S_A(f_1, \zeta_1)$ becomes dominant. $S_A(f_k, \zeta_k)$ at subsequent f_k locally influences FRS shapes, depending on $S_A(f_k, \zeta_k)$ values and modal participation.

Influence on AF from the ratio of structure's motion to ground's motion $\frac{S_A(f_k, \zeta_k)}{S_A(f_0, \zeta_0)}$

- When $f_0 < f_1$, AF is very consistent for a given primary structure; the only term affecting the consistency in AF shapes, this ratio, has little influence.
- When $f_0 \approx f_1$, AF is also very consistent, since this ratio is close to unity regardless of the associated GRS.
- When $f_0 > 1.5 f_1$, AF can be highly inconsistent due to this ratio. Generally, a smaller f_1 will result in more significant inconsistency.

Factors affecting consistency of seismic capacities for MDOF linear structure

- When higher-mode responses make a strong contribution and when the relative higher-mode responses from different GRS differ from each other, additional inconsistency of seismic capacities can be significant.
- The effect of relative higher-mode response on the inconsistency of seismic capacity depends on the relativity of both higher-mode response and the first-mode response from GRS, which requires a case-by-case analysis.

Recommendations of GMP for more consistent seismic capacity estimates

Denote f_1^0 as the 1st-mode frequency of the secondary structure.

- When $f_1^0 < f_1$ or $f_1^0 \approx f_1$, $S_a(f_1^0)$ is a more proper GMP for defining seismic capacity in the sense that it gives more consistent capacity estimates.

- When $f_1^0 > 1.5 f_1$, $S_a(f_1^0)$ is not recommended since it gives highly inconsistent capacity estimates. PGA and $S_{a,\text{avg}}$(3-8) can be better choices. Generally, for typical nuclear structures with $f_1 < 10$ Hz, $S_{a,\text{avg}}$(3-8) is a more proper GMP than PGA.

5.4 Numerical Examples

In this section, two realistic example problems are presented to validate and support the parametric study. The three chosen GRS shapes and primary structure S-2 defined in Section 5.2 are adopted. The block masonry wall and horizontal heat exchanger are adopted as the secondary structures.

5.4.1 Block Wall Median Seismic Capacity

As described in Section 4.2, the block masonry wall is a commonly used barrier in power plant. The primary load imposed on the wall during seismic events is the horizontal floor acceleration. Its seismic capacity is governed by the out-of-plane bending. All calculations follow the same procedure illustrated in Section 4.2.

In dynamic analysis, the wall can be modelled as a SDOF system, which is the simplest case of secondary structure. Its seismic demand can be conveniently represented by the horizontal FRS at its vibration frequency. Correspondingly, its static strength capacity can also be represented by S_a, called static S_a capacity, determined from the best-estimate of moment strength considering strength reduction due to the P-Δ effect.

Note that the inelastic energy absorption factor F_μ and the response factor F_R do not actually influence the consistency of seismic capacity. Hence, taking $F_\mu = F_R = 1.0$ and letting the strength factor F_S be the only concern, as did in the parametric study.

F_S characterize the ratio of static S_a capacity, $S_{a,C} = \left(1.71 - 4\,\frac{\Delta}{L}\right) g$, given by equation (4.2.6), to median seismic demand, $S_{a,D} = S_a^F(f_e)$, which is the median FRS amplitude at effective frequency f_e of the wall. For simplicity, the median FRS are taken to be the same as those used in the parametric study, as shown in Figure 5.6 (i.e., 5% damping ratio is used for both primary structure and the block wall).

It was found that the maximum F_S occurs at drift limit $\frac{\Delta}{L} = 0.07$, which gives $S_{a,C} = 1.43\,g$. Using equation (4.2.10), $f_e = 1.51$ Hz is obtained and seismic demand $S_{a,D} = S_a^F(f_e)$ can be determined. Hence, median seismic capacities of the block masonry wall are given by

$$\text{Median seismic capacity} = F_S \cdot \text{PGA}, \quad F_S \cdot S_a(f_e), \quad \text{and} \quad F_S \cdot S_{a,\text{avg}}(\text{3-8}).$$

The resulting point seismic capacities are shown in Figure 5.22. For comparison, they are plotted against seismic capacity curves from parametric study of SDOF beam model mounted on structure S-2. It shows that the point capacities have the same inconsistency patterns to those in the parametric study. Note that the block wall has different seismic capacities than the shear beam, hence there is no reason that the point capacities lie exactly on the curve. However, when properly scaled, seismic capacity curves can accurately match the point capacities. This validates the results of parametric study.

It is also seen that at component frequency $f_e = 1.51$ Hz less than structural frequency $f_1 = 5.6$ Hz, only $S_a(f_e)$ capacity is very consistent, whereas PGA capacity and $S_{a,\text{avg}}$(3-8) capacity are highly variable. This complies with the recommendations of GMP for more consistent seismic capacity from the parametric study.

5.4.2 Heat Exchanger Median Seismic Capacity

In this example, the evaluation procedure follows that presented in Section 4.3 except that seismic inputs to the heat exchanger are FRS instead of GRS.

Under seismic excitations, the heat exchanger responses primarily as a SDOF system in each of the three earthquake directions. The fundamental frequencies for the longitudinal, translational, and vertical directions have been determined to be $f_{\text{L}} = 8.15$ Hz, $f_{\text{T}} = 25.4$ Hz, $f_{\text{V}} = 33$ Hz, respectively.

Among all potential failure modes, steel failure of the anchor bolt is dominant. Hence, only this failure mode is considered here. Median static capacities of the steel anchor bolt are determined to be 24.03 kips for shear and 34.89 kips for tension.

Tri-directional seismic inputs a_{L}, a_{T}, and a_{V} are obtained from the FRS shown in Figure 5.6. Force equations for tension and shear of critical anchor bolts, under seismic excitations

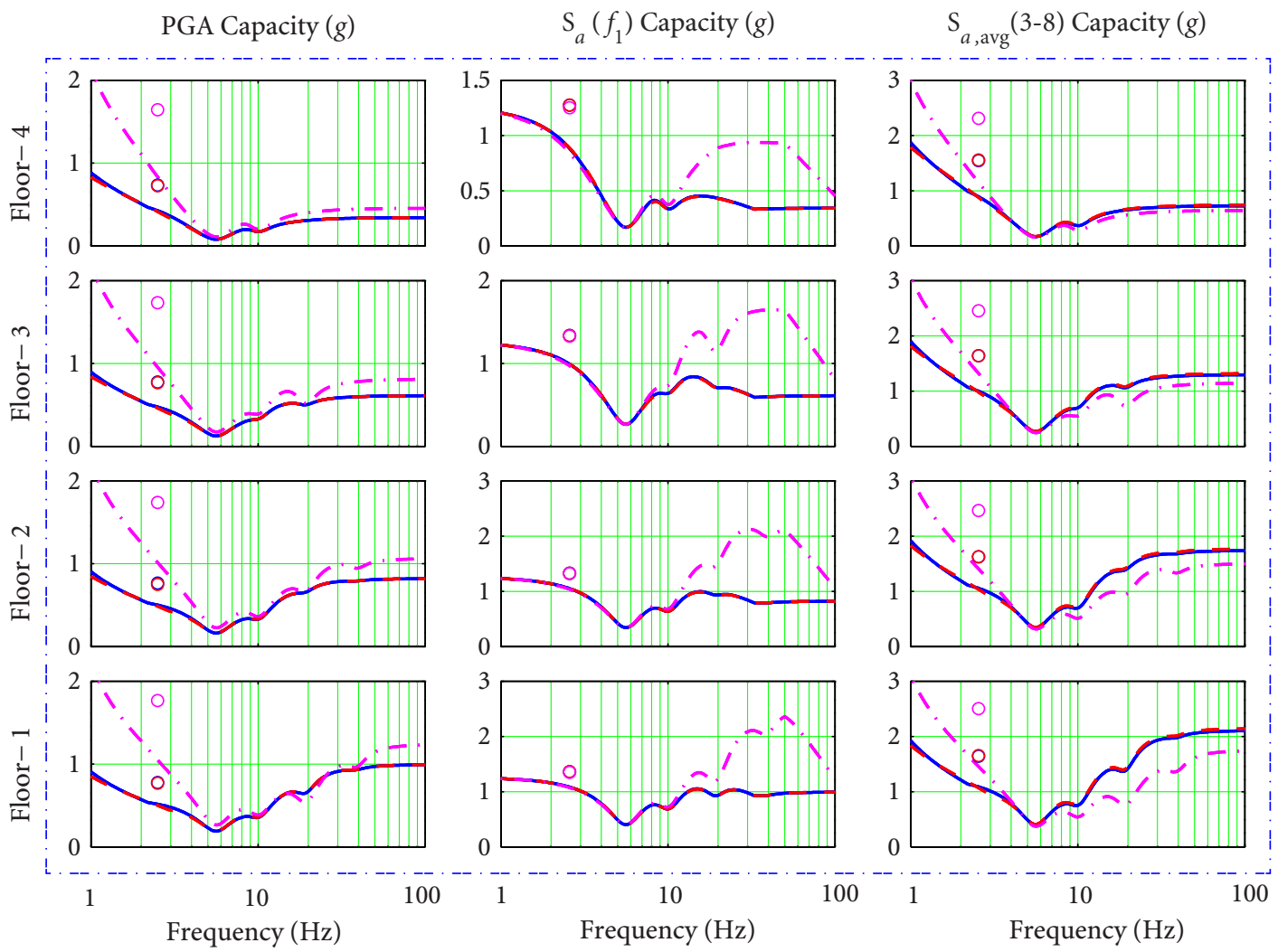

Figure 5.22 Median seismic capacity of block masonry wall in structure S-2, in comparison with results from parametric study

and gravity load, are given in Table 4.12. The maximum seismic demand is estimated using the 100-40-40 combination rule.

To determine the minimum factor of safety, the bilinear tension/shear interaction model is consistently used along with the controlling direction being longitudinal. The strength factor F_S is obtained by using equations (4.3.13) and (4.3.14). The inelastic energy absorption factor $F_\mu = 1.0$ is taken consistently, since the steel shear/tension failure is non-ductile.

Noting that the frequency ratio of the exchanger in the two horizontal directions $f_L : f_T = 8.15 : 25.4 \approx 1 : 3$, similar to the frequency ratio of the first two modes of the shear beam. Hence, to further illustrate the results, change some parameters of the exchanger to allow for the variation of horizontal frequencies. Table 5.4 lists 5 sets of parameters and the resulting horizontal frequencies, representing 5 heat exchangers.

The resulting seismic capacities of these 5 exchangers are shown in Figure 5.23. It shows similar consistency patterns to those from the parametric study of the original 10-DOF beam model, as shown in Figure 5.20. When properly scaled, these point capacities can match well with seismic capacity curves in Figure 5.20, which confirms the parametric study.

Table 5.4 5 heat exchangers having different sets of parameters and frequencies

Parameter†	h_1 (in)	h_2 (in)	t_s (in)	d_{bolt} (in)	f_L (Hz)	f_T (Hz)
Base case	60	26	0.5	1.0	8.15	25.4
Variation	70	36	0.5	0.75	5.35	17.4
	55	21	0.5	1.125	10.9	30.0
	55	21	0.8	1.25	13.7	33.3
	50	16	0.8	1.25	19.2	35.0

† See Table 4.8 for parameter definitions.

5.5 Conclusions

A comprehensive parametric study is performed to evaluate analytically the possible factors affecting the consistency of median seismic capacity.

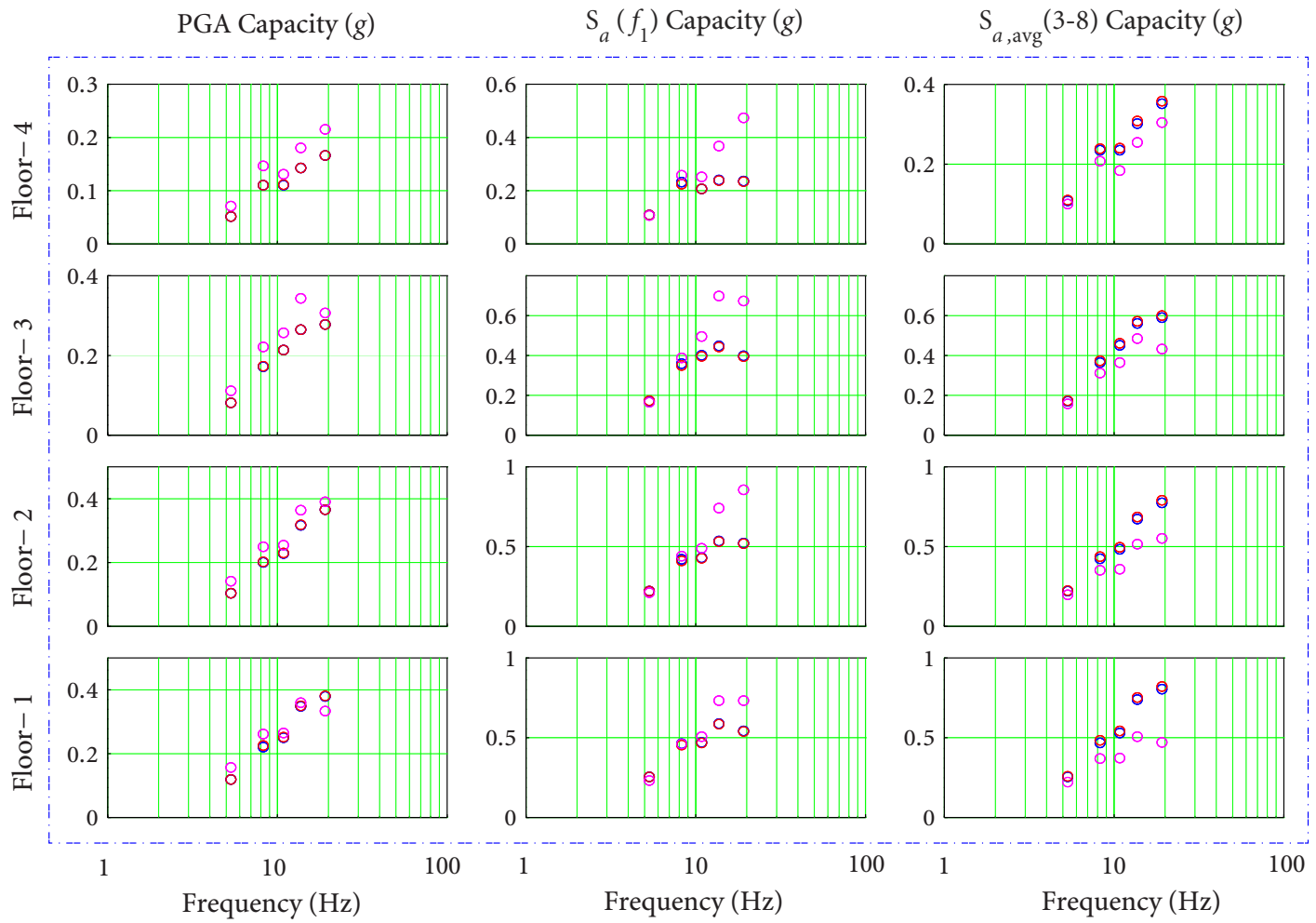

Figure 5.23 Median seismic capacity of heat exchanger in structure S-2

- For simple equipment or components modelled as single degree-of-freedom (SDOF) linear systems:

  1. PGA capacity varies inversely with floor response spectrum (FRS).
  2. $S_{a,\text{avg}}$ capacity primarily varies inversely with FRS and slightly with $S_{a,\text{avg}}$.
  3. $S_a(f_0)$ capacity varies inversely with amplification factor (AF).

- Ground response spectrum (GRS) shapes and primary structures both influence FRS and AF, hence affect the consistency of seismic capacity. Their influences can be described in a frequency-dependent manner, as summarized in Subsection 5.3.3.
- To achieve more consistent seismic capacity, proper GMP can be recommended.
  (let f_0 = frequency of equipment and f_1 = fundamental frequency of primary structure)

  1. when $f_0 \leqslant 1.5\, f_1 \implies$ use $S_a(f_0)$ Capacity (very consistent)
  2. when $f_0 > f_1$, recommendations is more structure-specific, depending on the f_1 value
     (a) when $f_1 \leqslant 5$ Hz $\implies$ use $S_{a,\text{avg}}$ Capacity (fairly consistent)
     (b) when $5\text{ Hz} < f_1 \leqslant 12$ Hz $\implies$ use PGA Capacity (fairly consistent)
     (c) when $f_1 > 12$ Hz $\implies$ none is consistent, requiring further study

- For complex equipment or components modelled as multiple DOF systems:

  1. When higher-mode responses make a comparatively strong contribution to the total demand, seismic capacities can be different from those using the SDOF model.
  2. The effect of higher-mode responses on the inconsistency of seismic capacity requires a case-by-case analysis. If the relative higher-mode responses evaluated using different GRS have similar orders as the first-mode response, the inconsistency will be strengthened after modal combination. Otherwise, it will be partially reduced.

Two realistic example problems are presented to support the parametric study. Given the wide coverage of parametric study, the results can be used to guide current engineering practice.

CHAPTER 6

Conclusions

Seismic probabilistic risk analysis (SPRA) has been widely used in seismic analysis and design of critical engineering structures such as nuclear power plants. Quantitative assessment of seismic risk is challenging due to its multi-disciplinary nature and uncertainties present in many aspects of the assessment. The purpose of this study is to bridge the gap between seismological analyses and engineering applications, i.e., to address some issues in current SPRA framework so that it can be better applied into engineering practice. Several contributions have been made for this purpose as summarized in the following.

6.1 New Deaggregation Procedure for Seismic Risk Analysis

For seismic hazard analysis, conventional seismic hazard deaggregation (SHD) procedures have been used to extract a single controlling earthquake that contributes to hazard at a given reference probability λ_a.

However, due to the integrative nature of PSHA, no single event can fully represent the seismic hazard at a site. In many practical cases, multiple (m, r)-pairs show comparable contributions to a specific level of seismic hazard. Considering only one (m, r)-pair is not likely to provide correct ground motion estimate. In addition, the controlling earthquake extracted from deaggregation may be very different as the reference probability level varies.

It is impossible to extract a single controlling earthquake that induces dominant hazard at the site applicable to all probability levels.

In this study, the concept of conventional SHD is extended. Resorting to the mean value theorem of integration, a new SHD procedure is proposed to determine a set of controlling earthquakes in terms of magnitude m_{C_i}, source-site distance r_{C_i}, and occurrence rate ν_{C_i} $(i=1,2,\cdots,N_C)$. Collectively, they recover seismic hazard in the probability range $\lambda_a = 1\times10^{-3}\sim1\times10^{-6}$/year that contribute most to seismic risk range of interest. The desirable features of a set of controlling earthquakes are:

(1) Better representation of seismic hazard at the site, including a complete description of representative earthquakes from small near-field to large far-field earthquakes.

(2) Better capability of representing seismic hazard in the major probability range of interest. Hence, the set-wise "controlling earthquakes" representation becomes more meaningful.

(3) Natural description of the importance of earthquake scenario (m_{C_i}, r_{C_i}) through ν_{C_i}. This information is useful in ground motion selections for dynamic analysis of structures.

6.2 Simplified Vector-valued Seismic Risk Analysis

A simplified approach to Vector-valued Seismic Risk Analysis (VSRA) is developed to achieve computational efficiency without compromising the accuracy.

- Vector-valued Probabilistic Seismic Hazard Analysis (VPSHA), along with the seismic fragility model considering multiple ground-motion parameters, are applied to establish a standard VSRA. However, due to the extensive computational effort required for the multiple dimensional cases, VSRA cannot be widely applied in current engineering practice.

- A simplified approach to VSRA is developed based on a set of controlling earthquakes. The integration in standard risk analysis with respect to all possible earthquake occurrences, i.e., all (m, r)-pairs from all N_S sources, are then avoided. Numerical examples show that the simplified approach can provide good risk approximations to standard

VSRA. The computational efficiency can be substantially improved with the typical time cost reduced to less than 0.5%.

- It is also demonstrated that this simplified approach can provide best achievable approximations using a typical 3×3 (M, R)-bins, i.e., a total of 9 controlling earthquakes. Finer binning can hardly improve the approximations. Coarser 2×2 (M, R)-bins may be acceptable. 1×1 (M, R)-bin is not recommended for risk approximations.
- In addition, the simplified approach is more sensitive to the R binning than M binning; good R binning helps improve the approximations in most situations.

6.3 Parametric Evaluation of Seismic Capacity for Nuclear Facilities

A comprehensive parametric study is performed to evaluate analytically the possible factors affecting the consistency of median seismic capacity. The input parameters include 3 ground response spectrum (GRS) shapes, 4 primary structures, 201 secondary structures (equipment), and 3 ground motion parameters (GMP).

From the parametric study, it is found that

- For simple equipment or components that can be modelled as single degree-of-freedom (SDOF) linear systems:

  1. PGA capacity varies inversely with floor response spectrum (FRS).
  2. $S_{a,\text{avg}}$ capacity primarily varies inversely with FRS and slightly with $S_{a,\text{avg}}$.
  3. $S_a(f_0)$ capacity varies inversely with amplification factor (AF).

- GRS shapes and primary structures both influence FRS and AF, hence affect the consistency of seismic capacity. Their influences can be described in a frequency-dependent manner, as summarized in Subsection 5.3.3.
- To achieve more consistent seismic capacity estimates, the proper GMP for defining seismic capacity is also recommended.

(let f_0 = frequency of equipment and f_1 = fundamental frequency of primary structure)

1. when $f_0 \leqslant 1.5\, f_1 \implies$ use $S_a(f_0)$ Capacity (very consistent)

2. when $f_0 > f_1$, recommendations is more structure-specific, depending on the f_1 value
   (a) when $f_1 \leqslant 5$ Hz $\Longrightarrow$ use $S_{a,\text{avg}}$ Capacity (fairly consistent)
   (b) when $5\text{ Hz} < f_1 \leqslant 12$ Hz $\Longrightarrow$ use PGA Capacity (fairly consistent)
   (c) when $f_1 > 12$ Hz $\Longrightarrow$ none is consistent, requiring further study

- For complex equipment or components modelled as multiple DOF systems:

1. When higher-mode responses make a comparatively strong contribution to the total demand, seismic capacities can be different from those using the SDOF model.
2. The effect of higher-mode responses on the inconsistency of seismic capacity requires a case-by-case analysis. If the relative higher-mode responses evaluated using different GRS have similar orders as the first-mode response, the inconsistency will be strengthened after modal combination. Otherwise, it will be partially reduced.

Two realistic example problems are presented to support the parametric study. Given the wide coverage of parametric study, the results can be used to guide current engineering practice.

APPENDIX A

A.1 Spectral correlation model by Baker&Jayaram (2008)

Developed empirically using the extensive Next Generation Attenuation (NGA) ground-motion database and the NGA GMPEs (Abrahamson and Silva, 2008; Boore and Atkinson, 2008; Campbell and Bozorgnia, 2008; Chiou and Youngs, 2008), this model is valid for a variety of definitions of horizontal spectral acceleration (arbitrary component and the geometric average of two horizontal components) and for vibration periods from 0.01 sec to 10 sec. Regardless of the accompanying GMPE models used, the correlation coefficients of spectral correlations all exhibit similar correlation structure.

The correlation coefficients between the horizontal spectral accelerations $\ln S_a(T_u)$ and $\ln S_a(T_v)$ at any two periods T_u and T_v ($T_u \leqslant T_v$) have been fit to the following predictive equations:

$$\rho_{\ln S_a(T_u),\ln S_a(T_v)} = \begin{cases} C_2, & \text{if } T_v < 0.109, \\ C_1, & \text{else if } T_u > 0.109, \\ \min\left(C_2, C_4\right), & \text{else if } T_v < 0.2, \\ C_4, & \text{else,} \end{cases}$$

where

$$C_1 = 1 - \cos\left\{\frac{\pi}{2} - 0.366 \ln\left[\frac{T_v}{\max\left(T_u, 0.109\right)}\right]\right\},$$

$$C_2 = \begin{cases} 1 - 0.105\left[1 - \dfrac{1}{1+\exp(100T_v - 5)}\right]\left(\dfrac{T_v - T_u}{T_v - 0.0099}\right), & \text{if } T_v < 0.2, \\ 0, & \text{otherwise,} \end{cases}$$

$$C_4 = C_1 - 0.5\left(\sqrt{C_3} - C_3\right)\left[1 + \cos\left(\frac{\pi T_u}{0.109}\right)\right], \quad C_3 = \begin{cases} C_2, & \text{if } T_v < 0.109, \\ C_1, & \text{otherwise.} \end{cases}$$

A contour of correlation coefficients of spectral accelerations using these predictive equations is shown in Figure 3.1.

As can be seen in Figure 3.1, The spectral correlations decrease with increasing separation of vibration periods when the periods are larger than around 0.1 sec, which cover the range of period of general engineering interest. However, the spectral correlations increase mildly when one period is fixed and the other one approaches shorter periods less than around 0.1 sec. For example, the correlation between spectral accelerations at $T_u = 0.05$ sec and $T_v = 1$ sec is larger than the correlation at $T_u = 0.1$ sec and $T_v = 1$ sec.

A.2 Empirical Scaling Relations

In site-specific PSHA, physically-based estimates of earthquake magnitude can be made using functions that relate moment magnitude $\mathbf{M}$ to fault dimensions or seismogenic area A, called "empirical scaling relations", given in the form of $\mathbf{M} - \log A$.

The most-widely used scaling relations were developed by Wells and Coppersmith (1994). From regression of data from 148 earthquake events including all slip types, Wells and Coppersmith found that (their Table 2A and Figure 16a)

$$\mathbf{M} = (4.07 \pm 0.06) + (0.98 \pm 0.03)\ \log_{10} A, \tag{A.2.1}$$

where A, in unit of km^2, is given by $A = L\,W\,R$, where L = segment length, W = down-dip segment width, and R = seismogenic scaling factor (0∼1). The regression is well determined for magnitude range of $\mathbf{M}$ = 4.8∼7.9 and length/width range from 2.2∼5184 km, as indicated by the small standard deviation of 0.24 and a large correlation coefficient of 0.95.

Another set of widely implemented scaling relations are by Hanks and Bakun (2002, 2008), mainly for strike-slip earthquakes

$$\mathbf{M} = \begin{cases} \log_{10} A + 3.98, & A \leqslant 537 \text{ km}^2, \\ 4/3 \ \log_{10} A + 3.07, & A > 537 \text{ km}^2. \end{cases} \tag{A.2.2}$$

In practical applications, expert-opinion weights of different $\mathbf{M} - \log A$ models are often used to account for the epistemic uncertainty.

A.3 Activity Rate

Activity rate is the mean rate of occurrence of earthquake above a minimum magnitude. In principle, the activity rate of a fault rupture segment can be computed by balancing the long-term build-up rate $\dot{M}_{0,\text{build}}$ of seismic moment M_0 (the most fundamental physical parameter of a seismic source that expresses its earthquake size) with its long-term release rate $\dot{M}_{0,\text{release}}$.

The moment build-up rate $\dot{M}_{0,\text{build}}$ of a fault segment is obtained from its seismogenic area A and its long-term slip rate $\dot{u}$ (WGCEP, 2003)

$$\dot{M}_{0,\text{build}} = \mu \, A \, \dot{u}, \tag{A.3.1}$$

where $\mu = 3 \times 10^{11} \text{dyne/cm}^2$ is shear modulus of the crust.

The moment release rate $\dot{M}_{0,\text{release}}$ is achieved by repeating sequence of earthquakes with mean seismic moment $\overline{M}$ at the mean rate ν_m

$$\dot{M}_{0,\text{release}} = \nu_m \, \overline{M}. \tag{A.3.2}$$

By expressing seismic moment M_0 as a function of moment magnitude m, $M_0 = 10^{(1.5\,m+c)}$, where $c = 9.05$ (SI unit) as originally defined by Hanks and Kanamori (1979), the general mean seismic moment $\overline{M}$ is given by

$$\overline{M} = \int_{m_{\min}}^{m_{\max}} M_0(m) \, f(m) \mathrm{d}m, \tag{A.3.3}$$

where $m_{\min}$ and $m_{\max}$ are the minimum and maximum magnitudes considered, respectively.

Equating equation (A.3.1) to equation (A.3.2) yields

$$\nu_{m_{\min}} = \mu \, A \, \dot{u} / \overline{M}. \tag{A.3.4}$$

In case when a sequence of similar-sized earthquakes with magnitude m_{char} is repeated, equation (A.3.4) gives the activity rate $\nu_{m_{\text{char}}}$ of m_{char}.

A.4 Basics of Lognormal Distribution

A variable might be modeled as lognormal if it can be thought of as the multiplicative product of many independent random variables, each of which is positive. The lognormal distribution is useful in those applications where the values of the random variable are known to be strictly positive; for example, the strength and fatigue life of a material, the intensity of rainfall, the time for project completion, and the volume of air traffic.

Let Y be a normally distributed random variable with mean α and standard deviation β, denoted as $Y \sim N(\alpha, \beta^2)$. The probability density function of Y is

$$f_Y(y) = \frac{1}{\sqrt{2\pi}\,\beta} \exp\left\{-\frac{(y-\alpha)^2}{2\beta^2}\right\}.$$

Random variable $X = e^Y$ is said to be lognormally distributed, denoted as $X \sim LN(\alpha, \beta^2)$. The probability density function of X, shown in Figure A.1, is given by

$$f_X(x) = \begin{cases} \dfrac{1}{\sqrt{2\pi}\,\beta x} \exp\left\{-\dfrac{(\ln x-\alpha)^2}{2\beta^2}\right\}, & x>0, \\ 0, \quad x \leqslant 0. \end{cases}$$

Parameters α and β are the mean and standard deviation of the normal random variable Y, which is the natural logarithm of the lognormal random variable X, i.e., $Y = \ln X$. Therefore, α and β are also called, respectively, the *logarithmic mean* and *logarithmic standard deviation* of the lognormal random variable X.

Cumulative distribution function of X is given by

$$P\{X<x\} = \Phi\Big(\frac{\ln x - \alpha}{\beta}\Big), \tag{A.4.1}$$

where $\Phi(\cdot)$ is the standard Gaussian cumulative distribution function.

For a lognormal distribution, the median characterizes the central tendency, while the logarithmic standard deviation β is a measure of the dispersion of the distribution. Let X_m be the median, then from equation (A.4.1) one has

$$P\{X<X_m\} = \Phi\Big(\frac{\ln X_m - \alpha}{\beta}\Big) = 0.5, \tag{A.4.2}$$

which yields

$$\alpha = \ln X_m, \quad \text{or} \quad X_m = e^{\alpha}.$$

In practice, there are cases that the lower limit of a random variable, such as the strength of material, or the acceleration of ground motion, is of engineering interest. A lower limit above which the variable may lie, properly determined in a probabilistic basis, is often used as a critical parameter. The probability that the variable will lie above the lower limit is called *confidence level*.

Designating Q (shaded area in Figure A.2) as the confidence level, letting

$$Z_Q = \frac{\ln X_Q - \alpha}{\beta}$$

be the standard normal random variable corresponding to the confidence level Q, i.e.,

$$P\{X > X_Q\} = P\{Z > Z_Q\} = Q,$$

and noting that $e^{\alpha} = X_m$, one has

$$X_Q = e^{\alpha+\beta Z_Q} = X_m e^{\beta Z_Q} = X_m e^{\beta \Phi^{-1}(1-Q)} = X_m e^{-\beta \Phi^{-1}(Q)}. \tag{A.4.3}$$

Therefore, for confidence levels $Q = 5\%,\ 50\%,$ and 95%, the lower limits of random variable

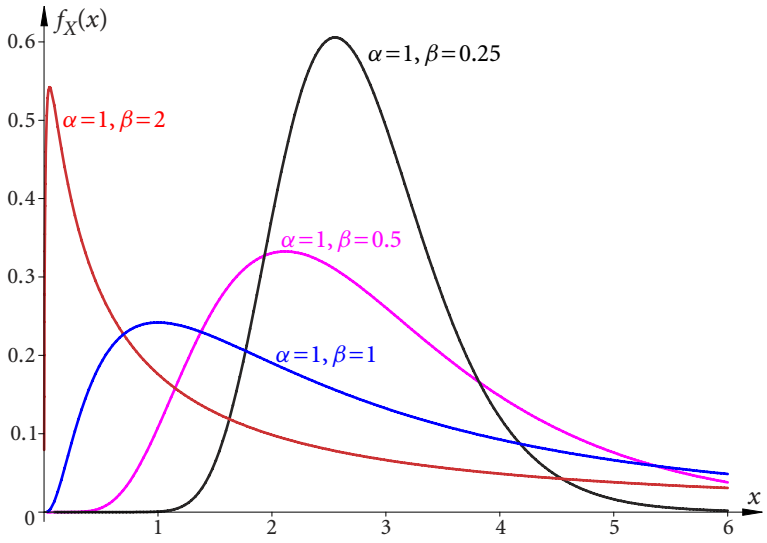

Figure A.1 Probability density function of lognormal distribution

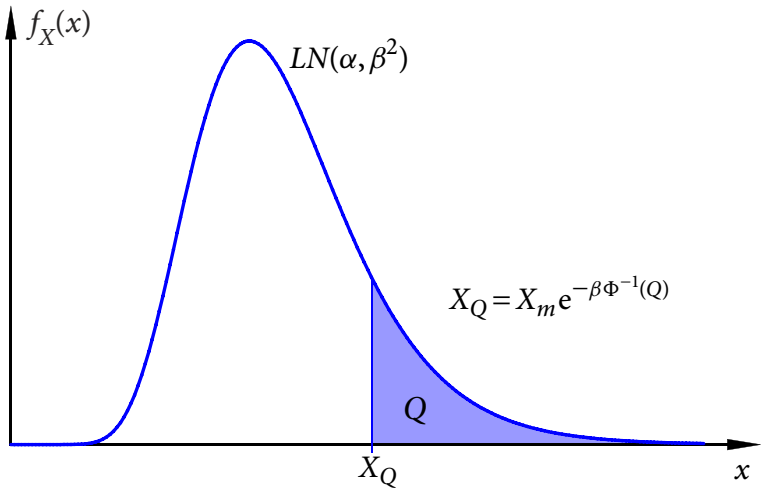

Figure A.2 Lognormal distribution of X

X_Q are given by, respectively,

$$X_{0.05} = X_m e^{-\beta\Phi^{-1}(0.05)} = X_m e^{1.645\beta},$$
$$X_{0.50} = X_m e^{-\beta\Phi^{-1}(0.50)} = X_m,$$
$$X_{0.95} = X_m e^{-\beta\Phi^{-1}(0.95)} = X_m e^{-1.645\beta}.$$

If X_1, X_2, and X_3 are independent lognormally distributed random variables, and if

$$X = C\frac{X_1^a \cdot X_2^b}{X_3^c}, \tag{A.4.4}$$

where a, b, c, and C are constants, then X is also a lognormal random variable, whose median X_m and standard deviation β_X are given by

$$X_m = C\frac{X_{1m}^a \cdot X_{2m}^b}{X_{3m}^c}, \qquad \beta_X^2 = a^2\beta_{X1}^2 + b^2\beta_{X2}^2 + c^2\beta_{X3}^2, \tag{A.4.5}$$

where X_{1m}, X_{2m}, and X_{3m} are the median values, and β_{X1}, β_{X2}, and β_{X3} are the logarithmic standard deviations of X_1, X_2, and X_3, respectively.

A.5 Basic Variables for the Block Masonry Wall

Earthquake response spectrum shape

The "peak-and-valley" randomness of a real earthquake spectrum towards the smooth reference earthquake spectrum, and the uncertainty of using a predicted reference spectral

shape must be considered. According to Table 3-2 of EPRI-TR-103959 (EPRI, 1994), this variable is frequency dependent. In case when the primary structure has a fundamental frequency of 6.58 Hz and the hazard curve is defined by PGA, $\beta_R = 0.20$ and $\beta_U = 0.215$ are estimated by interpolating recommended values for 5 Hz and 10 Hz.

Horizontal direction peak response

The block wall is mainly affected by the horizontal direction response perpendicular to the wall plane. Using a reference earthquake averaged in two horizontal directions results in a randomness variability corresponding to the "specific-direction-response" case. Table 3-3 of EPRI-TR-103959 recommends a median of 1.0 and $\beta_R = 0.13$ for this variable.

Vertical component response

Vertical earthquake component imposes normal force on wall section, hence influences the drift. However, this influence is negligible, since the wall oscillates vertically at a much higher frequency than the out-of-plane drift. Hence, this factor is not considered further.

Ground motion incoherence

The reduction to the input response spectra (either ground or floor level) due to ground motion incoherence depends on the size of structure foundation and the frequencies of response. For a fundamental frequency 6.58 Hz of primary structure, and a 130 feet foundation in both directions, the median factor F_m and the uncertainty β_U are estimated by interpolations according to Chapter 3 of EPRI/CR-103959

$$F_m = 1 - \frac{\ln 6.58 - \ln 5}{\ln 10 - \ln 5}(0.1)\left(\frac{130}{150}\right) = 0.97, \tag{A.5.1a}$$

$$\beta_U = \frac{1}{2}\ln\left(\frac{1.0}{0.966}\right) = 0.017, \tag{A.5.1b}$$

where 0.1 is the reduction factor for a 150 ft-size foundation in the 5–10 Hz difference.

Since the primary structure is founded on a rock base, no contribution for SSI is expected; thus, this factor is not considered. There is also no contribution for the vertical spacial variation of ground motion since the structure is founded on the ground surface.

Structural damping

Damping is considered to be strain-dependent and has a wide spread. Table 3-4 of EPRI-TR-103959 recommends damping values for the median and the -1σ for uncertainty

of various structural systems and components at different stress levels (e.g., 1/2 yield or near yield). Suppose the primary structure has a relatively large seismic margin and is about only 1/2 yield when block wall component approaches stress limit. Following the recommendations, the median and the -1σ damping are taken as 5% and 3%, respectively.

Structural modelling, frequency, and mode shape

Uncertainty in structural modelling influences primarily modal frequency and mode shapes. Based on a four-DOF internal structure of a reactor building (Li *et al.*, 2005), structural modelling is assumed to represent the realistic case. The resulting modal frequency and mode shapes are median-centered. According to Chapter 3 of EPRI/CR-103959, $\beta_U = 0.15$ is taken for structural frequency. Its effect on component response depends on the spectral shape in the vicinity of structural frequency, which needs to be evaluated further. As a structure of moderate complexity, β_U in structural response due to mode shape is taken as 0.10, an average of 0.05 and 0.15 for simple and complex structures, respectively.

Torsional coupling

The primary structure is believed to be symmetric and regular in two horizontal directions. Eccentricity, if any, is considered to be very small and will only very slightly affect the floor acceleration. Thus, a median value of 1.0 is taken and no uncertainty is considered.

Modal combination

For primary structures with well-separated modal frequencies, the SRSS-computed FRS, using equation (5.2.1), is believed to be median centered for fragility analysis. The variability due to this factor also depends on the complexity of structure: for structures responding primarily in single mode, $\beta_U = 0.05$; for structures having multiple important modes, $\beta_U = 0.15$. Hence, $\beta_R = 0.10$ is taken for this primary structure. Note that the transformation between randomness in modal combination per se and its effect on response is already included in these values.

Quantification method

Component fragility analysis can be performed from scratch, based on analysis of critical failure modes, realistic response analysis and material properties. Using this approach, as for the block wall example, gives a unit median and zero variability for this factor. Otherwise, if

starting from an existing analysis, e.g., for Safe Shutdown Earthquake design, conservatism in the original design must be factored out to produce a median-centered response.

Component damping

Component damping should be set at about near-yield level, which will be realized at the limit state. For block walls at near-yield stress, Table 3-4 of EPRI-TR-103959 recommends a median damping of 10% and a -1σ damping of 7%. Note that these values are appropriate for psuedo-elastic analysis. For inelastic analysis, lower values should be used. Referring to the CDFM analysis of this block wall, given in Appendix R of EPRI-NP-6041 (EPRI, 1991a), the median and the -1σ damping values are taken as 6% and 4%, respectively.

Frequency and mode shape of component

Depending on the level of complexity of analysis model and boundary conditions, the uncertainty in component frequency can range from 0.10–0.30 and the uncertainty in response due to mode shape can range from 0.05–0.15. For both variables, small values are appropriate for simple component responding primarily in single mode and large values for complex cases. For the simple block wall, unit medians are taken for both variables, $\beta_U =$ 0.10 is taken for the frequency variable and $\beta_U = 0.05$ is taken for the mode shape variable.

Modal combination of Component

EPRI-CR-103959 recommends on Page 3-50 that randomness β_R for this variable ranges typically from 0.05–0.15, with small value appropriate for simple component responding in simple mode. Hence, $\beta_R = 0.05$ is taken.

Earthquake component combination

Component responses due to tri-directional earthquake components usually need to be combined. Either the SRSS or the "100-40-40" combination rule can be used and the response estimate is supposed to be median-centered. A randomness β_R value also needs to be estimated for this variable. However, since seismic capacity of this block wall is governed by one horizontal earthquake component only, this variable is not considered further.

Masonry strength

Compressive strength of masonry f'_{m} generally depends on the size of masonry unit, material (e.g., clay or concrete), and the type of mortar. Code-specified f'_{m} represents the

minimum value required in construction. Determination of the median f'_{m} for fragility analysis can be based on either the *unit strength method* or the *prism test method* (MSJC, 2011). However, f'_{m} can be highly variable. Test data on three-prism-set of concrete masonry unit from 80 laboratories showed the COV ranging from 0.14%–17.4%, with a mean of 6.3% (T.G., 2002). Suppose for the block wall that test results suggest a median $f'_{\mathrm{m}} = 2376$ psi and $\beta_R = 0.12$. The nominal strength, defined at about the 95% exceedance probability, is then given by $2376 \times \mathrm{e}^{-1.645 \times 0.12} = 1950$ psi.

The elastic modulus shall be determined using the nominal value as

$$E_m = 900\, f'_{\mathrm{m}} = 900 \times 1950 = 1.755 \times 10^6 \text{ psi.} \qquad \text{(Cl-1.8.2.2, MSJC-11)}$$

Tensile strength (modulus of rupture) f_t was traditionally estimated using the empirical formula $f_t = K\sqrt{f'_{\mathrm{m}}}$, where factor K typically ranges from 4.5–8.5 for fully-grouted masonry walls (Hamid *et al.*, 1989). f_t is also highly variable and had been conservatively estimated ($K = 2.5$) in code specifications. In contrast, MSJC-11 code provides a "Table Method" for determining f_t, based on the direction of flexural tensile stress, masonry material, and mortar type. For fully-grouted masonry elements, subjected to out-of-plane or in-plane bending, using M type mortar,

$$f_t = 163 \text{ psi.} \qquad \text{(Table 3.1.8.2, MSJC-11)}$$

Test data on prism specimens (NCMA, 1994) suggested an average $f_t = 166$ psi, which supports this code-specified value. However, it might be still conservative for masonry wall applications; the wall specimen tests showed an average $f_t = 216$ psi (NCMA, 1994), about 30% higher than the prism test value.

Steel strength

Grade 40 reinforcing steel is used for the block wall, where grade 40 refers to the code-specified minimum yield strength $f_y = 40$ ksi. For nuclear applications, this minimum strength is generally used as the nominal (or CDFM) strength. Only when plant-specific mill test data shows a mean strength at least 15% greater than this minimum strength and a COV less than 0.08, an increased strength can be justified. The COV of rebar strength depends on the bar size, grade, and stress level (yield or ultimate). Statistical analysis showed

that the COV of the yield strength of #4 Grade 40 reinforcing bar ranges from 0.08–0.09 (Bournonville *et al.*, 2004). Hence, $\beta_R = 0.09$ is taken for f_y and the median f_y is given by $40 \times e^{1.645 \times 0.09} = 46.4$ ksi.

A.6 Model Uncertainty for Block Wall Moment Strength

Error in Equation

Conservatism against the MSJC-11 equations should be characterized based on available test results. Hamid *et al.* (1989) conducted tests for 14 full-scale reinforced concrete masonry walls under out-of-plane monotonic and cyclic loads. Measured peak test moment capacities were compared with calculated capacities by using the mean test material properties (prism unit test of masonry and tensile testing of reinforcement) and the calculation procedure in Appendix-A of Hamid *et al.* (1989). In summary, the ratios of measured peak test to calculated capacity of 12 similar masonry walls are

$$\frac{M_u \text{ (Measured)}}{M_u \text{ (Calculated)}} = 1.14,\ 1.19\ 1.19,\ 1.02,\ 1.16,\ 1.01,\ 1.16,\ 0.83,\ 1.06,\ 1.19,\ 1.15,\ 1.09,$$

which gives a median ratio of 1.145 and a logarithmic standard deviation $\beta_{\text{eqn}} = 0.105$.

However, under cyclic loading to large displacements, the average "elasto-perfectly plastic" moment capacity tends to be somewhat less than the peak test capacity (see Figure A.3 for illustration). In addition, the maximum moment capacity reached in subsequent loading cycles might be somewhat less than the previously recorded peak value. Thus, using the peak test capacity as the ultimate moment capacity is overly optimistic. As a slightly conservative estimation, the average test capacity is taken as 90% of the peak test capacity, which gives a median equation factor of $F'_{\text{eqn}} = 1.145 \times 0.90 = 1.031$.

The above factor represents the conservatism against the calculated capacity by Hamid *et al.* (1989), obtained using slightly different equations (i.e., using equivalent block stress depth $a = 0.85\,c$ instead of $a = 0.80\,c$) and mean material strengths (approximately median). A conversion must be made to obtain the factor that applies to the MSJC-11 code equations.

Recalculating the moment strength using $a = 0.85\,c$ gives

$$a = \frac{A_s f_y}{0.85\, f'_{\text{m}}\, b} = \frac{0.0123 \times 46.4}{0.85 \times 2.38 \times 1} = 0.283 \text{ in},$$

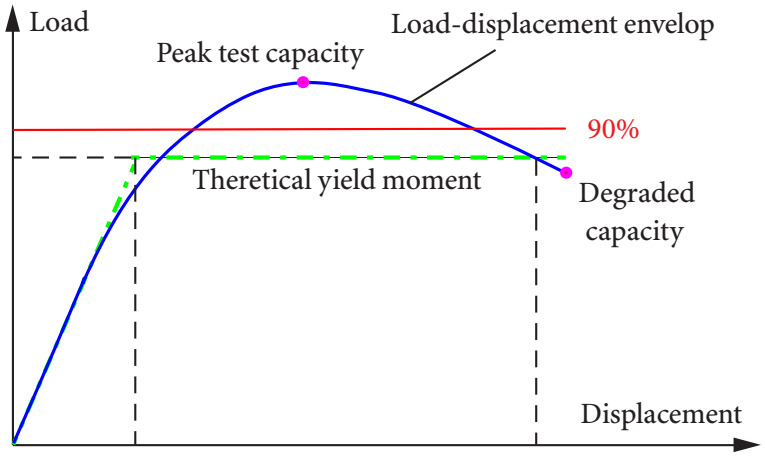

Figure A.3 Typical force-displacement relation

$$M_{\mathrm{u}}'' = (A_s f_y)\left(d - \frac{a}{2}\right) = (0.0123 \times 46.4)\left(3.812 - \frac{0.283}{2}\right) = 2.095 \left(\frac{\text{kip-in}}{\text{in}}\right).$$

Multiplying the factor F_{eqn}' to M_{u}'' gives the "best-estimate" of moment strength

$$M_u = F_{\mathrm{eqn}}' \times M_{\mathrm{u}}'' = 1.031 \times 2.095 = 2.160 \left(\frac{\text{kip-in}}{\text{in}}\right).$$

The equation factor that applies to the MSJC-11 code equations is then

$$F_{\mathrm{eqn}} = M_u / M_{\mathrm{u}}' = 2.160/2.090 = 1.034.$$

Hence, the equation error factor against the MSJC-11 moment strength equation is

$$\text{Median} \;\; F_{\mathrm{eqn}} = 1.034 \quad \text{and} \quad \beta_{\mathrm{eqn}} = 0.105.$$

☞ *The best-estimate of moment strength M_u is independent of the code equations; M_u should be the same, only the median equation factor F_{eqn} can be slightly different.*

Error in rebar placement

Under careful inspection, it is estimated that the standard deviation σ of depth d for a single bar is about 0.5 in (EPRI, 1991a). Assuming that the moment capacity over a section is governed by 4 bars, the corresponding σ for 4 bars is then $0.5/\sqrt{4} = 0.25$ in. For a nominal 8 in-thick wall, the moment strength due to reduction by 1σ of d reduces to

$$M_{\mathrm{u}}' = (A_s f_y)\left(d - 0.25 - \frac{a}{2}\right) = (0.0123 \times 46.4)\left(3.812 - 0.25 - \frac{0.300}{2}\right) = 1.948 \left(\frac{\text{kip-in}}{\text{in}}\right),$$

which is about 93.2% of M_u without considering this error. This results in

$$\beta_1 = \ln \frac{M_u}{M_u'} = \ln \frac{2.090}{1.948} = 0.071.$$

It is assumed that any strength reduction due to rebar placement is already lumped into the equation factor F_{eqn}. The factor accounting for error in rebar placement is given by

$$\text{Median } F_1 = 1.0 \quad \text{and} \quad \beta_1 = 0.071.$$

A.7 Capacities Analyses for the Heat Exchanger

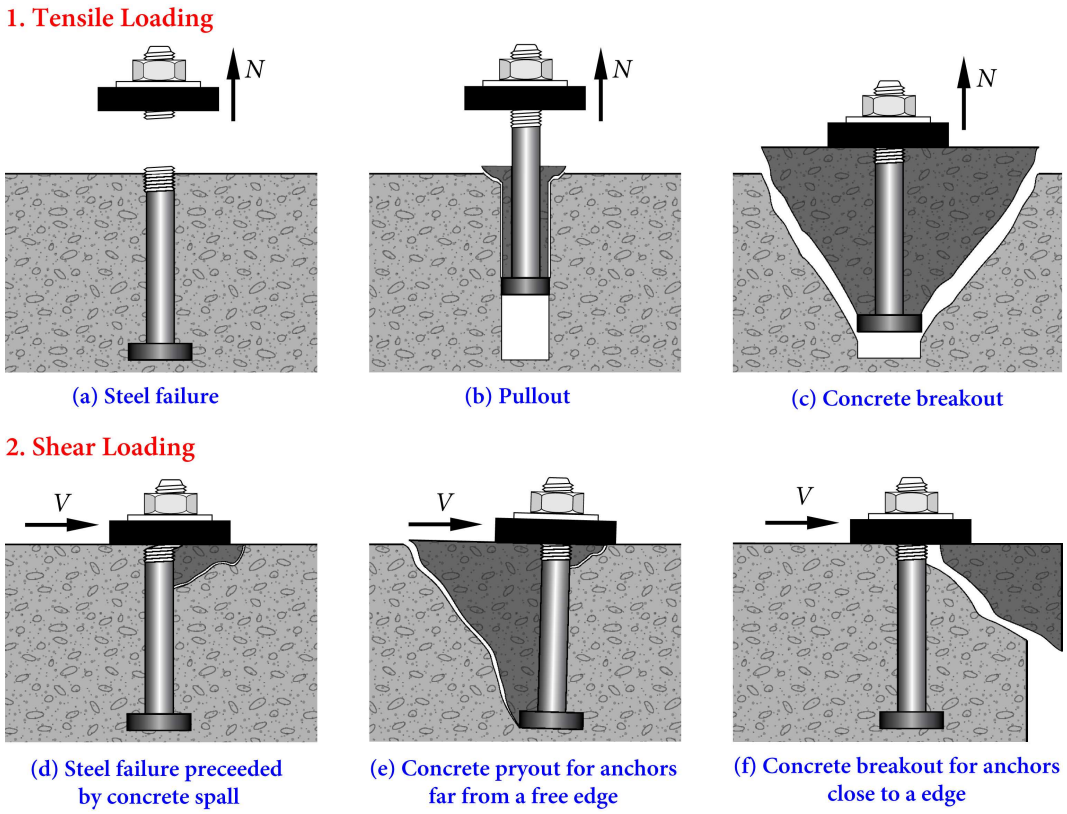

Figure A.4 Anchorage failure modes

Capacities of anchor bolts

Typical failure mechanisms of concrete anchor bolts under tensile and shear loadings are illustrated in Figure A.5. The American Concrete Institute (ACI) provides guidelines for the design of anchorage to concrete in Appendix D of ACI 349-06 (2007a). ACI 349.2R-07

(2007b) provides example applications of ACI 349-06 to the design of steel anchorage and embedment, in terms of the bolt effective area and embedment depth. In general, proper embedment length and spacing between anchor bolts are ensured to avoid the concrete cone failure, allowing the steel failure to be dominant.

Steel Failure in Tension

Using equation (D-3) in ACI 349-06 and applying a reduction factor $\phi = 0.9$ that considers the notch effect of threads and eccentricities in loading, one obtain the median tensile strength of a single anchor

$$N_{\text{tension},m} = 0.90\, A_{\text{net}}\, \sigma_{\text{u}} = 0.90 \times 0.6057 \times 64 = 34.89 \text{ kips}. \tag{A.7.1}$$

Steel Failure in Shear

From provision D.6.1.2 of ACI 349-06 (2007a), the median shear strength of a single A307 cast-in headed bolt is given by

$$V_{\text{shear},n} = 0.6\, A_{\text{net}}\, \sigma_{\text{u}} = 0.60 \times 0.6057 \times 64 = 23.26 \text{ kips}. \tag{A.7.2}$$

Pullout Strength of Anchor in Tension

From Clause D.5.3 of ACI 349-06 (2007a), the nominal pullout strength of a single anchor in tension is given by

$$N_{\text{pullout},n} = \psi_{\text{c,P}}\, N_{\text{p}}, \tag{D-14, ACI 349-06}$$

where $\psi_{\text{c,P}} = 1.0$ for cracked concrete, and the pullout strength in tension of a single headed stud or headed bolt, N_{p}, is

$$N_{\text{p}} = 8\, A_{\text{bearing}}\, f_{\text{c}}', \tag{D-15, ACI 349-06}$$

where A_{bearing} is the bearing area.

Hence, for a cast-in headed bolt with bolt diameter $d_{\text{o}} = 1$ in and head diameter $d_{\text{h}} = 1.5$ in,

$$A_{\text{bearing}} = \frac{\pi}{4}(d_{\text{h}}^2 - d_{\text{o}}^2) = \frac{\pi}{4}(1.5^2 - 1.0^2) = 0.9817 \text{ in}^2,$$

$$N_{\text{pullout},n} = 1.0 \times 8 \times 0.9817 \times 6.12 = 48.06 \text{ kips}. \tag{A.7.3}$$

Concrete Breakout Strength for Anchors in Tension

From Clause D.5.2 of ACI 349-06 (2007a), the nominal concrete breakout strength of a single anchor in tension is

$$N_{\text{breakout},n} = \frac{A_{\text{Nc}}}{A_{\text{Nc0}}}\,\psi_{\text{ed,N}}\,\psi_{\text{c,N}}\,\psi_{\text{cp,N}}\,N_{\text{b}}, \qquad \text{(D-4, ACI 349-06)}$$

where

- for a single stud away from edge $\dfrac{A_{\text{Nc}}}{A_{\text{Nc0}}} = 1.0$,
- $\psi_{\text{ed,N}} = 1.0$ is the modification factor for edge (Clause D.5.2.5),
- $\psi_{\text{c,N}} = 1.0$ is the modification factor for concrete cracking (Clause D.5.2.6),
- $\psi_{\text{cp,N}}$ is the modification factor for splitting control applicable to post-installed anchors only, $\psi_{\text{cp,N}} = 1$ is taken for cast-in anchors (Clause D.5.2.7),
- N_{b} is the basic concrete breakout strength of a single anchor in tension in cracked concrete given by

  $$N_{\text{b}} = k_{\text{c}}\sqrt{f'_{\text{c}}}\,h_{\text{ef}}^{1.5}, \qquad \text{(D-7, ACI 349-06)}$$

  in which $k_{\text{c}} = 24$ for cast-in headed stud, and h_{ef} is the embedment length.

Hence, the concrete breakout strength of a single anchor in tension is

$$N_{\text{b}} = 24\times\sqrt{6120}\times 16^{1.5} = 120162 \text{ lb} = 120.0 \text{ kips}, \qquad \text{(A.7.4)}$$

$$N_{\text{breakout},n} = 1.0\times 1.0\times 1.0\times 1\times 120.0 = 120.0 \text{ kips}. \qquad \text{(A.7.5)}$$

EPRI-TR-103959 (page 8-11) gives the median breakout strength of concrete

$$N_{\text{breakout},m} = 4\sqrt{f'_{\text{c}}}\,\pi\,l_{\text{e}}\,(l_{\text{e}}+d_{\text{h}})\cdot F_{\text{EQN}} \qquad \text{(A.7.6)}$$

$$= 4\times\sqrt{6120}\times\pi\times 16\times(16+1.5)\times 1.4 = 385.4 \text{ kips}, \qquad \text{(A.7.7)}$$

in which a median capacity factor of $F_{\text{eqn}} = 1.4$ is used to compensate for the bias between the ACI 349-97 capacity and the median capacity.

Concrete Pryout Strength for Anchors Far from a Free Edge in Shear From Clause D.6.3.1 of ACI 349-06 (2007a), the nominal pryout strength of a single anchor in shear is

$$V_{\text{pryout},n} = k_{\text{cp}}\,N_{\text{breakout},n}, \qquad \text{(D-28, ACI 349-06)}$$

where $k_{cp} = 2.0$ when the effective embedment depth $h_{ef} \geqslant 2.5$ in, and N_{cb} is the nominal concrete breakout strength for a single anchor in tension, given in equation (D-4, ACI 349-06).

Hence, for the anchor bolts of the heat exchanger, the concrete pryout strength of a single anchor in shear is, using equation (A.7.5),

$$V_{\text{pryout},n} = 2.0 \times 120.0 = 240.0 \text{ kips}. \tag{A.7.8}$$

Shear-Friction Failure

EPRI-TR-103959 (EPRI, 1994, page 8-11) gives a formula for evaluating the median shear-friction strength in terms of the ultimate stress

$$V_{\text{shear-friction},m} = 0.9\mu A_{\text{net}} \sigma_{\text{u}} = 0.9 \times 1.0 \times 0.6057 \times 64 = 34.89 \text{ kips}. \tag{A.7.9}$$

Failure of Support Base Plate due to Bending

The support base plate bending capacity can be realistically estimated using yield line theory. A postulated yield line pattern for the steel base plate is shown in Figure A.5. Because of symmetry, x is the only unknown dimension, to be determined so that the minimum capacity is obtained.

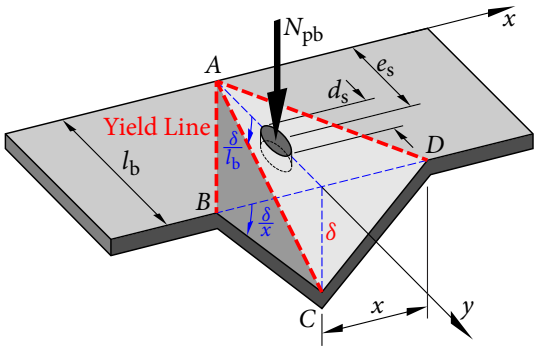

Figure A.5 Yield line pattern of the base plate

Give point C of the plate a small downward virtual displacement δ. The external work done by force N_{pb} from the anchor bolt is

$$N_{\text{pb}} \cdot \frac{e_{\text{s}}}{l_{\text{b}}} \delta.$$

Denote $M_{\mathrm{y}} = \frac{1}{4}(1 \cdot t_{\mathrm{b}}^2)\sigma_{\mathrm{y}}$ as the plastic (yield) moment of resistance per unit length. The internal work done is summarized in the following table

Segment	Components of Rotation		Components of Work	
	θ_x	θ_y	$M_{\mathrm{y},x} \cdot \theta_x \cdot y_0$	$M_{\mathrm{y},y} \cdot \theta_y \cdot x_0$
ABC	$\dfrac{\delta}{x}$	$\dfrac{\delta}{l_{\mathrm{b}}}$	$M_{\mathrm{y}} \cdot \dfrac{\delta}{x} \cdot (2l_{\mathrm{b}} - d_{\mathrm{s}})$	$M_{\mathrm{y}} \cdot \dfrac{\delta}{l_{\mathrm{b}}} \cdot x$
ADC	$\dfrac{\delta}{x}$	$\dfrac{\delta}{l_{\mathrm{b}}}$	$M_{\mathrm{y}} \cdot \dfrac{\delta}{x} \cdot (2l_{\mathrm{b}} - d_{\mathrm{s}})$	$M_{\mathrm{y}} \cdot \dfrac{\delta}{l_{\mathrm{b}}} \cdot x$

and is given by

$$M_{\mathrm{y}} \left\{ 2\frac{\delta}{x}(2l_{\mathrm{b}} - d_{\mathrm{s}}) + 2\frac{\delta}{l_{\mathrm{b}}}x \right\},$$

in which the slotted bolt hole length d_{s} is used, since it is the critical case.

From the Principle of Virtual Work

$$N_{\mathrm{pb}} \cdot \frac{e_{\mathrm{s}}}{l_{\mathrm{b}}}\delta = 2M_{\mathrm{y}} \left\{ \frac{\delta}{x}(2l_{\mathrm{b}} - d_{\mathrm{s}}) + \frac{\delta}{l_{\mathrm{b}}}x \right\},$$

which gives

$$N_{\mathrm{pb}} = \frac{2l_{\mathrm{b}}M_{\mathrm{y}}}{e_{\mathrm{s}}}\left(\frac{2l_{\mathrm{b}} - d_{\mathrm{s}}}{x} + \frac{x}{l_{\mathrm{b}}}\right), \qquad M_{\mathrm{y}} = \frac{t_{\mathrm{b}}^2}{4}\sigma_{\mathrm{y}}. \tag{A.7.10}$$

For the minimal value of N_{pb},

$$\frac{\mathrm{d}N_{\mathrm{pb}}}{\mathrm{d}x} = \frac{2l_{\mathrm{b}}M_{\mathrm{y}}}{e_{\mathrm{s}}}\left(-\frac{2l_{\mathrm{b}} - d_{\mathrm{s}}}{x^2} + \frac{1}{l_{\mathrm{b}}}\right) = 0 \quad \Longrightarrow \quad x = l_{\mathrm{b}}\sqrt{2 - \frac{d_{\mathrm{s}}}{l_{\mathrm{b}}}}\,. \tag{A.7.11}$$

Substituting equation (A.7.11) into (A.7.10) gives the median capacity of the base plate

$$N_{\mathrm{pb},m} = \sqrt{2 - \frac{d_{\mathrm{s}}}{l_{\mathrm{b}}}} \cdot \frac{l_{\mathrm{b}}t_{\mathrm{b}}^2}{e_{\mathrm{s}}}\sigma_{\mathrm{y}} \tag{A.7.12}$$

$$= \sqrt{2 - \frac{3.125}{6}} \times \frac{6 \times 0.5^2}{3} \times 44 = 26.76 \text{ kips}. \tag{A.7.13}$$

Failure of Fillet Weld between Saddle Plate and Base Plate

Fillet welds are commonly used in structures. A fillet weld can be loaded in any direction in shear, compression, or tension. However, it always fails in shear. The weld area A_{w} resisting

these applied loads is given by an effective length l_w times the effective throat thickness, which is equals to $t_w/\sqrt{2} = 0.707\,t_w$, where t_w is the weld leg size, as shown in Figure A.6; hence $A_w = 0.707\,l_w\,t_w$.

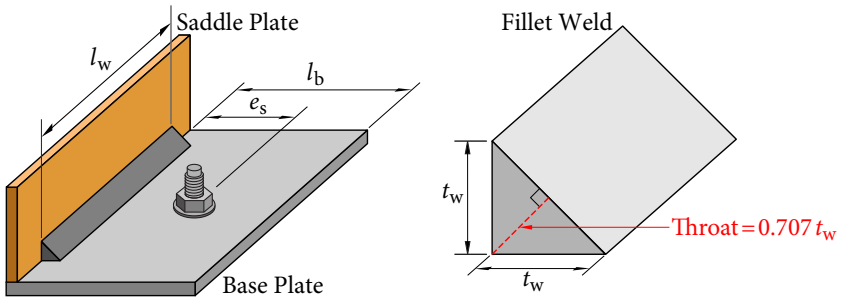

Figure A.6 Fillet weld failure

Formulas for evaluating the capacities of fillet-weld connections are given in Appendix P of EPRI-NP-6041-SL (EPRI, 1991a) and summarized in Table 3-10 of EPRI-TR-103959 (1994), in which $F_{EXX,m}$ and F_{EXX} are the median and nominal tensile strength of electrode. EPRI-TR-103959 (1994) recommends $F_{EXX,m} = 1.1\,F_{EXX}$.

The median capacity $P_{weld,m}$ can be written in the general form as

$$P_{weld,m} = 0.84\,A_w\,F_{EXX,m}\,(1.0 + 0.50\sin^{1.5}\theta), \tag{A.7.14}$$

where θ is the angle of loading measured from the weld longitudinal axis. In longitudinal direction, $\theta = 0$, and equation (A.7.14) reduces to

$$P_{weld,m} = 0.84\,A_w\,F_{EXX,m}\,(1.0 + 0.50\sin^{1.5} 0^\circ) = 0.84\,A_w\,F_{EXX,m};$$

in transverse direction, $\theta = 90^\circ$, and equation (A.7.14) reduces to

$$\begin{aligned} P_{weld,m} &= 0.84\,A_w\,F_{EXX,m}\,(1.0 + 0.50\sin^{1.5} 90^\circ) = 0.84\,A_w\,F_{EXX,m} \times 1.5 \\ &= 1.26\,A_w\,F_{EXX,m}. \end{aligned}$$

For the heat exchanger, the equivalent median tension capacity of the bolt based on the median capacity of the weld in the transverse direction is given by

$$A_w = 0.707\,l_w\,t_w = 0.707 \times 6 \times 0.25 = 1.0605\ \text{in}^2,$$

$$P_{weld,m} = 1.26\,A_w\,F_{EXX,m} = 1.26 \times 1.0605 \times (1.1 \times 60) = 88.19\ \text{kips}. \tag{A.7.15}$$

Bibliography

Abrahamson, N.A. and Silva, W.J., 1997. Empirical response spectral attenuation relations for shallow crustal earthquakes. *Seismological Research Letters*, **68**(1), 94–127.

Abrahamson, N.A. and Silva, W.J., 2008. Summary of the Abrahamson & Silva NGA ground-motion relations. *Earthquake Spectra*, **24**(1), 67–97.

ACI, 2007a. *Code Requirements for Nuclear Safety-Related Concrete Structures (ACI 349-06) and Commentary*, volume ACI 349-06. American Concrete Institute (ACI).

ACI, 2007b. *Guide to the Concrete Capacity Design (CCD) Method—Embedment Design Examples*, volume ACI 349.2R-07. American Concrete Institute (ACI).

Adams, J. and Halchuk, S., 2003. Fourth generation seismic hazard maps of Canada: Values for over 650 Canadian localities intended for the 2005 National Building Code of Canada. *Geological Survey of Canada, Open-File 4459*.

Anagnos, T. and Kiremidjian, A.S., 1988. A review of earthquake occurrence models for seismic hazard analysis. *Probabilistic Engineering Mechanics*, **3**(1), 3–11.

ASCE, 1998. *Seismic Analysis of Safety-Related Nuclear Structures and Commentary, ASCE Standard* 4-98. American Society of Civil Engineers (ASCE).

ASCE, 2005. *Seismic Design Criteria for Structures, Systems, and Components in Nuclear Facilities, ASCE/SEI Standard* 43-05. Structural Engineering Institute, American Society of Civil Engineers (ASCE).

Asgarian, B., Khazaee, H., and Mirtaheri, M., 2012. Performance evaluation of different types of steel moment resisting frames subjected to strong ground motion through incremental dynamic analysis. *International Journal of Steel Structures*, **12**(3), 363–379.

Atkinson, G.M. and Boore, D.M., 2006. Earthquake ground-motion prediction equations for eastern North America. *Bulletin of the Seismological Society of America*, **96**(6), 2181–2205.

Atkinson, G.M. and Goda, K., 2013. *Probabilistic seismic hazard analysis of civil infrastructure*. Woodhead Publishing, Ltd., Cambridge, UK.

Baker, J.W. and Cornell, C.A., 2006A. Correlation of response spectral values for multicomponent ground motions. *Bulletin of the Seismological Society of America*, **96**(1), 215–227.

Baker, J.W. and Cornell, C.A., 2006B. Which spectral acceleration are you using. *Earthquake Spectra*, **22**(2), 293–312.

Baker, J.W. and Jayaram, N., 2008. Correlation of spectral acceleration values from NGA ground motion models. *Earthquake Spectra*, **24**(1), 299–317.

Bazzurro, P. and Cornell, C.A., 1999. Disaggregation of seismic hazard. *Bulletin of the Seismological Society of America*, **89**(2), 501–520.

Bazzurro, P. and Cornell, C.A., 2002. Vector-valued probabilistic seismic hazard analysis. In *Proceedings of 7th U.S. National Conference on Earthquake Engineering*, Boston, Massachusetts.

Bertero, R.D. and Bertero, V.V., 2002. Performance-based seismic engineering: The need for a reliable conceptual comprehensive approach. *Earthquake Engineering and Structural Dynamics*, **31**, 627–652.

Bianchini, M., Diotallevi, P.P., and Baker, J.W., SEPTEMBER, 2009. Prediction of inelastic structural response using an average of spectral accelerations. In *10th International Conference on Structural Safety and Reliability (ICOSSAR09)*, Osaka, Japan.

Boore, D.M. and Atkinson, G.M., 2008. Ground-motion prediction equations for the average horizontal component of PGA, PGV, and 5%-damped PSA at spectral periods between 0.01 s and 10.0 s. *Earthquake Spectra*, **24**(1), 99–138.

Bournonville, M., Dahnke, J., and Darwin, D., 2004. Statistical analysis of the mechanical properties and weight of reinforcing bars. *University of Kansas Report*.

Campbell, K.W. and Bozorgnia, Y., 2008. NGA ground motion model for the geometric mean horizontal component of PGA, PGV, PGD and 5% damped linear elastic response spectra for periods ranging from 0.01 to 10 s. *Earthquake Spectra*, **24**(1), 139–171.

Chiou, B. S.-J. and Youngs, R.R., 2008. An NGA model for the average horizontal component of peak ground motion and response spectra. *Earthquake Spectra*, **24**(1), 173–215.

Cornell, C.A. and Winterstein, S.R., 1988. Temporal and magnitude dependence in earthquake recurrence models. *Bulletin of the Seismological Society of America*, **28**(4), 1522–1537.

Cornell, C.A., 1968. Engineering seismic risk analysis. *Bulletin of the Seismological Society of America*, **58**(5), 1583–1606.

Cosentino, P. and Ficarra, V., 1977. Truncated exponential frequency-magnitude relationship in earthquake statistics. *Bulletin of the Seismological Society of America*, **67**, 1615–1623.

EPRI, 1991A. *A Methodology for Assessment of Nuclear Power Plant Seismic Margin*, volume EPRI-NP-6041-SL. Electric Power Research Institute, California.

EPRI, 1991B. *Seismic Verification of Nuclear Plant Equipment Anchorage (Revision 1), Volume 1: Development of Anchorage Guidelines*, volume EPRI-NP-5228-SL. Electric Power Research Institute, California.

EPRI, 1994. *Methodology for Developing Seismic Fragilities*, volume EPRI-TR-103959. Electric Power Research Institute, Palo Alto, CA.

EPRI, 2000. *IPEEE Seismic Insights: Revision to EPRI Report TR-112932*. Electric Power Research Institute, Palo Alto, CA.

EPRI, 2007. *Program on Technology Innovation: The Effects of High Frequency Ground Motion on Structures, Components, and Equipment in Nuclear Power Plants*, volume 1015108. Electric Power Research Institute, California.

EPRI, 2009. *Seismic Fragility Applications Guide Update*, volume EPRI-TR-1019200. Electric Power Research Institute, Palo Alto, CA.

EPRI, 2012. *Guidelines for Nuclear Plant Response to Earthquake*. Electric Power Research Institute, Palo Alto, CA. 1025288.

EPRI, 2013. *Seismic Evaluation Guildance: Screening, Prioritization and Implementation Details (SPID) for the Resolution of Fukushima Near-Term Task Force Recommendation 2.1*. Electric Power Research Institute, Palo Alto, CA. 1025287.

FEMA, 2006. *Next-Generation Performance-Based Seismic Design Guidelines: Program Plan for New and Existing Buildings,* FEMA-*445*. Federal Emergency Management Agency, Washington, D.C.

Gelman, A., Carlin, J.B., Stern, H.S., Dunson, D.B., Vehtari, A., and Rubin, D.B., 2013. *Bayesian data analysis*. CRC press.

Gupta, A. and Krawinkler, H., 1999. *Seismic demands for performance evaluation of steel moment resisting frame structures*. The John A. Blume Earthquake Engineering Center, Report No. 132, California.

Gutenberg, B. and Richter, C.F., 1944. Frequency of earthquakes in California. *Bulletin of the Seismological Society of America*, **34**(4), 185–188.

Halchuk, S. and Adams, J., 2004. Deaggregation of seismic hazard for selected Canadian cities. In *Proceedings of 13th World Conference on Earthquake Engineering*, Vancouver, Canada. Paper No. 2470.

Hamid, A., Abboud, B., Farah, M., Hatem, M., and Harris, H., 1989. *Response of Reinforced Block Masonry Walls to Out-of-plane Static Loads. Report No. 3.2(a)*. U.S.-Japan Coordinated Program for Masonry Building Research, Philadelphia, PA.

Hanks, T.C. and Bakun, W.H., 2002. A bilinear source-scaling model for **M**-log A observations of continental earthquakes. *Bulletin of the Seismological Society of America*, **92**(5), 1841–1846.

Hanks, T.C. and Bakun, W.H., 2008. **M**-logA observations for recent large earthquakes. *Bulletin of the Seismological Society of America*, **98**(1), 490–494.

Hanks, T.C. and Kanamori, H., 1979. A moment magnitude scale. *Journal of Geophysical Research: Solid Earth (1978-2012)*, **84**(B5), 2348–2350.

Hardebeck, J.L., 2013. Geometry and earthquake potential of the Shoreline fault, central California. *Bulletin of the Seismological Society of America*, **103**(1), 447–462.

Jayaram, N. and Baker, J.W., 2008. Statistical tests of the joint distribution of spectral acceleration values. *Bulletin of the Seismological Society of America*, **98**(5), 2231–2243.

Jeong, S.H. and Elnashai, A.S., 2007. Probabilistic fragility analysis parameterized by fundamental response quantities. *Engineering Structures*, **29**, 1238–1251.

Kennedy, R.P., Cornell, C.A., Campbell, R.D., Kaplan, S., and Perla, H.F., 1980. Probabilistic seismic safety study of an existing nuclear power plant. *Nuclear Engineering and Design*, **59**, 315–338.

Kennedy, R.P. and Ravindra, M.K., 1984. Seismic fragilities for nuclear power plant studies. *Nuclear Engineering and Design*, **79**, 47–68.

Kramer, S.L., 1996. *Geotechnical Earthquake Engineering*. Prentice-Hall, New Jersey.

Kulak, G.K., Fisher, J.W., and Struik, J.H.A., 1987. *Guide to Design Criteria for Bolted and Riveted Joints*. John Wiley & Sons, New York.

Kulak, G.K., Fisher, J.W., and Struik, J.H.A., 2001. *Guide to Design Criteria for Bolted and Riveted Joints:*. American Institution of Steel Construction (AISC), second edition.

Li, Z.-X., Li, Z.-C., and Shen, W.-X., 2005. Sensitivity analysis for floor response spectra of nuclear reactor buildings (chinese). *Nuclear Power Engineering*, **26**(1), 44–50.

Matthews, M.V., Ellsworth, W.L., and Reasenberg, P.A., 2002. A Brownian model for recurrent earthquakes. *Bulletin of the Seismological Society of America*, **92**(6), 2233–2250.

McGuire, R., 1993. Computation of seismic hazard. *Annals of Geophysics*, **36**, 181–200.

McGuire, R., 1995. Probabilistic seismic hazard analysis and design earthquakes: Closing the loop. *Bulletin of the Seismological Society of America*, **85**(5), 1275–1284.

McGuire, R., 2004. *Seismic Hazard and Risk Analysis*. Earthquake Engineering Research Institute, Oakland.

Moehle, J. and Deierlein, G.G., 2004. A framework methodology for performance-based earthquake engineering. In *Proceedings of the 13th World conference on earthquake engineering*, p. 3812–3814, Vancouver, Canada.

MSJC, 2011. *Building Code Requirements and Specification for Masonry Structures, (TMS 402–11/ACI 530-11/ASCE 5–11 and TMS 602–11/ACI 530.1-11/ASCE 6–11)*. Masonry Standards Joint Committee (MSJC), Boulder, CO: The Masonry Society; Farmington Hills, MI: American Concrete Institute; Reston, VA: American Society of Civil Engineers.

NBCC, 2010. *National Building Code of Canada* 2010. National Research Council of Canada, Ottawa, Ontario.

NCMA, 1994. *Research Evaluation of the Flexural Tensile Strength of Concrete Masonry, Proj. No. 73-172*. National Concrete Masonry Association, Herndon, VA.

NCMA, 2007. *Section Properties Of Concrete Masonry Walls, 14-1B*. National Concrete Masonry Association TEK, Herndon, VA.

Ni, S.-H., Zhang, D.-Y., Xie, W.-C., and Pandey, M.D., 2012. Vector-valued uniform hazard spectra. *Earthquake Spectra*, **28**, 1549–1568.

Ni, S.-H., 2012. *Design Earthquakes Based on Probabilistic Seismic Hazard Analysis*. PhD thesis, University of Waterloo, Waterloo, Ontario, Canada.

NUREG, 1978. *Development of Criteria for Seismic Review of Selected Nuclear Power Plants*, volume NUREG/CR-0098.

NUREG, 1985. *An Approach to the Quantification of Seismic Margins in Nuclear Power Plants*, volume NUREG/CR-4334. Lawrence Livermore National Laboratory.

PG&E, 2011. *Section 6: Seismic Hazard Analysis, Shoreline Fault Zone Report. Report to the U.S. Nuclear Regulatory Commission*. Pacific Gas and Electric Company, San Francisco, CA.

Schwartz, D.P. and Coppersmith, K.J., 1984. Fault behavior and characteristic earthquakes: Examples from the Wasatch and San Andreas fault zones. *Journal of Geophysical Research: Solid Earth (1978-2012)*, **89**(B7), 5681–5698.

Shinozuka, M., Feng, M.Q., Lee, J., and Naganuma, T., 2000. Statistical analysis of fragility curves. *Journal of Engineering Mechanics*, **126**(12), 1224––1231.

Shome, N., 1999. *Probabilistic seismic demand analysis of nonlinear structures*. PhD thesis, Stanford University, Stanford, California.

Silva, W.J., Youngs, R.R., and Idriss, I.M., 1999. Development of design response spectral shapes for Central and Eastern U.S. (CEUS) and Western U.S. (WUS) rock site conditions. In *Proc. of the OECE-NEA Workshop on Engineering Characterization of Seismic Input Nov*, 15–17.

Singh, M.P., 1975. Generation of seismic floor spectra. *Journal of the Engineering Mechanics Division*, **101.5**, 593–607.

T.G., Clayford, 2002. Quality control of concrete masonry compressive strength. *The Masonry Society Journel*, **20**(1).

Tothong, P. and Luco, N., 2007. Probabilistic seismic demand analysis using advanced ground motion intensity measures. *Earthquake Engineering and Structural Dynamics*, **36**, 1837–1860.

USGS and CGS, 2006. Quaternary fault and fold database for the United States, accessed Jan. 9, 2014, from USGS website: http//earthquake.usgs.gov/hazards/qfaults/.

USGS and CGS, 2013. Uniform California earthquake rupture forecast, version 3 (UCERF3): the time-independent model. *USGS Open-File Report* 2013–1165, *CGS Special Report* 228.

USGS, 2008. Documentation for the 2008 update of the United States National Seismic Hazard Maps. *U.S. Geological Survey Open-File Report 2008-1128*.

USNRC, 1973. *Design Response Spectra for Seismic Design of Nuclear Power Plants, Regulatory Guide* 1.60. U.S. Nuclear Regulatory Commission.

USNRC. Regulatory Guide 1.122, Development of floor design response spectra for seismic design of floor-supported equipment or components, 1978.

USNRC, 2006. *Combining Modal Responses and Spatial Components in Seismic Response Analysis*, volume USNRC REGULATORY GUIDE 1.92 (REVISION 2).

USNRC, 2007. *A Performance-based Approach to Define the Site-specific Earthquake Gound Motion, Regulatory Guide* 1.208. U.S. Nuclear Regulatory Commission, Washington, DC.

USNRC, 2012A. *Confirmatory Analysis of Seismic Hazard at the Diablo Canyon Power Plant from the Shoreline Fault Zone*, volume RESEARCH INFORMATION LETTER 12-01.

USNRC, 2012B. *Guidance on Performing a Seismic Margin Assessment in Response to the March 2012 Request for Information Letter*, volume USNRC/JLD-ISG-2012-04.

Villaverde, R., 2009. *Fundamental concepts of earthquake engineering*. CRC/Taylor & Francis.

Wang, Z.-L., Ni, S.-H., Xie, W.-C., and Pandey, M.D., JUNE 16-20 2013A. Computationally efficient seismic risk analysis for engineering structures using seismic hazard deaggrega-

tion. In *Proceedings of the 11th International Conference on Structural Safety & Reliability*, New York, NY.

Wang, Z.-L., Pandey, M.D., and Xie, W.-C., June 9-12 2013b. A bayesian formulation of seismic fragility analysis of safety related equipment. In *Proceedings of the 34th CNS Annual Conference*, Toronto, Ontario, Canada.

Wang, Z.-L., Pandey, M.D., and Xie, W.-C., August 24-28 2014. Seismic fragility analysis of the block masonry wall in nuclear power plants. In *Proceedings of the 19th Pacific Basin Nuclear Conference*, Vancouver, British Columbia, Canada.

Wells, D.L. and Coppersmith, K.J., 1994. New empirical relationships among magnitude, rupture length, rupture width, rupture area, and surface displacement. *Bulletin of the Seismological Society of America*, **84**(4), 974–1002.

Wen, Y.K., 2001. Reliability and performance-based design. *Structural Safety*, **23**, 407–428.

WGCEP, 2003. Earthquake probabilities in the San Francisco Bay Region: 2002–2031. *U.S. Geological Survey Open-File Report 03-214*.

Wills, C.J., Weldon, R.J., and Bryant, W.A., 2008. Appendix A: California fault parameters for the National Seismic Hazard Map and Working Group on California Earthquake Probabilities. *U.S. Geological Survey Open File Report 2007-1437A*.

Youngs, R.R. and Coppersmith, K.J., 1985. Implications of fault slip rates and earthquake recurrence models to probabilistic seismic hazard estimates. *Bulletin of the Seismological society of America*, **75**(4), 939–964.